The Synthesis and Characterization of Nanothermites and Their Precursors

A Thesis Submitted to the Division of Graduate Studies
of the Royal Military College of Canada
by

Wan Lin Yvette Liu

In Partial Fulfillment of the Requirements for the Degree of
Master of Science

July, 2023

This thesis is dedicated to my husband, Zhe She, without him talking me into thinking I needed another degree, this would never happen.

I'd also like to dedicate this thesis to my children, Marcus and Hadrian. They did not help much, but they are what get me out of bed and get to work each morning.

Acknowledgements

Much thanks and gratitude for:

- Dr. Fiona Kelly. For her infinite patience and tolerance of my questions and the constant knocking on her door. I will forever be grateful for her guidance and support, both in science and in life.

- Dr. Jason Loiseau. For providing the engineering perspective.

- Dr. Pavel Samuleev. For the frequently solicited and occasional unsolicited helpful advice and tips.

- Heather Hennessy and Laura Brockman. For sharing office space, snacks, plants, and baby photos with me, listening to my rants and complaints, and most importantly for keeping me sane by sharing their friendship with me.

Abstract

Nanothermites have attracted attention as “next generation” or “green alternative” energetic materials. The advantages of nanothermites include the ability to alter the fuel and oxidizer ratio, options of different fuels and oxidizers, and the possibility of remote ignition. However, nanothermites are exceedingly sensitive to friction and electrostatic discharge. Their sensitivity and unpredictability represent a safety issue during production and use and thus prevents the transfer of nanothermites to real-life applications. The main goal of the project is to minimize the sensitivities of nanothermites.

This project is divided into two parts, as two different routes were used to achieve the goal of desensitizing nanothermites.The first part of the project investigated if sensitivities of nanothermites could be described as a function of the different layers of nanothermites. Three different types of nano aluminum were used, nano aluminum with oxide passivation (O-Al), palmitic acid coated nano aluminum (L-Al), and Viton coated nano aluminum (V-Al). Nanothermites were made by sonicating each nano aluminum with MoO_3 at a 1.2:1 molar ratio in either acetone or isopropanol (IPA). Nanothermites were allowed to settle for various amount of time and pipetted into vials to dry layer by layer. Coatings affect the settling significantly as both L-Al and V-Al started to settle within the first 15 minutes after sonication while O-Al was evenly distributed among the layers. However, it appeared that nanothermite sensitivity does not have a clear relationship with either aluminum coating or the layers of nanothermites.

The goal of the second part of the project was to find oxidizers that could make nanothermites less sensitive. It focused on the synthesis and characterization of nano metal molydates, as well as the characterization of nano aluminum made by wire explosion (Alex). Co-precipitation method (CPS) and solution combustion synthesis (SCS) were used to synthesize the molybdates. The identities of the products were confirmed using X-ray Powder Diffraction (XRD). $CaMoO_4$, $SrMoO_4$, and $BaMoO_4$ were synthesized successfully using CPS and $MgMoO_4$, $CaMoO_4$, $SrMoO_4$, $NiMoO_4$, $ZnMoO_4$, Fe_2MoO_4, and $CuMoO_4$ were synthesized using SCS with varying degrees of impurities. Products of CPS were nano sized distinct particles while products of SCS exhibit porous structures composed of heavily agglomerated nanoparticles. Additional characterizations, resistivities and surface areas, of $MgMoO_4$, $CaMoO_4$, $SrMoO_4$, and $BaMoO_4$ synthesized using both methods were completed. The products of SCS had lower resistivity and lower surface area than those of CPS. The active content of Alex was determined to be 90.4%. Aging tests were performed to determine the stability of Alex, which was believed to be extremely sensitive to moisture. Aging tests found that contrary to popular belief, Alex was able to resist oxidation by water for up to 100 days at a humidity level of

32.5%; however Alex wasoxidized completely in approximately 50 days under high humidity condition, at a humidity of 75.5%.

$Al/CaMoO_4$ (CPS), $Al/SrMoO_4$ (CPS), $Al/BaMoO_4$ (CPS), $Al/MgMoO_4$ (SCS), $Al/CaMoO_4$ (SCS), and $Al/SrMoO_4$ (CPS) nanothermites were made, and SEM images were taken. Nano aluminum particles were mixed more homogeneously with the CPS molybdates that aluminum particles mixed relatively evenly in between molybdate particles. SCS molybdates contained heavily agglomerated particles that could not be broken up by sonication. In some areas, aluminum particles were shown to cluster in one area instead of spreading out between the molybdates; in other areas, aluminum particles spread out and covered the surface of the molybdate. Possible future direction includes focusing on thermochemical, friction, and electrostatic discharge testing.

Résumé

Les nanothermites ont attiré l'attention en tant que matériaux énergétiques de « nouvelle génération » ou « alternative verte ». Les avantages des nanothermites comprennent la possibilité de modifier le rapport carburant/oxydant, les options de différents carburants et oxydants et la possibilité d'allumage à distance. Cependant, les nanothermites sont extrêmement sensibles au frottement et au décharge électrostatique. Leur sensibilité et leur imprévisibilité représentent un problème de sécurité durant la production et de l'utilisation et empêchent ainsi le transfert des nanothermites vers des applications réelles. L'objectif principal du projet est de minimiser les sensibilités des nanothermites.

Ce projet est divisé en deux parties. La première partie du projet a étudié les différentes couches de nanothermites. Trois types différents de nano-aluminium ont été utilisés, le nano-aluminium avec passivation d'oxyde (O-Al), le nano-aluminium revêtu d'acide palmitique (L-Al) et le nano-aluminium revêtu de Viton (V-Al). Les nanothermites ont été fabriquées en sonifiant chaque nanoaluminium avec du MoO3 à un rapport molaire de 1,2 :1 dans de l'acétone ou de l'isopropanol (IPA). Les nanothermites ont été laissées se déposer pendant une durée variable et pipetées dans des flacons pour sécher couche par couche. Les revêtements affectent la sédimentation de manière significative car L-Al et V-Al se sont comportés différemment de O-Al. Cependant, il est apparu que la sensibilité à la nanothermite n'a pas de relation claire avec le revêtement d'aluminium ou les couches de nanothermites.

La deuxième partie du projet portait sur la synthèse et la caractérisation de nanomolybdates métalliques, ainsi que sur la caractérisation de nanoaluminium fabriqué par explosion de fil (Alex). La méthode de co-précipitation (CPS) et la synthèse par combustion en solution (SCS) ont été utilisées pour synthétiser les molybdates. L'identité des produits a été confirmée par diffraction des rayons X sur poudre (XRD). $CaMoO_4$, $SrMoO_4$ et $BaMoO_4$ ont été synthétisés avec succès à l'aide de CPS et $MgMoO_4$, $CaMoO_4$, $SrMoO_4$, $NiMoO_4$, $ZnMoO_4$, Fe_2MoO_4 et $CuMoO_4$ ont été synthétisés à l'aide de SCS avec divers degrés d'impuretés. Les produits de CPS étaient des particules distinctes de taille nanométrique tandis que les produits de SCS présentent des structures poreuses composées de nanoparticules fortement agglomérées. Des caractérisations supplémentaires, des résistivités et des surfaces de $MgMoO_4$, $CaMoO_4$, $SrMoO_4$ et $BaMoO_4$ synthétisés à l'aide des deux méthodes ont été réalisées. Les produits de SCS avaient une résistivité et une surface plus faibles que ceux de CPS. Le contenu actif d'Alex a été déterminé à 90,4 %. Des tests de vieillissement ont révélé qu'Alex était capable de résister à l'oxydation par l'eau jusqu'à 100 jours à un taux d'humidité de 32,5 % et qu'il était complètement oxydé en environ 50 jours à un taux d'humidité de 75,5 %.

Des nanothermites $Al/CaMoO_4$ (CPS), $Al/SrMoO_4$ (CPS), $Al/BaMoO_4$ (CPS), $Al/MgMoO_4$ (SCS), $Al/CaMoO_4$ (SCS) et $Al/SrMoO_4$ (CPS) ont été réalisées et des images SEM ont été pris. Les nanoparticules d'aluminium ont été mélangées de manière plus homogène avec les molybdates CPS que les particules d'aluminium mélangées de manière relativement uniforme entre les particules de molybdate. Les molybdates SCS contenaient des particules fortement agglomérées qui ne pouvaient pas être brisées par sonication. Dans certaines régions, il a été démontré que les particules d'aluminium se regroupaient dans une zone au lieu de se répandre entre les molybdates; dans d'autres zones, des particules d'aluminium s'étalent et recouvrent la surface du molybdate. Les travaux futurs porteront sur les tests thermochimiques, de frottement et de décharge électrostatique.

List of Symbols, Abbreviation, Acryonyms, and Nomenclature

BAM - Bundesanstalt für Materialforschung und Prüfung
CPS – Co-precipitation Synthesis
DNA – Deoxyribonucleic Acid
DSC – Differential Scanning Calorimeter
EDX – Energy Dispersive X-ray Spectroscopy
EG – Ethylene Glycol
EEW – Electrical Explosion of Wires
ESD – Electrostatic Discharge
FGS – Functionalized Graphene Sheet
GO – Graphite Oxide
HMX – Octahydrotetranitrotetrazine, $C_4H_8N_8O_8$
IPA – Isopropyl Alcohol
L-Al – Palmitic Acid-coated Nano Aluminum
MDM – Meld Dispersion Mechanism
MIC – Metastable Intermolecular Compositions
NAA – Neutron Activation Analysis
O-Al – Nano Aluminum
PRI – Pre-ignition Reaction
RDX –Hexahydrotrinitrotriazine, $C_3H_6N_6O_6$
RGO – Reduced Graphene Oxide
TEG – Triethylene Glycol
SCS – Solution Combustion Synthesis
TGA – Thermogravimetric Analysis
TMD – Theoretical Maximum Density
TNT - Trinitrotoluene
V-Al – Viton-coated Nano Aluminum
XRD – X-ray Powder Diffraction

Table of Contents

List of Tables

List of Figures

1. Introduction

1.1. Objective

Nanothermites are extremely sensitive to friction and ESD that could easily lead to unintentional ignition. Without mitigating these sensitivities, the real-life applications are limited for nanothermites. The goal of this project is to desensitize nanothermites to friction and ESD. The desensitization was attempted with two different approaches.

The first approach examines the sedimentation trends of nanothermites and their precursors, which will be discussed further in Chapter 3. As nanothermites settle after sonication, different layers of nanothermites can be separated. The goal is to find and single out the layers, if any, that exhibit low sensitivities to friction and ESD.

The second approach, discussed in Chapter 4, entails synthesizing and characterizing novel oxidizers. Different synthetic routes were employed to produce oxidizers with different characteristics, such as morphology and surface area. The goal is to produce nanothermites with these oxidizers with minimal sensitivities and to further understand the causes of the sensitivities of these nanothermites.

The structure of this thesis is as followed: a literature review of nanothermites is presented in Chapter 1. Methods of both approaches are described in Chapter 2, the results and discussion of these two approaches are presented in Chapter 3 and 4. Lastly, the project is summarized in Chapter 5, which also includes recommendations for future directions of this project.

1.2. The Chemical Principles of Nanothermites

1.2.1 Thermites and Thermite Reactions

The term thermite reaction was first used to describe the redox reaction between aluminum and Fe_2O_3. This reaction was discovered by Hans Goldschmidt in 1893 (Weiser et al. 2010). Notably, this postdates the synthesis of many organic energetic materials. However, it is significant that aluminum metal was only isolated in the early 19^{th} century, and the cost of its production only fell to viable levels at the end of that century. The thermite reaction has been used as a heat source for railway welding since 1898. Other applications include freestanding insertable heat sources

and methods to produce alumina liners *in situ* for pipes (Fisher and Grubelich, 1998). Access to a wide range of metals and metal oxides means that, in modern systems, the fuel and the oxidizer involved are no longer limited to aluminum and Fe_2O_3. However, for reasons that will be discussed in Section 1.3.1, aluminum is still the most common and the most studied fuel. Thus, unless otherwise stated, aluminum is considered as the fuel of nanothermites in this thesis.

The nature of the thermite reaction is one of oxygen transfer, as shown in Equation 1.1 for idealized divalent metals.

$$M + M'O \rightarrow MO + M' + \Delta H \qquad \text{Equation 1.1}$$

Where M is the metal being oxidized, M′ is the metal being reduced, and ΔH is the heat generated during the reaction (Wang, Munir, and Maximov 1993). The oxygen is transferred from M′ to M to produce a more stable metal oxide, MO. Due to the relative enthalpies of the formation of M′O and MO, it is sometimes possible that a tremendous amount of heat is released during the process of oxygen transfer. However, the energy released from the redox reaction and the adiabatic flame temperature both vary and depend on the combination of fuel and oxidizer. Fisher and Grubelich compiled a comprehensive list of thermite reactions and their theoretical energy of reaction (Fisher and Grubelich 1998). One important point from this work relates to adiabatic flame temperatures and the heat of phase transition. Theoretical adiabatic flame temperatures calculated previously were inaccurately high since the heats of phase transition were not taken into an account.

Compared to other explosives, the reaction rates of thermites are relatively slow. Most explosives have fuels and oxidants in the same molecule. When considering the atomic radius of aluminum, 1.84 Å (Mantina et al., 2009), it is evident that micron-size particles contain very large numbers of atoms. On a micron, rather than Angstrom, scale, the diffusion of oxygen from one metal to another becomes rate limiting and reactions often proceed in seconds rather than the microseconds associated with explosive reactions.

1.2.2 The Differences between Thermites and Nanothermites

Nanothermites, also known as metastable intermolecular compositions (MIC), and thermites have the same stoichiometry and thermodynamics. The same exothermic redox reaction occurs between a metal and a metal oxide. The difference between thermites and nanothermites lies in the particle size of the reactants. The reactants of nanothermites are, rather obviously, nano-sized, whereas thermite reactions typically contain micron-sized materials. The reaction rate of thermites strongly depends on the size of the reactant (Sun, Pantoya, and Simon 2006). When Brown et al.

decreased the size of antimony particles of a 40% antimony Sb/$KMnO_4$ system from 14 to 2μm, the burn rate increased from 5.5 mm/s to 12.5 mm/s. The same trend was observed by varying percentage of the antimony presented in the Sb/$KMnO_4$ (Brown, Taylor, and Tribelhorn 1998). Aumann et al. showed that nanothermites made with aluminum of an average size of 20-50 nm react almost 1000 times faster than traditional micron size thermites (Aumann, Skofronick and Martin, 1995).

The size of the oxidant and fuel particles has a tremendous effect on the proximity of fuel and oxidant atoms. There are approximately 550 atoms across a 100 nm aluminum particle, as opposed to approximately 55,000 atoms across a 10 μm aluminum particle. The shorter diffusion distance between fuel and oxidant in nanothermites significantly decreases the diffusion time, which leads to a much faster reaction rate. In addition, the large surface areas of fuel and oxidant increases the contact surface and therefore, increases the area over which diffusion occurs. The size of the particles also affects the mechanisms with which nanothermites particles react with each other, including how heat is transferred between the molecules and how the fuel is oxidized. Notably, these are frequently not always the same as their micron size counterparts. These mechanisms are described in more detail in the following section.

The particle size of nanothermite is not the only factor that affects the burn velocity of the nanothermites. Other factors that could affect burn velocity include confinement (Malchi et al., 2008), packing density (Pantoya and Granier, 2005), contacting surface area (Shende et al., 2008) and the elemental composition of fuel and oxidizer (Sanders et al., 2007). Although these factors are recognized in many chemistry disciplines, the term confinement is particularly significant in the field of energetic materials. Confinement pertains to physical structures that prevent the expanding gas associated with the reaction of an energetic material from; (a) rapidly diffusing away from the site of reaction, carrying energy with it, and (b) carrying unreacted material away from the reaction, such that the reaction rate is reduced, and the reaction does not reach completion.

1.3 Nanothermite Systems

Conventional nitro-organic explosives such as HMX, RDX, or TNT are monomolecular explosives that contain both fuel (carbon, hydrogen) and oxidizers (oxygen) in one molecule. Their reaction rates for decomposition depend on the intramolecular interactions and the kinetics of decomposition. Since both the oxidizers and fuels are contained within the same molecule, they have higher reaction rates than those of nanothermites. The detonation velocities of HMX, RDX, and TNT are 9.11 km/s, 8.97 km/s, and 6.93 km/s, respectively (Cooper and

Kurowski, 1996); while the highest flame velocity of nanothermite reported is 2.5 km/s (Martirosyan et al. 2009; Wang, Luss, and Martirosyan 2011). The drawback of conventional explosives is that their fuel to oxidizer ratio is rarely ideal, most are deficient in the oxygen required to maximize reaction enthalpy. As a result, they have moderate energy densities that cannot be optimized (Dreizin 2009; Shen et al. 2014).

Nanothermites are made of separate fuels and oxidizers. The performance and reactions depend on the intramolecular interaction between the fuel and oxidizer. Their properties and responses to stimuli depend heavily on the specific fuel and oxidizer combinations and ratios. Different combinations can be chosen to achieve certain desired effects such as high flame temperature (Jacob, Kline, and Zachariah 2018) or minimum gaseous products (Gibot et al. 2021).

1.3.1 Fuel: Nano Aluminum and Others

Aluminum is the most commonly used fuel in nanothermites. To understand why aluminum is such an attractive candidate, the properties of aluminum must be discussed first.

1.3.1.1 Aluminum and Alumina in Nano Aluminum

All aluminum particles consist of a pure aluminum core that is covered by a layer of alumina shell. Different production methods produce a slightly different thicknesses of the shell, but it is generally between 2 - 8 nm (Gromov, Strokova, and Ditts 2010). Due to the small size of nano aluminum particles, the oxide shell takes up a significant portion of the particle. In other words, the surface-to-volume ratio of nano aluminum is notably larger than that of micro aluminum. As a result, some of the characteristics of nano aluminum particles deviate from their micron-size counterpart; these differences in properties have been extensively reviewed (Sundaram, Yang, and Zarko 2015). Nano aluminum has a lower melting point and ignition temperature due to its high surface area to volume ratio; it is also more reactive and has higher electroconductivity than micron-size aluminum (Kwok et al. 2002; Sun et al. 2002; Sun and Simon, 2007).

Although the physical presence of the aluminum shell plays a role in the performance of the nanothermite, it does not react during the nanothermite reaction or contribute to the overall enthalpy. Therefore, the actual amount of “active” aluminum, in its elemental form, needs to be determined. The percentage of aluminum can be measured by more than one technique, with thermogravimetric analysis (TGA) under an air atmosphere and reaction with ethanolic aqueous NaOH being the most common (Puszynski, 2009). In the former technique, as the nano aluminum is

gradually heated, the aluminum core is gradually oxidized into Al_2O_3. In other words, the alumina shell increases in thickness until the whole particle turns into alumina. As the aluminum particles are oxidized, their masses increase due to the addition of oxygen. The mass gain is then used to calculate the amount of aluminum being oxidized during the heating process, and therefore the original active content of the nano aluminum particles (Yarrington et al. 2011). In the latter technique, aluminum active content can be measured using the aqueous ethanolic NaOH reaction method. The core principle of the reaction is that aluminum reacts with water to produce hydrogen gas, as shown in Equation 1.2. By measuring the increased pressure, the amount of aluminum can be calculated (Cliff, Tepper, and Lisetsky, 2001). NaOH catalyzes the reaction by forming sodium ethoxide, C_2H_5ONa, with ethanol. It attacks the alumina shell and exposes the pure aluminum core to water (Puszynski, 2009). The ethanolic aqueous NaOH is the chosen method to measure the aluminum active content in this project, which will be discussed in more detail later chapters.

$$Al + 3H_2O \rightarrow Al(OH)_3 + 3/2\ H_2 \qquad \text{Equation 1.2}$$

1.3.1.2 Nano Aluminum Production

Nano aluminum particles can be synthesized by a few different techniques, such as vapour phase condensation (Schefflan et al., 2006), or electrical explosion of wires (EEW) (Ivanov et al. 2003).

For the vapour phase condensation method, aluminum is raised to a temperature that is significantly above its melting point but still below its boiling point to establish an adequate vapour pressure. The aluminum gas is then carried away and cooled by an inert carrier gas, such as argon. At low partial pressures nanoparticles are formed. At this point, nano aluminum particles can be passivated with coatings (Schefflan et al. 2006).

For the electrical explosion of wire technique, high current pulses are applied to the wire to create high plasma temperature and explosive evaporation of the wires. Each pulse lasts from microseconds to nanoseconds. Ivanov et al. believe this to be a superior method than the vapour phase condensation because all the energy is transmitted directly into heat. Thus, it represents a more efficient way to produce nano aluminum particles (Ivanov et al. 2003).

The most common way of passivating nano aluminum particles is to place them in contact with air in a controlled manner to slowly form the Al_2O_3 shell. Once the shell reaches 5-7 nm, air can longer gain access to the aluminum core; therefore, the passivation layer can stop the further oxidation from air. However, the alumina shell

does not prevent moisture from further oxidizing the aluminum core; therefore, other coatings have been explored to further protect nano aluminum from aging, instead of, or in addition to, the controlled oxidization of aluminum particles (Kwon et al, 2007). For example, succinic acid and ammonium dihydrogen phosphate have been coated on aluminum particles. The coatings did not prevent the aluminum core reacting with water completely but slowed the reaction enough to enable aluminum-based nanothermite to be made using water as the solvent, instead of the usual organic solvents such as hexane or isopropanol (Puszynski et al., 2007).

1.3.1.3 Nano Aluminum as Fuel

Fuel in nanothermites accepts oxygen from the oxidant to produce materials that are more thermodynamically stable than the original compound. Following that principle, any metal that would form a thermodynamically stable oxide could be used. In practice, certain metals and non-metals are more attractive than others. In practical use, nanothermites need to be reasonably stable in air and water. For this reason, some metals are obviously unfit to be used as a fuel as they may react with air and moisture, and even spontaneously ignite in air. In this context, aluminum is probably the most useful element, having high reactivity combined with reasonable air stability.

The low atomic mass of aluminum and the presence of a high readily accessible oxidation state offer favourable properties as a nanothermite fuel. Aluminum oxide has one of the highest molar enthalpies of formation at approximately -1675 kJ/mol. Due to its relatively low atomic mass, 26.97 g/mol, aluminum is also one of the most energy-dense metals (Yen and Wang 2012). These properties are also due, in part, to the low electronegativity of aluminum. Electronegativity is used to describe the ability to gain or lose electrons of an element. Aluminum has an electronegativity value at the lower end of the range, suggesting that energetic reactions occur as a result of electron loss. Its value of 1.61 can be compared to magnesium (1.33) and zinc (1.65) (Radel and Navidi, 1994).

In addition to the low mass of aluminum, high molar enthalpy and low electronegativity, it is also abundant, and its ore is readily available. Widespread aluminum use means that the element, if not the nano materials, can be obtained at a reasonable cost. Its toxicity as bulk metal and in aqueous systems is low. This has the potential to make nanothermite the “green alternative” to replace certain traditional explosives such as lead azide or lead styphnate (Higa, 2007b). Nano aluminum particles are also relatively easy to mass-produce, as discussed above, although the required technology significantly increases their cost and limits access to this resource.

When the chemical properties of aluminum are examined individually, there is almost always a metal that outperforms aluminum. For example, aluminum is not the only metal with relatively low mass and forms stable oxide after combustion. Beryllium can form stable oxide as well, and it is even more energy-dense than aluminum. Every gram of beryllium is able to produce 67 kJ of enthalpy on oxide formation; however, oxide formation has a smaller molar enthalpy at -600 kJ/mol and smaller enthalpy produced per electron. Beryllium is also highly carcinogenic, which makes it unsafe and impractical. Lanthanum also loses three electrons to form its oxide and it is able to produce slightly larger negative molar enthalpy for oxide formation (-1794 kJ/mol) and enthalpy per electron, but since it is a heavier metal than aluminum, its energy density is much lower than that of aluminum (12.8 kJ/g) (Fisher and Grubelich 1998). Lanthanum metal is also not stable in air. Titanium has an even lower electronegativity with a higher oxidation state than aluminum, but it is has a higher molar mass which makes it less energy dense. Considering the above discussion as a whole, it is clear that aluminum represents an excellent fuel candidate.

1.3.1.4 Other options

As attractive as aluminum is, it has not stopped researchers from exploring other potential fuel options. For example, titanium and magnesium have both been studied as alternative fuels to aluminum. Titanium, although not as energy-dense as aluminum, became an interest because it has the potential to generate higher combustion enthalpy per unit volume than aluminum (Rehwoldt et al. 2018). Titanium has a higher oxidation state, which allows it to lose typically four electrons. Therefore, even though it is heavier than aluminum, it still has the potential to generate larger negative enthalpy than aluminum. However, it has significant safety concerns, such a low ignition temperature. Titanium can ignite anywhere between 100ºC - 200ºC (Comet et al., 2019). Magnesium has also been studied as a potential pyrotechnic heater where gaseous products are undesirable. Magnesium-based nanothermite, Mg/Fe_2O_3, produced 7 to 8 times less maximum pressure after ignition compared to the Al/Fe_2O_3 nanothermite. Its burn velocity, however, is significantly lower such that it would not have any practical application as an explosive (Monogarov et al., 2019).

Non-metal fuels have piqued the interests of researchers for their unique properties and benefits. Comet et al. have reported using red phosphorus as a fuel in nanothermites, such as P/NiO, P/Fe_2O_3, and P/CuO. Red phosphorus is a strong reducing agent that has been used widely in pyrotechnics. It generates slightly less enthalpy of oxidation than aluminum. Due to its low sublimation temperature at around 400°C, it produces a large amount of gas, while aluminum does not exhibit this characteristic. The sensitivities and reaction rates of phosphorus-based nanothermites strongly depend on the metal oxides used. For example, while P/NiO

and P/Fe_2O_3 have friction sensitivity greater than 360 N and electrostatic discharge (ESD) sensitivity at 358.69 mJ and 24.12 mJ, respectively, P/CuO shows extreme sensitivity to both (8N and 0.21 mJ). P/CuO reacts as fast as it is sensitive, it has a superior burn velocity than the other two; while the burn velocity of P/NiO is not obvious enough to be measured properly (Comet et al., 2010).

Silicon has been a fuel of interest for nanothermite because of the ease of integration into other devices or microelectromechanical systems. Unlike aluminum, silicon nanoparticles are not required here, but rather silicon substrates with nanopores are used Silicon-based nanothermites are made by depositing oxidizer molecules into the silicon nanopores. Porous silicon substrate allows intimate contact between the silicon and the oxidizer resulting in short diffusing distance that allows the fast reaction rate. Silicon substrate also acts as a structural support for the oxidizer, which nano silicon particles would not be able to achieve. The choices of oxidizers are more limited for silicon. In most cases, oxidizers are required to have high oxygen content to overcome the diffusion barrier. Certain perchlorate, nitrates, and sulphur have the ability to stay in the pores and be ignited successfully (Clément et al., 2005; Churaman, Currano, and Becker 2010).

1.3.2 Oxidizers

Unlike fuel where aluminum is predominantly used, the options for oxidizers are far more diverse; any compound that is able to produce negative enthalpy when reacting with a metal could be used as an oxidizer, although such a statement stretches to definition of nanothermite. It is simply impossible to discuss all of the oxidizers ever used, the objective here is to describe the oxidizers of particular interest. This subject has been extensively reviewed by Dombroski et al. and Kabra et al. (Kabra et al., 2020; Dombroski et al., 2022).

MnO_3, CuO, Fe_2O_3, WO_3 are the most widely studied oxidizers for nanothermites. MoO_3 is the most commonly used oxidizer for military applications (Xu et al., 2022); CuO is frequently used when the surface deposition is involved in the process of making nanothermites (Wang et al., 2014; Mao et al., 2019). These five oxidizers are often chosen for their high theoretical energy release, high adiabatic flame temperature (Elbasuney et al., 2017; Tai et al., 2018), reasonable cost due to their abundance and availability, and relatively low toxicity (Vukasovich and Farr 1986; Ahn et al., 2015).

Changing the composition of the nanothermite oxidizer changes the properties of nanothermites in a discrete and discontinuous manner. For example, Al/MoO_3 is extremely sensitive to electrostatic discharge and Al/CuO is less sensitive, their response to a stimulus is discrete. It would be desirable to fine-tune responses to

different stimuli by using some form of oxidizer with intermediate properties. One effort to achieve a response continuum was reported in which mixtures of different oxidizers, such as Al/MoO_3/CuO with different MoO_3 and CuO ratios were studied for friction, ESD sensitivity and laser ignition properties (Kelly et al., 2017b; Petre et al., 2019). Unfortunately, a discontinuous response was still observed in these properties.

1.4 The Mechanism of Nanothermite Reaction

The behaviour of nanothermites differs significantly from traditional explosives or micron-sized thermites. In an effort to understand these behavioural differences, a vast amount of work has been done to understand the mechanisms by which nanothermites react. Despite the amount of research on the subject, there are no definitive answers to explain the mechanisms of nano aluminum oxidation or nanothermite reaction.

Unlike traditional explosives or micron-sized thermites, the reaction rates of nanothermites decrease as the packing density increases (Pantoya and Granier 2005; Prentice, Pantoya, and Gash 2006; Apperson et al., 2007). Pantoya and Granier compared the flame velocity of micron size thermites and nanothermites versus packing density. They discovered that when the packing density is higher than 60% theoretical maximum density (TMD), the flame velocity of micron size thermite exceeds that of nanothermites (Pantoya et al., 2009). Researchers have attempted to explain the phenomenon. One hypothesis is based on the dominant heating model of nanothermites. There is evidence that suggests that while conductive burning occurs when nanothermites react, a convective mechanism dominates; heat and hot gaseous reactants are transferred through the spaces within the material and drive the reaction forward (Bockmon et al., 2005; Weismiller et al., 2009). As a result, the heat can travel faster and further than the flame front. When the density of the nanothermite increases, the free space that allows the heat to travel decreases, therefore the efficiency of convection burning decreases. This model only applies to nanothermites that produce enough gaseous products. For nanothermites with minimal gas production, the governing burning mechanism is still most likely to be conductive burning. (Khasainov et al., 2017; Wang et al., 2021)

In parallel with the uncertainty of nanothermite reaction mechanisms, there is currently no consensus on the exact mechanism of aluminum oxidization. It has been agreed that at a low heating rate ($< 10^6$ K/s), the oxidation of the fuel is a diffusion process. Aluminum atoms move toward the surface, passing through the aluminum shell, while the oxygen atoms from the metal oxide move inward. When the heating rate is high, the mechanism is still debated. Currently, there are two proposed

mechanisms attempting to explain the reasons that the reaction rate and flame velocity of nanothermites are superior to micron-sized thermites, diffusion and melt dispersion mechanism (MDM).

Levitas and Pantoya first proposed MDM to explain the high reaction rates of nanothermites, compared to thermites, when the heating rate is greater than 10^6 - 10^8 K/s (Levitas et al., 2006). Through calculation and experimental data, they believed that there exists a critical value (M), defined by the ratio of the diameter of the aluminum core (R) to the thickness of the shell (δ), where $M = R/\delta$. When $M < 19$ with high heating rate, diffusion does not govern the reaction process; instead, MDM takes over. MDM describes a process where the aluminum core melts before the oxide shell. As the aluminum core melts, its volume increases and thus creates tremendous pressure against the oxide shell. Once the pressure buildup exceeds the tensile strength of the oxide shell, it starts to crack, and the liquid aluminum core ejected in the form of nano aluminum clusters. They also believed that the mechanism helped explain why in their experiment and calculation, the flame velocity of the nanothermite does not depend on a single parameter, such as the thickness of the alumina or the size of the particles, but rather the ratio of the aluminum core - oxide shell. Furthermore, they have made recommendations on how to encourage the initiation of MDM in micron-sized thermites and shown that the flame velocity of the micron-sized thermite can be increased by simulating nanothermite conditions (Levitas, Pantoya, and Watson 2008; Levitas, Pantoya, and Dean 2014).

Chowdhury et al., however, do not agree with MDM; they believe that the diffusion mechanism is still the governing mechanism. They agree that the aluminum core melts before the shell, and just as MDM, the melted core exerts pressure onto the oxide shell and causes the shell to crack. Unlike the process described in MDM, the core is not violently dispelled, but it simply diffuses through the crack. The fast reaction rate is credited to the lowered melting temperature, due to the size of the particles, thinner oxide shell, and the shorter diffusion distance (Chowdhury et al., 2010; Henz, Hawa, and Zachariah, 2010).

1.5 Producing Nanothermites

1.5.1 Producing the Precursors

The methods of producing metal oxides in nano form are too diverse for a meaningful discussion in this work. However, focusing on nano metal molybdates, several different methods have been reported, including the hydrothermal method (Z. Zhang et al., 2015; L. Zhang et al., 2018), electrolysis (W. Zhang et al., 2017),

citrate complex methods (Ryu et al., 2005), co-precipitation method (Thongtem et al., 2010), and combustion synthesis (Seevakan et al., 2018; Ramachandran et al., 2017). The final two methods have been used in this thesis and will be discussed further.

1.5.1.1 Co-precipitation

The co-precipitation method typically uses solutions of either the nitrate or the chloride salts of the desired metal and sodium molybdate. The products are synthesized through the simple double displacement reaction, as shown below for a divalent metal.

$$MCl_2 + Na_2MoO_4 \rightarrow MMoO_4 + 2NaCl \qquad \text{Equation 1.3}$$

Or

$$M(NO_3)_2 + Na_2MoO_4 \rightarrow MMoO_4 + 2NaNO_3 \qquad \text{Equation 1.4}$$

The solubility of the reactants, chloride and nitrate products from Equations 1.3 and 1.4, are all at least four magnitudes higher than that of the targeted molybdate products. As a result, the molybdates are the only compound to precipitate. Table 1.1 summarizes the solubilities of a few relevant compounds. The solubilities between nitrate and chloride salts vary, but all are significantly more soluble than the metal molybdates. The solubility product constants (K_{sp}) of the two metal molybdate products are also included (Rumble, 2021). The solubility product constant is another way to represent the solubility of slightly soluble solids. Suppose a compound M_mA_n is slightly soluble in water, the equilibrium can be represented by equation 1.5.

$$M_mA_n \rightleftharpoons mM^+_{(aq)} + nA^-_{(aq)} \qquad \text{Equation 1.5}$$

And its K_{sp} is defined as

$$K_{sp} = [M^+]^m[A^-]^n \qquad \text{Equation 1.6}$$

Therefore, the solubility product constant of $MMoO_4$ is

$$K_{sp} = [M^{2+}][MoO_4^{2-}] \qquad \text{Equation 1.7}$$

Solubility product constant is a useful parameter to consider when calculating how much salt could be dissolved, particularly when there are more than one salt that share the same ion. Note that the solubility product constant is only used for sparingly soluble compounds by convention. Technically, all the solubility product constants of the compounds listed in Table 1.1 can be calculated using Equation 1.6, but only the solubility product constants of the molybdates are listed for this reason (Tro, 2010).

Table 1.1 Solubility products of various compounds

Compounds	Solubility at 20°C (g/100 g of H_2O)	Solubility Product Constant
Na_2MoO_4	65.02	
NaCl	35.86	
$NaNO_3$	87.21	
$BaCl_2$	35.73	
$Ba(NO_3)_2$	8.93	
$BaMoO_4$	0.0021	3.54×10^{-8}
$CaCl_2$	72.80	
$Ca(NO_3)_2$	130.95	
$CaMoO_4$	0.0011	1.46×10^{-8}

Metal ion concentration is a big factor influencing the size of the product particles. Precipitation will start nucleation once the concentration of the mixture exceeds a certain threshold and start to grow in size. To ensure that the particle size is nano, surfactants or chelating agents are added to the solution (Sen and Pramanik 2001; Oliveira et al., 2018). Morphologies of the products depend on the reactants and surfactants used. For example, Xiang et al. used both Na_2MoO_4 and $(NH_4)_6Mo_7O_{28}$ as the source of MoO_4^{2-} to synthesize $CaMoO_4$, they found out that the two $CaMoO_4$ have very different morphologies (Xiang et al., 2015).

1.5.1.2 Combustion Synthesis

Combustion synthesis is a self-sustainable reaction that is often used to synthesize a variety of simple metal oxides, or mixed oxide with complex crystal structures. The basic principle of combustion synthesis is that parts of reactants form exothermic gases while the remaining components form metal oxide. As the name suggested, the reactants include at least one oxidizer, often a metal nitrate, and fuel, an ammonium-containing compound. Ammonium and nitrate react at an elevated temperature and produce gaseous nitrogen, oxygen, and water. Secondary fuels such as urea (Senthilkumar et al., 2013) or glycine (Shang et al., 2009) are present to remove excess oxygen. The reaction requires a high temperature to initiate, but once the reaction is initiated, it is self-sustaining due to its exothermic nature. The final solid product often occupies a large volume and is friable. The volume of the final

solid is caused by the fast expansion of gaseous products of the combustion reaction which limits the size and connectivity of the solid particles formed. Combustion synthesis is frequently used when nano-sized particles are required. The short reaction time does not allow the particles to grow; the fast-cooling rate after the reaction also prevents the product from forming larger particles by a sintering process (Varma et al., 2016). Heating rate, cooling rate, and fuel to oxidizer ratio all affect the structures and morphologies of the products (Martirosyan et al., 2009; Gu et al., 2017).

1.5.2 Characterization techniques

1.5.2.1 Nanothermite Precursor Characterisation

To better understand the precursors of nanothermites, they are characterized by several different techniques. A fingerprint to identify material, shape, and thermal properties are analyzed by X-ray powder diffraction (XRD), Scanning Electron Microscopy (SEM), thermogravimetric analysis (TGA) and differential scanning calorimetry (DSC), respectively. Each of the techniques will be discussed in more detail below.

1.5.2.2 TGA

Thermogravimetric analysis measures the mass change of a sample as the sample is being heated at a preprogrammed rate. Samples are placed in a pan that is hooked to a thermobalance. As the sample is being heated, the thermobalance continuously measures the mass of the sample, and a mass versus temperature curve is produced. Different gases, such as nitrogen, argon, or air, can be purged into the sample chamber to create different heating environments if needed. Changes in mass over temperature ranges are identified, often using first derivative data. The mass change of the sample could be caused by physical processes such as evaporation, desorption, or chemical processes such as decomposition, or oxidation. TGA is often used in conjunction with, but not limited to, DSC to identify more accurately the thermal events that cause the mass change of the sample (Saadatkhah et al., 2020).

1.5.2.3 DSC

Differential scanning calorimetry is a thermal analytical technique that measures the difference in the heat flow between the reference and the sample when the temperature is increased or decreased at a constant rate in a specified gaseous environment. Samples are contained in an aluminum crucible and placed in a furnace along with an empty crucible as the reference. As the analysis progresses, the furnace is heated at a pre-programmed rate and the difference in heat energy required to heat

the sample and the reference is measured. During the heating process, the sample will go through different thermal events, such as melting or crystallization. If the sample absorbs more heat than the reference during an endothermic event, such as melting, an endothermic peak will appear on the thermogram produced by the DSC. On the other hand, if the sample absorbs less heat than the reference during an exothermic event, such as crystallization, an exothermic peak will appear on the thermogram (Harvey et al., 2018).

1.5.2.4 SEM

Samples in the scanning electron microscope are scanned *in vacuo* in a raster pattern with an electron beam generated by an electron gun. Once the electrons interact with the sample, secondary electrons, back-scattered electrons, and characteristic X-rays can be generated as signals and detected by the detectors. Secondary electrons are responsible for generating surface images of the sample; they are the result of inelastic interactions between the electron beam and the sample. All SEMs are equipped with detectors that can detect secondary electrons. Back-scattering electrons allow SEM to determine the elemental distribution of the sample, without identifying composition. After the electrons from the electron beam interact with the sample elastically, they are reflected to the detector through scattering. Interactions with different elements result in different backscattering intensities. This characteristic allows the elemental distribution of samples to be analyzed however, the element itself must be identified by the characteristic X-ray emitted from the sample. When an inner-shell electron is removed by the electron beam, an outer shell electron will replace the original electron and emit X-rays in the process. Each element produces unique wavelengths of X-rays. If a SEM is equipped with an energy dispersive X-ray spectroscopy (EDX) detector, elements within the sample can be identified (Dunlap and Adaskaveg 1997).

1.5.2.5 XRD

X-ray powder diffraction (XRD) method is used to identify compounds and their phases. The samples used for XRD analysis are in their powder form, as the name suggested. Powder samples are more easily obtained than large single crystals, but loss of data is inherent in the random orientation of the micro-crystalline material. Each powder particle can be made of multiple crystals, as illustrated in Figure 1.1. During the analysis, an X-ray beam is directed toward the sample at different angles. As the X-ray beam travels through the sample, it may be diffracted at specific angles based on the repeating unit of electron density, or unit cell, of the sample. The detector moves along with the X-ray source synchronously such that the incident angle is equal to the reflected angle. If the X-ray is diffracted, the detector can detect its intensity. A diffractogram is generated by plotting the intensity of the scattered rays against the angle at which the X-ray is diffracted. Different compounds have

different crystal structures, the X-ray will be diffracted differently; each unique crystal structure will produce a unique diffracted pattern. Therefore, each diffractogram is a fingerprint unique to its compound and the crystalline phase present. (Lavina, Dera, and Downs, 2014; Holder and Schaak, 2019).

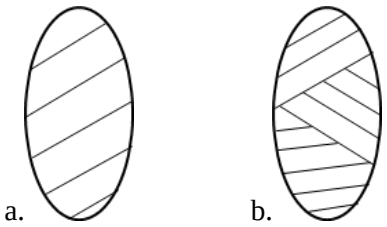

Figure 1.1 Sample powder particles made of a) a single crystal and b) multiple crystals.

1.5.2.6 Nanothermite Performance Characterization

When discussing the "performance" of nanothermites, parameters often examined are ignition delay, peak pressure, flame velocity, ignition temperature, and activation energy.

1.5.2.6.1 Ignition delay

Ignition delay is used to determine the ignitability of nanothermites. It is defined as the time it takes for the nanothermites to show visible burning after the energy source is applied. The most common energy sources for ignition delay measurement are laser and hotwire ignition (Chowdhury et al., 2010; Granier and Pantoya, 2004). Ignition delay is strongly dependent on particle size, packing density, and fuel-oxidizer equivalence ratio; small particle size, low packing density, and fuel rich equivalence ratio lead to short ignition delay (Granier and Pantoya, 2004; Stacy, Massad, and Pantoya, 2013; Saceleanu et al., 2018).

1.5.2.6.2 Peak Pressure

Pressure produced by nanothermite ignition can be measured by initiating nanothermits in a closed reaction chamber with an attached pressure transducer. The maximum pressure produced by the reaction is the peak pressure of the nanothermite. Different nanothermite compositions produce different amounts and compositions of gas, and the gas generation rates also vary. Both heavily depends on the boiling point of the oxidizer. If the boiling point of the oxidizer is below the adiabatic flame temperature, the peak pressure and the gas generation rate tend to be relatively high. Martirosyan et al. reported that Al/Bi_2O_3 and Al/I_2O_5 generate

significant pressure (>10 MPa) in a short amount of time, while Al/Fe_2O_3 barely produces any pressure increase. The adiabatic flame temperature and the boiling point of the metals and metal oxides play a central role in pressure generation. The adiabatic flame temperature of Al/I_2O_5 and Al/Bi_2O_3 nanothermites are both around 2000°C, while the boiling points of I_2O_5 and Bi_2O_3 are 184°C and 1560°C, respectively. I_2O_5 and Bi_2O_3 would be in the gas phase once the reaction takes place. On the other hand, Al/Fe_2O_3 has a similar adiabatic flame temperature but the boiling point of Fe_2O_3 is 2750°C. As a result, Fe_2O_3 is in the condensed phase while the reaction takes place (Martirosyan et al., 2009; Martirosyan, 2011). Galvier et al. realized that the adiabatic flame temperature of Al/Bi_2O_3 is above the boiling point of bismuth while the adiabatic flame temperature of Al/MoO_3 is below the boiling point of molybdenum. As a result of the generation of the gaseous bismuth product, Al/Bi_2O_3 is a better pressure generator than Al/MoO_3 (Glavier et al., 2015).

1.5.2.6.3 Flame Velocity

Flame velocity is the velocity of flame propagate through ignited nanothermite and it is a visible indication of the nanothermite reaction rate. Flame velocity depends on many factors, such as the compositions of nanothermite, additives, packing density, and confinement. The composition of nanothermite and additives affect the activation energy of the nanothermite systems. Nanothermite systems with lower activation energy have faster flame velocity. Confinement helps increase the flame velocity by encouraging the gas and intermediate species to interact with aluminum instead of diffusing away (Michelle Pantoya and Kappagantula, 2016a). Comparing the flame velocity before and after adding an additive is an indication if the additives have compromised the performance of nanothermites. Flame velocity is typically measured in two ways, either by a high-speed camera (Asay et al., 2004; Granier and Pantoya, 2004) or by photodiodes placed at a constant distance apart (Sanders et al., 2007). When the flame passes through a photodiode, the high intensity of the flame causes the photodiode to generate an electrical signal, the signal is then recorded (Martirosyan, 2011).

1.5.2.6.4 Activation Energy

Activation energy is the energy barrier needed to be overcome to achieve a chemical reaction. All chemical reactions have activation energy. Equation 1.8, the Starink equation, approximates the activation energy of nanothermites with DSC data.

$$ln\frac{B}{T_p^{1.95}} = -\frac{E_a}{RT_p} + ln\,A \qquad \text{Equation 1.8}$$

Where B is the heating rate, T_p is the temperature of the peak of the reaction, R is the universal gas constant, E_a is the activation energy, and A is the pre-exponential

factor. By plotting $ln\frac{B}{T_p^{1.95}}$ as a function of $\frac{1}{RT_p}$, the activation energy can be determined as the slope of the trend line (Starink, 2004; Pantoya and Kappagantula, 2016b). Starink equation is based on the Arrhenius equation, Equation 1.9, in which Arrhenius related activation energy to the reaction rate of chemical reactions.

$$k = Ae^{-E_a/RT} \qquad \text{Equation 1.9}$$

where k is the reaction rate, A is the pre-exponential factor, E_a is the activation energy, R is the gas constant, and T is the temperature. Taking the natural logarithm on both sides, Equation 1.9 can be rewritten as Equation 1.10.

$$\ln k = -\frac{E_a}{RT} + \ln A \qquad \text{Equation 1.10}$$

The similarity between equations 1.8 and 1.10 is apparent. The rate of a chemical reaction depends on many factors, but assuming enough energy is provided to initiate and sustain the reaction, lower activation energy suggests a faster reaction rate. This relationship is quite intuitive; the reaction starts with the first fuel particles being oxidized. The heat released from the exothermic reaction is absorbed by the adjacent particles, once the adjacent particles absorb enough energy to overcome the activation energy barrier, the adjacent particles are oxidized, and the process continues until all the particles are oxidized. The lower the activation energy a mixture has, the less energy barrier must be overcome, and thus the faster this process can progress, which leads to a faster reaction rate. The Starink method is not the only method to estimate activation energy; the approaches of Kissinger and Ozawa are used as well. While differences exist among these methods, they are all based on the Arrhenius equation (Pal and Katiyar, 2017).

1.5.3 Different Methods of Making Nanothermite

The most common and simple way of mixing the fuel and the oxides together is by suspending them in a solvent and mixing them in an ultrasonic bath. Choices of solvents include isopropanol (Sanders et al., 2007) and hexane (Walter, Pesiri, and Wilson, 2007), among others. Particle sizes greatly affect the performance and reactivity of nanothermites, therefore it is imperative that agglomerations need to be broken up (Sun, Pantoya, and Simon, 2006). Ultrasonic mixing provides good mixing quality due to its ability to break the agglomeration of nanoparticles. The quality of mixing, however, will suffer if the batch quantity exceeds a certain level (Dreizin, 2009). Nanothermite can also be mixed dry, without solvent (Schoenitz, Umbrajkar, and Dreizin, 2006; Comet et al. 2015). Dry mixing methods are less desirable and should only be used when the precursors are extremely sensitive to solvents and insensitive to friction.

The performance of nanothermites largely depends on their mixing quality. The more homogeneous the metal and the oxide are mixed, the better their performance. In addition to mixing in liquids and dry mixing, other methods have been explored to achieve structures that are more sophisticated. These structures aim to maximize uniformity and fuel-oxidant contact. Synthesis methods include the sol-gel technique (Plantier, Pantoya, and Gash, 2005), vapour deposition techniques (Zhang et al., 2007a; Petrantoni et al., 2010), electrophoresis deposition (Miao et al., 2021), and DNA directed assembly (Séverac et al., 2012; Calais et al., 2018).

The sol-gel method involves first gelatinizing an oxidizer into a porous structure then slowly adding metal fuels to the pores. The metal can be added before or after the removal of solvents. The porous structure ensures that the metal fuel and oxidizers are very well mixed (Clapsaddle et al., 2003; Wang et al., 2021). Mehendale et al. took the sol-gel method to the next level by adding a surfactant to the oxidizer to increase the order of the pores in an Al/Fe_2O_3 nanothermite system. The ordered pores improved the flame velocity of the nanothermite (Mehendale et al., 2006).

Vapour deposition and electrophoresis deposition are two methods that enhance fuel-oxidizer contact by coating a thin layer of fuel and oxidizer onto a surface. Zhang et al. produced Al/CuO nanothermite using the vapour deposition technique. As the first step, a thin layer of titanium is thermally evaporated and deposited onto a layer of the silicon substrate as an adhesive layer. To create the oxidizer layer, copper is electroplated onto the titanium layer and oxidized to form CuO nanowires. Finally, aluminum is deposited onto the copper oxide by thermal evaporation. (Zhang et al., 2007b; Petrantoni et al., 2010).

The electrophoresis deposition method utilizes the principle that species with surface charge suspended in a solvent can migrate toward a direction under the presence of an applied electric field (Besra and Liu, 2007). Both Al/CuO and Al/MoO_3 nanothermites have been produced using this technique. To start the deposition process, fuel and oxidizer are suspended in a solvent. To ensure that the fuel and oxidizer will move toward the desired electrode once the electric field is applied, it is common to add polyelectrolyte such as polyethyleneimine into the suspension to ensure the fuel and oxidizer have the correct surface charge. Two metal electrodes are then immersed into the prepared suspension and an electric field is applied. At the end of the process, nanothermites are deposited onto the desired electrode (Zhu et al., 2016; Yin, 2017; Miao et al., 2021).

Al/CuO nanothermites have been assembled by DNA-directed assembly. This particular method takes the advantage of the spontaneous formation of DNA double helix via hydrogen bonds when single strands of complementary bases are present. Nano aluminum and CuO are both functionalized first then coated with complementary DNA strands, separately. After both aluminum and CuO are coated

with DNA strands, they are then mixed together, the self-assembly process is monitored in real-time with dynamic light scattering (Calais et al., 2017).

1.6. Issues Associated with Nanothermite

Sensitivity is crucial for all energetic materials. Energetic materials need to be sensitive and readily ignitable. However, on the principle of safety, an unintended ignition must never occur. Ignition fundamentally must always be a result of temperature. However, a number of stimuli can produce heat energy because of their actions; of particular interest to the present project are friction and electrostatic discharge. In the section below the excess sensitivity of nanothermite in relation to other energetic material to stimuli will be discussed as well as attempts to mitigate excess sensitivity.

1.6.1 Sensitivity to Friction

In order for an explosive to be transported on public roads, it needs to be able to be insensitive to friction at a level of 80 N, tested by a BAM friction apparatus. Currently, most nanothermite systems do not meet this standard (United Nations, 2019). To test the friction sensitivity of nanothermites with a BAM friction apparatus, samples are placed on a ceramic plate and friction is applied by a pivot arm with a ceramic peg at the end. By placing different masses at different positions on the pivot arm, different levels of friction are generated. If the sample does not react with six consecutive tests, then the sample is considered insensitive to the specific level. The probability of obtaining no combustion at all is 98.4% at that threshold value (NATO Standardization Agency, 2009; Gibot et al., 2019).

In efforts to desensitize nanothermites toward friction, different fuel-oxidizer options and different additives have been explored. Kelly et al. explored the possibility of using different additives to desensitize nanothermites. Three different types of nano aluminum, nano aluminum (O-Al), Viton coated aluminum (V-Al), and palmitic acid coated aluminum (L-Al), were examined with two different oxidizers, CuO and MoO_3. Additives of choice include a common lubricant, graphene, a high-temperature friction modificator, MoS_2, and hexadecane, a non-volatile hydrocarbon that is readily added into solvents. The results showed that no additive would work for all the systems. The benefits and effectiveness of the additives depend heavily on the fuel oxidizer combinations; for example, graphene can reduce the sensitivity of L-Al/MoO_3 nanothermite but makes O-Al/CuO nanothermite more sensitive to friction. Adding additives could, but does not necessarily, reduce the thermochemical performance of nanothermites (Kelly et al., 2017b).

Gibot et al. have also tried using carbohydrate derivatives and polyaniline to desensitize Al/WO_3 nanothermites. The rationale behind using carbonized sucrose and polyaniline are their abundance, low cost, and ease of synthesis. Like other materials that have been examined before, although they are able to mitigate the sensitivity issue, they inevitably decrease the flame velocities of the nanothermites (Bach et al., 2015). The degree of decrease in performance depends on the mixing of additives and nanothermites. The more homogeneous the mixture, the less decrease in performance. In the case of carbohydrate derivatives, accurate velocities were not reported; however, images taken from a high-speed camera showed that the entire event initiated with flames that produce intense white light followed by yellow orange toned flames, which is typical of binary nanothermite Al/WO_3, and noise caused by the combustion was quieter with the additives. The similar flame colour profiles suggest the reactivity is not destroyed by the addition of carbohydrate additives; however, the quieter noise indicates less powerful energetic character. In the case of polyaniline, the flame speed was slowed down with the addition of polyaniline, but it was within one order of magnitude, which is a smaller loss in performance than other additives. The threshold of friction ignition has been raised to above 200 N with carbonized sucrose. Cellulose and long polyaniline can push the threshold above 300 N. The lubricant nature of polyaniline could be the reason behind its ability to desensitize the nanothermite composite. Polyaniline has a low interchain crosslink rate and interchain interactions are weak, mostly through hydrogen bonding and π-π stacking. When friction is applied to the composite, the breaking of these interactions absorbs the mechanical energy; the leftover energy is then not enough to ignite the nanocomposite (Gibot et al., 2017; Gibot et al., 2019). It is worth noting that although different additives used to desensitize nanothermites have been reported in the literature, it is extremely difficult to compare them directly. Firstly, the nanothermite systems investigated are not the same, and nanothermite characteristics are heavily dependent on the fuel/oxidizer combinations. Secondly, the ignition settings are different; therefore, directly comparing the face values of the data does not hold much meaning.

1.6.2 Sensitivity to Electrostatic Discharge

Nanothermites are extremely sensitive to electrostatic discharge (ESD). Weir et al. defined any explosives that are insensitive to ESD at a level of 100 mJ or greater as insensitive to ESD, but nanothermite can be ignited with much less energy (Weir et al. 2013). The sparks generated by human bodies, between 8.33 mJ to 20 mJ, can ignite nanothermites (Greason, 2003; Talawar et al., 2006).

ESD sensitivity is tested using a spark test. A sample is loaded into a sample holder with ESD sparks discharged onto the sample. The sample is insensitive to a certain

level of energy if it is not ignited with five consecutive sparks (Weir, Pantoya, and Daniels, 2013). For nanothermites to have any practical application, this sensitivity must be mitigated.

The exact reasons behind the sensitivity of nanothermites toward ESD are unknown, but there is some evidence that the extent of the sensitivity depends on the particle size of the aluminum (Weir, Pantoya, and Daniels, 2013), and the conductivity of the nanothermites (Weir et al. 2013; Kelly et al. 2017a). Weir et al. examined the ESD sensitivity of Al/MoO_3 nanothermite with varying sizes of aluminum. It was found that as the size of aluminum decreased, ESD sensitivity increased significantly. Weir et al. speculated that the Al_2O_3 shell acts as an electrical capacitor that helps accumulate ESD energy for the aluminum core, so that a greater surface to volume ratio increases ESD sensitivity. (Weir, Pantoya, and Daniels, 2013).

Weir et al. continued to explore the relationship between electrical conductivity and ESD sensitivity. Micron aluminum was used and combined with oxidizers, including CuO, Fe_2O_3, MoO_3, among others. Nine different aluminum mixtures were studied, but only Al/CuO was able to be ignited by ESD at 25 mJ. Weir et al. hypothesized that there are two factors that could contribute to the ESD sensitivity; the different conductivity of CuO and Al_2O_3 and the ability of CuO to store heat. As ESD is applied to the thermite mixture, most of the energy is dissipated to CuO, since CuO is relatively more conductive than the Al_2O_3 shell. CuO acts as a heat sink to heat up the aluminum particle and ignite the thermite mixture. From this study, Weir et al. concluded that the higher the conductivity of the thermite mixture, the more ESD sensitive it is (Weir et al. 2013). It is worth reiterating that the aluminum used in the study was micron-sized, therefore the ignition results are quite different from that of nanothermite mixtures, where most would have been ignited with the same ESD energy.

Kelly et al. further examined the relationship between ESD sensitivity and the resistivity of individual components. They tried altering the compositions of the oxidizers in nanothermite systems to minimize nanothermite ESD sensitivity. The oxidizers used in this study include CuO, MoO_3, and Fe_2O_3, either used separately or combined with MoO_3. The aluminum used in this study included O-Al, V-Al, or L-Al. In this study, the resistivity of each individual component was measured. They found a nanothermite system is the most ESD sensitive when the resistivity of fuel is low and the resistivity of the oxidizer is high. Among the three different oxidizers, MoO_3 has the highest resistivity. For the simple binary nanothermite system, Al/MoO_3 is the most sensitive nanothermite, and when it is combined with either CuO or Fe_2O_3, the greater the amount of MoO_3 is in the mixture, the more sensitive the nanothermite. On the other hand, the aluminum with the lowest resistivity seems to be the most sensitive toward ESD. The ESD results showed that V-Al nanothermites are consistently less sensitive than the other two systems regardless

of the oxidants used. One hypothesis for this observation is that when nanothermite is exposed to an external spark, fuel and oxidants "experience" different amounts of current due to different resistivities. More current passes through aluminum because it has a lower resistivity than the oxides therefore it experiences Joule heating. The more resistive an oxide is the more current passes through aluminum and generates more heat, which could break down the passivating layer and ignite the nanothermites (Kelly et al., 2017a).

Carbon-based additives are very popular choices for researchers attempting to desensitize nanothermite, because of their ability to form conductive networks and lead energy away from the nanothermite (Poper et al., 2014; Gibot et al., 2019). Carbon-based compounds or Viton fluoropolymers have proven to be useful. One percent of carbon has been added to the Al/Bi_2O_3 system to desensitize ESD sensitivity (Glavier et al., 2017). Foley et al. reported Al/CuO nanothermite could be desensitized with the addition of Viton A. The more Viton A was added to the nanothermite, the less sensitive the nanothermite. Unfortunately, the peak pressure decreased with the addition of Viton A; when 10% of Viton A was added to the nanothermite mixture, only about 0.6 atm is produced, which is far too low for explosive or propellant purposes (Foley et al., 2007). Carbon nanotubes were also used to reduce both friction and ESD sensitivities. Siegert et al. have tried to coat MnO_2 in carbon nanofibres to decrease sensitivity (Siegert et al., 2010). For most of these additives, a minimum amount is required to achieve the desensitizing goals, about 5 wt.%. There is a huge drawback, however, with the use of these additives. Significant reduction of the flame velocities of these nanothermite systems was reported by all these studies (Collins et al., 2015; Steelman et al., 2015; Gibot et al., 2017).

1.7. Applications

Since nanothermites are energetic materials, their abilities to produce heat, gas, and fast-moving particles give them military and civilian applications. It is impossible to discuss all the potential applications here; a few are chosen to showcase how diverse nanothermite applications can be.

Nanothermites have been used in micro rocket systems as an initiator. Glavier et al. used Al/CuO and Al/Bi_2O_3 to ignite RDX to shoot a metallic flyer out of their micro rocket. In their design, the nanothermite was coated onto a silicon substrate, which was then placed in front of an RDX die. The nanothermite ignition pellet was connected to an electrical supply. When the current was supplied, within 10 microseconds, a reaction would take place and spark through the pellet, which in turn ignites RDX (Glavier et al., 2017).

The ability to ignite low explosives enables nanothermites to have the potential to be used as a lead-free primer. Currently, lead styphnate is the most widely used component in the current formulation. The lead content in the primer causes environmental contamination and affects human health. Lead in primer makes up about 20% of airborne lead originating from conventional ammunition (Higa, 2007). Some commercial lead-free primers are available, but they do not meet the minimum military safety or performance standards. In addition to their fast reaction rate, nanothermites are ignitable remotely by laser and electronic delay making them even more attractive as lead-free primers. (Granier and Pantoya, 2004; Higa, 2007).

Nanothermites have been manufactured as microthrusters with the intention to stabilize and control low Earth orbit satellites. Puchades et al. housed $Al/Bi(OH)_3$ in their in-house 3D printed microthrusters for its superior gas-producing ability. The team design microthruster systems such that each thruster can be ignited individually, simultaneously, or in desired sequences to provide the precision required to control and adjust the course of the satellites. (Puchades et al., 2017).

In addition to the traditional energetic material applications such as propellants and ignitors, nanothermites also have the potential to be used as biocidal agents. The reasons to use nanothermites as biocide agents are three-fold, the heat generated from the reaction, the biocidal properties of the products, and the ability to propel the products onto the infected surface. $Al/AgIO_3$, Al/I_2O_3, and Al/Ag_2O have all been investigated as possible biocidal systems since both nano silver and iodine-based substances have been shown to have disinfecting and antibacterial properties. In particular, Al/I_2O_3 and Al/Ag_2O systems have even been shown to stop *E. Coli* growth in enriched agar plates (Sullivan et al. 2010; Hobosyan and Martirosyan, 2020).

1.8. State of Art

In this section, the new emerging trends of nanothermites research will be discussed. The recent nanothermite research can be broken down into these categories: unconventional fuel and oxidizers, combining of other nanomaterials with nanothermites, and modification of synthetic material to achieve complex structure. A few studies are briefly discussed here to provide some details of these new trends.

Instead of using a pure metal as the fuel, Fahd et al. synthesized a 3D energetic metal-organic framework $[Cu_4Na(Mtta)_5(CH_3CN)]_n$ (Mtta = 5-Methyl-1H-tetrazole) (EMOF-1) as the fuel. They mixed this with different oxidizers and compared their characteristics with the classic aluminum-based thermites. They reported the EMOF-

1 based nanothermites had lower activation energies, ignition temperatures in the 200-300°C range as opposed to the 600-700°C range, and when compared gram to gram, higher heat of combustion was obtained (Fahd, Zorainy, et al., 2021).

Carbon nanomaterials attract attention for their hardness, optical properties, and large surface area. Graphite oxide (GO) was firstly added to conventional energetic materials such as nitrocellulose and ammonium perchlorate. It was found that by adding GO to these energetic materials, their burning rates were improved (Li et al., 2013; Memon, McBain, and Son, 2016). When GO is added to nanothermites, they are also capable of enhancing the heat release. Fahd et al. found that GO was able to improve the propulsion characteristics and energy release of aluminum-based nanothermite in ternary and quaternary, GO/Al/$KClO_4$ and NC/GO/Al/$KClO_4$, nanothermites (Fahd, Baranovsky, et al., 2021; Fahd, Dubois, et al., 2021). Similar to GO, other carbon nanomaterials such as functionalized graphene sheets (FGS) and reduced graphene oxide (RGO) have both been added to nanothermites and show promising performance enhancements (Thiruvengadathan et al., 2014; Yan et al., 2017).

In addition to nano carbon material, fluoropolymers have also been added to nanothermite compositions. Unlike carbon additives, which often decrease nanothermite flame velocity and increase ignition delay significantly (Song et al. 2020), fluorinated additives have been shown to have the ability to maintain or decrease the loss of nanothermite performance, due to pre-ignition reaction (PIR) (Osborne and Pantoya, 2007). PIR takes place before the main Al oxidation occurs; the decomposed fluoropolymer reacts with the Al_2O_3 shell to produce AlF_3, which is a catalyst that lowers the activation energy of Al oxidation (Pantoya and Kappagantula, 2016a). Nie et al. and Song et al. took the advantage of PIR and developed a novel energetic fluoropolymer binder to increase the physical strength and potential application of nanothermites (Nie et al., 2021; Song et al., 2021).

Engineering novel sophisticated architectures has always been an important part of nanothermite research. A few techniques that produce sophisticated architectures have been discussed before. However, these techniques are often complicated and laborious. There is a drive for simpler synthetic techniques to achieve complex structures. As 3D printing technology matures, it gradually becomes a viable simple technique to print nanothermite structures (Shen et al, 2020; Zhong et al, 2021). Core-shell nanothermite, in which aluminum particles (core) are covered with a layer of oxidizer (shell), is one of the nanothermite structures that offer great fuel-oxidizer contact area (Qin et al., 2013; Qin et al., 2017; Wang et al. 2019); however, conventional techniques of producing core-shell structured nanothermites often require high temperatures. Shi et al. reported using alcohol-thermal synthesis to produce core-shell structured nanothermite. This new approach promises a low-temperature one-step synthesis (Shi et al., 2021). Wang et al. developed a new

nanothermite structure utilizing carbon sphere templates to synthesize the double-shell NiO hollow nanospheres. They reported that not only the size of the double-shell NiO is customizable; the distance between the NiO shells further promotes the convective heat transfer of the nanothermite, thus improving the combustion characteristics of nanothermites (Wang et al., 2020).

1.9. Conclusion

Nanothermites started gaining interest in the last 20-30 years because of their fast reaction rate, high energy density, and the flexibility of altering their compositions. In the context of scientific research, it is still a relatively new field. Extensive research has been done to understand this type of energetic material; however, the current knowledge has only scratched the surface. Much about nanothermite is still unknown or has not reached appoint of consensus. A majority of what is understood about nanothermites is based on studies of a few common fuel-oxidizer combinations. To truly understand the working principles of nanothermites, more systematic research is required.

Nanothermites have much to offer as the next generation of energetic materials. As discussed previously, nanothermites could be integrated into a wide range of applications. However, they also have their limitations. Nanothermites are not readily formulated by mixing different oxides, as oxides display discrete characteristics. Sensitivity toward friction and ESD is a critical problem. Unless these issues are mitigated, the practicality of using nanothermites remains restricted. Moreover, reduced sensitivity must be achieved with a retention of performance. The goal of this project is to understand the reasons behind the sensitivity of nanothermites and find a solution without sacrificing its performance. Specifically, the settling effects of nanothermites produced by a common method will be investigated. In addition, novel nanothermites will be fabricated and their friction and ESD sensitivities will be quantified.

2. Method and Materials

This chapter outlines the experimental procedures and setups for the experiments discussed in this thesis. All the reagents and equipment used are listed below in sections 2.1 and 2.2.

2.1 Reagents

Aluminum

- Nanopowder (Reactive Energetics, Montreal, Canada),
  - Oxide passivation (O-Al)
  - Palmitic acid coating (L-Al)
  - Viton coating (V-Al)
- Alex
  - Uncoated nano aluminum powder, UN1396 (Obtained from DRDC Suffield, Canada)

Ammonium molybdate tetrahydrate ($(NH_4)_6Mo_7O_{24}\cdot 4H_2O$)

- 82.7%, ACS certified, (Fisher Scientific, Fair Lawn, USA)

Barium chloride ($BaCl_2$)

- 60 mesh, 99.9%, Lot TX 06421PX (Aldrich Chemical Company, Milwaukee, USA)

Barium nitrate ($Ba(NO_3)_2$)

- 99%, reagent grade, (J. T. Baker, Radnor, USA)

Calcium chloride, anhydrous ($CaCl_2$)

- 96.7%, ACS certified, 20 mesh (Fisher Scientific, Fair Lawn, USA)

Calcium nitrate tetrahydrate ($Ca(NO_3)_2\cdot 4H_2O$)

- 99.98%, Lot 61600281 (Alfa Aesar, Haverhill, USA)
- 99.0%, reagent grade, Lot 83974 (Caledon Laboratory Chemicals, Georgetown, Canada)

Cupric nitrate hydrate ($Cu(NO_3)_2\cdot 2.5H_2O$)

- 98.0%, reagent grade (Caledon Laboratory Chemicals, Georgetown, Canada)
- 99%, reagent grade, ACS certified, Lot 033761, (Fisher Scientific, Fair Lawn, USA)

Cobalt nitrate hexahydrate ($Co(NO_3)_2\cdot 6H_2O$)

- 98%, ACS certified (Fisher Scientific, Fair Lawn, USA)

Ethanol denatured (C_2H_4OH)

- 15% methanol and 0.85% ethyl acetate, reagent grade, Lot 106153 (Caledon Laboratory Chemicals, Georgetown, Canada)

Ethyl ether, anhydrous ($(C_2H_5)_2O$)

- Reagent grade, Lot 104938 (Caledon Laboratory Chemicals, Georgetown, Canada)

Ethylene glycol ($C_2H_6O_2$)

- Certified, Lot 207225 (Fisher Scientific, Fair Lawn, USA)

Ferric nitrate nonahydrate ($Fe(NO_3)_3 \cdot 9H_2O$)

- ACS certified, Lot 864401 (Fisher Scientific, New Jersey, USA)

Glycine ($C_2H_5NO_2$)

- USP Grade, Lot 061753 (Fisher Scientific, Fair Lawn, USA)

Manganese (II) nitrate tetrahydrate ($Mn(NO_3)_2 \cdot 4H_2O$)

- Lot A0297879 (Acros Organics, Fair Lawn, USA)

Magnesium chloride hexahydrate ($MgCl_2 \cdot 6H_2O$)

- ACS certified, Lot 066051 (Fisher Scientific, Fair Lawn, USA)

Magnesium nitrate hexahydrate ($Mg(NO_3)_2 \cdot 6H_2O$)

- 99+%, Lot A0401589 (Acros Organics, Fair Lawn, USA)

Molybdenum (VI) trioxide (MoO_3)

- 100 nm nanopowder, 99.5%, Lot 3851070116 (Aldrich Chemistry, Milwaukee, USA)

Nickel nitrate hexahydrate ($Ni(NO_2)_3 \cdot 6H_2O$)

- Certified, Lot 793809 (Fisher Scientific, Fair Lawn, USA)

Sodium molybdate (VI) dihydrate ($Na_2MoO_4 \cdot 2H_2O$)

- 99+%, Lot A0358978 (Acros Organics, Fair Lawn, USA)

Strontium chloride hexahydrate ($SrCl_2 \cdot 6H_2O$)

- ACS reagent, 99%, Lot MKCK1730 (Sigma-Aldrich, Milwaukee, USA)

Strontium nitrate ($Sr(NO_3)_2$)

- 99+%, ACS reagent, Lot A0413445 (Acros Organics, Fair Lawn, USA)

Triethylene glycol

- 99%, Lot B0533754 (Acros Organics, Fair Lawn, USA)

Zinc nitrate hexahydrate $Zn(NO_3)_2 \cdot 6H_2O$

- 98% (Aldrich Chemical Company, Milwaukee, USA)

2.2 Equipment

BAM Friction Apparatus
- FSA-12 (OZM Research, Hrochuv Tynec, Czech Republic)

Centrifuge
- Rotofix 32 A (Hettich, Tuttlingen, Germany)

DC power supply
- Model 1671A (B&K Precision Corporation, Yorba Linda, USA)

ESD gun
- Model 930D (electro-tech system, Glenside, USA)

Furnace
- Thermolyne 114300 (Fisher Scientific, Fair Lawn, USA)

Gas Soprtion System
- Autosorb iQ Model 7 (Quantachrome Instruments, Boynton Beach, USA)

Microwave Oven
- MARSXpress (CEM Corporation, Matthews, USA)

Picoammeter
- Model 6485 (Keithley, Cleveland, USA)

Peristaltic Pump
- Precision micro peripump Model MP2-6 (Elemental Scientific, Omaha, USA)

SEM
- Quanta 250 FEG ESEM (FEI, Hillsboro, USA)

Ultrasonic Bath
- FS69 (Fisher Scientific, Fair Lawn, USA)
- Symphony (VWR, Radnor, USA)
- A40 (Co-Z Supplies, Montreal, Canada)

Vacuum pump
- V-500 (Buchi Labortechnik, Flawil, Switzerland)

Vacuum Controller
- B-721 (Buchi Labortechnik, Flawil, Switzerland)

XRD
- Empyrean series 2 (Malvern Panalytical, Malvern, UK)

Zetasizer
- Zetasizer Nano ZS (Malvern Panalytical, Malvern, UK)

2.3 Precursors

This section outlines the methods used to synthesize and characterize metal oxides (Section 2.3.1) and the characterization method of nano aluminum (Section 2.3.2). These metal oxides and nano aluminum are the precursors of various nanothermites.

2.3.1 Metal Oxide Synthesis and Characterization

$MMoO_4$ (M = Mg, Ca, Sr, Ba, Mn, Fe, Co, Ni, Cu, Zn) were synthesized using two different methods, co-precipitation and combustion synthesis.

2.3.1.1 Co-precipitation Method (CPS)

The co-precipitation method was used to synthesize nano alkaline earth metal molybdates, $CaMoO_4$, $SrMoO_4$, and $BaMoO_4$. Three different protocols were developed to achieve the desirable particle size. Each protocol is slightly different from the others, but the basic principle is that of double displacement reactions. The method of each protocol is described in detail below. Figure 2.1 shows the basic working procedure for the three protocols.

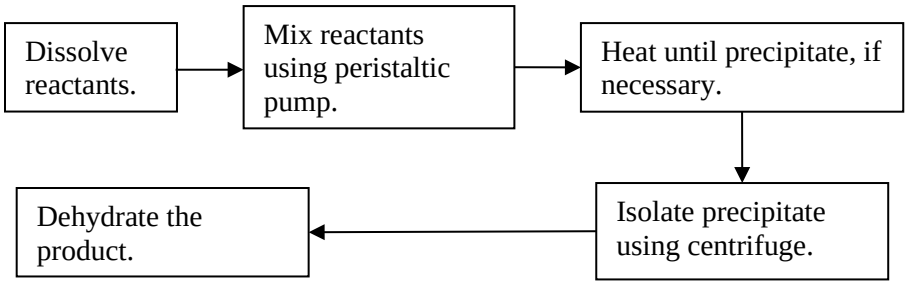

Figure 2.2 A workflow diagram to demonstrate the basic procedure of the three synthesis protocols.

Protocol 1

$CaCl_2$ was dissolved in 50 mL of triethylene glycol (TEG) to make 80 mM $CaCl_2$ solutions. The solution was added dropwise using the MP2-6 Precision micro peripump at a 1 mL/min rate to a 50 mL Na_2MoO_4 (80 mM) aqueous solution, with constant stirring. The reaction is shown in Equation 2.1.

$$CaCl_2 + Na_2MoO_4 \rightarrow CaMoO_4 + 2NaCl \qquad \text{Equation 2.1}$$

Precipitates formed during and immediately after the addition of the solution was complete. To remove the solvent, the precipitate was centrifuged and washed with denatured ethanol three times (6 mL), followed by three washes with 6 mL of diethyl ether with a Rotofix 32A centrifuge at 35000 rotations per minute (RPM) for 5 minutes (Hettich, Tuttlingen, Germany). After washing, the products were left in the fume hood to dry overnight and subsequently kept in an oven at 120°C. The identities of the products were confirmed using XRD. $SrMoO_4$ and $BaMoO_4$ were synthesized the same way with the starting reagents $SrCl_2 \cdot 6H_2O$, and $BaCl_2$, respectively. Protocol 1 was inspired by the procedure described by Zhang et al., without boiling the mixture in an autoclave (Zhang et al, 2015).

Protocol 2

Protocol 2 is very similar to Protocol 1, although $Na_2MoO_4 \cdot 2H_2O$ was dissolved in TEG as opposed to deionized water. Precipitates did not form immediately after the mixing of the solutions. To achieve precipitation of the metal molybdates, the mixture was heated until the precipitation process was completed, around 120°C. The mixture was cooled to room temperature before commencing the centrifugation and washing procedures described in Protocol 1. The products obtained from Protocol 2 were stored under the same conditions.

Protocol 3

Protocol 3 was developed because Protocols 1 and 2 did not produce nano sized metal molybdates. Thongtem et al. used lower reagent concentrations and volumes to achieve good particle size (Thongtem et al., 2010). This principle was applied here. Instead of the metal chlorides, metal nitrates were used. $CaMoO_4$ was synthesized using $Ca(NO_3)_2 \cdot 4H_2O$ and $Na_2MoO_4 \cdot 2H_2O$. Both $Ca(NO_3)_2 \cdot 4H_2O$ and $Na_2MoO_4 \cdot 2H_2O$ were dissolved, separately, in 40 mL of ethylene glycol (EG) to make 5mM solutions. The reaction is shown in Equation 2.2.

$$Ca(NO_3)_2 + Na_2MoO_4 \rightarrow CaMoO_4 + 2NaNO_3 \qquad \text{Equation 2.2}$$

$Ca(NO_3)_2 \cdot 2H_2O$ solution was added to $Na_2MoO_4 \cdot 2H_2O$ solution using the same peristaltic pump at the rate of 0.5 mL/min. After the addition, the mixtures were left stirring for 24 hours at *ca* 32°C. After the mixtures had been stirred for 24 hours, the same heating procedure described in Protocol 2 and the centrifugation and washing procedures described in Protocol 1 with different rotation durations were used. The precipitation was centrifuged and washed with denatured ethanol three times for 2 hours at 35000 RPM and followed by three washes of diethyl ether for 1 minute at 3500 RPM. The products were then dehydrated at 80°C for 24 hours and stored in a desiccator. $SrMoO_4$ and $BaMoO_4$ were synthesized using the same procedure with the starting reagents $Sr(NO_3)_2$, and $Ba(NO_3)_2$, respectively.

The protocols used in precipitation methods are summarized in Table 2.1.

Table 2.2 A summary of the three protocols used to synthesize $MgMoO_4$, $CaMoO_4$, $SrMoO_4$, and $BaMoO_4$.

Protocol	**1**	**2**	**3**
Reactant Concentration (mM)	80	80	5
Reactant Volume (mL)	50	50	40
Solution Addition Rate (mL/min)	1	1	0.5
Source of Metal and Solvents	$CaCl_2$ $SrCl_2{\cdot}6H_2O$ $BaCl_2$	$CaCl_2$ $SrCl_2{\cdot}6H_2O$ $BaCl_2$	$Ca(NO_3)_2{\cdot}4H_2O$ $Sr(NO_3)_2$ $Ba(NO_3)_2$
	TEG	TEG	EG
Solvent for $Na_2MoO_4{\cdot}2H_2O$	Water	TEG	EG
Precipitation Method	Formed during and immediately after	Heated to *ca.* 120°C	Mixed for 24 h and heated to *ca.* 120°C

2.3.1.2 Solution Combustion Synthesis

Solution combustion synthesis (SCS) was the second method used to synthesize metal molybdates. The principles of SCS were discussed in Section 1.4.1.2. However, it is worth reiterating that this type of redox reaction involves a fuel and oxidant which combine to produce one or more gaseous products and a target material. In general, excess oxygen is also present which is removed by the presence of an additional fuel material. In this case, the fuel was $(NH_4)_6Mo_7O_{24}{\cdot}4H_2O$, the oxidizers were the metal nitrate hydrates, and glycine was the secondary fuel that removed the excess oxygen. The metal molybdates synthesized using SCS were $MgMoO_4$, $CaMoO_4$, $SrMoO_4$, $MnMoO_4$, $Fe_2(MoO_4)_3$, $CoMoO_4$, $NiMoO_4$, $CuMoO_4$, and $ZnMoO_4$.

The synthesis of $MgMoO_4$ is typical of the SCS procedure. 0.2359 g of $Mg(NO_3)_2{\cdot}6H_2O$ and 0.3479 g of $(NH_4)_6Mo_7O_{24}{\cdot}4H_2O$ were dissolved in 1 mL of water, separately. 0.1135 g of glycine was then added to the $(NH_4)_6Mo_7O_{24}$ solution. An additional 0.5 – 1 mL of water was added to ensure the dissolution of glycine. The two solutions were mixed and poured into a ceramic dish, which was then placed in a muffle oven pre heated to 500°C. The reaction was taken out of the oven after two minutes.

The exact mass required of reagents used depended on the compounds. To determine the amount of metal nitrate hydrates and $(NH_4)_6Mo_7O_{24}{\cdot}4H_2O$ required, 0.25 g was set as the target mass of the desired metal molybdate. The ratio of metal nitrates to $(NH_4)_6Mo_7O_{24}{\cdot}4H_2O$ was stoichiometric. The general equation of the reaction is shown in Equations 2.3 and 2.4:

$$63\ M(NO_3)_2 + 9\ (NH_4)_6Mo_7O_{24} + 52\ C_2H_5NO_2 \rightarrow 63\ MMoO_4 + 104\ CO_2 + 238\ H_2O + 116\ N_2$$

Equation 2.3

where M = Mg, Ca, Sr, Mn, Co, Ni, Cu, and Zn. In the case of iron (III), Equation 2.4 applies.

$$126\ Fe(NO_3)_3 + 27\ (NH_4)_6Mo_7O_{24} + 156\ C_2H_5NO_2 \rightarrow 63\ Fe_2(MoO_4)_3 + 312\ CO_2 + 714\ H_2O + 348\ N_2$$

Equation 2.4

The mass of glycine required was determined using the fuel to oxidizer ratio equation, Equation 2.5. Fuel to oxidizer ratio equation is

$$\Phi = \frac{(F/A)actual}{(F/A)stoichiometric}$$

Equation 2.5

where F and A are the amount of fuel and the oxidizer, respectively. To ensure a fuel-rich condition, the fuel to oxidizer ratio (Φ) 1.346 is used (Shang et al. 2009). F, the amount of glycine in moles, was calculated by substituting the amount of the $(NH_4)_6Mo_7O_{24}{\cdot}4H_2O$ in moles, for A, and the stoichiometric amount of glycine, in moles, for F.

Microwave synthesis was also considered as an alternative heating method for the synthesis of $CuMoO_4$, $NiMoO_4$, and $ZnMoO_4$. The reactant solutions were made using the procedure described above. However, rather than using in a muffle furnace, the solutions were transferred into a MARSXpress digestion vessel (CEM Corporation, Matthews, USA) and microwaved for 10 minutes at 800W.

2.3.1.3 Resistivity Analysis

The resistivity measurements were based on ASTM D 257 (ASTM, 2007) and the detailed dimensions of the measurement apparatus are described by Kelly et al. (Kelly et al. 2017a). The apparatus of resistivity measurements consists of a base unit with two electrodes and a Teflon cell with a sample chamber with the dimension

of 6.0 mm in length and 3.0 mm^2 cross-section, as shown in Figure 2.2. The base unit connects to a power supply and a high resistance metre. During the measurement, the sample cell sits on top of the base unit.

a. 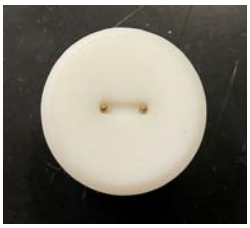 b.  c. 

Figure 2.3. Resistivity measurement apparatus. a) Sample cell b) base unit c) cell base arrangement.

The power source was a BK Precision 1671A DC power supply (Yorba Linda, USA) and the current was measured with a Keithley 6485 picoammeter (Cleveland, USA). Figure 2.3 illustrates the measurement setup. Before any sample was loaded to the sample chamber, the sample cell was weighed. The cell was reweighed after the sample was loaded, and the packing density was calculated using Equation 2.6,

$$\rho = \frac{m}{0.018} \qquad \text{Equation 2.6}$$

where ρ is the sample packing density, in g/cm^3, and m is the mass of the sample, in gram. Each sample was packed into the sample holder with five different packing densities. The current of each packing density was measured with the voltage from 30 V to 2.5 V, at 2.5 V intervals, and finally at 1.5V. Each packing density was repeated 5 times across the whole voltage range. Between each sample, the sample cell was rinsed with water, immerse in a Co-Z 40A ultrasonic cleaner (Co-Z Supplies, Montreal, Canada) for 15 minutes and rinsed with acetone. The cell was then allowed to dry overnight before the resistivity of the next sample was measured. The resistivities of the samples of each packing density and voltage were calculated using Equation 2.7 (Engel and Reid, 2005),

$$Resistivity = \frac{V \cdot Area}{I \cdot L} \qquad \text{Equation 2.7}$$

where V is the voltage, $Area$ is the cross-section area of the sample cell, I is the current measured by the picoammeter, and L is the length of the sample.

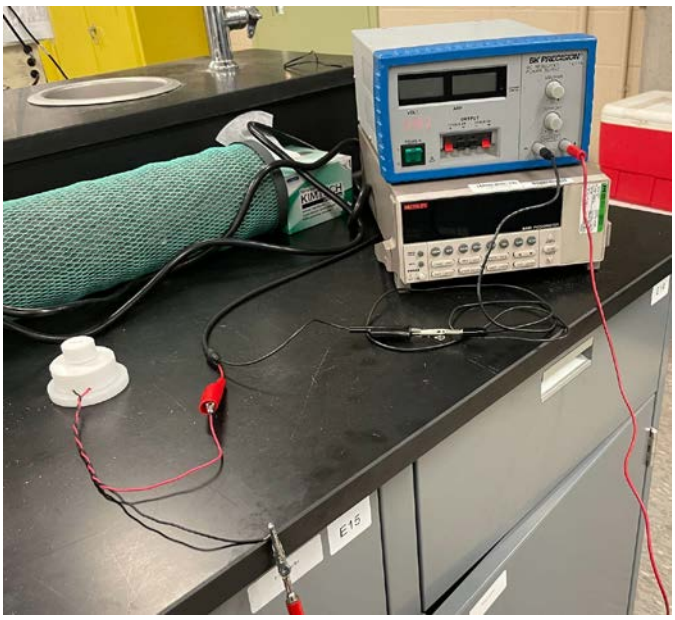

Figure 2.4 Resistivity experimental setup

2.3.1.4 Specific Surface Area

The specific surface areas of $CaMoO_4$, $SrMoO_4$, and $BaMoO_4$ synthesized using Protocol 3 of the co-precipitation method and $MgMoO_4$, $CaMoO_4$, and $SrMoO_4$ synthesized through SCS were measured. The surface areas of the metal molybdate precursors were measured using Autosorb iQ Model 7 (Quantachrome Instruments, Boynton Beach, USA). The typical procedure started with an initial 3-hour-degassing process at 180°C. To ensure the degassing process was completed, a degassing test was carried out every 15 minutes in the second segment of the degassing process, at the same temperature. During the test, autosorb iQ closes the vacuum valves and measures the rate of rise of pressure in the sample cell. The sample was considered properly degassed if the pressure rate of rise is less than 21 mtorr/min. Once the sample passed the test, the degassing process is completed. The sample was then moved to the analyzing station to go through the adsorption and desorption measurements with nitrogen gas as the adsorbate. Twenty data points were collected for the adsorption process and twenty data points were collected for the desorption process. The linear branch of the adsorption process was used to analyze the surface area of the sample using the multi-point BET method (Anton Paar GmbH, 2021).

2.3.2 Nano Aluminum Characterization

2.3.2.1 Nano Aluminum Active Content

The NaOH volumetric method was used to measure the active content of the aluminum based on the evolution of hydrogen gas. A three-neck round bottom flask was immersed in a water bath to maintain the reaction temperature at around 25°C. The first neck was connected to a Buchi V-500 vacuum pump (Buchi Labortechnik, Flawil, Switzerland) via a Buchi B-721 vacuum controller (Buchi Labortechnik, Flawil, Switzerland) with a built-in pressure sensor, the second neck was sealed with a rubber septum, and the third neck was sealed by a rubber stopper with a digital thermometer inserted. The setup is shown in Figure 2.4. NaOH was dissolved in an 80% water:20% ethanol solution by volume to make a 2M NaOH solution.

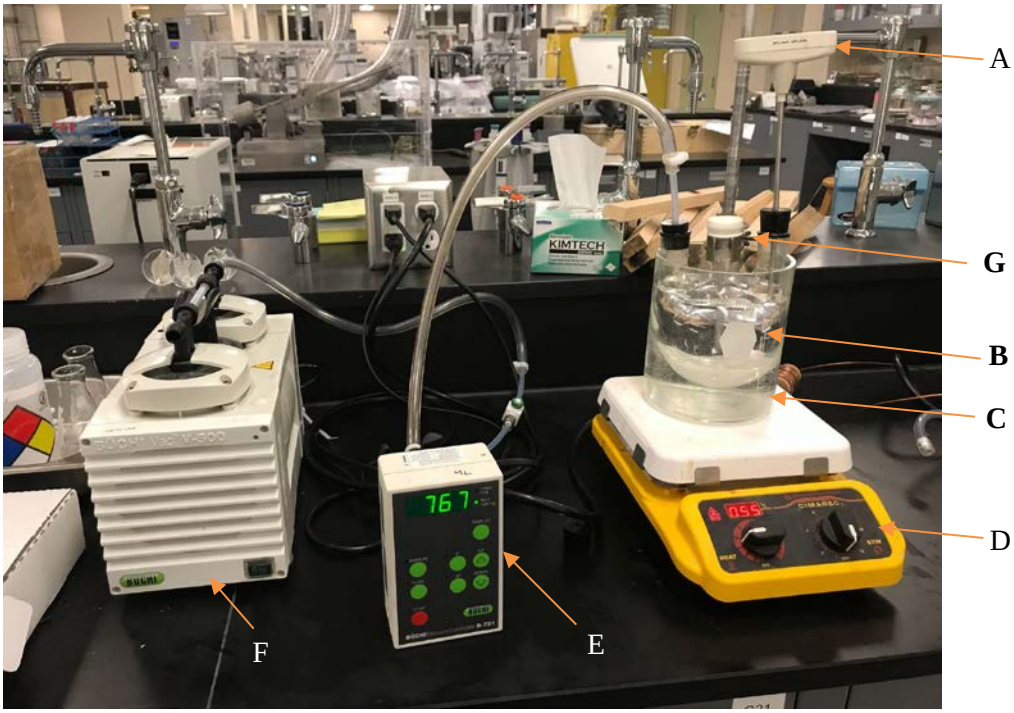

Figure 2.5 The setup for measuring the aluminum active content. A thermometer (A) was used to measure the temperature within the three-neck-flask (B). The flask was immersed in a water bath (C) to control its temperature. The temperature of the water bath was maintained by a hot plate stirrer (D). A vacuum pump (F) was used to pump the air out of the flask and a pressure sensor (E) was used to monitor the pressure

within the flask. Once the pressure in the flask was pumped down, NaOH solution was injected with a syringe through the septum (G) covering one of the necks.

To measure the vapour pressure of the solution, P_{NaOH}, the pressure in the flask was firstly pumped down to an initial pressure, P_0, 30 torrs. A syringe containing 25 mL of NaOH solution was weighed before the solution was injected through the rubber septa in the flask. After the injection, P_{NaOH} was measured, and the syringe was weighed again. The procedure was repeated five times. To measure the active content of aluminum, a 1.5 mL neutron activation analysis (NAA) vial containing an accurate mass of *ca.* 300 mg of nano aluminum was added to the flask with a stir bar and the pressure of the flask was pumped down to 30 torr. As in the previous procedure, 25 mL of NaOH solution was injected and the peak pressure, P_f, was recorded once the reaction had been completed. The masses of the syringe before and after injection were recorded as well. This procedure was also repeated five times. A workflow diagram illustrates this procedure is shown in Figure 2.5.

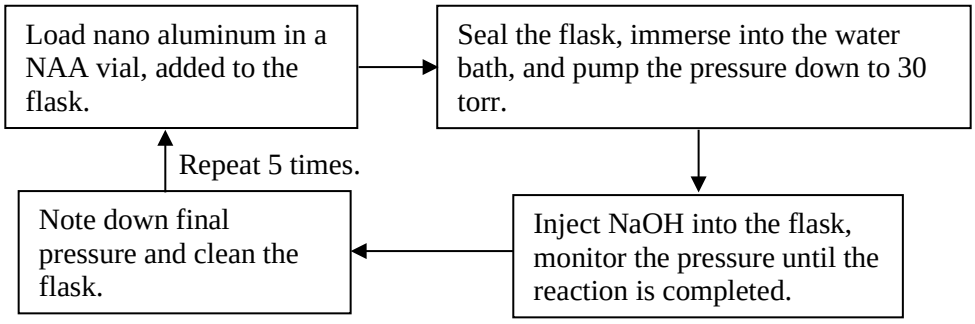

Figure 2.6 The procedure of measuring the activity content of nano aluminum.

2.3.2.2 Nano Aluminum Aging Study

To create a 32.5% relative humidity environment, $MgCl_2$ saturated solution was used (Winston and Bates, 1960). $MgCl_2$ saturated solution was made by gradually heating the water while continually stirring and adding the salt to it until boiling and no more solid could be dissolved. After the solution was partially cooled, some more $MgCl_2 \cdot 6H_2O$ was added; when the solution is cooled to room temperature, more $MgCl_2 \cdot 6H_2O$ was added to ensure the longevity of the solution. The saturated $MgCl_2$ solution was transferred into a desiccator along with the undissolved salt. An accurate mass of *ca.* 200 mg of nano aluminum was added to a pre-weighed glass vial and placed in the desiccator uncapped and maintained at 25 - 30°C. The same procedure was repeated for NaCl to create a 75.5% relative humidity environment

(Winston and Bates, 1960). The two vials of nano aluminum were taken out to be weighted every few days for 106 days. The setup is shown in Figure 2.6.

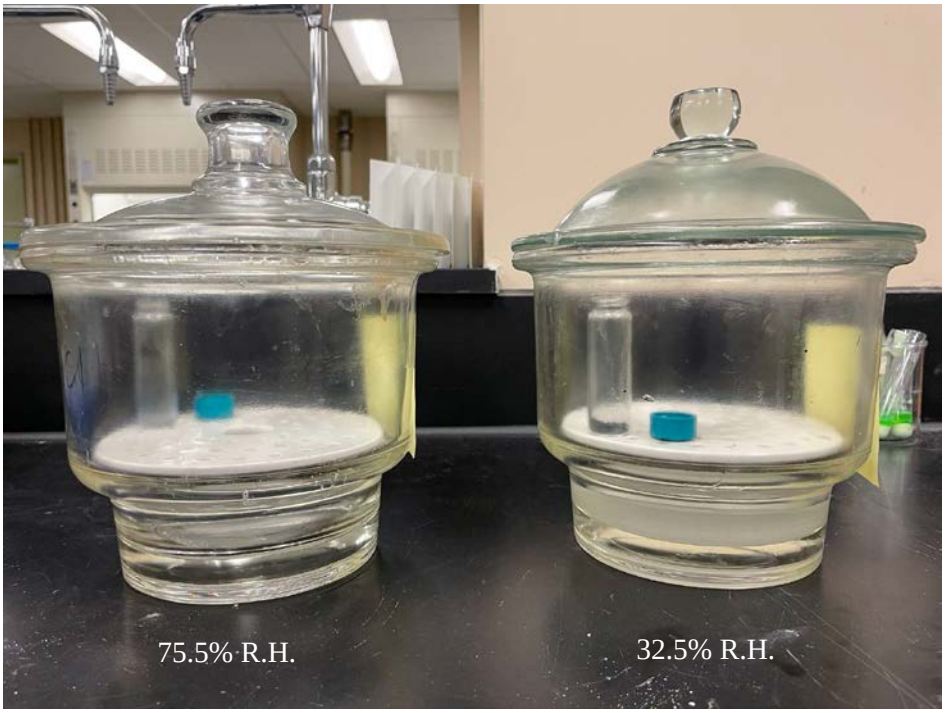

Figure 2.7 The setup of the experiment, uncapped nano Al powder under two different relative humidity environments. The left desiccator has a relative humidity of 75.5% and the right desiccator has a relative humidity of 32.5%.

2.4 Sedimentation

2.4.1 Precursor Trial Set Up

All the 15 trials were set up using the same basic protocol. Each trial started with labelling seven vials with the trial number, batch number, and layer number. The vials were then weighed with a 1 mL Eppendorf tip included in each vial and set aside. An additional vial was labelled as Layer 8 and weighted without a pipette tip. An accurate mass of *ca.* 100 mg of sample was added to Vial 8 and then weighed again. 8 mL of solvent was added to Vial 8 and sonicated for 15 minutes with a FS60 tabletop ultrasonic cleaner (Fisher Scientific, Fair Lawn, USA). The content was

pipetted using an Eppendorf pipette layer by layer, top-down, into the 7 vials with 1 mL in each vial, with the designated tip, either immediately, after 15 minutes delay, or 60 minutes after the sonication. Each trial contained three different batches, which indicated the different periods of settling time after sonication. Batch 1 samples were pipetted immediately after sonication, Batch 2 samples were allowed 15 minutes of settling time, and Batch 3 samples were allowed to settle for 60 minutes before the layers were pipetted. The vials were left in the fume hood to evaporate the solvent until the difference in mass measurement is less than 0.0001 g. The trials and their content are listed in Table 2.2. Figure 2.7 demonstrates the process of setting up each trial.

Table 2.3 The material and solvent used for each trial.

Trials	Material	Solvent
1, 2, 3	MoO_3	Acetone
4, 5, 6	Nano Al (O-Al)	Isopropanol (IPA)
7, 8, 9	Viton coated nano Al (V-Al)	IPA
10, 11, 12	Palmitic acid coated Al (L-Al)	IPA
13, 14, 15	MoO_3	IPA

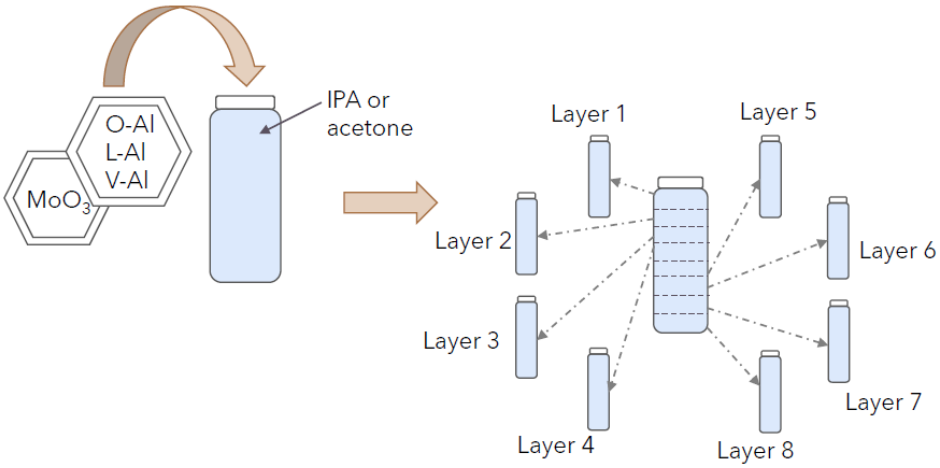

Figure 2.8 Each precursor was suspended in solvent individually through 15 minutes of sonication. The suspension was pipetted out layer by layer after either 0 minute, 15 minutes, or 60 minutes of wait time.

2.4.2 Nanothermite Trial Set Up

Unlike the previous trials, Trials 16, 17, and 18 are nanothermites. These trials have the same principle of suspending solids in the solvent, but the procedure of making nanothermite was not described previously, it will now be described here. An accurate amount of *ca.* 100 g of aluminum is added to Vial 8. The amount of MoO_3 was calculated using Equation 2.5, where $\Phi = 1.2$.

Once the correct amount of MoO_3 was weighed in a weighing boat, most of the MoO_3 was transferred into Vial 8, and the remaining was washed with an accurate volume of 4.0 mL of IPA into the vial. Another 4.0 mL of IPA was added to the vial using an Eppendorf pipette. As the set up from the previous trials, all the vials were labelled and weighed prior to adding any aluminum, MoO_3, or solvent. In addition to the 1.0 mL Eppendorf pipette tips, an extra 1.0 µL Eppendorf pipette tip was added to each vial, including Vial 8, for Trials 16, 17, 18. They were used to pipette subsamples onto the SEM stages and into 4 mL vials for further analyses.

Table 2.4 Nanothermite Sedimentation Trials

Trials	Material	Solvent
16	O-Al/MoO_3 nanothermite	IPA
17	L-Al/MoO_3 nanothermite	IPA
18	V-Al/MoO_3 nanothermite	IPA

2.4.3 Analysis

2.4.3.1 Mass Distribution

Once it was determined visually that most of the solvent had evaporated, the vials were weighed daily until two consecutive measurements of a vial differed less than 0.0001 g.

2.4.3.2 Zeta Potential Analysis

The zeta potential of O-Al, L-Al, V-Al, and MoO_3 samples were analyzed using a Zetasizer Nano ZS (Malvern Panalytical, Malvern, UK), at the Department of Chemical Engineering, Queen's University. The indices of refraction of the three types of aluminums and MoO_3 were assumed to be 1.6275 (Mathewson and Myers 1971) and 2.0666 (Lajaunie et al. 2013), respectively. The effect of coatings was neglected. Two different concentrations were used to measure the zeta potential for each sample. The high concentration samples contained 50 mg of one of the aluminum materials or MoO_3 suspended in 10 mL of IPA. The low concentration samples were made by diluting the high concentration samples with IPA using a 1:5 ratio. In each case, the sample was sonicated for 15 minutes before being injected into the sample cells to be analyzed.

2.4.3.3 SEM Analysis of Nanothermite Trials

Each layer of the nanothermite Trials, 16, 17, and 18 were pipetted onto an SEM stage to be imaged. At least three different locations on each stage were examined, and the size of at least 20 aluminum and 20 MoO_3 particles were measured at each location. In total, at least 60 to 70 images were taken to ensure the images represent the actual morphology of the sample.

2.4.3.4 ESD sensitivity of Nanothermite Trials

For each batch of nanothermites, samples from Layers 1 to 7 were scraped out and mixed gently with a spatula. The nanothermite samples were transferred into the sample cell where 5 -25 kV sparks are discharged onto the samples. The sample cell was placed 0.5 cm away from the tip of the discharge output probe. If a nanothermite sample was not ignited after five consecutive sparks, then the nanothermite sample was considered insensitive to the spark at that level of energy, and the tests were repeated with higher energy sparks. The testing procedure was repeated for layer 8 samples.

The same procedure was followed for other nanothermites produced in this project but without the layer distinction.

2.4.3.5 Friction sensitivity

As the ESD sensitivity test, samples are separated between Layers 1 to 7 and Layer 8. A small amount of nanothermite was transferred to a ceramic plate, with specific friction applied to the sample with a ceramic peg. If a sample was not ignited after six consecutive trials, then the sample was considered insensitive to the specific force, and more friction was applied. If the sample was ignited within the first six trials, less force was applied until the sample was shown to be insensitive to the friction.

The same procedure was followed for other nanothermites produced in this project but without the layer distinction.

3. Sedimentation Trends of Nanothermites – Results and Discussion

It is essential that energetic materials can be readily initiated under specific and well-defined conditions. However, initiation by stimuli from the environment at energies that are readily encountered during storage, transport and use are unacceptable. In the case of nanothermites, such unacceptable behaviour occurs as the result of friction and electrostatic discharge. In addition to overall sensitivity, there is an unpredictability in nanothermite response. This thesis addresses these issues with two studies in the present and following chapters; the potential for the separation of nanothermite powders into regions of different sensitivity is reported here, followed by attempts to widen the scope of available oxidants to identify systems that are less sensitive to undesirable stimuli in the next chapter**.**

The work is a continuation of previous work done within the group (Starchuk, 2019). The main objective of this section is to examine the settling effect of nanothermites and their precursors in organic solvents, and to examine the sensitivities of nanothermites as a function of settling time and sedimentation layer. If a relationship between sensitivities and settling time or sedimentation layer indeed exists, a mean to tailor specific level of sensitivities can be developed. To achieve these goals the settling trends, size distribution, and zeta potential of aluminum and MoO_3 were examined and analyzed.

3.1. Precursors of Nanothermites – MoO_3, O-Al, V-Al, and L-Al

The sedimentation trends of the precursors, O-Al, V-Al, L-Al and MoO_3 were examined, as well as the sedimentation trend of nanothermites. The purpose of studying the precursors and the nanothermites separately was to establish the baseline behaviours of these precursors. Once the baseline settling effects were established, whether the properties of these precursors changed once they were made into nanothermites can be concluded. In this section, the settling behaviours of the precursors were described and analyzed in detail. The different trials of precursors in solvent sedimentation were summarized in Table 2.2.

3.1.1 Sedimentation Trends of Nanothermite Precursors

O-Al, L-Al, and V-Al were suspended in IPA, or in the case of MoO_3 in IPA and acetone, using sonication, separately. After the sonication was completed, the suspension was pipetted layer by layer into eight separate vials. To explore if the sedimentation trend can be described as a function of wait time, they were allowed to rest for three different periods. 0-minute wait time refers to the batches where the suspensions were pipetted immediately, and all the layers were pipetted into the designated vials within the first 2 minutes. These batches were referred to as Batch 1. Batch 2 suspensions were pipetted with 15 minutes delay and Batch 3 suspensions were allowed to rest for 60 minutes before the pipetting process began. The vials were allowed to dry in the fume hood and the solvent was considered completely evaporated when the mass of the vials varied less than or equal to 0.1 mg between two consecutive measurements.

3.1.1.1 MoO_3 in Acetone and IPA

MoO_3 was suspended in both acetone and IPA as described in Method, Section 2.4. Figure 3.1 and Figure 3.2 show the residual mass in each layer of MoO_3 in acetone and IPA, respectively, with different wait times. Readers are reminded that different scales are used in figures to optimally display the results. MoO_3 displayed an evenly distributed top seven layers, at approximately 10%, and the remaining 28% was settled in the 8^{th} layer in acetone, with 0-minute wait time. With the 15-minute wait time, a similar trend was observed. The top seven layers were relatively evenly distributed; however, it can be shown that Layer 1 contained less mass than Layer 2-7, and each of the first six layers contained less mass than Batch 1 MoO_3. Layer 7 of Batch 2 contained 2% more of MoO_3 than Batch 1 Layer 7. Batch 2 Layer 8 contained 43% of the MoO_3, approximately 15% more than the same layer of Batch 1. These trends indicated that during the 15-minute delay, MoO_3 gradually settled toward the bottom of the vial. Batch 3, where the MoO_3 layers were pipetted 60 minutes after the sonication, the increase of residual mass in each subsequent layer of the first seven layers was even more noticeable. Each layer contained more MoO_3 than the previous layer, with Layer 1 containing only 2.1% of the MoO_3 and Layer 7 containing 11% of MoO_3. Layer 8 contained more than 62% of the MoO_3, which was 20% more than the same layer of Batch 2 and 34% more than Batch 1. The settling process of MoO_3 in acetone was not complete within the first 15 minutes, as the mass of the bottom layers continued to increase as the wait time increased. For the top six layers, as the wait time increased, the mass of MoO_3 decreased in each layer. However, there was some uncertainty in Layer 7, where Batch 2 contained the most MoO_3 and Batch 1 and Batch 3 contained approximately the same mass of MoO_3. This uncertainty could be caused by the pipetting process. With each layer being pipetted out of the sample vial, the sedimentation process was inevitably disturbed and therefore created some uncertainty.

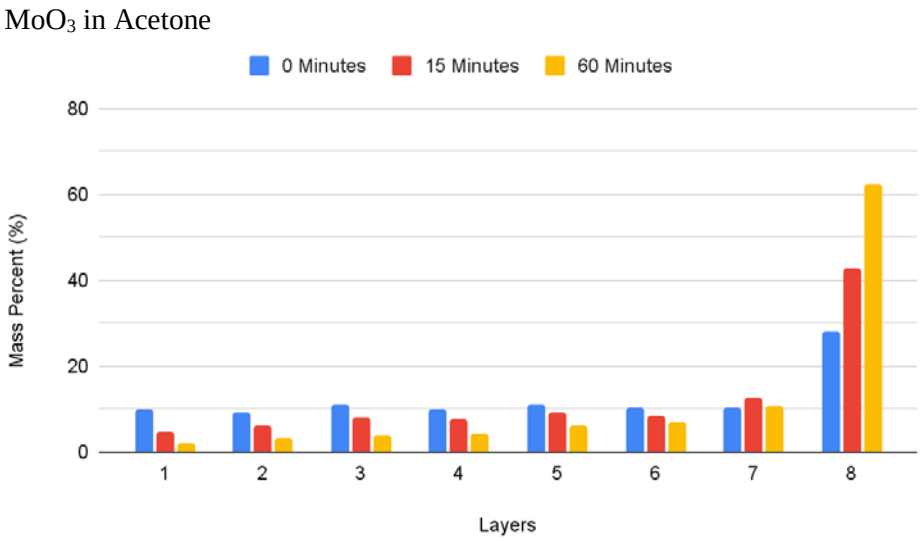

Figure 3.9 Settling trend of MoO_3 in acetone with different wait times.

Batch 1 of MoO_3 showed a similar trend in IPA as in acetone, as shown in Figure 3.2; evenly distributed layers 1 – 7 at 11% and the remaining mass was settled in the 8th layer at 19%. The mass distribution of MoO_3 in IPA was more uniform relative to data in acetone, where 28% of mass was settled in Layer 8. This showed that MoO_3 suspension was more stable in IPA than in acetone. This tendency was not only true for Batch 1, the same evenly distributed layers were observed for both Batch 2 and 3 as well. At Layer 8, the residual masses were 19%, 31%, and 44%, at 0-minute, 15-minute, and 60-minute wait times, respectively. The difference in mass between the longest wait time and 0 wait time was 25% instead of 34%, in the case of MoO_3 in acetone. For the top seven layers, the effect of wait time was also less pronounced. Compared to MoO_3 in acetone, the mass differences between layers of the same wait time and the mass differences between the same layer of different wait times of MoO_3 in IPA were both smaller. Layer 1 of Batch 2 contained 8% of the mass, being the layer with the least amount of MoO_3, while Layer 7, which contained the most MoO_3 in the first seven layers, contained 11% of MoO_3. The difference in these layers was a 3% mass difference in IPA, while the difference between Layer 1 and layer 7 with the same wait time was more than 8% in acetone. The difference in Layer 1 and Layer 7 was approximately 4% in Batch 3 in IPA and 8% in acetone. Given that the densities of IPA (0.785 g/cm^3 at 20°C) (USCG, 1999) and acetone (0.785 – 0.791 g/cm^3 at 20°C) (USCG, 1999; CRC Handbook 2014) are very similar, the density difference between IPA and acetone cannot explain the relative stability of MoO_3 in IPA. The difference in suspension stability is most likely caused by

intermolecular interaction between the solvents and MoO_3 that is reflected in the zeta potential measurement. MoO_3 in IPA generated a zeta potential of -56 mV, indicating a stable suspension system. Unfortunately, due to instrumental limitation, the zeta potential of MoO_3 in acetone could not be analyzed. Zeta potential will be discussed in more detail in Section 3.1.2.

MoO_3 in IPA

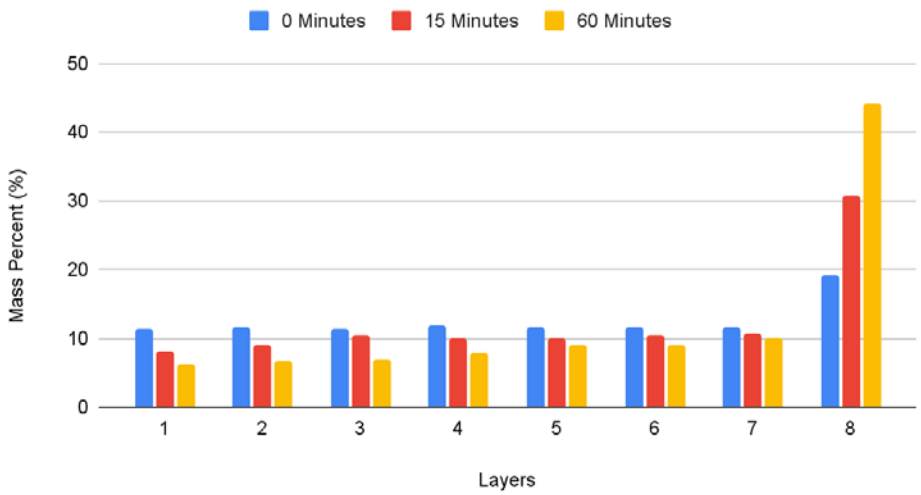

Figure 3.10 Settling trend of MoO_3 in IPA with different wait times.

3.1.1.2 Settling Trends of Different Aluminums in IPA

As with MoO_3, all three aluminums were sonicated for 15 minutes before the layers were pipetted into the designated vials. Figures 3.3 – 3.6 illustrate that each aluminum behaves differently. L-Al started to settle very fast, V-Al has the most skewed settling trend, and O-Al had the most evenly distributed top layers.

At 0-minute wait time, O-Al shows a very evenly distributed top seven layers with approximately 11% of O-Al with some variations at Layer 4 and Layer 5, most likely caused by the pipetting motion, and Layer 8 contained 18% of O-Al. The difference between Layer 8 and Layers 1-7 was quite small compared to the MoO_3 results. The effect of wait time was not significant. The first seven layers still contained 11 -12% of O-Al, while Layer 8 contained 17% of O-Al 15 minutes after sonication and 22% of O-Al 60 minutes after sonication. The results indicated that O-Al in IPA as a colloid was very stable. Although there were some minor variations between layers and wait times, the system was already established once sonication was completed,

and 60 minutes of settling time did not make much difference in terms of layer distribution. The data obtained from zeta potential analysis of O-Al was consistent with the settling trend. The zeta potential of O-Al in IPA was greater than 30 mV, the repulsion force between aluminum helped stabilize the particles in IPA. O-Al settling trend served as a baseline result as the particles were not coated, therefore the different behaviours of V-Al and L-Al could be attributed to the effects of coating.

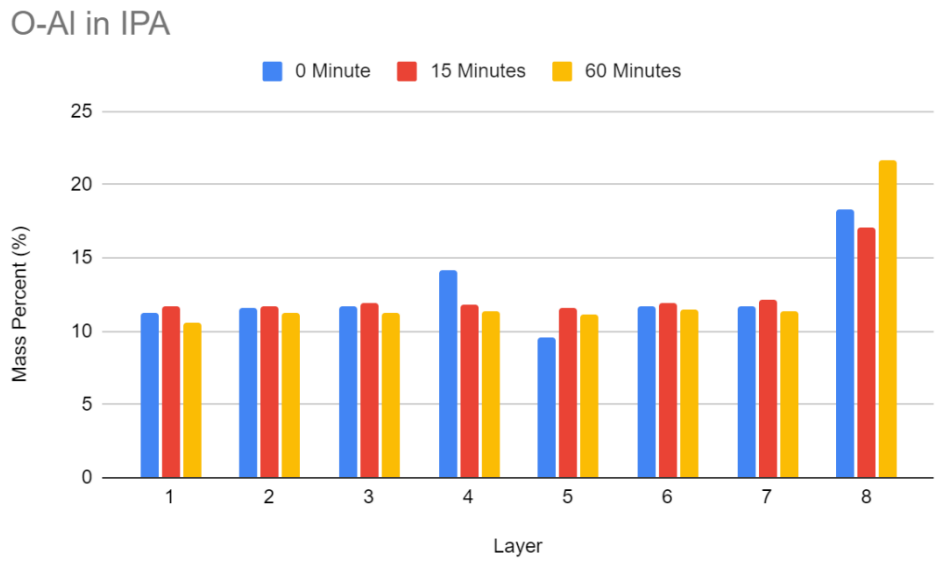

Figure 3.11 Settling trends of O-Al in IPA

The settling trends of L-Al were significantly different than O-Al, as shown in Figure 3.4. It shows with 0-minute wait time, the mass of L-Al in the first three layers was 11% and started to decrease and reached a minimum at Layer 5 (8%) before the mass started to increase toward the lower layers. Layer 8 contained the most L-Al at 29%. It indicates that L-Al settled faster than it was being pipetted out of the vial that L-Al started to aggregate and settled at a higher rate within the first 2 minutes after sonication. After 15 minutes, there was hardly any L-Al left in the first five layers, with more than 60% of L-Al at Layer 8. After 60 minutes of settling time, Layer 6 contained less than 5% of L-Al and Layer 8 contained almost 85% of L-Al. The measurement of zeta potential analysis (12.1 mV) suggested an unstable colloid system, which was consistent with the settling trend. The coating of L-Al, palmitic acid could be the cause of the different behaviour between O-Al and L-Al. Palmitic acid is a long chain saturated fatty acid with no branches; the Van der Waal forces between the molecules increase as palmitic acid pack together lengthwise. This could contribute to the aggregation and the fast settling of L-Al particles.

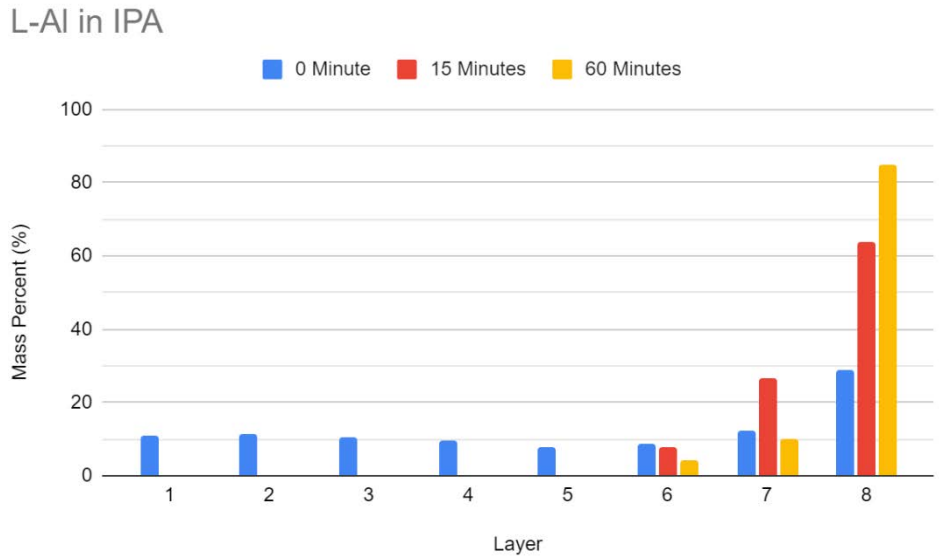

Figure 3.12 Settling trends of L-Al in IPA

V-Al behaved differently than both O-Al and L-Al. As illustrated in Figure 3.5, Layer 8 of V-Al contained the largest mass of particles when compared to O-Al and L-Al. Within the first 2 minutes of sonication, Layer 8 had already accumulated 34% of V-Al, after 15 minutes, the residual mass increased to 79% and after 60 minutes, the residual mass increased to 92%. Even though the settling trends of V-Al were heavily skewed toward Layer 8, the top layers still contained some V-Al; unlike L-Al, where there was hardly any L-Al within the top layers after 15-minute wait time. Interestingly, the residual mass in the top layers, although minimal after 15-minute and 60-minute wait times, was evenly spread out between the layers. It showed that there existed some repulsion between V-Al particles, although the system as whole was unstable. This result was not consistent with zeta potential analysis; a strongly positive result suggested that the V-Al/IPA system should have been stable. The Viton coating could be the reason behind this contradiction. Viton is a fluorocarbon polymer and fluorocarbon compounds have been known to have unusual behaviours that would not be expected from hydrocarbon compounds.

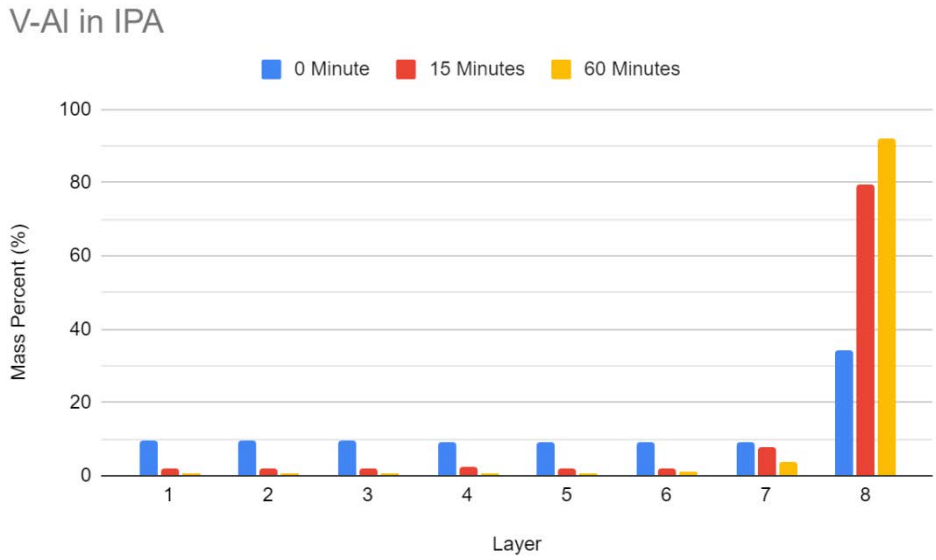

Figure 3.13 Settling trends of V-Al in IPA

Figure 3.6 provides a comparison of the settling trends of three different aluminums with 0-minute wait time. This figure provides a glimpse of the settling trends of the three different aluminums. O-Al had the most evenly distributed layers, the settling rate of L-Al was faster than the pipette rate, which can be shown by the decreasing-then-increasing pattern between layers, and lastly V-Al contained the most residual mass in Layer 8 with minimal aluminum evenly remained in the top layers.

3.1.2 Zeta Potential

In the previous section, Section 3.1.1, zeta potential has been mentioned to explain the stability of the MoO_3 and aluminum suspensions in IPA, in this section, the results of zeta potential are discussed in detail. Zeta potential is often measured as an indication of the stability of colloid systems. It is for this reason the zeta potential was measured, to gain insight and explore the settling behaviours of the precursors of nanothermites. At the same time, zeta potential was also measured to explain the different settling behaviours of nanothermites relative to the individual precursors, as observed by the previous work done.

Zeta potential is the potential difference between the suspension medium, IPA in this case, and the portion of the medium that is strongly bound to the particles and moves with the particles (Lowry et al, 2016). The specific value at which a colloidal system is considered stable depends on the compounds involved, but as a rule of thumb, a colloidal system is considered stable when its zeta potential measurement is greater

than |±30 mV|. High absolute values of zeta potential indicate high repulsion between particles, which prevents agglomeration of the particles that causes the particle sedimentation (Lunardi et al. 2021).

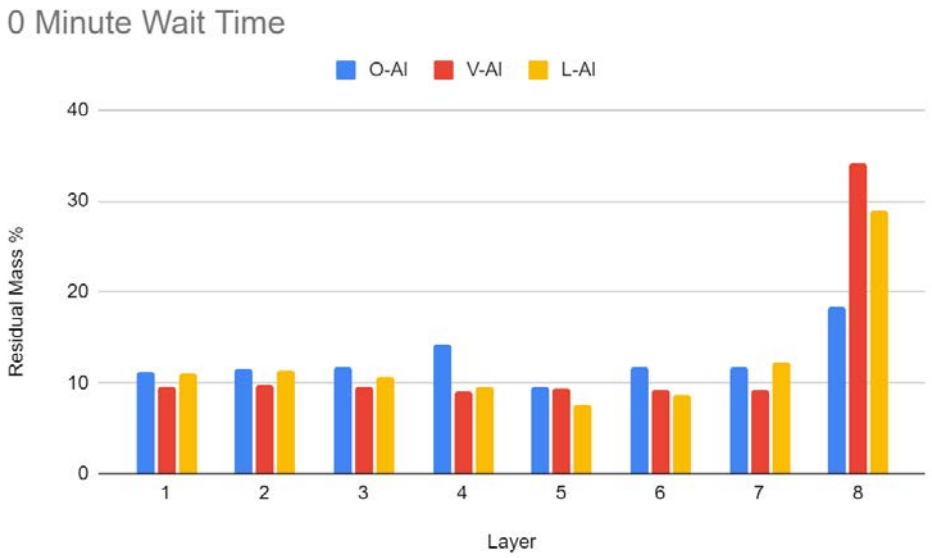

Figure 3.14 A comparison of the settling trend of all three Al nanoparticles at 0-minute wait time

Table 3.1 summarizes the results from zeta potential analysis. Two different dilution factors were used to measure the zeta potential of each aluminum in IPA and MoO_3 in IPA, 0.5 w/v% and 0.1 w/v%. The higher loading was chosen for maximum concentration as being reasonably close to the concentration used in the sedimentation experiments, whilst within instrument limitations. A lower loading was chosen due to the high attenuation rate of V-Al in IPA system.

Three measurements were made for each concentration and the values reported in Table 3.1 present the average of the three analyses. Zeta deviation indicates the distribution of zeta potential distribution, in other words, the spread of the peak. Figure 3.3 is the zeta potential measurement spectrum of 0.1% loading MoO_3 in IPA. It shows a broad peak, with a zeta deviation of 38.1 mV. As a comparison, the zeta deviation of the standard used for the zetasizer is 4.89 mV. The width of the MoO_3 peak was typical for the peaks of aluminum samples as well. Both the size and the size distribution of the samples affect the width of the peaks; small particle size and large size distribution both cause the broadening of the peaks (Malvern Panalytical 2020). Since the aluminum particles are nanosized, it is reasonable to assume that it

causes the broadening of the peak. The particle sizes of aluminum and MoO_3 are summarized in Table 3.2. The size distribution will be discussed in more detail later in Section 3.2.2, but it is worth mentioning here that the average size of MoO_3 is approximately 1.2 μm with a standard deviation of 2.0 μm. The lack of size uniformity could also contribute to the broadening of the peaks.

Table 3.5 Reported zeta potential value for MoO_3 and Al nanoparticles.

	Concentration (w/v%)	Average Zeta Potential (mV)	Zeta Deviation (mV)
MoO_3	0.5	-56	48
	0.1	-54	40
O-Al	0.5	50	43
	0.1	-5.8	41
L-Al	0.5	12	47
	0.1	-3.8	38
V-Al	0.5	46*	127
	0.1	0.10	56

* High uncertainty

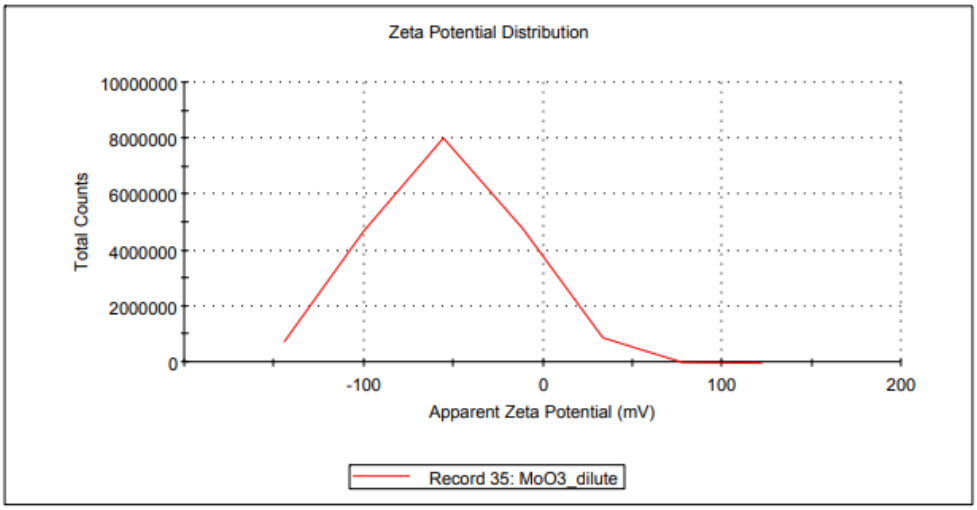

Figure 3.15 0.1% loading MoO_3 spectrum shows a broad signal peak.

The evenly distributed layers of MoO_3 could be contributed by its strongly anionic zeta potential. Unfortunately, presently it could not be concluded if zeta potential contributed to the different behaviour of MoO_3 in acetone and IPA. Acetone is not compatible with the sample cells of the zeta sizer due to its ability to dissolve the sample cell material, the zeta potential MoO_3 in acetone could not be measured; no data have been reported in the literature.

The zeta potential measurements of MoO_3 were quite consistent between the different concentrations. However, the same could not be said for the three aluminum materials. The concentration of aluminum significantly affects the zeta potential reported. The zeta potential analysis reported that at low concentration all three aluminum samples are somewhat neutral and cationic to different degrees at the higher concentration. The zeta potentials are usually more extreme at high concentrations and closer to neutral at lower concentrations (Bhattacharjee 2016). Since the aluminum concentrations used in the sedimentation experiments were even higher than the high concentrations used zeta potential measurement, the zeta potentials of high concentration measurements are discussed here.

At 0.5% loading, the O-Al and V-Al were strongly cationic, while L-Al was the least cationic. L-Al is slightly cationic with a zeta potential of 12.1 at 0.5% loading. The fast-settling L-Al pattern agrees with the zeta potential value. Since L-Al is only slightly cationic, there is not enough charge around Al particles to repel each other and maintain a stable suspension. Figure 3.4 shows that L-Al settled the fastest among all three aluminum samples. After waiting for 15 minutes, L-Al was presented only in Layers 6, 7, and 8, while both V-Al and O-Al were still present in all 8 layers.

As discussed above, O-Al suspension is the most stable suspension out of the three aluminums. Its stability could be explained by its zeta potential. At 0.5% loading, O-Al has a zeta potential value of 49.9 mV, which is considered strongly cationic. The charges surrounding O-Al particles were strong enough to prevent them from aggregating and therefore continue to be suspended in the solvent.

The values reported for V-Al has a high uncertainty. A reliable result requires the difference between the average measurement and the individual measurements to be less than 2 mV. The average zeta-potential measurement for V-Al at 0.5% loading is 46 mV, but not all three measurement values lie within the 44 – 48 mV range. In addition, the report has shown that at 0.5% loading, the concentration is too high that not enough forward scattered light detected was insufficient (Malvern Panalytical 2020).

Indices of refraction were required to measure and calculate the zeta potential of the samples. As outlined in Section 2.4.3.2, all three Al samples were assumed to have

the same index of refraction, regardless of the coating. This could also contribute to the uncertainties of the results. Taking the difference in concentration and assumption of index of refraction into account, the specific value should be interpreted with caution; interpreting them qualitatively may be more meaningful.

3.2 Al/MoO_3 Nanothermites

3.2.1 Sedimentation Trend

From previous work (Starchuk, 2019), it was observed that the settling trends of nanothermites are not necessarily the same as their precursors. This is particularly evident in the case of O-Al/MoO_3 nanothermites, as shown in Figure 3.8. As shown in Figures 3.2 and 3.3, both MoO_3 and O-Al were relatively stable in IPA and had evenly distributed top layers with less than 20% of mass at respective Layer 8 at 0-minute wait time. This was not observed again in the case of O-Al/MoO_3 nanothermite. Right after sonication, with 0-minute wait time, there was 7% of nanothermite contained in Layer 1; however, there was no measurable mass of O-Al/MoO_3 left in the second and the third layers. Approximately 2% of nanothermite was observed in Layer 4 and increased with each layer, with 33% of nanothermite settled in Layer 8. As in the case of L-Al in IPA, the decreasing-and-increasing pattern suggested that the settling rate of O-Al/MoO_3 nanothermite was faster than the pipetting rate. As described in Section 2.4.2, there was an extra pipetting step to pipette the layers onto SEM stages, which further delayed the pipetting rate slightly. After 15 minutes delay, there was no measurable mass from Layers 1 – 5, with 4% of nanothermite in Layer 6, 39% in Layer 7, and the remaining 57% in Layer 8. After a 60-minute wait time, only Layer 7 and 8 contained a measurable amount of nanothermite, at 19% and 81%, respectively. The fast settling might be caused by the big difference between the zeta potential between O-Al and MoO_3 in IPA, where they could self-assemble in a very short time due to the electrostatic attraction (Hees, Kriele, and Williams, 2011).

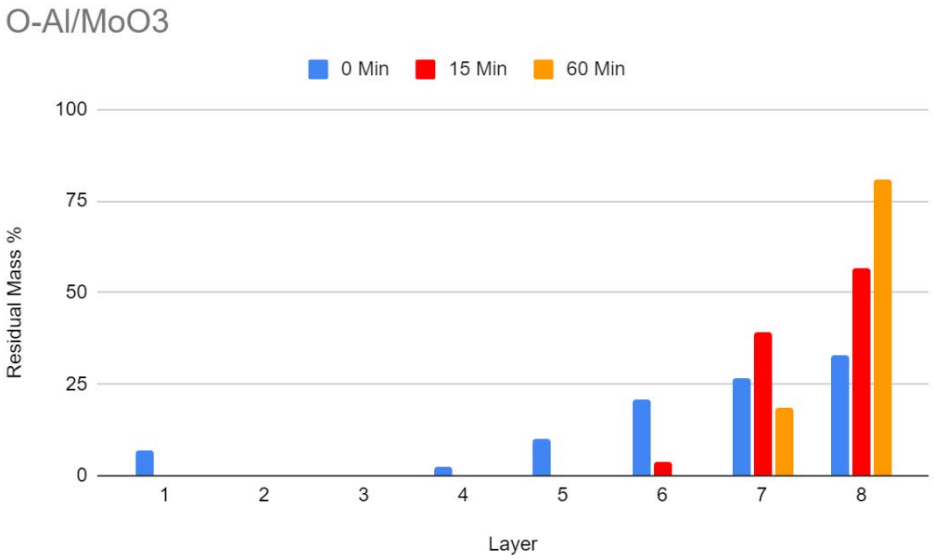

Figure 3.16 The settling trends of O-Al/MoO_3 nanothermite in IPA

Figure 3.9 illustrates the settling trends of L-Al/MoO_3 nanothermite system. By comparing Figures 3.4 and 3.9, it can be concluded that the settling trends of L-Al in IPA and L-Al/MoO_3 nanothermite in IPA are quite similar. The same valley shape pattern appeared in L-Al/MoO_3 nanothermite system as it did in L-Al in IPA system. The sedimentation percentage of the nanothermite in Layer 8 in all wait times were also close to those of L-Al in IPA. Layers 8 in L-Al suspension contained 29%, 64%, and 85% of L-Al after 0-minute, 15-minute, and 60-minute wait time, respectively; Layers 8 in L-Al/MoO_3 contained 36%, 65%, and 87% after 0-minute, 15-minute, and 60-minute wait time, respectively. Unlike O-Al, L-Al did not become even less stable after it was made into nanothermite; in fact, it might be slightly more stable than the pure L-Al system. In the L-Al in IPA system, after 15 minutes delay, the top layers did not contain any quantifiable
mass; however, although minimal amount, even with 60 minutes wait time, there were close to 1% nanothermite in each of the top five layers. Unfortunately, the concentration of Layers 1 – 5 for 15-minute and 60-minute wait times were too low that the 1 µL deposited onto the SEM carbon tape contained no observable particles for the top five layers. Figure 3.10 shows the SEM samples of L-Al/MoO_3 layers for each batch. The samples in the top row were pipetted right after sonication, at 0-minute wait time. Each sample belongs to a layer, Layers 1 – 8 from left to right. The second row was the layers of 15-minute wait time and the bottom row 60-minute wait time. Not all carbon tapes contained nanothermite and some tapes contain more nanothermites than others did, even though the same amount of suspension were pipetted onto each tab; the darker spots on the carbon tape meant that more

nanothermite was deposited onto the tape. The images of the stages that appear empty had been taken and analyzed by EDAX, the results showed that these stages do not contain any nanothermite. The colour intensity of the samples of each layer and batch corresponded well with the sedimentation trends. The stages of the top rows all contain nanothermite deposition. The first five layers show somewhat similar colour intensity and Layers 7 and 8 show more saturated grey. No nanothermite can be seen in the first five layers of the second and third rows and the sixth layers are also only barely visible. The seventh and the 8th layers show saturated colour. The colour intensity corresponds to the heavy lower layer L-Al/MoO_3 sedimentation trend with evenly distributed and light deposit for the top layers.

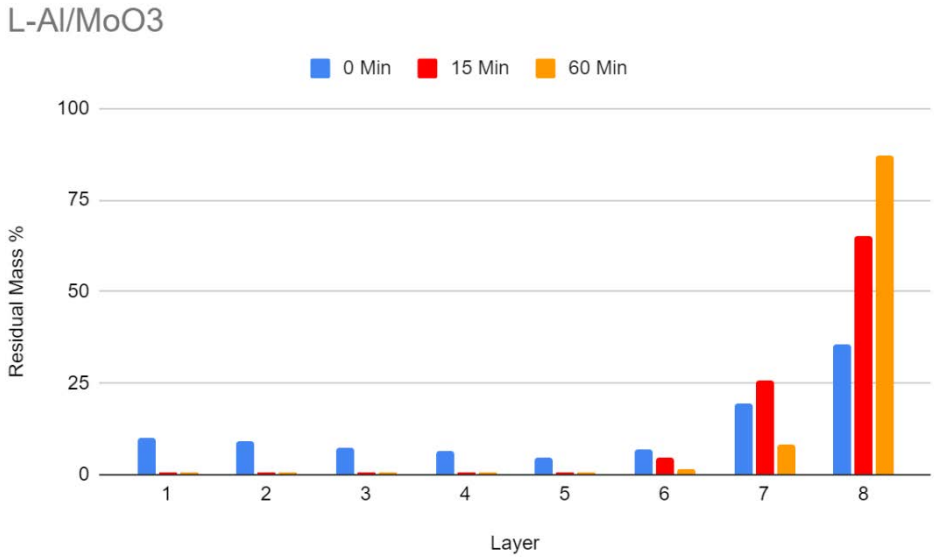

Figure 3.17 The settling trends of L-Al/MoO_3 nanothermite in IPA

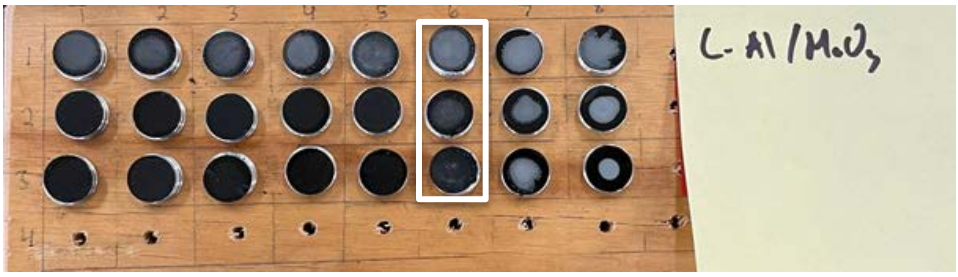

Figure 3.18 SEM samples of L-Al/MoO_3. The top-row stages contain the layers of 0-minute wait time sedimentation, the second row 15-minute wait time, and the

bottom row 60-minute wait time. From left to right, the stages contain layers 1 – 8. The colour intensity of the sample deposited on the holders resembles the sedimentation trends. For the 0-minute wait time, the tabs show a lighter grey for the top layers, while Layers 7 and 8 show a darker grey, which corresponds to more mass in layers 8 and 8. The sedimentation trends of 15- and 60-minute wait times indicate that the majority of the mass was settled in Layers 7 and 8. On the carbon tab, Layers 7 and 8 showed the most intense grey colour. The sediment trend of Layer 6 of the three wait times indicates the mass decreases as the wait time increases. The colour of the Layer 6 tabs also decreases in intensity as the wait time increases.

Figure 3.11 shows the settling trends of V-Al/MoO_3 nanothermite. V-Al/MoO_3 was less stable in IPA than V-Al. Figure 3.5 shows a settling trend with a heavy aggregation of mass in Layer 8, but still somewhat evenly distributed Layers 1-7. As in Figure 3.10, the valley shape of a high settling rate is again observed. The 8th layer of V-Al/MoO_3 in each wait time contained more mass than their V-Al in IPA counter parts. Furthermore, SEM images showed that the top layers of V-Al/MoO_3 contained only MoO_3, which means that all the nanothermites had settled toward the bottom layers, and only the extra MoO_3 was suspended in the top layers of IPA. This would explain the evenly distributed top layer, as discussed in Section 3.1.1, MoO_3 in IPA had evenly distributed top layers with various wait times.

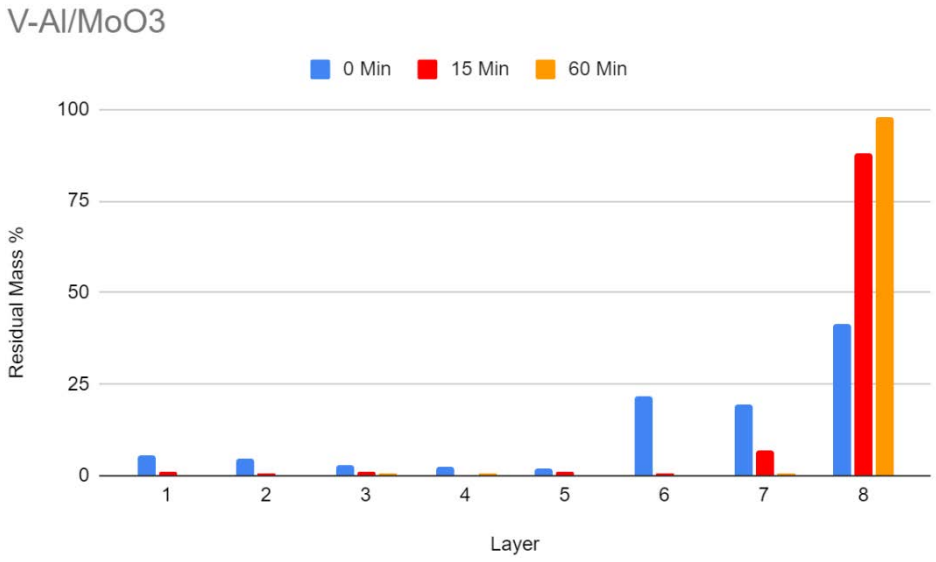

Figure 3.19 The settling trends of V-Al/MoO_3 nanothermite in IPA

Figure 3.12 presents a comparison of the settling trends of all three nanothermites with 0-minute wait time. The O-Al/MoO_3 nanothermites settled the fastest such that there were already layers without any nanothermite within the first minute or so, possibly due to the large electrostatic attraction between O-Al and MoO_3. L-Al/MoO_3 and V-Al/MoO_3 although still contained masses in all layers, there were more masses contained in the 8^{th} layer. The skewed 8^{th} layer was especially pronounced for V-Al/MoO_3. From the settling trends, it can be concluded that nanothermites do not settle the same way as their precursors, they settled faster and more aggressively than the precursors. However, the coating on nano aluminium still affects how the nanothermites settle, as each nanothermite settled differently. Interestingly, the same phenomenon was not observed in L-Al/MoO_3 nanothermite. It is possible that palmitic acid coated on the aluminum allowed better mixing of MoO_3 and L-Al than the Viton coating did.

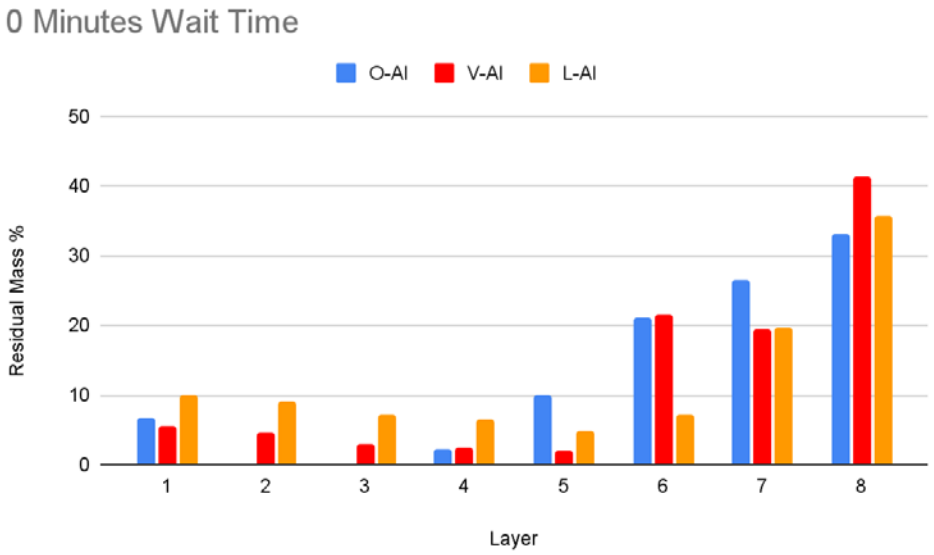

Figure 3.20 A comparison of all three nanothermites in IPA with various wait times

3.2.2 Average particle Size

The particle size was analyzed using SEM, as described in Section 2.4.3.3. The purpose of measuring particle size was to examine if it could explain the settling trends and nanothermite sensitivity. As discussed in the introduction, the performance and sensitivity of nanothermites are hugely influenced by their particle size. Therefore, it is beneficial to analyze the particle size of each layer and wait time.

Table 3.2 summarizes the average particle sizes of aluminum and MoO_3 within the top 7 layers and the bottom layer and their standard deviation. The sizes of aluminum particles are not statically different between the nanothermite samples, wait times or layers; the same applies to MoO_3 particles. Aluminum particles are approximately 113 nm and MoO_3 particles are approximately 1.2 μm. Aluminum particles have a smaller size distribution while MoO_3 shows a bigger size distribution. Since neither aluminum and MoO_3 particles exhibit statistically different particle sizes, it is unlikely that particle size contributes to the different settling trend or nanothermite sensitivity, which will be discussed in more detail later.

Table 3.6 Average particle size of each aluminum and MoO_3

Wait Time (Min)	Aluminum				MoO_3			
	Layers 1 - 7		Layer 8		Layers 1 - 7		Layer 8	
	Size (nm)	σ (nm)	Size (nm)	σ (nm)	Size (nm)	σ (nm)	Size (nm)	σ (nm)
O-Al								
0	110.8	58	104.2	32	1376	4600	1124	1200
15	106.7	54	94.38	41	1137	1200	775.0	560
60	98.93	44	110.5	57	989.3	800	831.9	630
V-Al								
0	108.4	49	117.6	69	869.8	980	1095	1100
15	115.6	37	132.2	62	653.7	250	937.2	830
60	114.0	38	125.9	48	1625	1700	1500	1500
L-Al								
0	116.7	74	115.1	42	1659	1200	1256	1600
15	113.4	51	114.3	43	1182	730	1582	1600
60	105.7	38	134.5	83	1278	1500	1670	1700

3.2.3 Nanothermite Sensitivity

The sensitivity of each nanothermite toward friction and ESD is summarized in Table 3.3 as a function of wait time and layer. As discussed earlier, the goal of the project is to find a solution to mitigate the undesirable traits of unintentional initiation of nanothermites. If the sensitivity of nanothermites could be quantified as a function of settling time and layer, it would be a step forward toward this goal.

To measure ESD sensitivity, the voltage that is discharged through the capacitor is altered and recorded. The energy of the electric discharge (E_{ESD}) is calculated by Equation 3.1.

$$E_{ESD} = \frac{1}{2} CV^2 \qquad \text{Equation 3.1}$$

Where C is the capacitance of the capacitor of the ESD apparatus and V is the voltage applied (Weir et al. 2013). In the current setup, the capacitance is 500 pF.

All the nanothermites were very sensitive to ESD. For the most part, less than 6 mJ of discharge was enough to ignite the nanothermites, except for 60-minute wait time O-Al/MoO_3. The nanothermite ignited at 25 mJ; however, there is reasonable doubt that it could withhold higher than 6 mJ of electrostatic discharge. Due to the long wait time, there was not enough material in Layers 1 - 7 to produce accurate results for both friction and ESD sensitivities. The amount of nanothermite loaded in the sample cell was less than desirable, therefore the uncertainty of this measurement was particularly high. The lack of material in layers 1-7 is especially pronounced in V-Al/MoO_3 nanothermite due to its heavily skewed sedimentation result, as shown in Figure 3.11.

No universal trend of friction sensitivity among all the nanothermites was observed. Even within the same nanothermite, the relationship between wait time and sensitivity varies. For O-Al/MoO_3, the friction sensitivity stayed somewhat constant for the combined layers 1 - 7, but the sensitivity decreased as the wait time increased for the 8th layer. For V-Al/MoO_3, it is not clear if there is a trend for layers 1 - 7 as a function of wait time due to the lack of material. Layers 1 -7 showed less sensitivity toward friction compared to the 8th layer, although it is uncertain how much less sensitive the top layers are. For L-Al/MoO_3, the top 7 layers were less sensitive toward friction with 0-minute wait time and the reverse for 15 minutes wait time, while all the layers showed extreme sensitivity with 60-minute wait time. Comparing the different aluminums, the top 7 layers of O-Al/MoO_3 were less sensitive toward friction when compared to L-Al/MoO_3, but due to the lack of data, it is unclear if O-Al/MoO_3 was less sensitive to friction than V-Al/MoO_3 or not. It is clear that the 8^{th} layer of O-Al/MoO_3 was less sensitive than the 8^{th} layer of V-Al/MoO_3 and L-Al/MoO_3.

Table 3.7 Sensitivity measurements of nanothermites

Friction (N)			ESD (mJ)	
Wait Time (Min)	Layers 1 - 7	Layer 8	Layers 1 -7	Layer 8
O-Al				
0	20	10	<6	<6
15	40	40	<6	<6
60	20	120	25*	<6
V-Al				
0	20	10	<6	<6
15	>10[+]	5	Insufficient Material	<6
60	>10[+]	5	Insufficient Material	<6
L-Al				
0	10	<5	<6	<6
15	5	20	<6	<6
60	<5	<5	Insufficient Material	<6

[*] Less than ideal amount of sample.
[+] Not enough material to test further.

Currently, there is no good explanation for the difference in friction sensitivity of these nanothermites. None of the factors analyzed seems to be able to predict the sensitivity differences between the top layers and the bottom layers. The different settling speeds did not correspond to any correlation with the sensitivity and layering. As discussed in the introduction, smaller particles usually mean higher

sensitivity; however, the size difference here is not big enough to make this difference. In fact, for O-Al/MoO_3, for all three wait times, Layer 8 showed higher friction insensitivity than the top layers, while the mean particle size of MoO_3 was slightly smaller.

3.3 Conclusion

The coatings of aluminum play a vital role in the settling trends of the aluminums and the nanothermites, as the coatings interact with the suspension solvent differently. Both L-Al and V-Al behaved very differently than the uncoated O-Al when they were suspended in IPA. O-Al settled relatively slowly with evenly distributed top layers, L-Al had the fastest settling speed, and V-Al had the most skewed 8^{th} layer. Zeta potentials of aluminum and MoO_3 have been analyzed, however, the analysis result was not always consistent with settling behaviours. The unusual behaviour of the fluorocarbon polymer in the Viton coating could be a reason for this inconsistency. It is also clear that the settling trends of aluminums change once they are made into nanothermite. As discussed above, the settling trends of nanothermites deviated from the settling trends of the aluminums and MoO_3. The most obvious case was O-Al/MoO_3 nanothermite, where the precursors were relatively stable in IPA, started to settle within the first 2 minutes of sonication.

The properties of top layers nanothermites and the 8^{th} layer nanothermites were characterized separately. The particles sizes of aluminum and MoO_3 did not differ between layers or wait times. It implies that the different sensitivities between layers and wait times are unlikely rooted in particle size. All the nanothermites were extremely sensitive to ESD, except for the top layers O-Al/MoO_3 with 60-minute wait time; however, the uncertainty of the result was high. Different sensitivity thresholds toward friction were displayed. More work is required to explain the difference in sensitivities. Currently it does not appear that the sensitivity could be easily described as functions of wait time, aluminum coatings, or settling layer.

4. Metal Molybdate as Nanothermite Oxidant - Result and Discussion

The purpose of synthesizing metal molybdates is to widen the scope of available oxidants. To have more oxidants available is beneficial in two ways: 1) increasing the opportunities to discover an oxidant that results in a nanothermites that is less sensitive to ESD and friction, therefore less prone to unintended initiation and 2) enhancing the possibility of tailoring a specific level of nanothermite performance from a spectrum. As discussed before, the risk of unintended initiation of nanothermites limits their real-life applications. Additionally, nanothermites display discrete characteristics and sensitivities. It is desirable that the performance and characteristics could be mapped out into a spectrum such that its performance could be easily adjustable. Therefore, to explore as many possible oxidants is to increase the possibility of finding a nanothermite with controlled initiation and performance.

MoO_3 is the most widely used nanothermite oxidant in military applications. It has a high oxidation state and therefore a good source of oxygen. Al/MoO_3 nanothermite are readily initiated, able to produce reasonably good burn velocities when compared with other nanothermites. However, it is also extremely sensitive to ESD and friction. Kelly et al. and Petre et al. have shown that the sensitivities are somewhat lessened by using a mixture of MoO_3 and CuO as the oxidant when making nanothermites. Therefore, it is of interest to explore the effects of having metal molybdates as the oxidant of nanothermites (Kelly et al., 2017; Petre et al., 2019).

4.1 Oxidizer Synthesis

Two different synthesis methods are used to fabricate metal molybdates, co-precipitation synthesis (CPS) and solution combustion synthesis (SCS). CPS is the more conventional method, in which a simple displacement reaction took place, as described in Section 1.4.1.1. Different solvent options were explored in attempting to synthesize nano particles. SCS was used to efficiently produce metal molybdates, including those that had not been successfully synthesized using the CPS. The characteristics and morphologies of the metal molybdates synthesized using these two methods are discussed here.

4.1.1 Co-precipitation Method (CPS)

Three different protocols were developed for the CPS to achieve the desirable particle size. Detailed description of the three protocols were described in Method Section 2.3.1.2, a brief summary of the protocols used are described here. All three protocols follow the same basic principle; reactants were dissolved in solvents and mixed dropwise using a peristaltic pump. If the products did not precipitate during and immediately after mixing, the mixture was heated to 120ºC. The products were obtained through centrifugation and washing procedures. In this section, the results of synthesizing attempts were presented and discussed.

4.1.1.1 Protocols 1 and 2 - Synthesizing metal molybdate with water and Triethylene Glycol (TEG)

The main difference between Protocols 1 and 2 is the solvent used for Na_2MoO_4, water versus triethylene glycol (TEG); Protocol 2 also requires an additional calcination step, four hours in a 600°C furnace, to purify the product. Several criteria were used to determine the success of a synthetic method. Initial consideration focused on whether a precipitate would form and whether the material was the expected $MMoO_4$ product (M = Mg, Ca, Sr, Ba). Product identification and qualitative purity were determined by X-ray Powder Diffraction (XRD), quantitative purity was determined using thermogravimetric analysis (TGA), often before and after calcination. Scanning electron microscopy (SEM) was then used to determine the size and morphology of the particles present, as well as the morphological variation observed. In these nominally white products, visual inspection also provides some evidence of the presence of amorphous impurity not captured by XRD.

Precipitate formed from the reactions intended to synthesize $CaMoO_4$, $SrMoO_4$, and $BaMoO_4$, while reaction for $MgMoO_4$ did not precipitate. XRD confirmed the identities of precipitates were $CaMoO_4$, $SrMoO_4$, and $BaMoO_4$. See Figure 4.1 for the XRD patterns of $CaMoO_4$ for Protocols 1, 2, and 3 and Appendix for the complete spectra. Table 4.1 lists the yields of the molybdate compounds synthesized using the three protocols and Table 4.2 summarizes the particle sizes of $MMoO_4$ synthesized using the three protocols.

a)

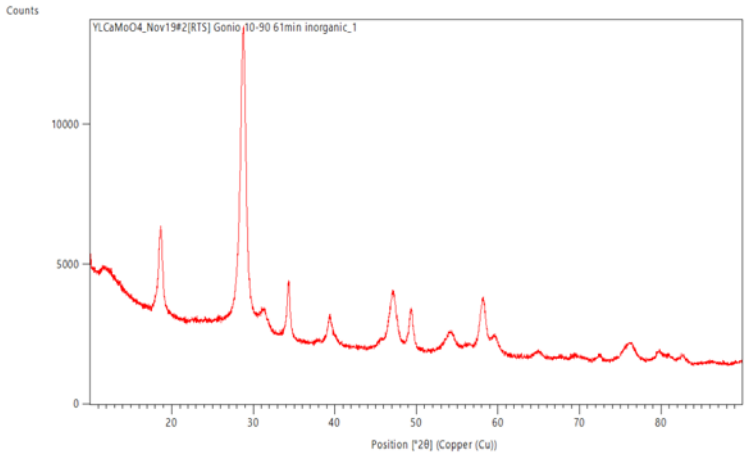
Counts
YLCaMoO4_Nov19#2[RTS] Gonio 10-90 61min inorganic_1
10000
5000
0
20
30
40
50
60
70
80
Position [°2θ] (Copper (Cu))

b)

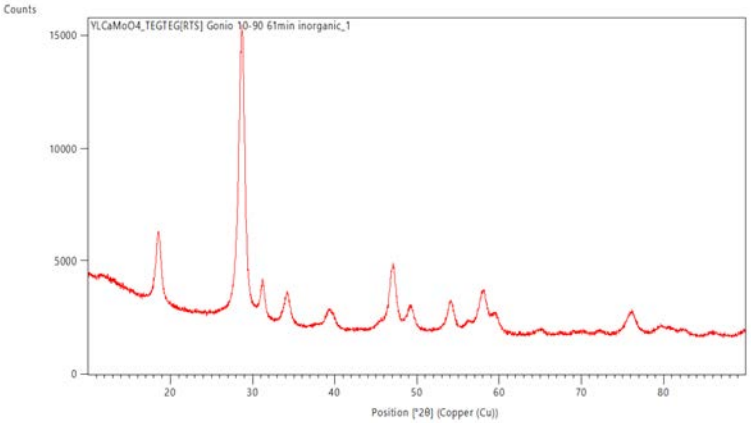
Counts
YLCaMoO4_TEGTEG[RTS] Gonio 10-90 61min inorganic_1
15000
10000
5000
0
20
30
40
50
60
70
80
Position [°2θ] (Copper (Cu))

c)

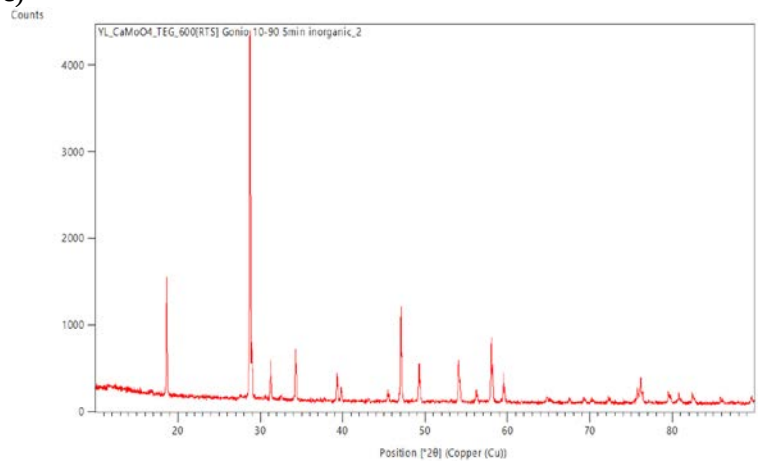
Counts
YL_CaMoO4_TEG_600[RTS] Gonio 10-90 5min inorganic_2
4000
3000
2000
1000
0
20
30
40
50
60
70
80
Position [°2θ] (Copper (Cu))

d)

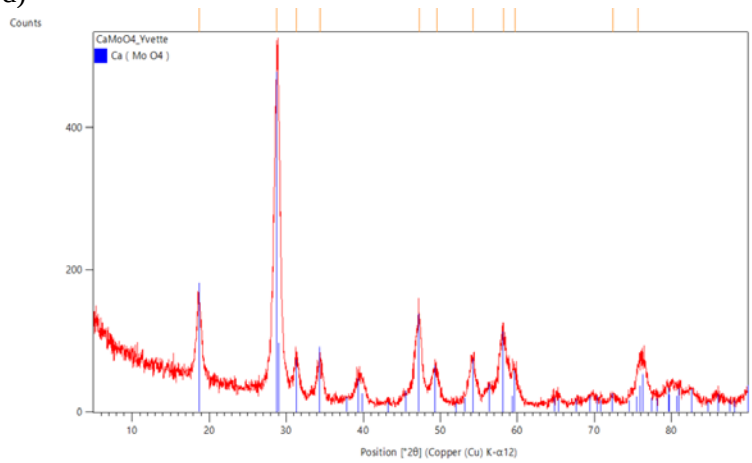

Figure 4.21 XRD patterns a) of pre-calcinated $CaMoO_4$ synthesized using Protocol 1 b) pre-calcinated $CaMoO_4$ synthesized using Protocol 2, c) post-calcinated $CaMoO_4$ synthesized using Protocol 2, and d) pre-calcinated $CaMoO_4$ synthesized using Protocol 3.

$MgMoO_4$ was never synthesized successfully with the CPS method. Protocol 1 failed to produce any solid product. Protocol 2 was also used to attempt synthesizing $MgMoO_4$. Once the Protocol 2 mixture was heated, some precipitation formed. After washing and drying, XRD was used to identify the product; $MgMoO_4$ was not the compound formed, but likely a version of $Na_xMg_yMoO_4$, where x and y are non-stoichiometric.

Solubility could be the reason why $MgMoO_4$ is extremely difficult to synthesis using CPS. As discussed in the introduction, the solubility of $MgMoO_4$ is 15.9 g/ 100 mL of water at 25°C, which is significantly greater than the solubility of other metal molybdate compounds. 15.9 g/ 100 mL of water is the equivalent of 0.86 M, which is a higher concentration than used in all three protocols, albeit that this value is in aqueous solution. The low concentration of the reactants used for the CPS would never reach a concentration level that allows $MgMoO_4$ to precipitate.

Table 4.8 The average yield of $CaMoO_4$, $SrMoO_4$, and $BaMoO_4$

Compound	Protocol 1		Protocol 2		Protocol 3	
	Yield (%)	σ (%)	Yield (%)	σ (%)	Yield (%)	σ (%)
$CaMoO_4$	71.33	--	133.0	63	31.95	22
$SrMoO_4$	68.03	19	76.95	--	33.52	14
$BaMoO_4$	66.66	--	57.67	--	36.87	12

Not all standard deviations of the yields for Protocol 1 and Protocol 2 were calculated due to the low number of syntheses performed. Since Protocol 1 and 2 produced could produce a thousand times more products per synthesis than Protocol 3, one or two syntheses produced enough product for the necessary analyses. Protocol 1 and 2 produce more than 50% of theoretical yield of products; most of them range from 57% to 71%. $CaMoO_4$ synthesized using Protocol 2 often produced more than 100% of theoretical yield, which suggests impurity from the solvent. Impurity caused by TEG will be discussed in more detail later.

Table 4.9 The average particle size of $CaMoO_4$, $SrMoO_4$, and $BaMoO_4$

Compound	Protocol 1		Protocol 2		Protocol 3	
	Size (nm)	σ (nm)	Size (nm)	σ (nm)	Size (nm)	σ (nm)
$CaMoO_4$	1097	900	642.1	280	122.6	60
$SrMoO_4$	1208	1100	605.6	460	92.58	26
$BaMoO_4$	2536	2200	491.8	300	149.5	56

In general, the products formed using TEG as the only solvent are superior based on their more uniform shape and size. For example, Protocol 1 $CaMoO_4$ contained some cotton-like structure along with disc structure. Protocol 2 $CaMoO_4$ did not contain the same type of morphology. Figures 4.2 a) and b) illustrate the cotton-like and disc structures of Protocol 1 $CaMoO_4$ and Figure 4.2c) shows the more uniformly shaped and sized particles of $CaMoO_4$ synthesized with Protocol 2. Figure 4.3 shows the SEM images of $BaMoO_4$ synthesized using Protocols 1 and 2, where the particles of Protocol 1 $BaMoO_4$ were larger than the particles of Protocol 2 $BaMoO_4$. The

decrease in the size of the nanoparticles in Protocol 2 could be attributed to the higher concentration of TEG. TEG acted as a capping agent that controlled the growth of the metal molybdates, and as the concentration of the capping agent increased, the particle size decreased (Pramanik, Tarafdar, and Pramanik, 2007; Sun et al, 2010). At the same time, since Protocol 2 required heating to precipitate, the nucleation process was controlled with limited duration, and the size distribution of the particles was also narrower than that of Protocol 1.

a)

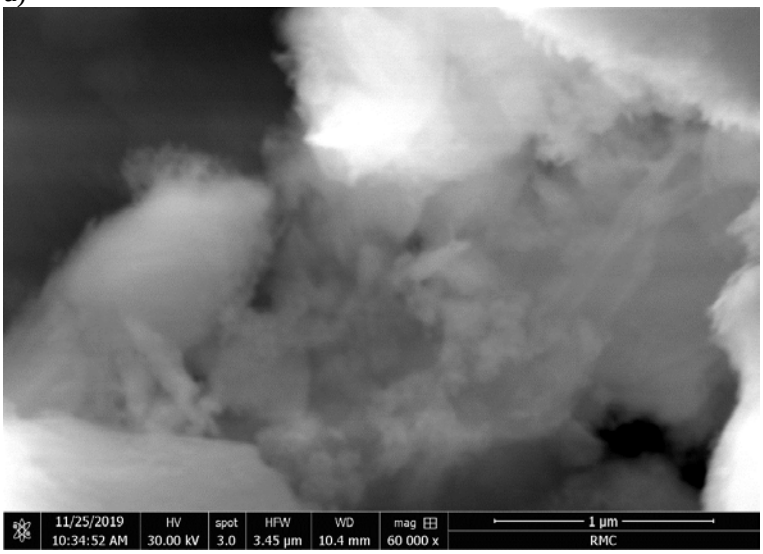

b)

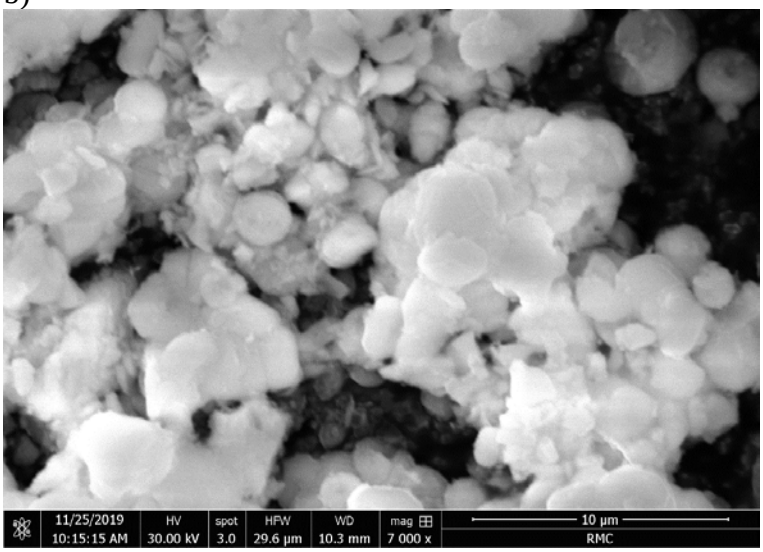

c)

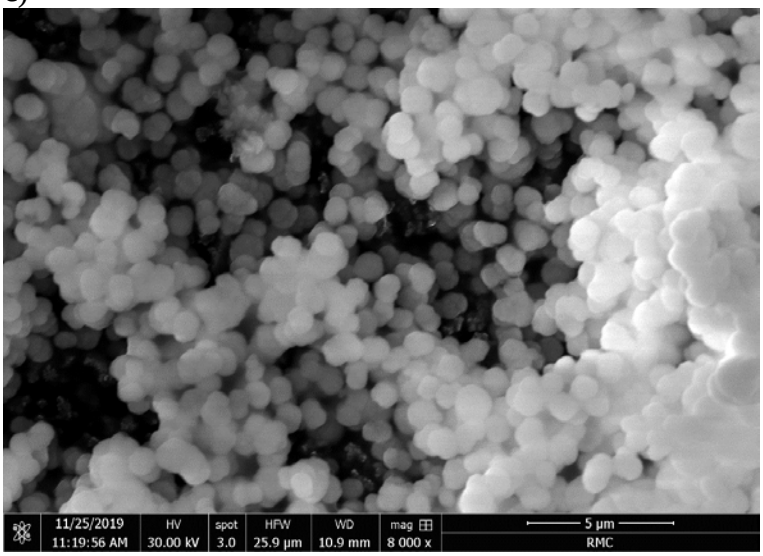

Figure 4.22 SEM images of a) the fluffy and b) disc-like $CaMoO_4$ synthesized using Protocol 1 and c) $CaMoO_4$ synthesized using Protocol 2 exhibited more uniformed size and shape.

a)

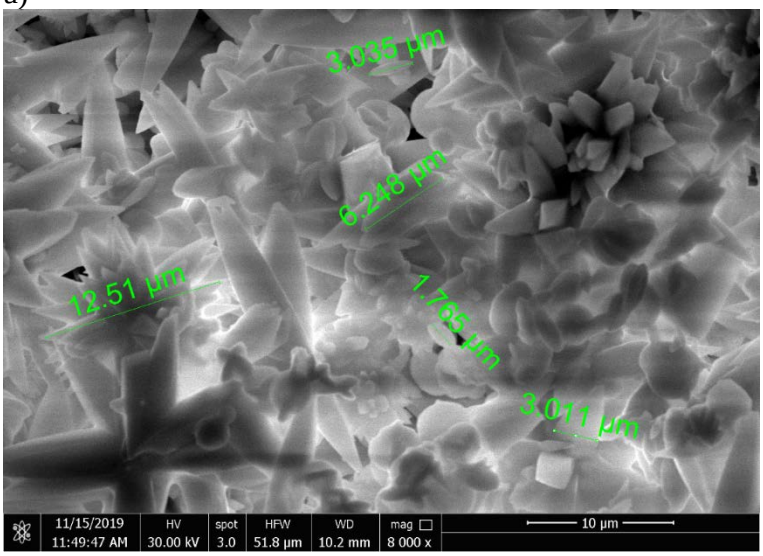

b)

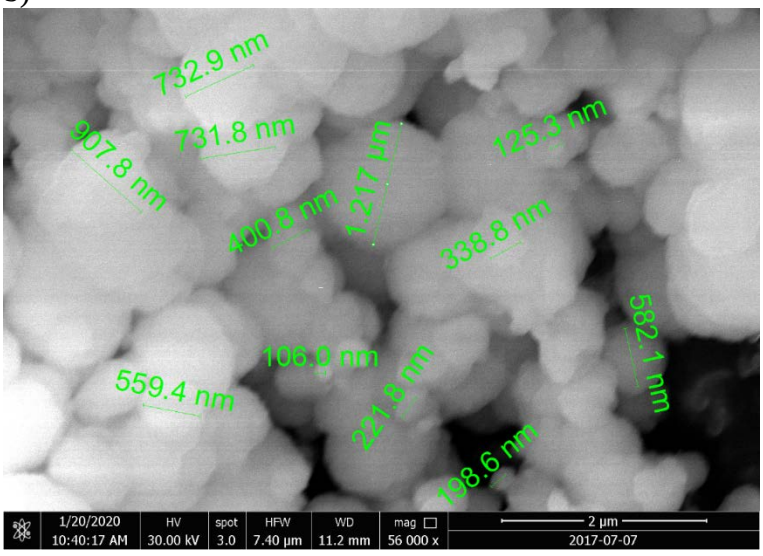

Figure 4.23 $BaMoO_4$ synthesized with a) Protocol 1 and b) Protocol 2. $BaMoO_4$ synthesized with Protocol 1 produced micron sized irregular particles and Protocol 2 produced smaller disc shaped $BaMoO_4$ particles.

TGA were used to analyze the purity of the products formed. As shown in the XRD patterns in Figure 4.1, $CaMoO_4$ synthesized using Protocol 1, 2, and 3, before or after calcination, patterns show very similar characteristics. The peaks have different width and intensity due to the different particle size, but it is not immediately obvious

that an impurity is present; XRD was not able to identify TEG within the samples clearly. However, it is obvious from TGA and by the different colours the sample presented, an impurity was present. Figure 4.4 shows the TGA curves of pre- and post-calcinated $CaMoO_4$ synthesized using Protocol 1 and 2. TGA were performed both before and after the calcination steps for all the products. All the products lost significant mass prior to calcination.

a)

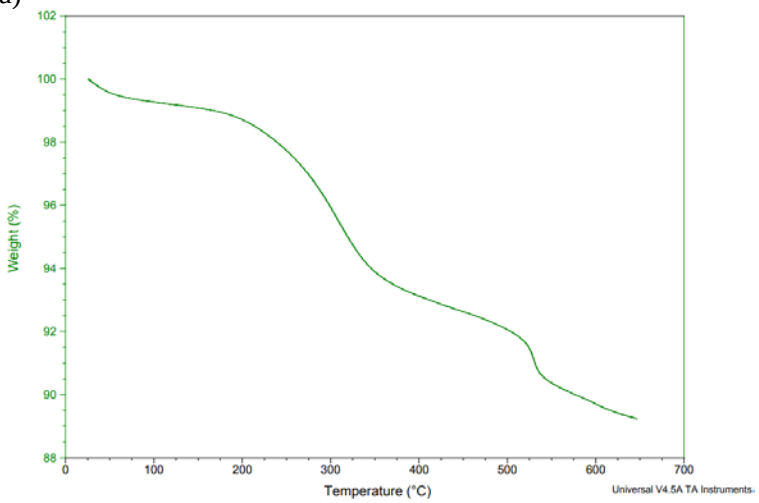

b)

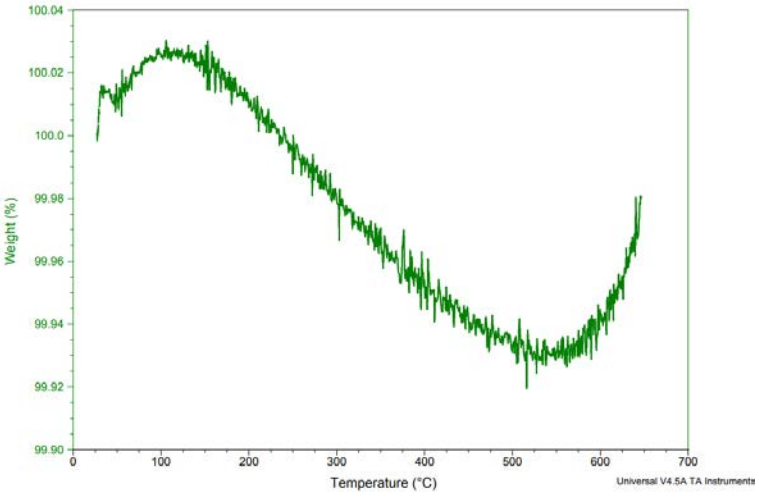

c)

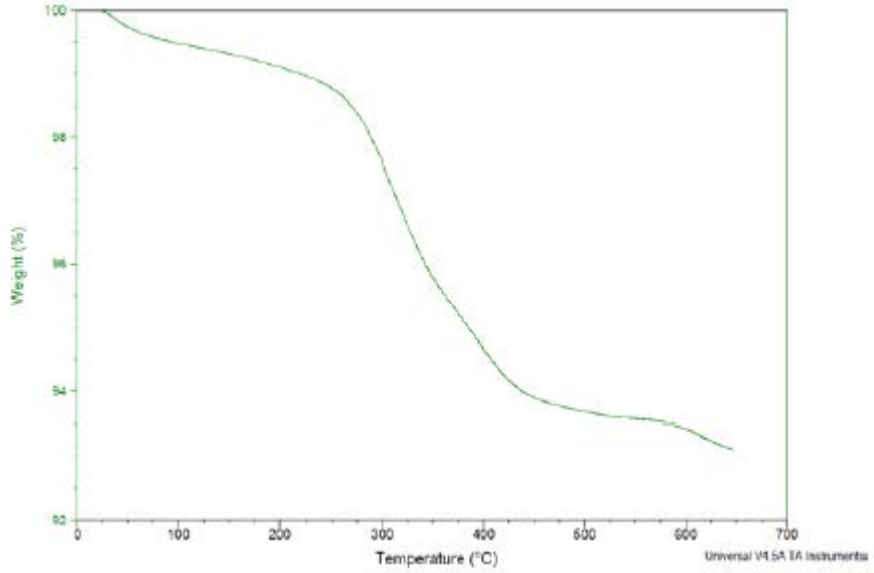

d)

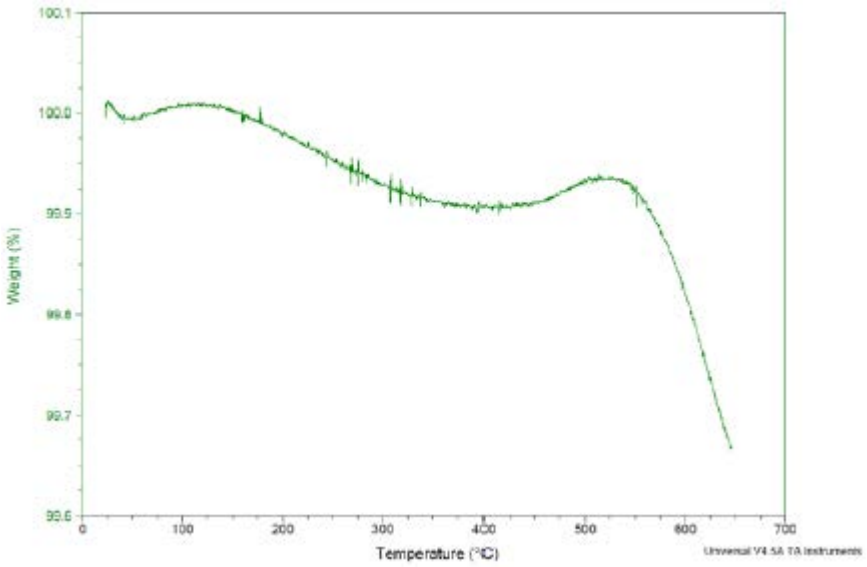

Figure 4.24 TGA curves of pre- and post- calcined $CaMoO_4$ synthesized using Protocols 1 and 2. a) Pre-calcined and b) Post-calcined $CaMoO_4$ synthesized using Protocol 1. c) Pre-calcined and d) Post-calcined $CaMoO_4$ synthesized using Protocol 2.

Products synthesized using Protocol 1 would likely contain water because water was part of the solvent. Any mass loss prior and around 100°C would be caused by the evaporation of remaining water and any solvent used during the washing process. The mass loss around 300°C could be caused by TEG remaining in the product; the boiling point of TEG is 298°C. Figure 4.4 a) shows a three-step mass loss process within the temperature range. The first step, 30°C to 110°C, lost approximately 1% of total mass, the second step, between 110°C to 400°C, lost approximately 6% of mass, and the third step, 400°C and beyond, lost. Approximately 3% of mass. The first step of mass loss was most likely due to the loss of remaining water and solvents used in the washing process. Part of the second and third step mass lost might be caused by the evaporation of TEG, as TEG has a boiling point of 285°C. It is also possible that $CaMoO_4$ could have formed $CaMoO_4$ hydrate and the second and third step mass loss were associated with the dehydration process. Gmelin handbook had reported alkaline earth metal molybdate compounds with hydrate forms; however, molydbate hydrates has not been reported in more recent research (Tytko et al, 1985). Figure 4.4 b) shows the TGA curve of post-calcinated $CaMoO_4$ synthesized using Protocol 1. Although the curve seems to exhibit extreme change, the total mass loss was 0.08%. This indicated that after the calcination process, the mass of the sample would not change significantly. Figure 4.4 c) contains the TGA curve of $CaMoO_4$ synthesized using Protocol 2 without calcination. This curve also shows the sample experienced the first mass loss prior to approximately 110°C. Like Protocol 1 pre-calcinated $CaMoO_4$, this mass loss is likely caused by the loss of solvent used during the washing process. The second mass loss was the biggest mass loss, approximately 6%, between 110°C to 475°C. Since the only solvent used was TEG and the reagents were in anhydrous form, this $CaMoO_4$ was less likely to form $CaMoO_4$ hydrate; the mass loss was most likely due to the leftover TEG. Figure 4.4 d) shows the TGA curve of Protocol 2 post-calcinated $CaMoO_4$. The mass loss at 600°C was approximately 0.2%. The mass loss compared to the pre-calcinated $CaMoO_4$ mass loss was insignificant. However, the curve shows that the mass could have continued beyond 600°C if the experiment continued. Both Figure 4.4 c) and d) show that the curves trend down at around 660°C. The downward trending curves suggest that TEG was not evaporated completely. The colour of the samples agreed with this conclusion. The colours of the normally white compounds were light brown after four hours of calcination in the 600°C furnace. The light brown colour suggested some burnt solvent remained in the sample.

Additionally, the process of purifying the sample by calcination changes the morphology of the molybdate compounds. After calcination, the particle size approached micron size and the particles were heavily agglomerated, as shown in Figure 4.5, which eliminated the advantage of using Protocol 2 completely. The increase in particle size after calcination is not surprising. The enlarged particles were caused by the grain boundary diffusion of the smaller particles which leads to

heavier particle agglomeration and coalescence (Choodamani et al., 2014; Kusuma and Chandrappa, 2019)

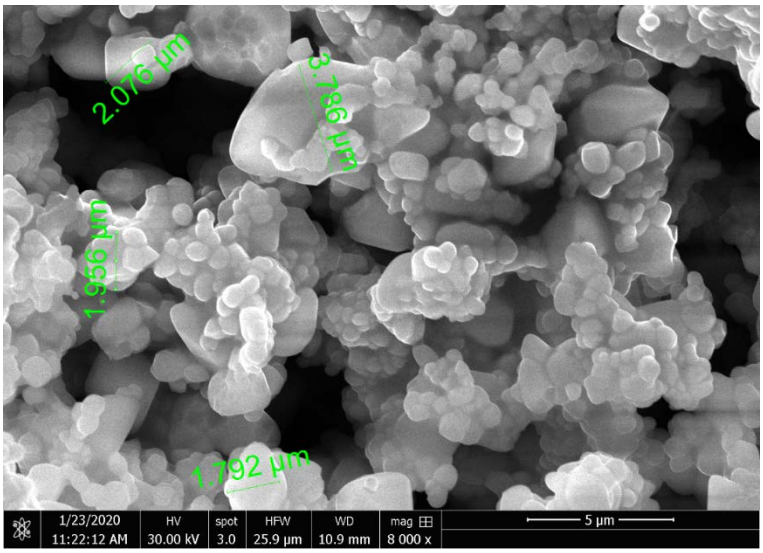

Figure 4.25 SEM image shows that $SrMoO_4$ particles are micron-sized after calcination.

Neither Protocol 1 nor 2 produced satisfactory results. Protocol 1 produced large irregular shaped particles. While Protocol 2 produced smaller particles, the molybdates contained impurities from the solvent TEG and particle size was enlarged during the process of purifying the products. An alternate protocol is required to produce nano molybdate compounds.

4.1.1.2 Protocol 3 - Synthesizing metal molybdates with ethylene glycol (EG)

Since Protocols 1 and 2 failed to produce ideal nano-sized particles Protocol 3 was developed as an alternative. The goal of Protocol 3 was to decrease the particle size of the synthesized molybdates, therefore the concentration of the reactants was decreased, as well as the batch size, following the work of Thongtem et al. (Thongtem et al. 2010). Protocol 3 utilized a different solvent and reagents than Protocols 1 and 2. $M(NO_3)_2$ (M = Mg, Ca, Sr, Ba) were used instead of MCl_2. Both $M(NO3_3)_2$ and Na_2MoO_4 were dissolved in ethylene glycol (EG). $M(NO_3)_2$ was added dropwise, at the half of the addition rate of Protocols 1 and 2, into Na_2MoO_4 solution and allowed to stirred overnight. The slow addition rate also helped prevent bigger particles from forming. By making sure each drop had time to disperse before the next drop of the reactant was being added to the mixture, high local concentration was avoided. In the original procedure described by Thongtem et al., the product precipitated after the mixture was left stirring for 24 hours at 30°C. In this case,

precipitation did not initiate after 24 hours. Precipitation could form either by leaving it stirring for a few days or being heated to around 120°C, in a similar way to Protocol 2. However, unlike Protocol 2, product would not precipitate without being stirred for 24 hours first. Although the precipitation could form without being heated if left stirring, the time required varied from batch to batch, ranging from 3-5 days. The particle size varied more widely when it was left to form on its own. Therefore, the standard procedure was to heat the reactant mixture instead of letting it precipitate naturally. This phenomenon was not surprising. By increasing the temperature of the solution, the process of reaching the supersaturation of the metal molybdates was accelerated. For nanoparticles to form, the particles must reach a critical concentration that they become supersaturated, and the supersaturation is relieved when nuclei of nanoparticles start forming and growing. The size distribution of the particles formed during the process can be limited by shortening the time that allows the nuclei to grow and preventing more nuclei from forming. And due to the short nucleation time, the size distribution was narrow. When the precipitation occurred naturally without being heated, the nucleation process was unavoidably prolonged, thus the larger size distribution. (Solanki and Murthy, 2011).

$CaMoO_4$, $SrMoO_4$, and $BaMoO_4$ were produced using Protocol 3, while $MgMoO_4$ did not precipitate. Figure 4.1d) presents the XRD pattern of $CaMoO_4$ synthesized using Protocol 3. The rest of the XRD patterns are attached in the Appendix. Protocol 3 had achieved its goal of producing nano sized particles. Figure 4.6 shows the images of rod like nano particles of $CaMoO_4$, $SrMoO_4$, and $BaMoO_4$. As summarized in Table 4.2, the average particle size of $CaMoO_4$ is 122.6 nm, $SrMoO_4$ is 92.58 nm, and $BaMoO_4$ is 149.5 nm.

a)

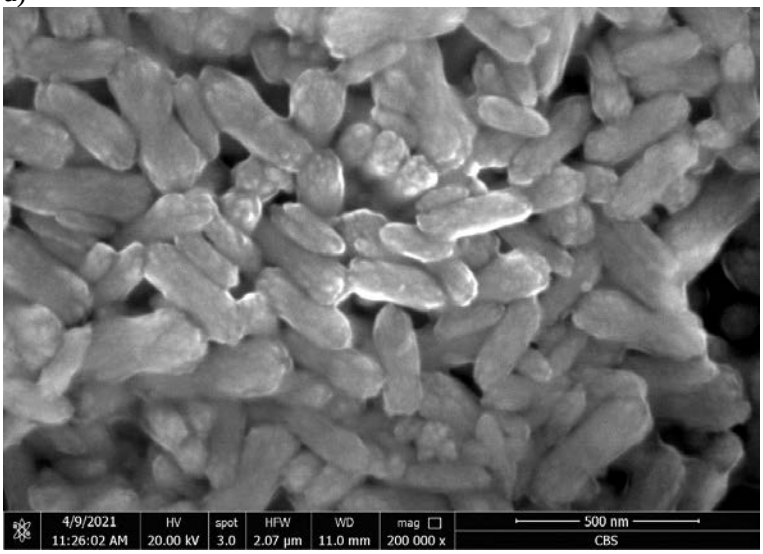

b)

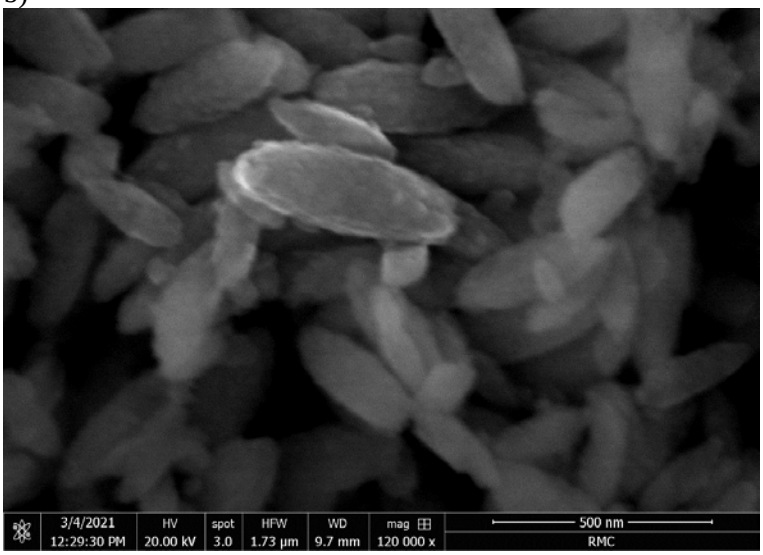

c)

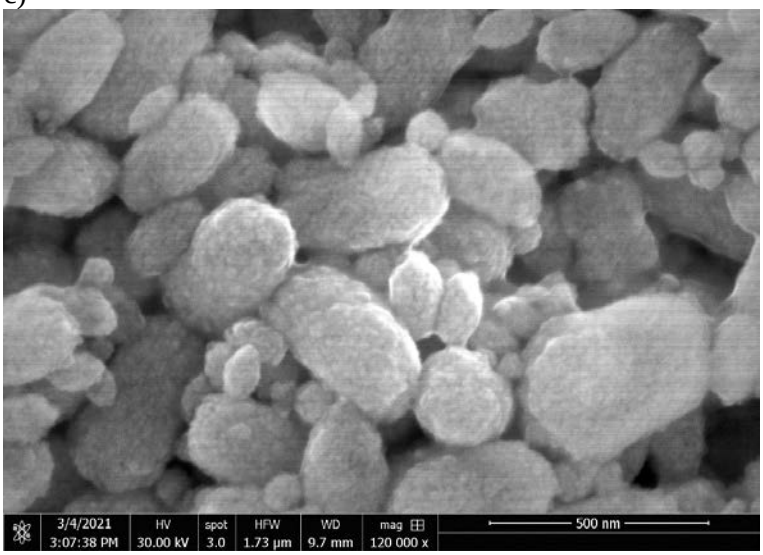

Figure 4.26 Nano-sized a) $SrMoO_4$, b) $BaMoO_4$, and c) $CaMoO_4$ synthesized by Protocol 3

As discussed above, the slow addition rate, the low reagent concentration, and the short nucleation time encouraged the formation of nanosized particles. Solvent also played a vital role in keeping the particle size small. Like TEG, EG acted as a capping agent to prevent the particles from growing into micron size particles. As in Protocol 1 and 2, XRD did not show obvious impurity, but TGA curves indicate

impurity within the sample. Figure 4.7 is the TGA curve of un-calcinated $CaMoO_4$ synthesized using Protocol 3. The mass loss steps of the curve are less distinct than those of in Figure 4.4. Nevertheless, there was a rapid initial mass loss prior to 100°C. This again could be caused by the evaporation of the solvent used during the washing process. The mass continued at a slightly slower rate again sped up again from 225°C to 400°C. The mass loss slowed down again and started to plateau at approximately 650°C. It was possible that $CaMoO_4$ could have formed $CaMoO_4$ hydrate, since the reactant $Ca(NO_3)_2 \cdot 4H_2O$ contained water. Since the boiling point of EG is 197°C, loss of EG could also contribute to the rapid mass loss at approximately 225°C. The plateau after 650°C could suggest that EG has evaporated completely. EG has shorter chain and less oxygen than TEG, therefore the intermolecular force between EG would be weaker than TEG. As a result, the boiling point of EG is lower than the boiling point of TEG and would be separated from the molybdates more easily. Since the limited quantity of the Protocol 3 molybdates, the products were not calcinated. Therefore, there was not any pre- and post-calcination comparison for these products. However, qualitatively speaking, the product did not feel sticky after the washing process and all the products were white.

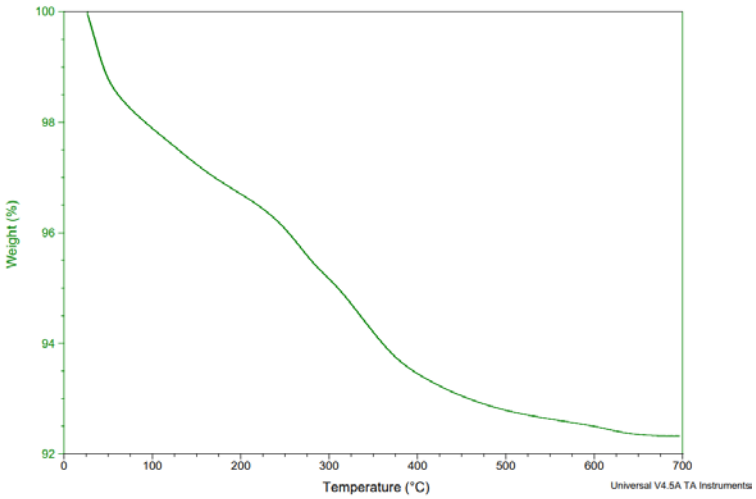

Figure 4.27 TGA curve of $CaMoO_4$ synthesized using Protocol 3.

One significant drawback of Protocol 3 was the amount of product Protocol 3 produced. Protocol 3 produced lower yield than Protocol 1 or 2, in the 30% range of theoretical yield, as presented in Table 4.1. Products were lost during the washing process. The molybdates suspended better in EG than other solvents; it took longer to centrifuge the suspension into pellets and some suspension remained at the end of the centrifugal process. Considering that even with 100% theoretical yield, the mass of the product would be approximately 50 – 75 mg, small amounts of products

remained in the solvent contributed considerably to the amount of product lost, percentage wise.

Protocol 3 successfully synthesizes nano particles that can be easily purified. In this respect, Protocol 3 was a superior alternative to Protocols 1 and 2. The synthesis procedure of Protocol 3, however, was long and laborious; the yields of the products were also less than ideal. It was clear that another alternative method should be explored to produce usable amounts of the molybdate compounds more efficiently. As a result, solution combustion synthesis was explored.

4.1.2 Solution Combustion Synthesis (SCS)

Even though nano $CaMoO_4$, $SrMoO_4$, and $BaMoO_4$ were successfully synthesized using CPS Protocol 3, $MgMoO_4$ was never synthesized successfully using the CPS. In addition, all the yields of CPS Protocol 3 were minimal due to the low concentration of the reagents. Typically, around 10 mg was produced in each batch. To synthesize $MgMoO_4$ and increase production yields of the molybdate compounds, SCS was explored, where solutions contained metal nitrates, glycine, and $NH_4Mo_7O_{24}$ were heated quickly by either a microwave or a furnace to initiate a combustion reaction. Given the relative ease and speed of the method, some other molybdate compounds were also synthesized. In this project, both microwave and furnace were used as heat sources. The temperature of the muffle furnace was set to 550^{o}C to initiate the combustion reaction. Both 800W and 1600W were used when the microwave was used as a heat source. Some products were put through the calcination steps for two purposes: to purify the products and to observe if the morphologies of the products would be altered.

$MgMoO_4$, $CaMoO_4$, $SrMoO_4$, $NiMoO_4$, $ZnMoO_4$, Fe_2MoO_4, and $CuMoO_4$ were synthesized using SCS. The identities of the products were confirmed using XRD, the patterns that are not shown as a figure are attached in the Appendix. Most XRD patterns of the products showed that although the desired molybdate compounds were present in the product, varied amounts of impurities were also produced. Table 4.3 summarized the results of synthesis attempts, including any impurities and particle size of SCS. The results of CPS are also included in the table.

Table 4.10 Summary of molybdate compound synthesis results using various methods.

Target Compound	**Synthesis Method**			
	CPS	SCS - Furnace	SCS - Microwave	
$MgMoO_4$	No	Yes	---	
Particle Size (nm)		72.31 ± 23		
$CaMoO_4$	Yes	Yes	---	
Particle Size (nm)		64.57 ± 16		
$SrMoO_4$	Yes	Yes	---	
Particle Size (nm)		77.32 ± 43		
$BaMoO_4$	Yes	No	No	
$NiMoO_4$	---	No	Impure	
			800 W $NiMoO_4$ C_3N_4 MoO_2 Mo_2N	800 W $NiMoO_4 \cdot 0.7H_2O$
Particle Size (nm)			55.92 ± 20	4126 ± 1600

$ZnMoO_4$	---	Impure $Zn_3Mo_2O_9$ $ZnMoO_4$	Impure 800 W $ZnMoO_4$	No 1600 W
Particle Size (nm)		112.0 ± 54	57.46 ± 29	
$Fe_2(MoO_4)_3$	---	Impure $Fe_2(MoO_4)_3$ MoO_3	No	
Particle Size (nm)		181.9 ± 110		
$CuMoO_4$	---	No $Cu_6Mo_4O_{15}$ MoO_2	Impure† $CuMoO_4$ $(NH_4)_2Mo_4O_{13}$	

* --- indicates that the synthesis was not attempted with that method.
† SEM images of the product were not taken; particle size was not available.

$MgMoO_4$ was synthesized successfully using SCS. Figure 4.8 a) is the XRD curve of $MgMoO_4$. It shows the characteristic peaks of $MgMoO_4$ without obvious peaks from other compounds. It is likely that it contained amorphous impurities that XRD was not able catch. Figure 4.8 b) contains the TGA curve of $MgMoO_4$, it shows a 17.5% of mass loss, and the mass loss only started to plateau around 700°C, which also indicated some impurities in the sample. In addition, $MgMoO_4$ is usually white and Figure 4.9 a) clearly shows light brown product. When the product came out of the muffle furnace, it contained fluffy and porous substance with a layer of denser material at the bottom of the ceramic dish. Although the two components looked physically different, upon examining using SEM, they showed very similar structures that they both showed porous structures that are made with heavily agglomerated nano particles, as shown in Figure 4.9.

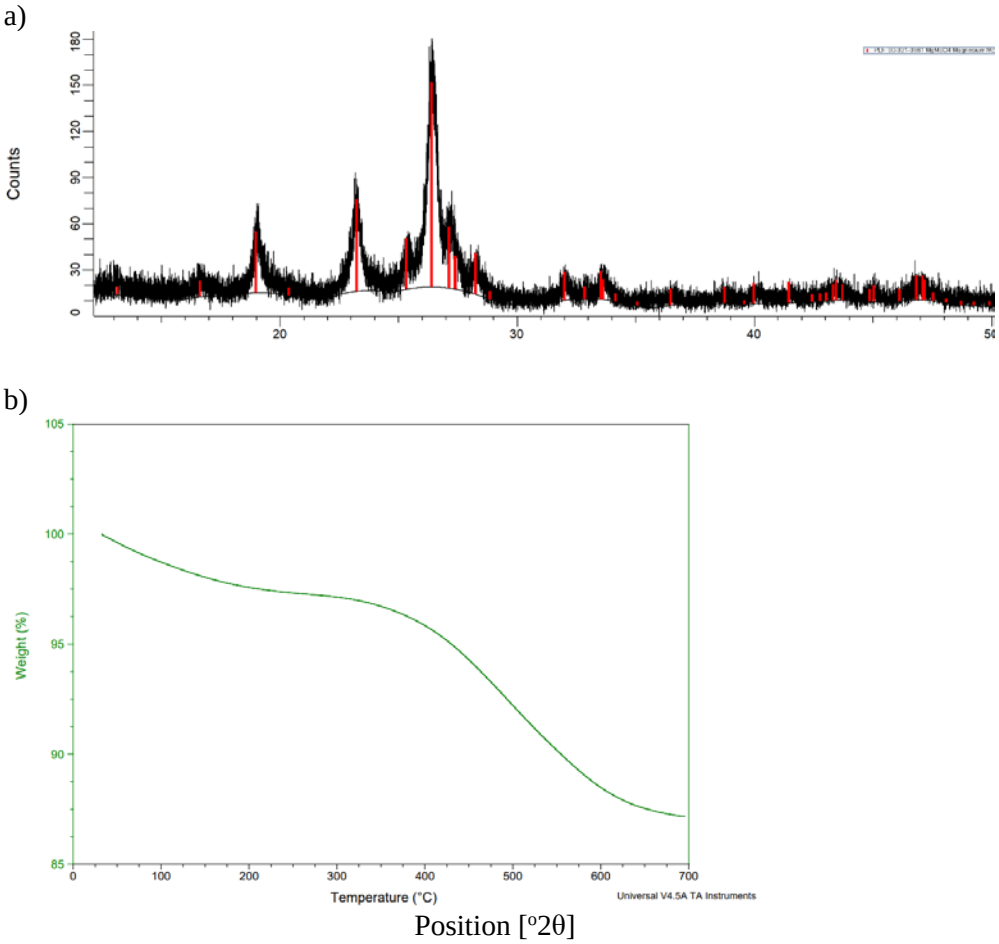

Figure 4.28 a) XRD pattern of $MgMoO_4$ and b) TGA curve of $MgMoO_4$

a)

b)

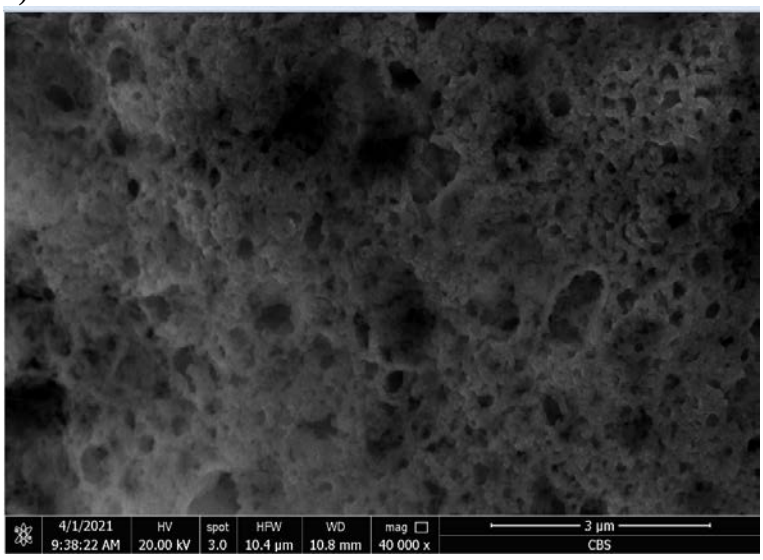
4/1/2021
9:38:22 AM
HV
20.00 kV
spot
3.0
HFW
10.4 µm
WD
10.8 mm
mag
40 000 x
3 µm
CBS

c)

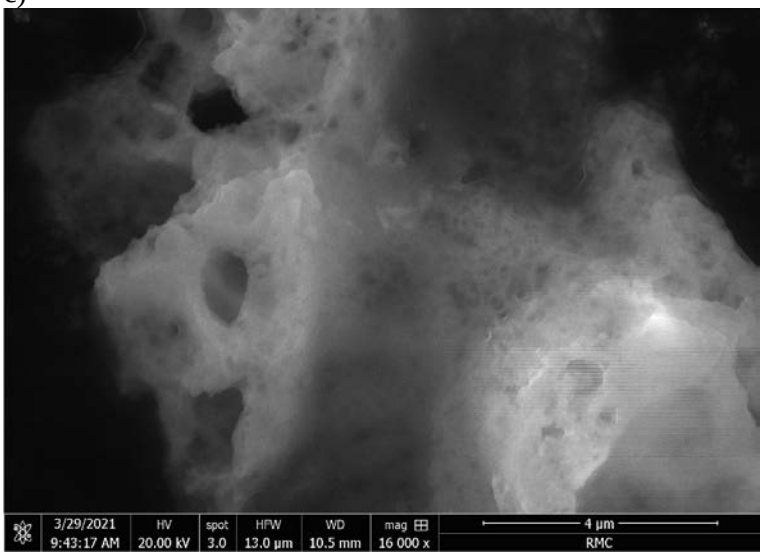

d)

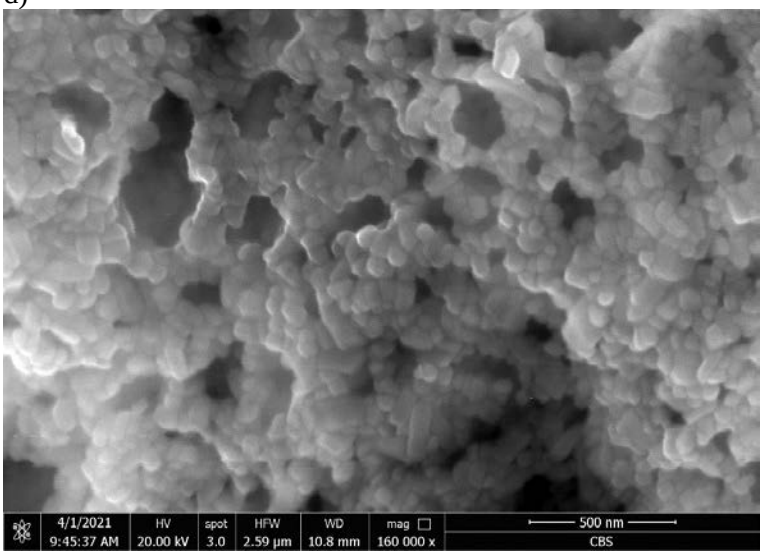

Figure 4.29 a) Ceramic dish containing $MgMoO_4$ synthesized using SCS and the SEM images of $MgMoO_4$ sub samples of the b) fluffy substance, c) denser material at the bottom of the ceramic dish, and d) SEM images with a higher magnification.

The SCS results for $CaMoO_4$ and $SrMoO_4$ were very similar to $MgMoO_4$. Fluffy material was formed, and their identities confirmed by XRD, as shown in Figure 4.10. Just like $MgMoO_4$, their spectra did not show obvious extra peaks caused by any impurities, but both of their TGA curves also show mass loss, like $MgMoO_4$.

Additionally, the products that came out of the oven were not the normally white colour of $CaMoO_4$ and $SrMoO_4$, as shown in Figure 4.11. Since the reactants were dissolved in water when SCS reactions were initiated, metal molybdate hydrates were formed, and part of the mass loss was due to transforming molybdate hydrates into anhydrous molybdates. Further oxidation of the incomplete combusted fuel in TGA might also contribute to some of the mass loss process.

a)

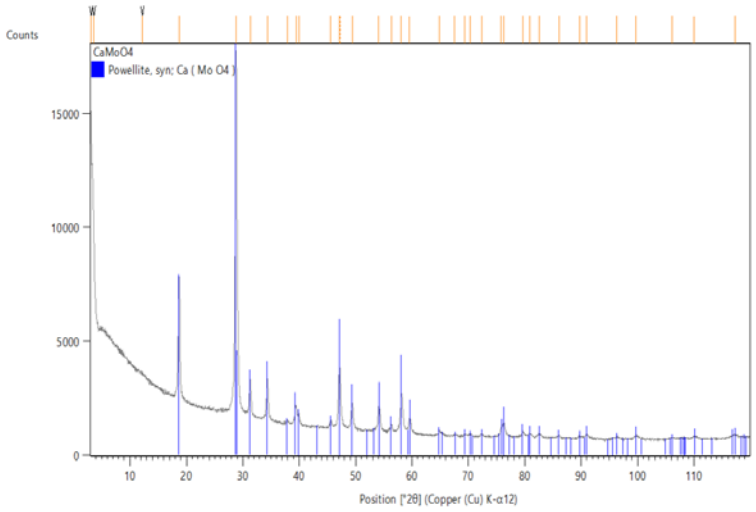

b)

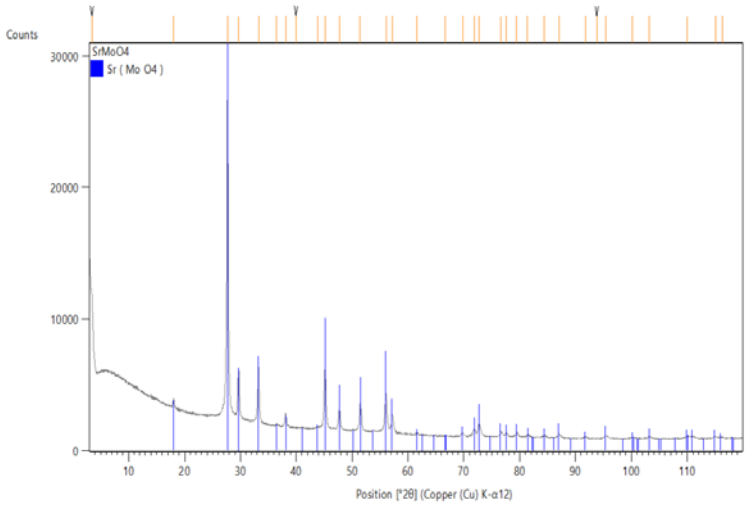

c)

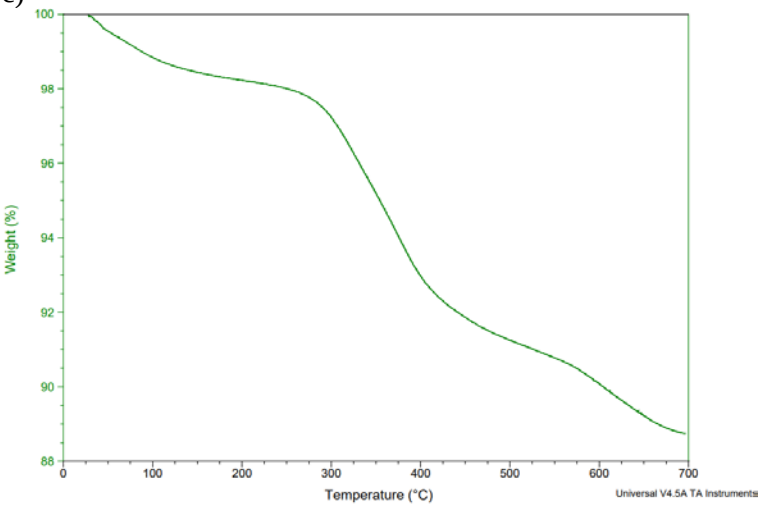

d)

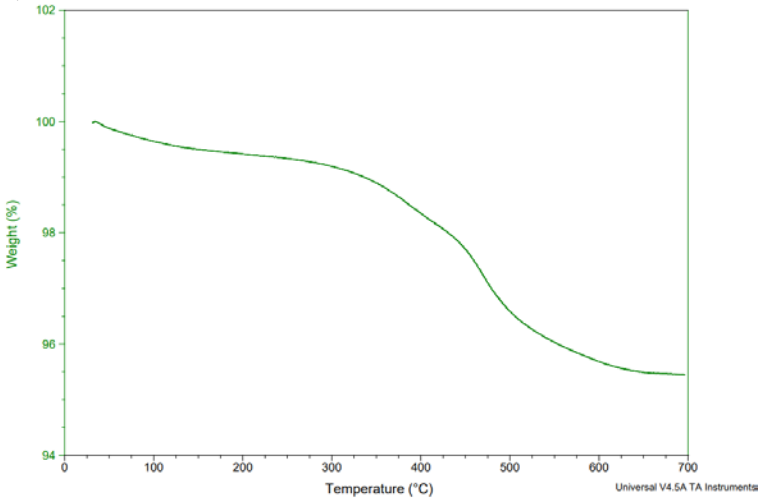

Figure 4.30 XRD patters of a) $CaMoO_4$ and b) $SrMoO_4$. GTA curve of c) $CaMoO_4$ and d) $SrMoO_4$.

a)

b)

Figure 4.31 SCS a) $CaMoO_4$ and b) $SrMoO_4$ products that just came out of the muffle furnace.

Compared to $MgMoO_4$, $CaMoO_4$ particles were less distinct even with high SEM magnification. $MgMoO_4$ contained distinct particles, although heavily agglomerated, but distinct, nonetheless; $CaMoO_4$ did not exhibit regular shaped individual particles, but rather a continuous structure with pores and other nano features, as shown in Figure 4.12 a). It is possible that even higher magnification is required to make out of the size and shapes of each individual particles. Having said that, some images showed some signs of individual particles even with a lower magnification factor, as shown in Figure 4.12 b). Both images were taken from the same sub sample but just different locations on the SEM stand. This would imply that $CaMoO_4$ synthesized using SCS might have more than one type of morphology.

a)

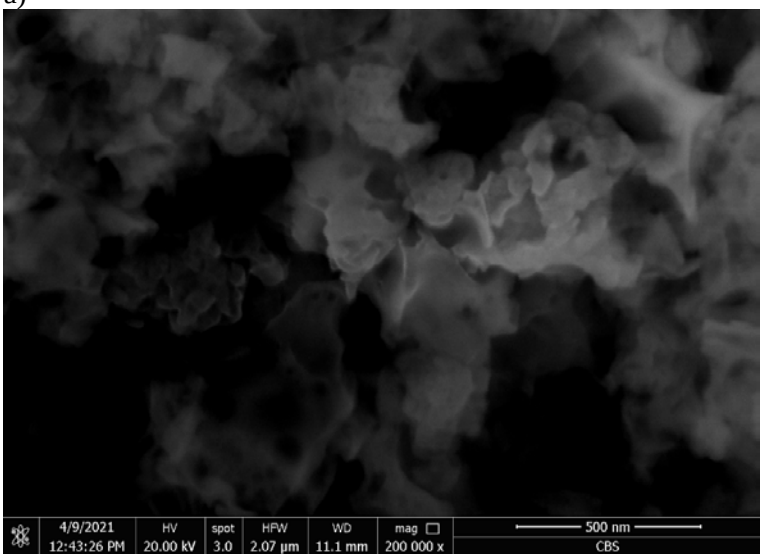

b)

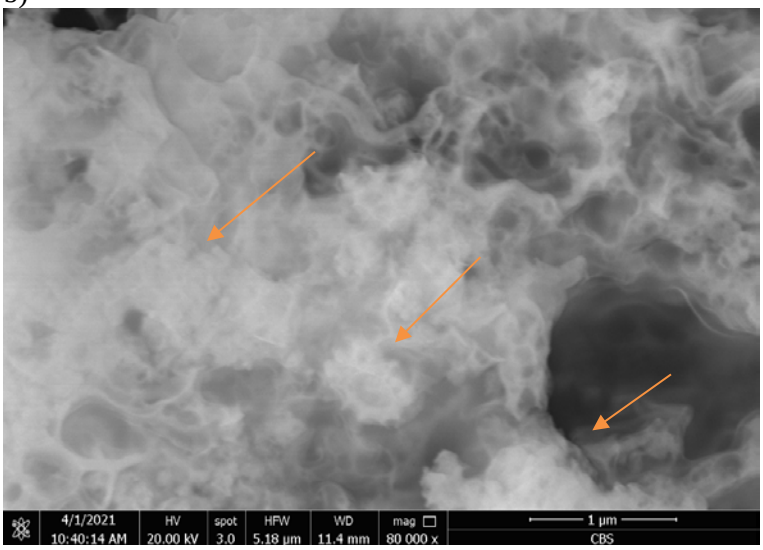

Figure 4.32 SEM images showed $CaMoO_4$ contained a) continuous structures with nano features while b) some locations show signs of individual particles.

Similar to $CaMoO_4$, $SrMoO_4$ also showed areas where individual particles were clearly identifiable and areas where the image showed a whole structure; however, the particles of $SrMoO_4$ were more unambiguous than those of $CaMoO_4$, as shown in Figure 4.13.

a)

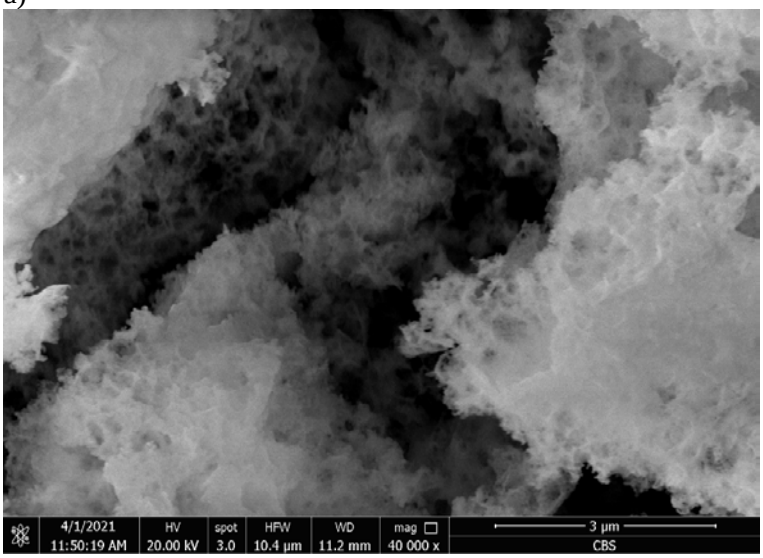

b)

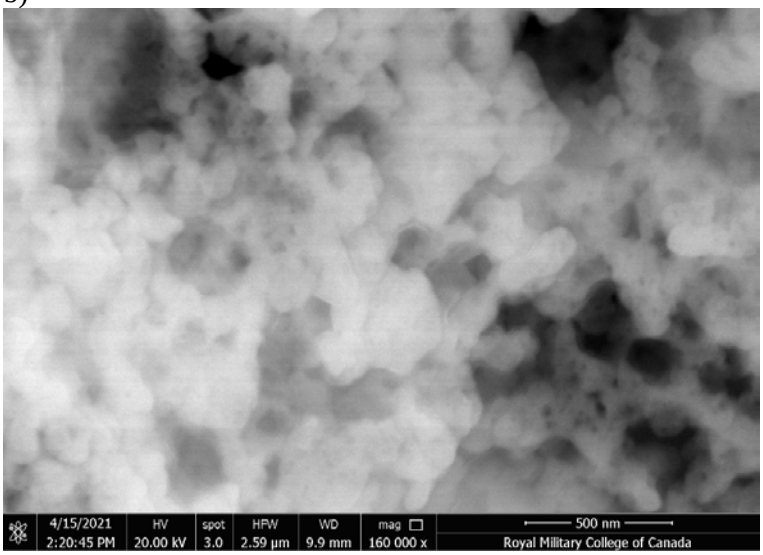

Figure 4.33 SEM images of $SrMoO_4$. They show a) the porous structure that is made with b) nano particles and areas where individual particles are not as obvious.

Nano $BaMoO_4$ was not synthesized successfully using SCS. The mixture always precipitated before the reactant could be sent into the oven to initiate the reaction. $BaMoO_4$ was not produced without the high temperature initiation. XRD was not able to confirm the identity of the product. SEM images showed heavily agglomerated micron size particles. Out of the original four main group elements, reagent mixture containing Ba was the only reaction that precipitated before the reaction was initiated with heat.

$NiMoO_4$ was not synthesized successfully using solution combustion synthesis in the muffle furnace. Seevakan et al. reported using urea as the secondary fuel and microwave to initiate the combustion reaction (Seevakan et al. 2018). Their result was not reproduced here; instead $NH_4Ni_2Mo_2O_8OH$ was synthesized. Additionally, if the mixture was not microwaved immediately, precipitate would form. Initially, the precipitation was speculated to be $Ni(OH)_2$, due to urea's ability to go through hydrolysis reactions; however, the identity of the precipitation could not be confirmed by XRD. Following the unsuccessful attempt, glycine was then used as the secondary fuel again with the reaction carried out in the microwave. This procedure successfully synthesized $NiMoO_4$, but the reproducibility of the reaction was not consistent. Figure 4.14 a) shows two batches of $NiMoO_4$ synthesized using glycine as the secondary fuel of the reaction. Both batches were microwaved for 10 minutes at 800W. The batch at the left has a black appearance and XRD analysis showed that in addition to $NiMoO_4$, C_3N_4, MoO_2, and Mo_2N were also present in the batch. The batch on the right is a yellowish-green powder and XRD the compound

as $NiMoO_4$ hydrate. Although the later batch is pure $NiMoO_4$ hydrate, the material did not have the porous structure previously described; it contained micron-sized particles. The batch on the left side contained nano $NiMoO_4$ along with other byproducts, showing a porous structure typical of the products of SCS. Figures 4.14 b) and c) show the SEM images of the two different structures of $NiMoO_4$. The presence of these byproducts was likely caused by the fuel-rich combination of the reaction that led to the incomplete combustion of the reactants.

a)

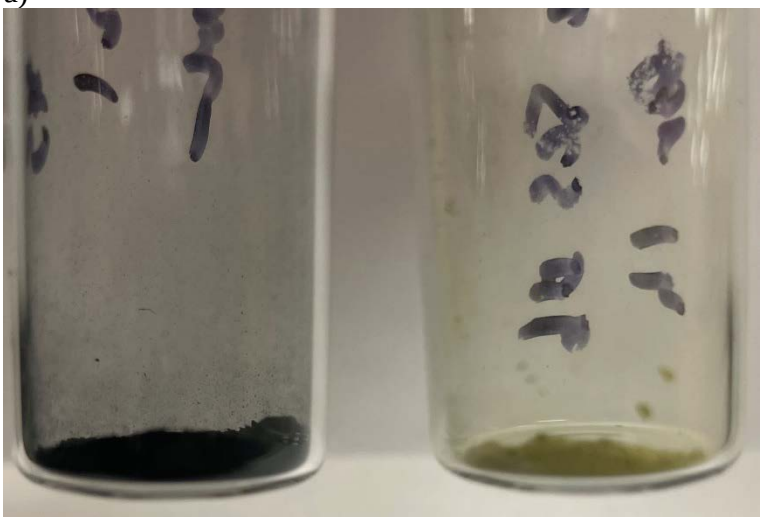

b)

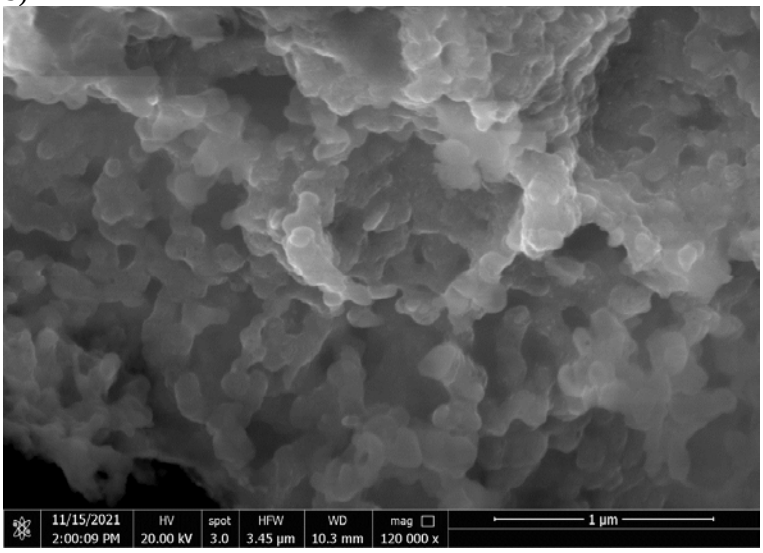

c)

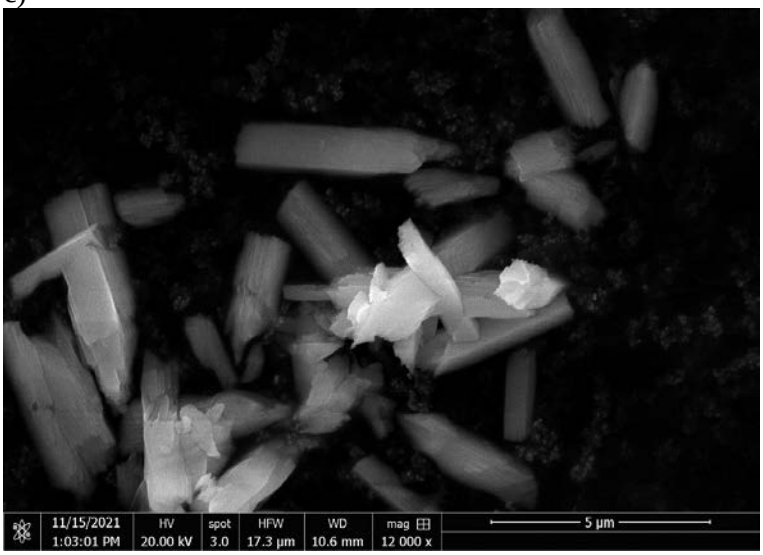

Figure 4.34 a) The two different batches of $NiMoO_4$ and SEM images showing the morphology of b) the batch on the left and c) the batch on the right.

$ZnMoO_4$ had been synthesized successfully with impurities in both the muffle furnace and the microwave at 800W. The spectra of the $ZnMoO_4$ containing products are shown in Figure 4.15. In the muffle furnace, the XRD pattern shows that in addition to the simple zinc molybdate, zinc molybdate complexes $Zn_2Mo_3O_8$ and $Zn_3Mo_3O_8$ were also presented. When the reaction was attempted in the microwave oven, two different power levels, 800W and 1600 W were used. Both power levels produce white precipitation, 800W power level produced $ZnMoO_4$ hydrate ($ZnMoO_4 \cdot 0.8H_2O$). The 1600 W level power produced glycine tetramolybdate. Glycine, in addition to removing the excess oxygen, acts as a chelating agent during combustion synthesis and forms a metal complex with the metal precursor (Deganello and Tyagi 2018; Carlos et al. 2020). It is possible that when the reactant mixture was heated to 1600W, glycine coordinated to the molybdenum in molybdate and precipitated before $ZnMoO_4$ was formed.

a)

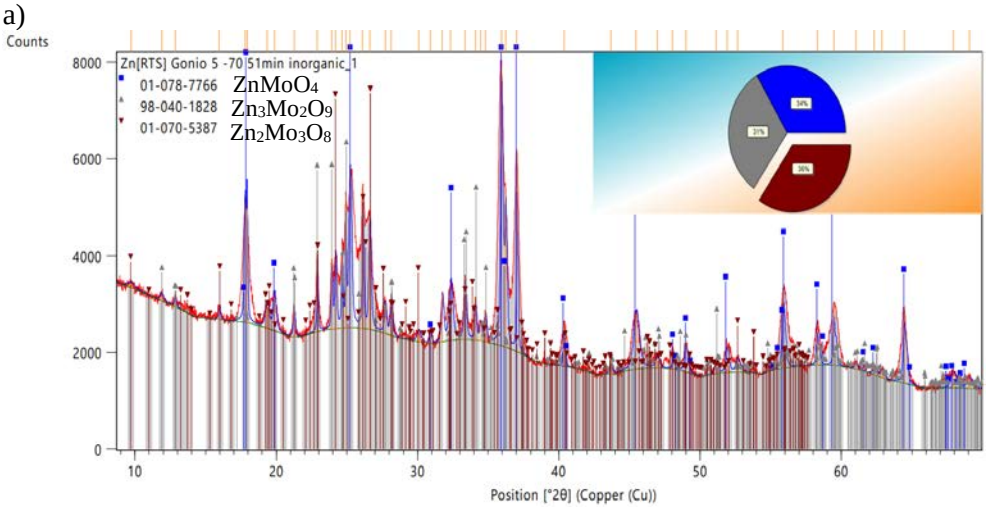

b)

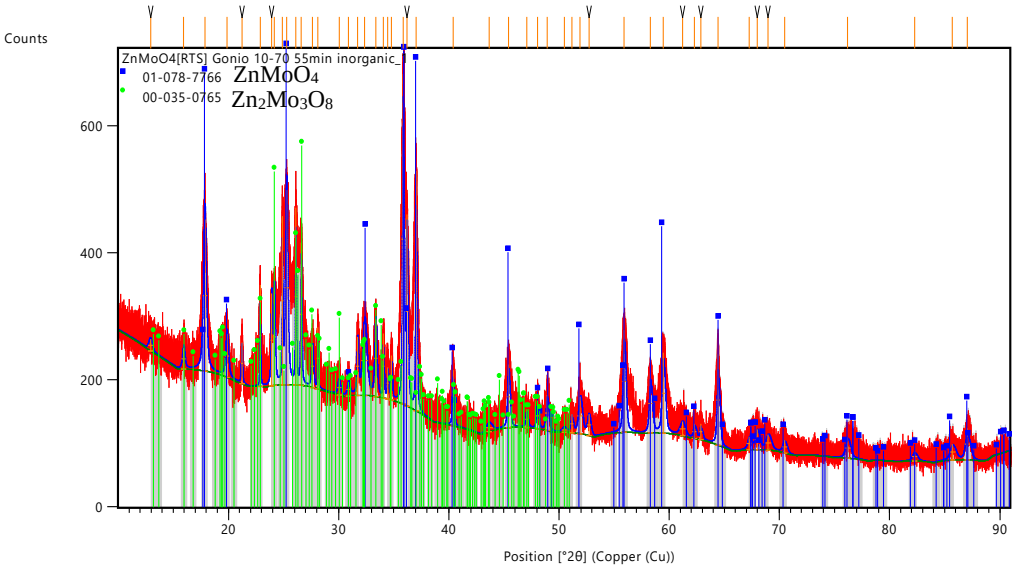

Figure 4.35 XRD patterns of a) products from the muffle furnace synthesized at 550ºC and b) products synthesized in 800 W microwave oven containing containing $ZnMoO_4$ (01-078-5378), and other impurities. The XRD software matches the patterns with $Zn_2Mo_3O_8$, although a reduction of molybdate is unlikely under the reaction condition described here.

$Fe_2(MoO_4)_3$ was only synthesized using the muffle furnace. The microwave synthesis route was attempted but was not successful. $Fe_2(MoO_4)_3$ was attempted using SCS a few times, the reactant mixtures always precipitated immediately, before the reactants could be sent into the oven to initiate the reaction. The unheated precipitations were analyzed using XRD which was not able to identify the compound since the pattern could not match any of the compounds in the database. Once the precipitation was heated, $Fe_2(MoO_4)_3$ was produced with MoO_3 as a byproduct. $Fe_2(MoO_4)_3$ did not exhibit the porous structure; distinct but agglomerated nano $Fe_2(MoO_4)_3$ discs were formed. Figure 4.16 a) shows the XRD pattern of the products from the muffle furnace synthesis and b) shows the SEM image of the $Fe_2(MoO_4)_3$.

a)

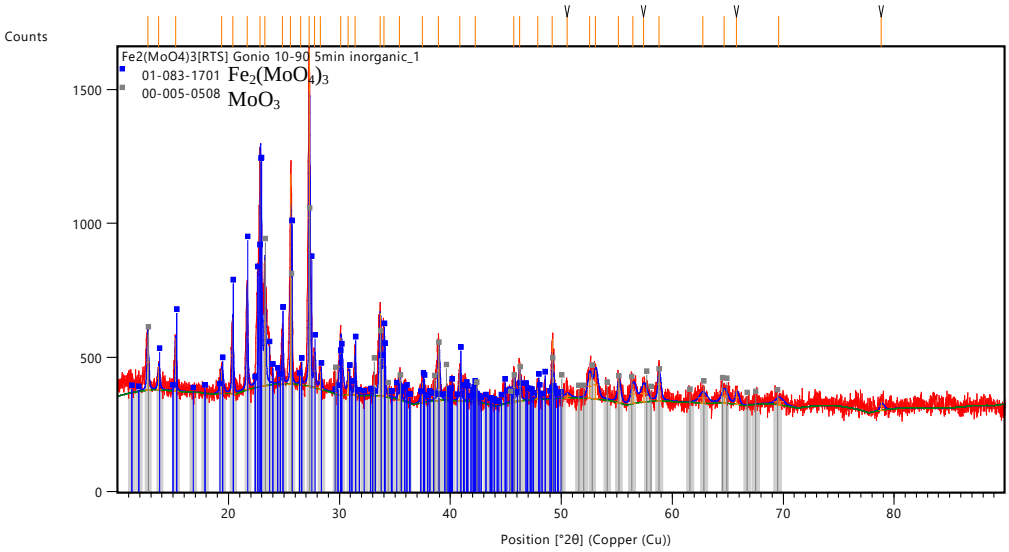

b)

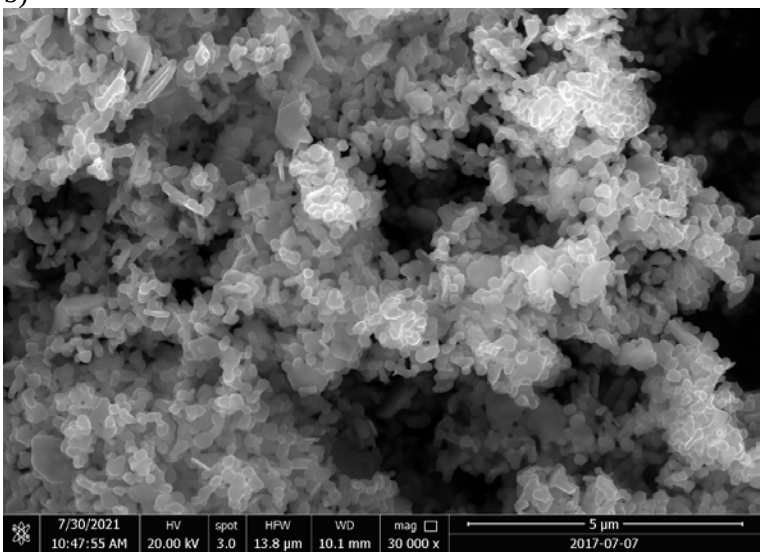

c)

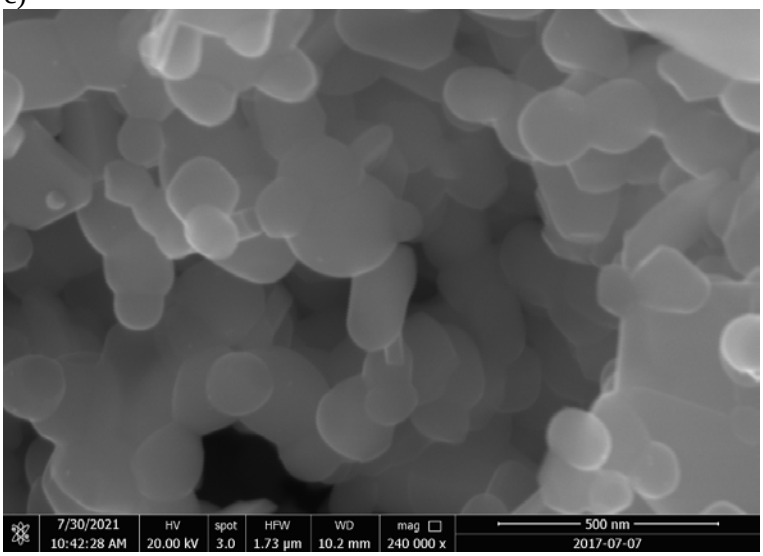

Figure 4.36 a) XRD pattern showed that $Fe_2(MoO_4)_3$ (01-083-1701) and MoO_3 (00-005-0508) were both produced in the muffle furnace at 550ºC. b) The SEM image shows agglomerated nano particles without the porous structures like other SCS products, and c) at a higher magnification.

$CuMoO_4$ was only synthesized using the microwave, even though the reactants were identical when the synthesis was attempted in the muffle furnace. XRD pattern shows that the product also contained $(NH_4)_2Mo_4O_{13}$, as shown in Figure 4.17. When the reaction was carried out in the muffle furnace, copper molybdate complex $Cu_6Mo_4O_{15}$ formed. However, with the microwave as a heat source, the products were not consistent, glycine anhydride, ammonium molybdate, and copper oxide nitrate with non-stoichometric Cu, O, and NO_3 ratio were produced in one of the attempts.

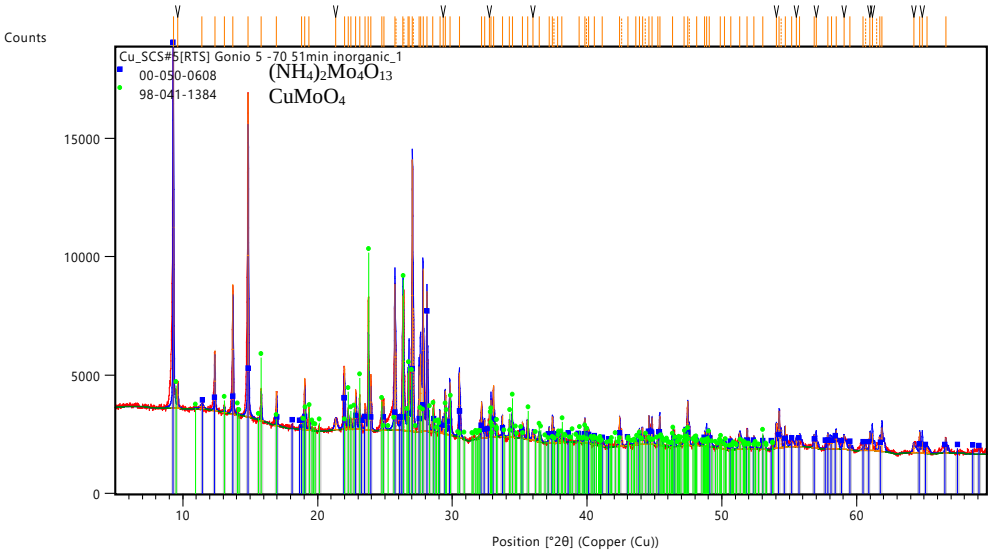

Figure 4.37 XRD pattern showed that $CuMoO_4$ (98-041-1384) was synthesized with $(NH_4)_2Mo_4O_{13}$ (00-050-0608) as a byproduct.

From these results, it was clear that for transition metals, the heating sources affect the products. Some molybdates were never synthesized using muffle furnace while some were only synthesized using the muffle furnace, while all the reactant solutions were prepared using the exact same method. This could be related to how the microwave heats up the reaction. The microwave heats by exciting the water molecules directly, while the furnace heats up the mixture through conductive heating. The microwave has the potential to be an excellent alternate heat source; however, it does not currently produce a consistent result. Further investigations into settings and vessel arrangements are required to produce consistent results. In addition, the microwave tends to synthesize the hydrate version of the compound, due to its inability to evaporate all the liquid in the vessel. The residual liquid in the microwave vessels was most likely due to their geometry. The vessels are cylinders of approximately 2 cm in diameter and 20 cm in length. Unlike a muffle furnace,

where the entire interior volume has the same high temperature, the temperature within the microwave is not uniformly high. Water within the sample started to evaporate once the temperature of the sample was high enough; however, once the water vapour rose and cooled down, it condensed back into the sample. As a result, the samples tend to still sit in a puddle of liquid and in hydrate form.

From the results of $NiMoO_4$ synthesized by microwave, it can be concluded that a vigorous combustion is necessary to produce nano sized particles. In both cases shown in Figure 4.14, the energy provided by the microwave was enough to overcome the activation energy barrier, but the $NiMoO_4$ shown in Figure 4.14 b) had a more vigorous combustion process that some of the solvents were "burnt" and enough vapour was produced to break apart the particles. The $NiMoO_4$ shown in Figure 4.6 c) retained the colour of $NiMoO_4$, which suggested that the combustion process was less intense, and therefore not enough vapour was produced fast enough to create that porous structure and break apart the particles.

Muffle furnace as a heat source produced consistent results. The temperature condition did not need to be exact if it was high enough to initiate the reaction and overcome the activation energy barrier. For alkaline earth metal molybdate compounds, the temperature threshold appeared to be relatively low; 450°C was enough to produce the simple molybdates. However, some transition metal molybdates had higher energy barrier. $CuMoO_4$ and $NiMoO_4$ could potentially be synthesized in the muffle furnace, but the temperature must be raised higher. It is worth trying to synthesize $CuMoO_4$ and $NiMoO_4$ in the muffle furnace again with higher temperatures, as the muffle furnace produced more consistent results.

Products synthesized using CPS and SCS have strikingly different morphology. CPS was able to produce the classic white powder after the washing and the dehydration processes. SEM images of these products showed the products consisted of conventional particles as shown in Figures 4.2, 4.3, and 4.6. SCS produced products with different morphologies. When the products came out of the oven, there were fluffy and volumized parts and parts that were less puffy in the ceramic dishes, as shown in Figures 4.9 and 4.11. Upon examination using SEM, the morphologies of these parts with different volumes were not significantly different. SEM images also showed that in most cases, combustion synthesis produces porous structures with nano features that are made of heavily agglomerated mano particles. The porous structure and nano features are caused by the fast reaction speed. As discussed previously in the introduction, gaseous N_2, CO_2, and H_2O were formed during the reaction. When the reaction was initiated, the temperature rapidly rises by the combustion reaction, these products formed and expanded very rapidly and created the pores within the structure. The temperature then quickly lowered due to the escape of the gaseous products. The short cool down time means particles did not have the opportunity to be sintered and grow in size (Varma et al., 2016). As a result,

the particles, albeit heavily agglomerated, remained nano scaled. Table 4.3 also summarizes the particle sizes of the products from SCS, the largest particle belongs to $Fe_2(MoO_4)_3$, slightly smaller than 200 nm. The individual particles were nano sized, even though the porous structures were not. Sonic bath had been used to try to break up the porous structure but was not successful. Calcination, however, was able to remove the porous structure, but the particles were still agglomerated. Figure 4.18 shows the images of $SrMoO_4$ synthesized using SCS that had been calcinated for four hours at 550°C. Unlike previous CPS result where calcination increased the particle size to micron scale; after calcination, products of SCS remained nano scales. Table 4.4 summarizes the before and after calcination particle size of $MgMoO_4$, $CaMoO_4$, and $SrMoO_4$. Martyrosian et al. have shown that morphology of the products of SCS can also be altered by the amount of glycine used (Martyrosian et al, 2009).

a)

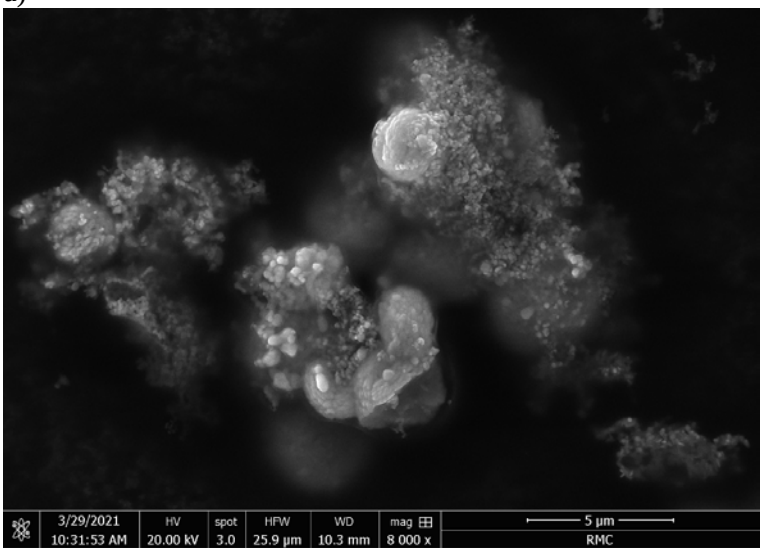

b)

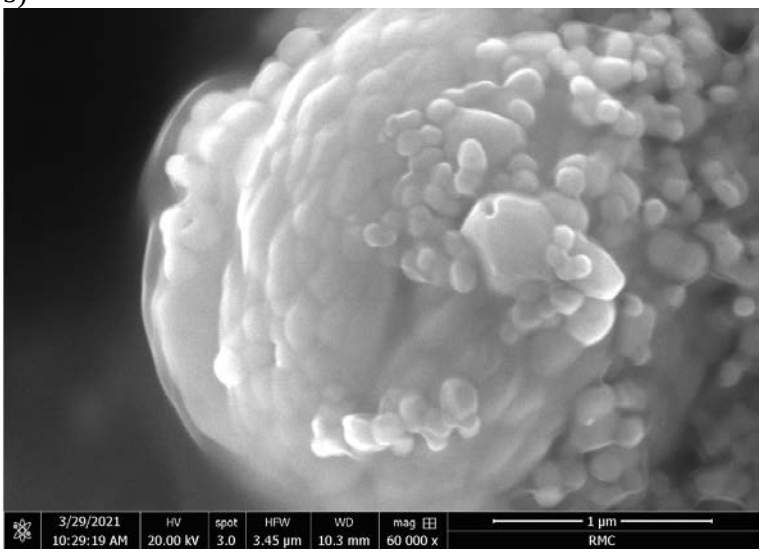

Figure 4.38 $SrMoO_4$ synthesized using SCS after 4 hours of calcination at 550°C. The porous structure is no longer present and b) shows the SEM image at a higher magnification factor.

Table 4.11 Particle size of pre- and post-calcination $MgMoO_4$, $CaMoO_4$, and $SrMoO_4$ synthesized using SCS.

	$MgMoO_4$		**$CaMoO_4$**		**$SrMoO_4$**	
	Particle Size (nm)	σ (nm)	Particle Size (nm)	σ (nm)	Particle Size (nm)	σ (nm)
Pre-Calcination	72.3	23	64.6	16	77.3	43
Post-Calcination	61.8	40	157	77	286	180

The morphologies of the products of SCS were not those of the typical nano particles, which raises the concern whether they would be good oxide candidates for nanothermites. Even though the porous structures were not broken up by sonic bath, the pores could still provide intimate contact between nano Al and the molybdates. Figure 4.19 shows the SEM images of Al/$SrMoO_4$ nanothermite shows contact between nano Al and $SrMoO_4$ synthesized using SCS, and the arrows point out where nano Al particles are present. More details on nanothermites made with SCS molybdates will be discussed later.

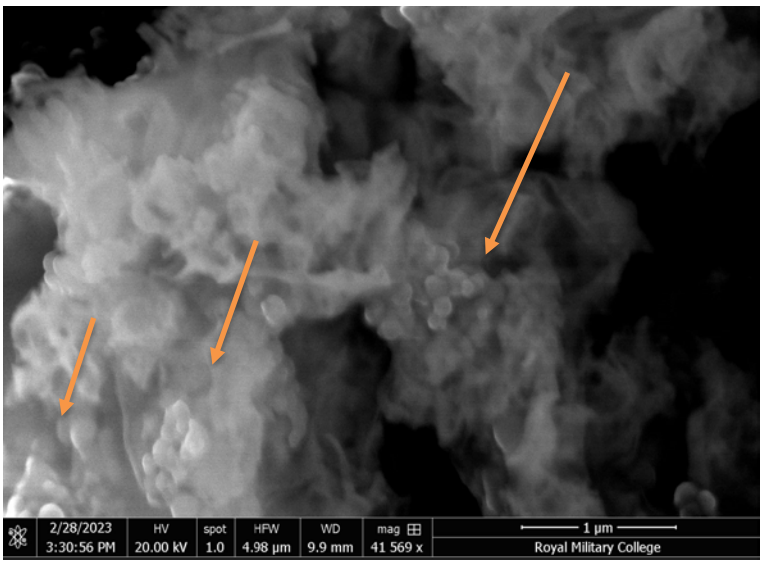

Figure 4.39 SEM images of Al/$SrMoO_4$ nanothermite shows contact between nano Al and $SrMoO_4$ synthesized using SCS. The arrows indicated the area where aluminum particles can be observed.

In conclusion, two different methods were used to produce metal molybdate compounds, each had their advantages and drawbacks. CPS produced less agglomerated molybdate particles with conventional nano particle morphology and less impurities. The process, however, was time consuming and produced low yield. SCS required significantly shorter time and effort. The products were not the classic nano particle but a porous network with nano features. The nano features and pores could provide contact locations between the molybdates and aluminum particles. However, the presence of byproducts was unavoidable, but might be able to be decreased by reducing the amount of secondary fuel used (Sherikar, Sahoo, and Umarji, 2020). However, in the context of making nanothermites less sensitive to friction and ESD, the presence of byproducts could be potentially beneficial. Synthesizing $MgMoO_4$, $CaMoO_4$, and $SrMoO_4$ using SCS were relatively straight forward; however synthesizing molybdates with other metal compounds became more complected. The final products depend on the choice of secondary fuel, heat source, heating power, and possibly heating temperature.

4.2 Resistivity of Metal Molybdates

The resistivities of the oxidizers were measured because there is evidence suggesting there exists a relationship between nanothermite ESD sensitivity and the resistivity of the fuel and oxidizers. Exploring if this relationship could be applied to all fuel oxidizer combinations or the specific nanothermites deepens the understanding of the fundamental principle of ESD sensitivity. The resistivities of various metal molybdate compounds were measured from 1.5V to 30V as functions of packing density and in some cases relative humidity, as described in Method, Section 2.3.1.4. In this section, the results and the significance of these measurements are discussed.

It is important to understand that discussing the resistivity measurement values on their own is meaningless; these data are meant to be compared with each other and interpreted as their relative resistivity. The reproducibility of these measurements was low. The readings tended to be unstable, and the differences of one order of magnitude are not unknown. The resistivity measurements and the extent of reading fluctuation heavily depend on the ambient relative humidity. When the measurements were performed under a low humidity environment, the reading fluctuation was more significant and could fluctuate up to 2 magnitudes. Therefore, rather than discussing the individual measurements, the relative values and trends are the focus here.

Figure 4.20 shows the resistivity measurements of nano MoO_3 from 1.5V to 30V. The trend shown in the figure is typical of all oxidizers, the resistivity decreases as the voltage and packing density increase. As the packing density increases, the contact between crystals increases and therefore increases the current flow through the particles. Increasing the voltage gradient also has the same effect. The resistivity measurements are lower than the previously reported values. At 20V, the resistivity values were previously reported at 10^9 - 10^{11} Ω·cm with packing density between 1.7 - 3.1 g/cm^3. As shown in Figure 4.8, at 20V the resistivity values here are between 10^6 - 10^9 Ω·cm with packing density between 0.68 - 2.07 g/cm^3 (Petre et al. 2019). The low resistivity might be due to the high humidity environment when the experiments were conducted.

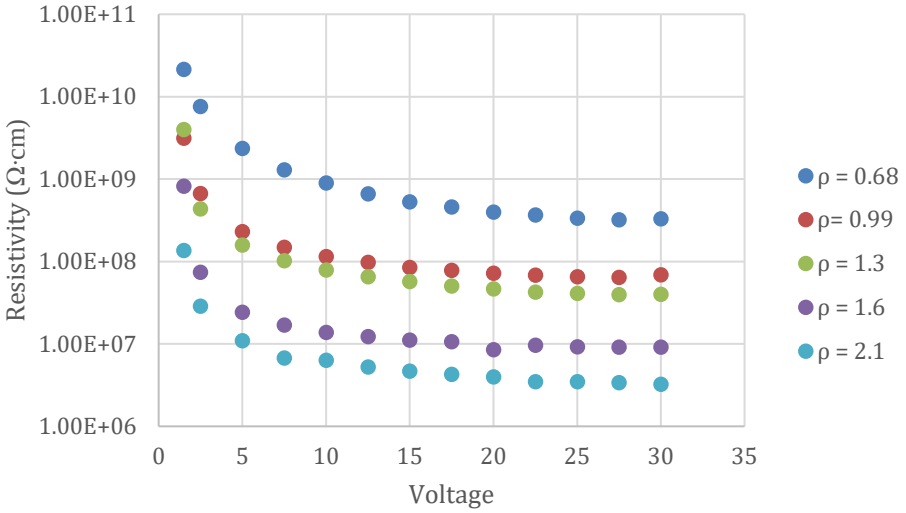

Figure 4.40 Resistivity data of nano MoO_3 powder as a function of voltage.

These specific measurements were made when the laboratory humidity was 65%. As mentioned above, the measurements were significantly affected by the environmental relative humidity. The resistivity of MoO_3 was measured again when the relative humidity in the laboratory was 18% and again when both the sample cell and MoO_3 powder were stored in a 33% relative humidity desiccator for 5 days, these results are shown in Figure 4.21. Figure 4.21 also illustrates the differences in the resistive measurements of MoO_3 and $SrMoO_4$ synthesized using combustion synthesis at 20V as a function of density. The number in the parentheses indicates the laboratory relatively humidity, and SCS indicates the compound was synthesized via solution combustion synthesis. The resistivity of $SrMoO_4$ (SCS) was measured three days before the measurement of MoO_3 (65%), in August, therefore the humidity in the lab was assumed to be similar to 65%.

As previously stated, resistivity measurements as subject to large uncertainties. However, considering the data obtained at 18%, 33% humidity and 65% humidity for MoO_3, a clear trend is apparent with resistivity decreasing over orders of magnitude as humidity increases. A similar, but less pronounced trend is also observed for $SrMoO_4$ produced by SCS. The packing densities of $SrMoO_4$ had a narrower range than that of MoO_3. MoO_3 were commercially made particles with the classic distinct nanoparticle morphology, but SCS $SrMoO_4$ had a porous structure. The porous structure of $SrMoO_4$ made it harder to achieve packing density variation within the sample cell. Given the large uncertainties in individual sample measurements, this proved to be a more pronounce effect than the narrow packing density. 18% and 33% relative humidity $SrMoO_4$ samples did not exhibit the inverse

packing density versus resistivity relationship. At the high relative humidity, the inverse relationship between packing density and resistivity was apparent. MoO_3 has a similar resistivity behaviour to SCS $SrMoO_4$ in the sense that humidity affects the accuracy of the resistivity measurement, and resistivity behaviour depends on the environmental relative humidity. It is suggested that surface hydration and hydrolysis of oxide anions may play an important role in increased conductivity at high humidity.

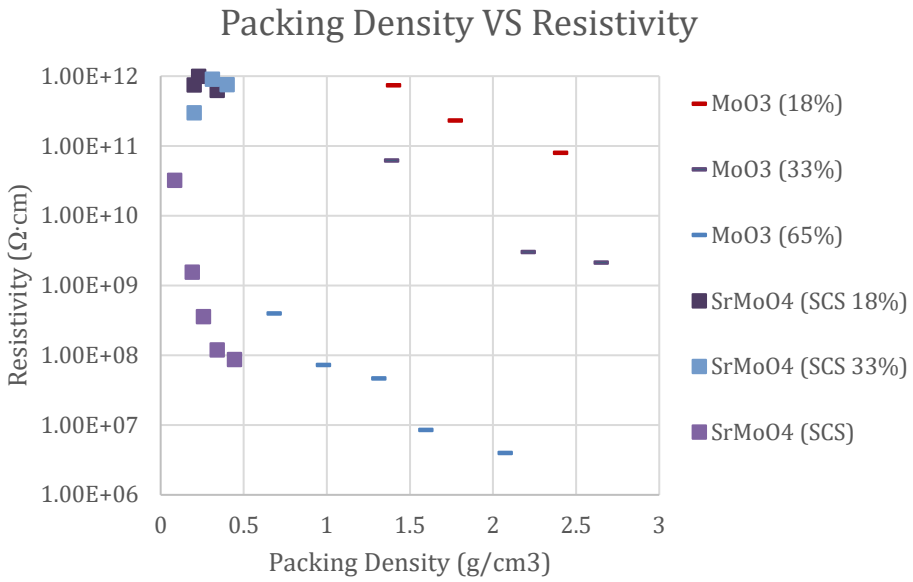

Figure 4.41 Resistivity measurements of $SrMoO_4$ and MoO_3 at 20V as a function of packing density, at different humidity.

Figure 4.22 shows the resistivity behaviours of $MgMoO_4$, $CaMoO_4$, and $SrMoO_4$ synthesized using solution combustion synthesis. An approximate humidity of 60-70% was associated with these measurements. At first glance, the resistivity measurements of the molybdates all fell within the same range. But it is worth noting that the packing densities of $SrMoO_4$ and $CaMoO_4$ were lower than the other $MgMoO_4$. Assuming the resistivity behaviour of $MgMoO_4$ can be extrapolated, $MgMoO_4$ appeared to have the highest resistivity among the three molybdates. $SrMoO_4$ and $CaMoO_4$ have similar packing densities and their resistivity results are within one magnitude of each other, therefore it can be concluded that they have a similar resistivity behaviour. $CaMoO_4$, $SrMoO_4$, and $BaMoO_4$ synthesized using Protocol 3 also exhibit similar resistivity behaviours as shown in Figure 4.23. These 3 measurements were done in a relatively short time frame; therefore the humidity condition differences were considered negligible. The resistivity of $BaMoO_4$, $CaMoO_4$, and $SrMoO_4$ synthesized using Protocol 3 were very similar. All of them

had similar packing densities and their measurements were within approximately one magnitude.

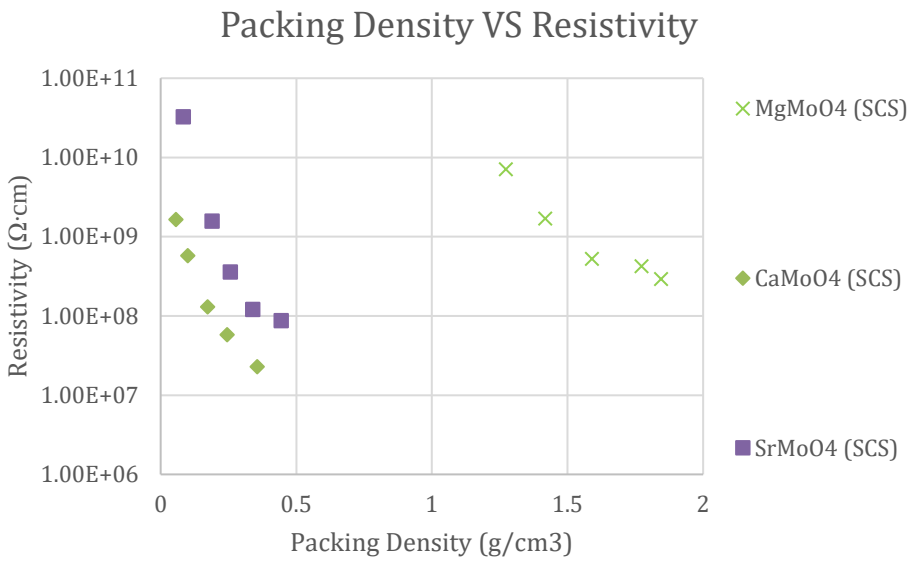

Figure 4.42 Resistivity measurements at 20V of $MgMoO_4$, $CaMoO_4$, $SrMoO_4$, and $CoMoO_4$ as functions of packing density.

Figure 4.24 shows the comparison of $CaMoO_4$ and $SrMoO_4$ using different synthesis methods. The products from combustion synthesis have lower resistivity measurements. The morphology of the compounds might be the reason behind this observation. As shown in the previous SEM images, combustion synthesis produces continuous porous structures while the co-precipitation method produces distinct nanoparticles. It is reasonable that the resistivity measurements are lower in a continuous structure. Although the measurements of $CaMoO_4$ (EG) and $SrMoO_4$ (EG) were done during the fall time, the dryer environment could contribute to the higher resistance, but by comparing $SrMoO_4$ (EG 33%) and $SrMoO_4$ (SCS 33%), it is still clear that $SrMoO_4$ synthesized with Protocol 3 has higher resistivity measurements. The porous structures also contribute to low packing densities. The molybdate compounds synthesized using SCS are consistently lower than their CPS Protocol 3 counterparts.

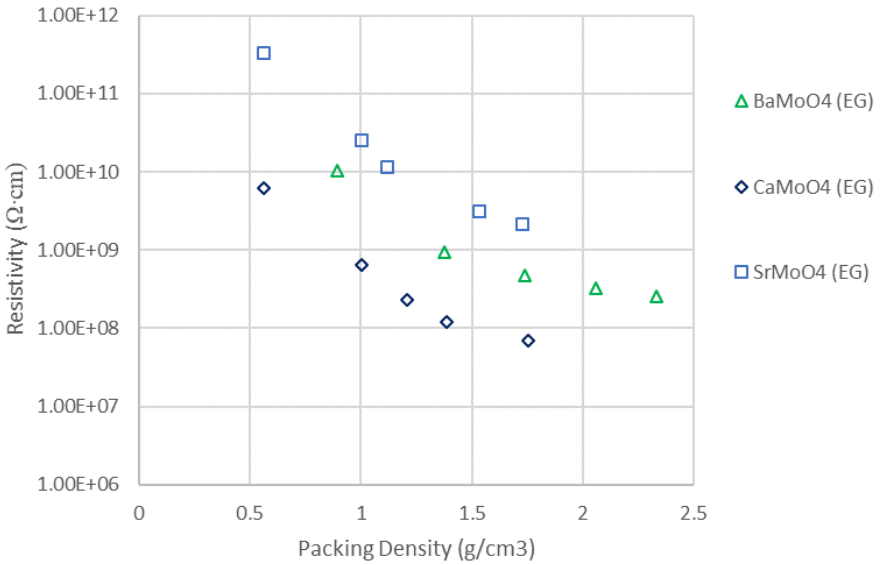

Figure 4.43 Resistivity measurements at 20V of $BaMoO_4$, $CaMoO_4$, and $SrMoO_4$, synthesized using Protocol 3, as functions of packing density.

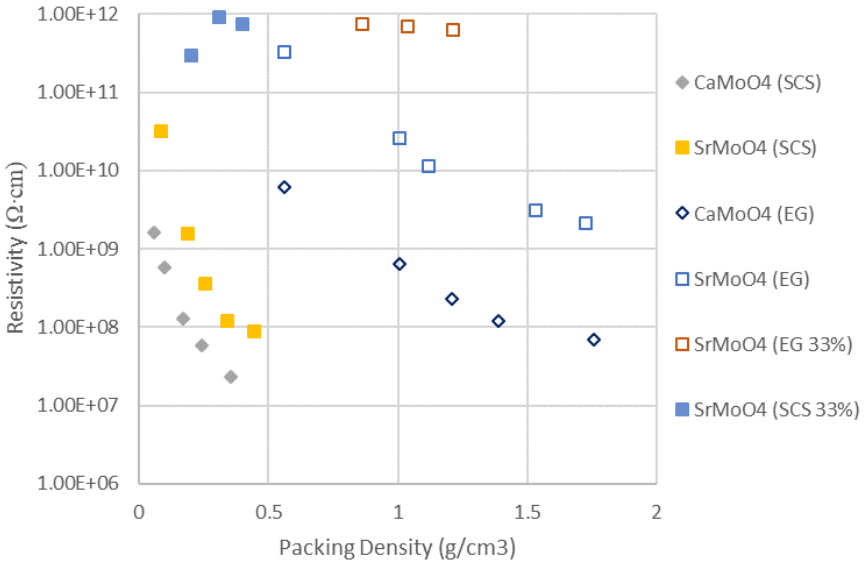

Figure 4.44 Resistivity measurements of $SrMoO_4$ and $CaMoO_4$ with different synthesis routes and relative humidity conditions.

4.3 Specific Surface Area of Metal Molybdates

Specific surface area was measured to explore the potential relationship between nanothermites and the specific surface area of the metal oxide. As mentioned in section 2.1.1.5, $MgMoO_4$, $CaMoO_4$, $SrMoO_4$, and $BaMoO_4$ were chosen to have the specific surface area measured because these compounds were attempted to synthesize using both CPS and SCS. If the sensitivity of nanothermites made with the same composition differs significantly, surface area could play an important role. Table 4.5 summarizes the measurement results and the relative pressure ranges used to calculate the specific surface area. The specific areas were analyzed using the BET method.

BET equation describes the physisorption of the first adsorbate layer as

$$\frac{{}^{P}/_{P_0}}{W(1-{}^{P}/_{P_0})} = \frac{1}{CW_x} + \frac{C-1}{CW_{ml}}\frac{P}{P_0} \qquad \text{Equation 4.1}$$

where P is the pressure within the sample cell and P_0 is the saturation vapour pressure at the reference cell, W is the mass adsorbed at relative pressure P/P_0, W_{ml} is the required adsorbate mass to form a complete monolayer, and C is a constant expressing the difference between the heat of adsorption of the first layer and the layers beyond. The specific surface area can then be calculated using the equation

$$SSA = \frac{W_{ml}}{M \cdot m} \times N \times A \qquad \text{Equation 4.2}$$

where M is the molar mass of adsorbate, m is the sample mass, N is Avogadro's number, and A is the molecular cross sectional area of the adsorbate, in the case of nitrogen gas, 0.162 nm^2 (Bardestani, Patience, and Kaliaguine 2019).

Autosorb IQ measures the volume of adsorbate adsorbed by the sample as a function of relative pressure. Figure 4.25 shows the isotherm of $BaMoO_4$. Typically, the relative pressure range that can be applied to BET is between 0.05 to 0.3, where the adsorption branch of the isotherm is linear. This is not always the case for the molybdate samples. If the linear range is appropriately selected, then the line of best fit across these points should have a good R^2 value, a positive slope, a positive y-intercept, and produce a positive C constant. To make sure only the true linear range is selected, only the data within the range that $W(1-\frac{P}{P_0})$ continuously increases with $\frac{P}{P_0}$ were selected (Thommes et al. 2015; Shimizu and Matubayasi 2022).

The isotherm shown in Figure 4.25 is typical of the rest of the isotherms, they all exhibit the same shape in which the volume absorbed increases gradually as the relative pressure increases and increases rapidly when the relative pressure exceeds 0.95. The rest of the isotherms are attached in the Appendix. This type of isotherm is classified as a Type 3 isotherm (Vyawahare et al. 2022).

Table 4.12 Specific surface areas of metal molybdates measured using autosorb iQ.

Compound	**Synthesis Method**	**Specific Surface Area (m^2/g)**	**Calculated Specific Surface Area (m^2/g)**
$MgMoO_4$	SCS	28.9	—
$CaMoO_4$	SCS	28.8	—
	CPS, Protocol 3	78.3	1.98
$SrMoO_4$	SCS	30.8	—
	CPS, Protocol 3	121	2.32
$BaMoO_4$	Protocol 3	19.8	1.85

Type 3 isotherm indicates that the interaction between adsorbent and adsorbate is weak, and adsorbate-adsorbate interaction is stronger. As a result, the adsorbate started to form multi-layer adsorption before monolayer adsorption is completed. Unlike other types of isotherms, there is no clear linear segment within the isotherm that correlates to the monolayer adsorption. The surface area produced by this type of isotherm is unlikely to be the true surface area since additional layers of nitrogen molecules are adsorbed before the first monolayer is completed (Kruk and Jaroniec 2001; Naderi 2015).

The specific surface area of CPS $CaMoO_4$, CPS $SrMoO_4$, and CPS $BaMoO_4$ have been calculated based on ionic radii of the metal cations and the molybdate anion and the average particle size observed using SEM. The result was also summarized in Table 4.5. The specific surface areas of the molybdates synthesized using combustion synthesis were not calculated. They did not form distinct individual particles and therefore the percentage of agglomeration was difficult to approximate. These calculations were meant to be an approximation instead of an accurate

representation of the specific surface areas; however, they should produce bulk part values that roughly agree with the BET values. The BET values are significantly greater than the calculated value, which would also suggest that the BET values were exaggerated due to the multi-layer adsorption.

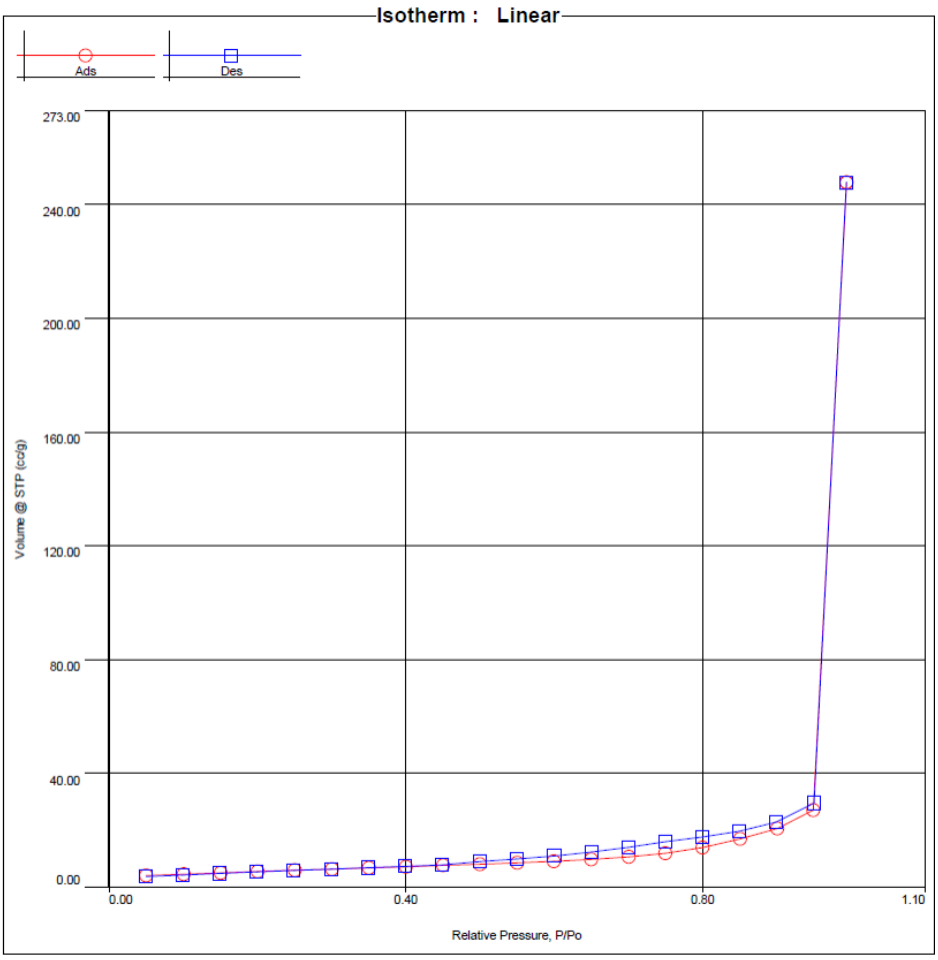

Figure 4.45 Isotherm of $BaMoO_4$ (EG)

Although the specific surface area measurements did not yield definite quantitative results, these values could still be compared qualitatively. The measurements suggest that the surface areas of the molybdates made with combustion synthesis have similar specific surface areas. Their similar morphologies shown in the SEM images agree with this conclusion. CPS $CaMoO_4$ and CPS $SrMoO_4$ have higher specific surface areas than those of SCS $CaMoO_4$ and SCS $SrMoO_4$.

4.4 Nano Aluminum Characterization

To truly understand nanothermites, both the oxidizer and the fuel must be properly studied and characterized. In this section, the fuel, nano aluminum, is the focus. The active content of Alex was determined through the NaOH volumetric method, and an aging test was performed. The active content of other types of nano aluminum, L-Al, O-AL, and V-Al, that were used and discussed in Chapter 3 was also determined using the NaOH method (Kelly et al., 2017; Petre et al., 2019).

4.4.1 Active Content of Alex

Nano aluminum particles are sensitive to the moisture in the air; they can be oxidized quickly under high humidity. As a result of oxidation, the active content of aluminum particles decreased with time. Therefore, it is important to measure the active content of nano aluminum. In addition, other factors such as the techniques or chemicals used for passivation and the size of the particle also produce nanoparticles with different active content (Gromov, Strokova, and Ditts 2010). The nano aluminum used here was Alex, a specific type of nano aluminum produced by the electroexplosion of aluminum wire (Cliff, Tepper, and Lisetsky, 2001). It is important to know the active content of nano aluminum before other tests, such as the aging test can be done. Knowing the active content of the aluminum is also necessary to fabricate nanothermite, otherwise the correct fuel to oxidizer ratio cannot be calculated.

As discussed in the introduction, Section 1.2.1.2, aluminum oxidized by water to produce H_2 in the presence of catalytic NaOH (Zou et al., 2013). As the reaction proceeds, hydrogen gas is produced and therefore generates pressure within the flask. By measuring the pressure generated, the amount of hydrogen gas generated, hence the amount of aluminum present in the nanoparticles, can be calculated using the ideal gas law. Excess solution was used to ensure all the aluminum content was reacted.

The final pressure is made of the partial pressures of the NaOH solution, the initial pressure, and the partial pressure caused by the generation of hydrogen gas. Therefore, to determine the actual pressure generated by hydrogen, the initial pressure and the NaOH solution partial pressure needed to be subtracted from the final pressure,

$$P_{H_2} = P_f - P_{NaOH} - P_0 \qquad \text{Equation 4.3}$$

However, the volume that was used to determine the initial pressure P_0 was different from the volume after the NaOH solution was injected into the flask. The volume

decreased after the NaOH solution was injected, therefore, instead of the P_0, a corrected pressure, P_{corr}, is needed to accurately calculate P_{H_2}, where

$$P_{corr} = \frac{P_0 V_{sys}}{V_{sys} - V_{inj}} \quad \text{Equation 4.4}$$

V_{sys} is the total volume of the flask and connecting tubes between the valve, pressure sensor, and flask. V_{inj} is the volume of the NaOH solution. Determining the volume of NaOH solution by its mass and density is more accurate than simply relying on the markings on the syringe; therefore, the mass before and after injection was measured. Taken the volume correction into an account, Equation 4.4 became

$$P_{H_2} = P_f - P_{NaOH} - P_{corr} \quad \text{Equation 4.5}$$

Since the mass of nano aluminum powder was known, the vapour pressure, $P_{100\%}$, would have been generated if the oxide shell did not exist and therefore 100% active aluminum content could be easily calculated using ideal gas law.

$$P_{100\%} = \frac{{}^3/_2 n_{Al} RT}{V_{sys} - V_{inj}} \quad \text{Equation 4.6}$$

R is the gas constant and T is the temperature of the flask in Kelvin.

P_{H_2} is then compared with $P_{100\%}$ to calculate the active content of aluminum particles,

$$Al\% = \frac{P_{H_2}}{P_{100\%}} \times 100\% \quad \text{Equation 4.7}$$

A summary of the results is presented in Table 4.4.

Table 4.13 The summary of Alex active content

Partial Pressure of NaOH, P_{NaOH} (Torr)	13.4
Total Volume, V_{sys} (mL)	6.20×10^2
Al Active Content, Al%	90.4%
Standard Deviation	1.0%

The active content of the nano aluminum is calculated to be 90.4% ±1.0%. The value agreed with the literature value well. It has been reported the oxide shell of Alex is approximately 14% by mass when it was freshly produced, which would be the equivalent of 92.3% active aluminum (Gromov, Strokova, and Ditts 2010).

4.4.2 Aging Test

The air and moisture sensitivity and the rate at which nano aluminum is consumed have not been studied extensively. Puszynski had done some studies regarding the manner in which humidity affects the active content of nano aluminum particles; however, the lowest humidity study was 43% relative humidity with a shorter period of time (Puszynski 2009, 2004). Cliff et al. studied the ageing process of Alex with a wider ageing condition with relative humidity ranging from dry at 22°C to 75% at 60°C. It was found that Alex was not affected by 32% relative humidity at 40°C for up to 40 days (Cliff, Tepper, and Lisetsky 2001). In this study, a longer ageing period was examined.

Saturated salt solutions with excess solids were used to control the humidity within the desiccators. These salt solutions establish defined constant water vapour pressure once equilibrium is reached at any given temperature. When excess water is presented in the environment, part of the excess solids dissolve into the solution, and when the water content is removed from the environment, more solids precipitate from the solution. NaCl and $MgCl_2$ creates environments with relative humidity of 75.5% and 32.5%, respectively. They were chosen for their ability to maintain the same relative humidity from 25°C to 35°C. Although experiments were conducted in an oven, variation between 25°C- 30°C occurred as a function of ambient temperature.

The mass of aluminum contained within the $MgCl_2$ desiccator, at a humidity of 32.5%, did not gain any mass. It is reasonable to conclude that the aluminum was not oxidized. The masses fluctuated over time, but all of them were lower than the original mass. Alex adsorbs gases on its surface, therefore it is possible that the gases within the desiccator simply adsorbed and desorbed from the aluminum surface (Mench et al. 1998; Cliff, Tepper, and Lisetsky 2001). The appearance of the aluminum powder also remained the same as the original condition.

Aluminum in the NaCl desiccator with a humidity of 75.5%, on the other hand, consistently gained mass, which means that the aluminum was oxidized. When aluminum with 90.4% active content is completely oxidized, it should gain 80.3% of its original mass based on the formation of Al_2O_3. As shown in Figure 4.26, aluminum stored in the NaCl gained mass to approximately the same level. The aluminum mass increased steadily initially and plateaued at around the 80% mark.

Further mass fluctuation beyond the plateau was likely due to the adsorption and desorption of water molecules on the particle surface. The colour of the aluminum powder changed from dark grey to lighter grey, which is also a sign that the aluminum powder had been oxidized. Figure 4.27 shows the difference in the colour of the two nano aluminum powders and Figure 4.28 shows the different morphologies of the two aluminums. In Figure 4.28 a) the image showed the classic nano aluminum morphology which is circular sphere. In Figure 4.28 b) the spheres had disappeared; instead, the image showed heavily agglomerated oxide, similar to those of molydates discussed earlier. The change in morphology indicated that Alex had been oxidized. The XRD pattern and EDX results indicated that the identity of the light grey powder is Al_2O_3. XRD pattern shows that aluminum was not completely oxidized as there are aluminum peaks present in the spectrum. However, EDX data showed that the sample contained 40 atomic percent of aluminum and 60 atomic percent of 60% of oxygen. Based on the mass change and the EDX data, only a trace amount of aluminum remained.

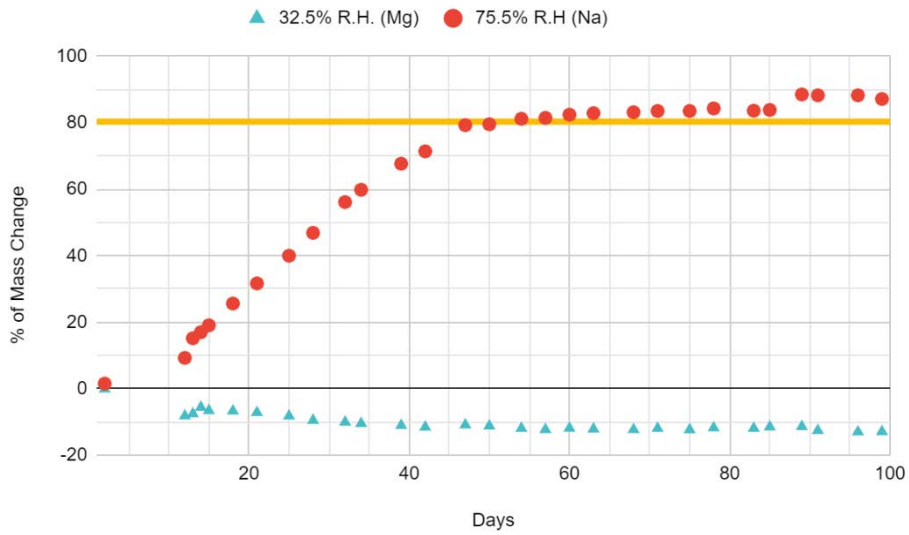

Figure 4.46 The mass change of nano aluminum powder due to oxidation under two different relative humidity. The horizontal line at approximately 80% mass change indicates the theoretical mass gain of completely oxidized aluminum.

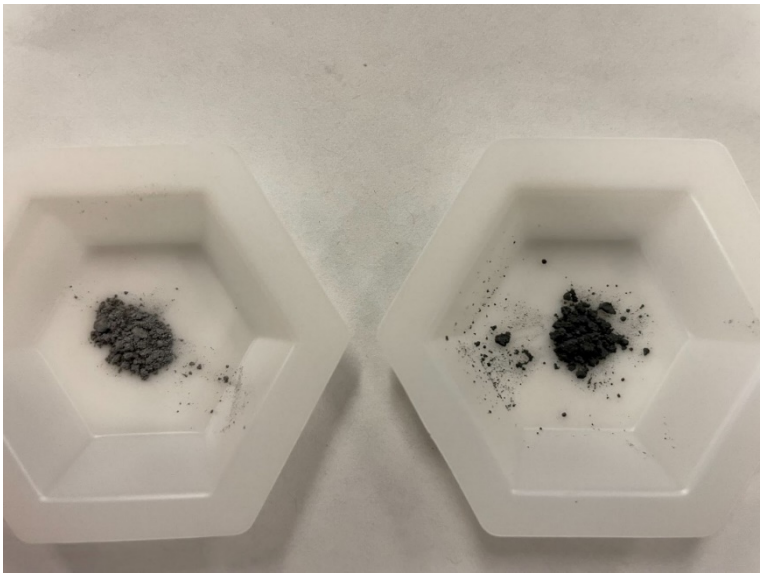

Figure 4.47 The colour of aluminum powder stored in the 75.5% relative humidity desiccator (left) turned to a lighter shade of grey compared to the aluminum powder stored in the 32.5% relative humidity desiccator.

a)

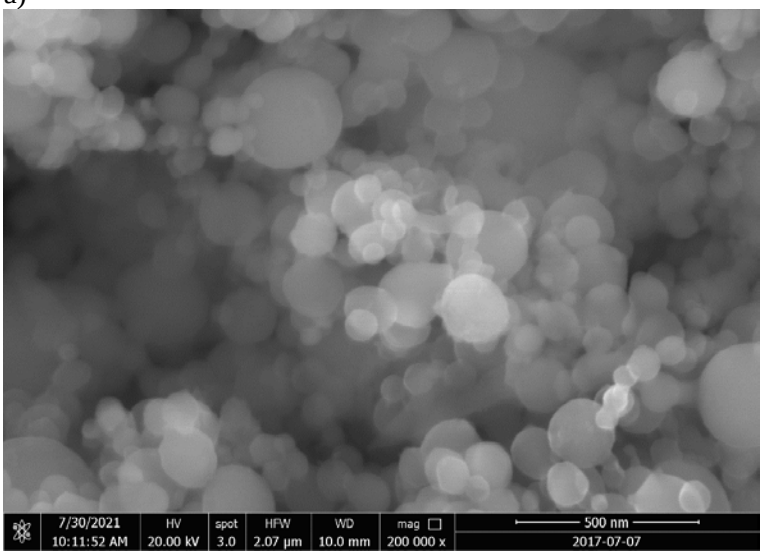

b)

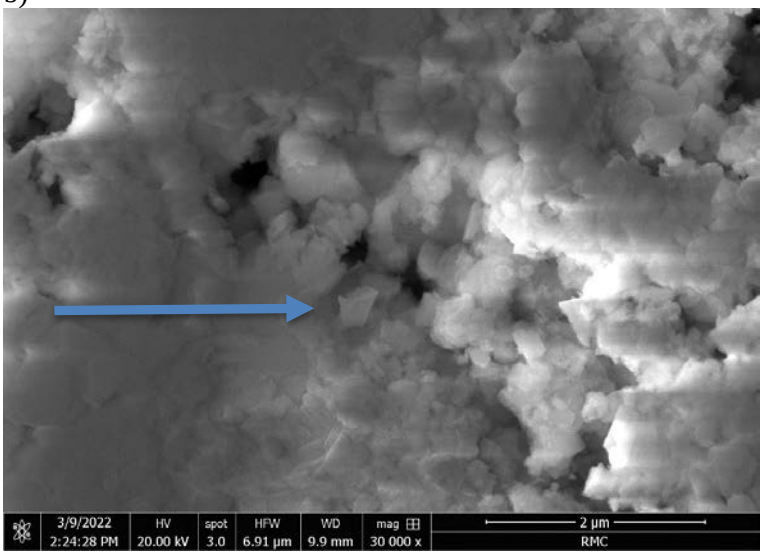

Figure 4.48 The SEM images of a) freshly opened nano aluminum and b) after being placed in the 75% RH desiccator for 100 days. On close inspection to grown of regular crystal faces associated with Al_2O_3 is apparent.

Upon further investigation, the initial mass increased at a linear rate, as illustrated in Figure 4.29. There are different models for aluminum oxidation at room temperature. These models suggest that oxidation is a stepwise process. The first step is a linear fast oxidation process is a linear process where aluminum cations and oxygen anions diffuse across the aluminum oxide film. As the oxide layer thickness increases, the diffusion process becomes less efficient and a slow oxidation process starts to take place (Fehlner and Mott 1970; Gorobez, Maack, and Nilius 2021). In this experiment, only the linear step is observed; however, none of these models were specifically simulated for nano aluminum. The linearity is in good agreement with Puzynski's data where he reported active content of aluminum decreased linearly with time under a 75% relative humidity environment (Puszynski 2009).

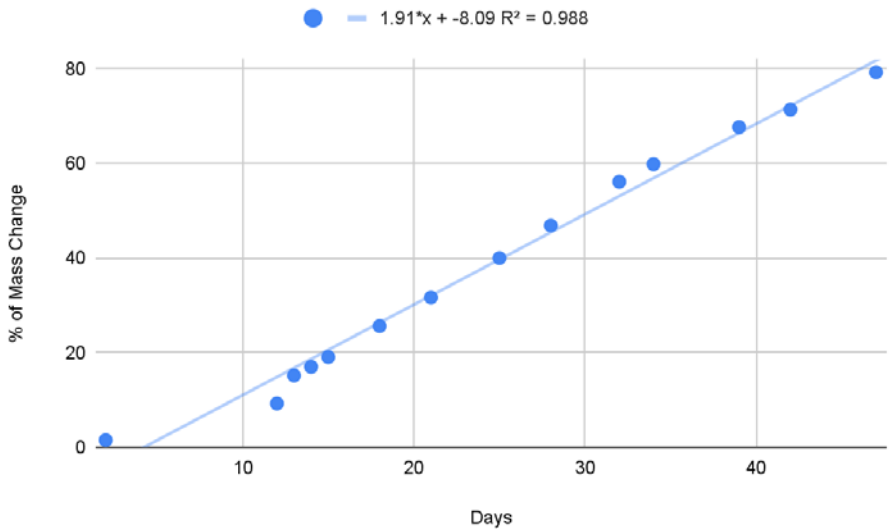

Figure 4.49 The mass change of aluminum oxidation process at a relative humidity at 75.5%.

4.5 Al/Metal Molybdate Nanothermite

CPS molybdates and SCS molybdates were made into nanothermites with Alex. From here on, unless specified, CPS metal molybdates refer to metal molybdates synthesized using CPS Protocol 3. As described in Method, they were suspended in IPA at a fuel-to-oxidation ratio of 1.2 and sonicated for 15 minutes. The nanothermites were then allowed to dry overnight in the fume hood. The following nanothermites were made, Al/$CaMoO_4$ (CPS), Al/$SrMoO_4$ (CPS), Al/$BaMoO_4$ (CPS), Al/$MgMoO_4$ (SCS), Al/$CaMoO_4$ (SCS), Al/$SrMoO_4$ (SCS).

As a reference, Al/MoO_3 mixtures are shown in Figure 4.30 a). The smaller spheres are aluminum particles, and the larger particles belong to MoO_3. The figure shows good mixing between aluminum and MoO_3, no significant agglomeration of either party is shown. This is also typical of the nanothermites made with CPS molybdates. Figure 4.30 b) shows the SEM images of Al/$BaMoO_4$, similar to Al/MoO_3, with no significant agglomeration of either aluminum or MoO_3.

a)

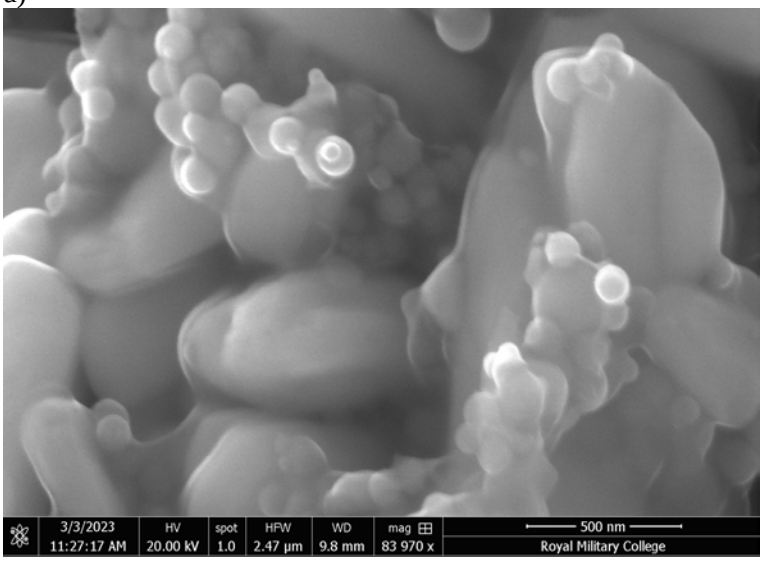

b)

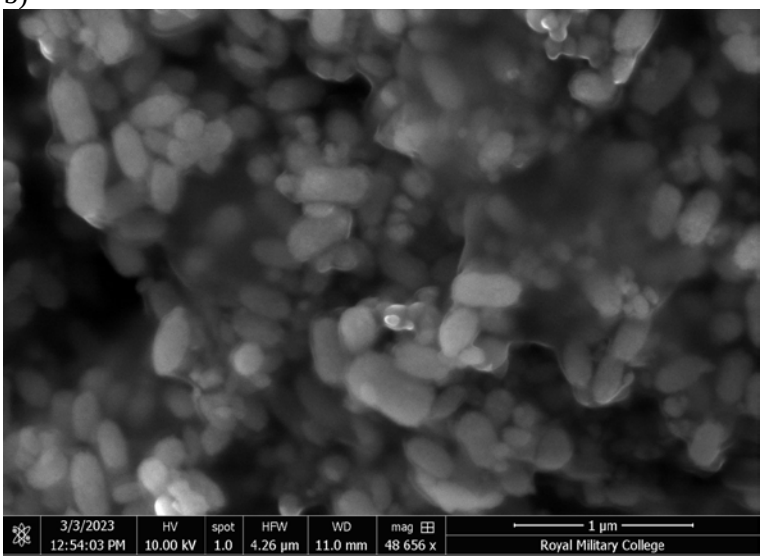

Figure 4.50 SEM images of a) Al/MoO_3 nanothermite and b) $Al/BaMoO_4$ (CPS) nanothermite. Both images show aluminum particles are evenly spread out and in contact with the surface of the oxidizers.

Nanothermites made with SCS molybdates showed less uniform mixing between the aluminum and the molybdate. SEM images have shown that the porous structure of the SCS molybdates cannot be eliminated using sonication, and some parts of SCS molybdates are still heavily agglomerated when made into nanothermites. Figure 4.31 a) shows the agglomeration that still exists after sonication. In some areas, aluminum particles tend to cluster together, but in some other area aluminum particles can be seen covering the porous structure, as shown in Figure 4.31 b). The uneven mixing between the aluminum particles and the SCS molybdate might affect the performance of nanothermites made with SCS molybdates.

a)

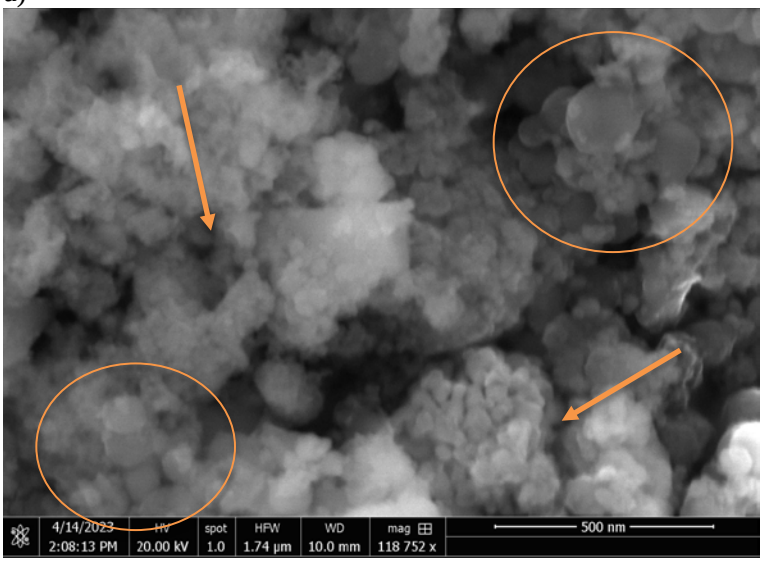

b)

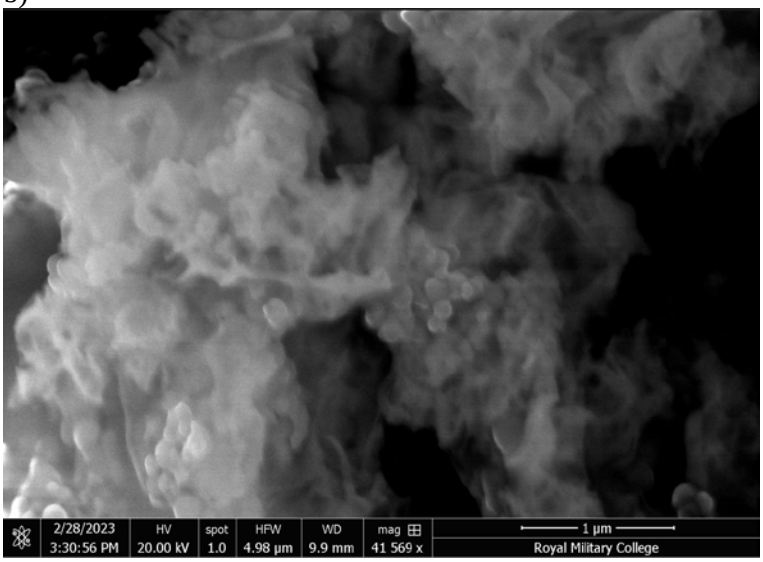

Figure 4.51 a) SEM image of Al/$CaMoO_4$ (SCS). The circles highlight the aluminum clusters, and the arrows point toward the $CaMoO_4$ agglomeration. b) SEM image of Al/$SrMoO_4$ (SCS). Aluminum particles in contact with the surface of $SrMoO_4$ (SCS), where the porous structure was unaffected by the sonication.

4.6 Conclusion

Two different synthesis methods, CPS and SCS, were used to synthesize metal molybdate compounds, the oxidizers of nanothermites. To achieve ideal particle size and product purity, three different protocols were developed. Protocols 1 and 2 produced micron size products with impurities. Nano $CaMoO_4$, $SrMoO_4$, and $BaMoO_4$ were synthesized successfully using Protocol 3. Protocol 3 had success in synthesizing nano particles due to the low concentration and low volume batches used during the synthesis procedure. However, the exact reasons that made Protocol 3 successful also made it laborious and time consuming to produce enough molybdates to be tested and characterized. To increase the efficiency of molybdate production an alternative synthesis method was explored, SCS. $MgMoO_4$, $CaMoO_4$, $SrMoO_4$, $NiMoO_4$, $Fe_2(MoO_4)_3$, $ZnMoO_4$, and $CuMoO_4$ were synthesized using SCS; the products, however, all contain different amounts of impurities that were difficult to purify. The products of SCS looked volumizing and fluffy when examined using the naked eyes, under SEM porous structures composed of agglomerated nano particles were observed.

The difference in their morphologies causes the products of CPS and SCS to have different physical properties such as resistivity and specific surface. It was shown

that SCS products consistently had lower resistivity than their CPS counterparts. $CaMoO_4$, $SrMoO_4$, and $BaMoO_4$ synthesized using CPS Protocol 3 had similar resistivity behaviour and were able to achieve similar packing density. $MgMoO_4$ synthesized using SCS had higher resistivity and achieved higher packing density than SCS $CaMoO_4$ and $SrMoO_4$. When comparing the products of CPS and SCS, SCS products had higher resistivity and packing density and CPS products.

The BET method was used to measure the specific area of CPS $CaMoO_4$, $SrMoO_4$, and $BaMoO_4$ and SCS $MgMoO_4$, $CaMoO_4$, and $SrMoO_4$. The BET method did not produce results that could accurately describe the specific surface area of the molybdates, due to multilayer adsorption of the nitrogen; however, the specific surface area could be interpreted qualitatively. It was concluded that the CPS $CaMoO_4$ and $SrMoO_4$ have higher specific surface areas than the rest, which have similar specific surface areas.

CPS Protocol 3 is considered a successful method to synthesize $CaMoO_4$, $SrMoO_4$, and $BaMoO_4$; the particles were well within the nano range, the colours of the product are white, XRD patterns did not catch impurities, and TGA curves show that mass loss reached plateau by 600^{o}C indicated that any remaining hydrate and solvent were evaporated completely. Products made with SCS were more complicated. All products contained impurities. XRD patterns of $NiMoO_4$, $Fe_2(MoO_4)_3$, $ZnMoO_4$, and $CuMoO_4$ all contained peaks of other compounds, even though XRD might have missed the amorphous impurities within $MgMoO_4$, $CaMoO_4$, and $SrMoO_4$, they were light brown after calcination, instead of white. SCS also produced porous structure, not the classic nano particles. However, the impurities and the unusual morphologies might not be a disadvantage in the context of minimizing sensitivities. Although products of SCS are not as clean and well defined as the products from CPS Protocol 3, they should not be written off just yet.

Characterization tests were also done for the nano aluminum (Alex) that were made into nanothermites with the CPS and CSC molybdates. The active content of Alex was determined to be 90.4% using the NaOH reaction method. An aging test was also performed to understand how easily Alex could be oxidized by the moisture in the air. The aging test indicated that Alex had some moisture resistance ability and remained unoxidized at a humidity level of 32.5% for at least 100 days; however, when the humidity level reaches 72.5%, Alex was completely oxidized by approximately 50 days.

SEM images show that different synthesis methods affect how aluminum particles mix with the molybdates. Nanothermites made with CPS molybdate are shown to be more evenly mixed aluminum and molybdate. Nanothermites made with SCS molybdates, on the other hand, show different degrees of heterogeneous mixing between aluminum and molybdates that in some areas, aluminum had good contact

with the molybdate, but clustered in other areas. The uneven mixing could potentially affect the performance of nanothermites, however, more study will have to be done to confirm this hypothesis.

5. Conclusions

5.1 Summary

Researchers have discovered nanothermites' versatility and potential; however, there is still much need to be understood before nanothermites could be used safely and reliably as real-life applications. The goal of the project is to gain a deeper knowledge of nanothermites and get a step closer to understanding their sensitivities to friction and electrostatic discharge (ESD).

The first part of the project focused on the settling trends of the three different nanothermites made of oxide passivated aluminum (O-Al), palmitic acid coated aluminum (L-Al), and viton coated aluminum (V-Al). The goal was to determine if it is possible to describe sensitivity of nanothermites as a function of wait time or layer of nanothermites, and thus tailoring nanothermite sensitivity by selecting specific wait time or layer. Each aluminum was sonicated with MoO_3 in isopropanol (IPA) at $\Phi = 1.2$. Nanothermites were allowed to settle with different amount of time, 0 minute, 15 minutes, and 60 minutes. To compare the difference between the precursors and the nanothermites, each aluminum and MoO_3 were also sonicated in IPA individually and allowed to settle in the same fashion as the nanothermites. After the settlement, nanothermites and the precursor were pipetted into vials layer by layer, top down; each layer is the topmost 1 mL of the suspension. Subsamples of nanothermites were taken from each layer to deposit on SEM stages for imaging.

Among the precursors, O-Al has the most evenly distributed layers, followed by MoO_3, evenly distributed top seven layers but slightly heavier 8^{th} layer. L-Al settled the fastest, after 15 minutes, the top five layers contained no L-Al at all. V-Al also settled fast; however, even after 60 minutes wait time, the top seven layers still contained minute amount of V-A; however, it consistently exhibits the heaviest 8^{th} layer. Zeta potential measurements of these precursors have been made. MoO_3 and O-Al had highly anionic zeta potential and highly cationic zeta potential measurements, respectively. The zeta potential measurement for L-Al was considered neutral, and the zeta potential of V-Al was inconsistent. A more extreme zeta potential measurement usually indicates a more stable suspension system. In this context, the settling patterns of MoO_3, O-Al, and L-Al agreed with the zeta potential measurements. V-Al was more difficult to interpret. The zeta potential was inconsistent due to its high attenuation rate, and even though it settled fast, the top layers were quite evenly distributed. This unique behaviour might be caused by the Viton coating, fluorocarbon molecules are known to have unusual behaviours. Figure 5.1 illustrates the difference in settling patterns between each precursor.

a)

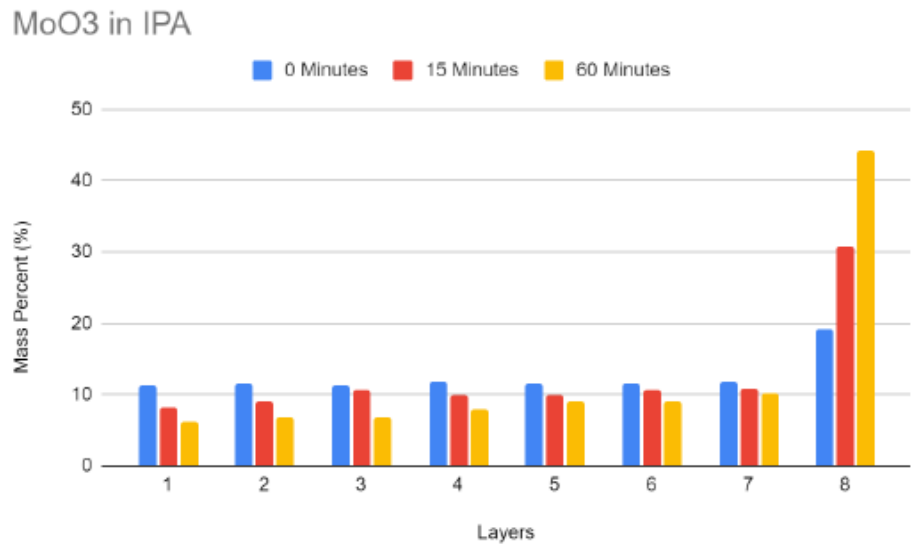

b)

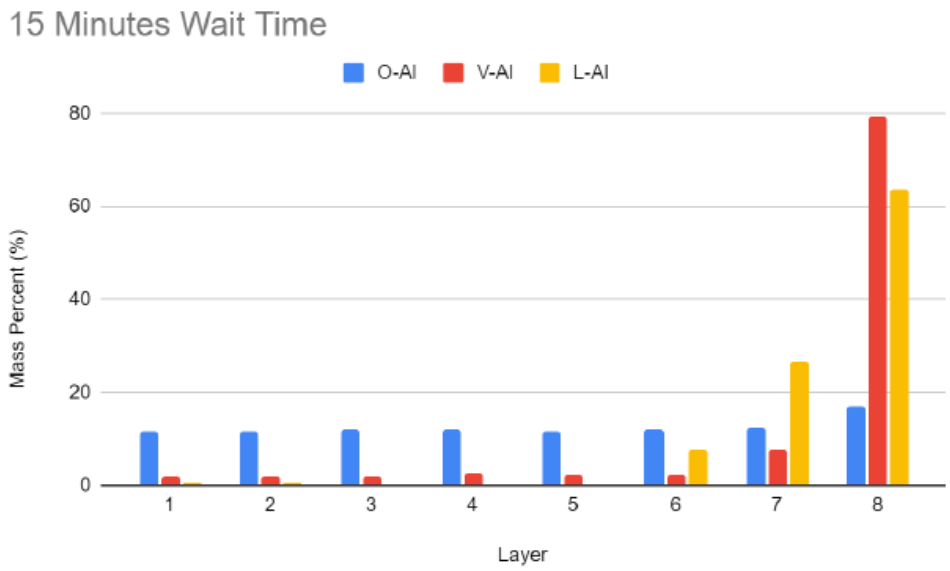

Figure 5.52 The settling trends of the a) MoO_3 in IPA with different wait times and b) the three types of aluminum in IPA with 15 minutes wait time. MoO_3 and O-Al had similar settling trends while V-Al and L-Al showed different settling trend.

The nanothermites settled differently than their precursors, as shown in Figure 5.2. All the nanothermites started to settle within the first minute or so and after they

were allowed to sit for 15 minutes, most of the top layers contained no nanothermites. O-Al/MoO_3 settled the fastest, even without letting the nanothermite settle after sonication, some top layers contained no nanothermite. L-Al/MoO_3 was the slowest settler among the three and V-Al/MoO_3 had the heaviest bottom layers. Particle sizes of aluminum and MoO_3 of each layer were measured to examine if the particle that settled faster were larger than the particles that suspended longer. The measurement showed that there was no significant size difference between layers. The sensitivities of these nanothermites toward friction and ESD were measured. Each nanothermite were divided into Layers 1 – 7 and Layer 8 and the sensitivities of friction and ESD of the two parts were measured separately. All the nanothermites were very sensitive to ESD regardless the layer or the coating, with one exception where less than ideal amount of nanothermite were used. Sensitivity toward friction showed more variation. In particular, the 8^{th} layer of O-Al/MoO_3 was the least sensitive and was insensitive to friction up to 120N of friction. There is not a clear trend that can describe the sensitivities across all three nanothermites and more than one factor can contribute to the sensitivity variations of the nanothermites.

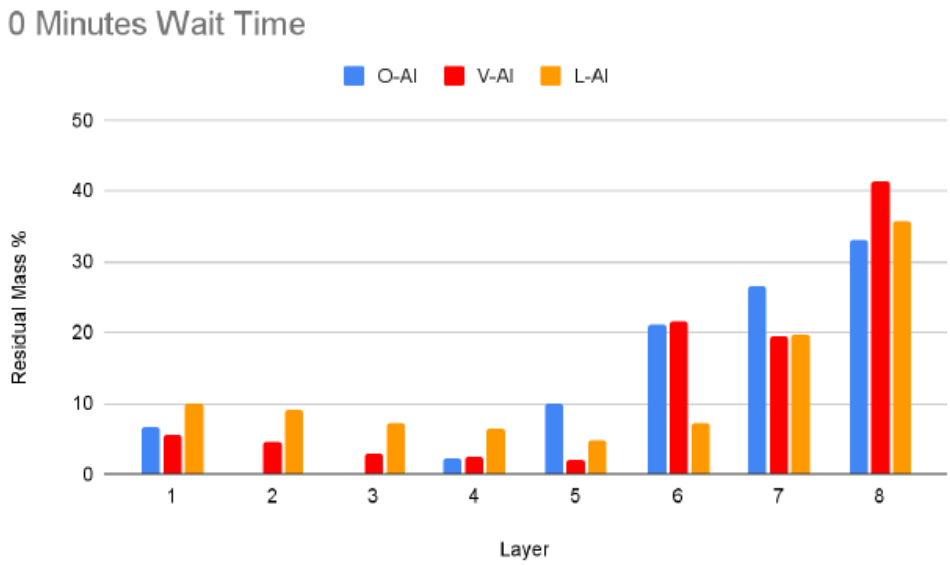

Figure 5.53 The settling trends of the three nanothermites with 0-minute wait time. The nanothermite exhibited different settling trend from their precursors.

The second part of the project focused on synthesizing metal molybdates as oxidizers of nanothermites. The interest in molybdates compounds arises from the desire of having the ability to fine tune nanothermites characteristics. By having two metals contained within the oxidizer, there is potential that the characteristics of the

nanothermites could be less discrete and could be mapped into a spectrum eventually.

Two different methods, co-precipitation method (CPS) and solution combustion synthesis (SCS), were used to synthesize the molybdate compounds. Within CPS, three different protocols were used. Protocol 1 produced particles micron sized particles. Protocol 2 produced smaller particles, but the solvent used in the synthesis, triethylene glycol (TEG), remained within the products even after calcination. The calcination process increased the particle size to micron-sizes. Protocol 3 was the most successful protocol, in terms of particle size and product purity. Protocol 3 was able to synthesize nano particles and the solvent, ethylene glycol (EG), was relatively easily separated from the sample. $CaMoO_4$, $SrMoO_4$, and $BaMoO_4$ were synthesized successfully using Protocol 3. A major drawback of CPS Protocol 3 was the low yield of the product. Low concentration and batch volume had to be used to ensure nano scale particle size, as a result, the amount of product produced each synthesis was minimal.

To increase the efficiency of the production, solution combustion synthesis was explored, where a heat source was required to quickly heat up the reactant mixture and initiate the reaction. $MgMoO_4$, $CaMoO_4$, and $SrMoO_4$ were synthesized using SCS, as well as additional molybdates, $NiMoO_4$, $CuMoO_4$, $Fe_2(MoO_4)_3$, and $ZnMoO_4$ were synthesized. When these molybdates were produced, it was obvious that impurities were present; they were all either brown or black which was mostly likely caused by the burnt organic molecule from the reaction of glycine and ammonia molybdate tetrahydrate. XRD did not catch these amorphous burnt impurities and displayed clean spectra of $MgMoO_4$, $CaMoO_4$, and $SrMoO_4$. However, spectra of $NiMoO_4$, $CuMoO_4$, $Fe_2(MoO_4)_3$, and $ZnMoO_4$ showed impurities such as molybdate complexes and MoO_3 that were difficult to be separated from the products. Products of SCS were porous structures that were made of heavily agglomerated nano particles.

Resistivity and specific surface area measurements were made on $MgMoO_4$ (SCS), $CaMoO_4$ (CPS, SCS), $SrMoO_4$ (CPS, SCS), and $BaMoO_4$ (CPS). Both the resistivity measurement and specific surface area measurement should be interpreted qualitatively instead of quantitatively. Resistivity measurement came with one magnitude of uncertainty and was hugely dependent of the humidity in air. The isotherms from the adsorption experiment showed that the adsorption was a multilayer process instead of the monolayer process. As a result, the specific surface areas calculated was exaggerations of the true values.

It was shown that the CPS molybdates had higher resistivity and higher packing density than their SCS counterparts. This result was not surprising considering SCS molybdates were made of porous structures while CPS molybdates were distinct

particles. Among the CPS products, the three molybdates had similar resistivities. $MgMoO_4$ had a higher resistivity than that of $CaMoO_4$ (SCS) and $SrMoO_4$ (SCS). The specific surface area measurements indicated that all three SCS molybdates and CPS $BaMoO_4$ had similar specific surface areas, while the CPS $CaMoO_4$ and CPS $SrMoO_4$ had larger specific surface area.

To make nanothermites with the right fuel-to-oxidizer ratio, the active content of the aluminum must be measured. The nano aluminum (Alex) used to make nanothermites with the molybdates are made using wire electroexplosion method. The active content of Alex was measured using NaOH method. The active content of the aluminum used previously (O-Al, V-Al, L-Al) were all measured using the same method here. The active content was measured to be 90.4%. The condition of Alex oxidation was also investigated. A vial of Alex was stored in a desiccator with relative humidity of 32.5% and another vial stored in a desiccator with a relative humidity of 75.5%. Both desiccators were kept at an oven with temperature between 25°C to 30°C. The two vials of Alex were weighted periodically. It was shown that Alex had a certain level of humidity resistance that it was not oxidized at all after 100 days at 32.5% relatively humidity. However, Alex was oxidized completely in approximately 50 days at 75.5% relative humidity.

Al/$CaMoO_4$ (CPS), Al/$SrMoO_4$ (CPS), Al/$BaMoO_4$ (CPS), Al/$MgMoO_4$ (SCS), Al/$CaMoO_4$ (SCS), and Al/$SrMoO_4$ (SCS) nanothermites were made. SEM images showed that aluminum and CPS molybdates mixed evenly while SCS molybdates contained heavily agglomerated structures that could not be broken up by sonication. Aluminum particles had the tendency to cluster together in the nanothermites made with SCS molybdates; however, from the same sample, images also show certain area where aluminum particles spread out across the surface of the molybdates porous structures.

5.2 Future Work

Future work could include exploring a method to increase the production the CSP Protocol 3 while keeping the particle size nano scaled. Protocol 3, which used metal nitrate and sodium molybdate as the reagents and EG as the sole solvent, produced the cleanest and the most well-defined nano particles of all the synthetic methods. However, the yields of the Protocol 3 products are so low that it would take a significant amount of time and labour to produce enough material for characterization. Lastly, it would also be worth the effort modify current SCS method to produce molybdates with fewer impurities. Conditions that can be modified include the temperature of the reaction, different fuel-to-oxidizer ratio for the secondary fuel, and the different choices secondary fuel.

The most important work that can be done in continuation of this project is to further characterize nanothermites made with the molybdate compounds synthesized using CSP Protocol 3 and SCS. The characterization that can be done include: 1) the sensitivities of these nanothermites toward friction and ESD, 2) TGA/DSC measurements, and 3) the burn velocity of the nanothermites. TGA/DSC measurement provides insights, such as onset temperature and the activation energy of the nanothermite ignitions. The burn velocity is important because ultimately nanothermites are used as explosive, an insensitive nanothermite with a very slow burn rate is not much more useful than a very sensitive nanothermite. By combining these data with what has already been found through this project, a more complete picture can be painted to better understand these nanothermites.

6. Bibliography

Ahn, Ji Young, Kim Sang Beom, Kim Hi Hoon, Nam Su Jang, Kim Dae Hyun, Hyung Woo Lee, Jong Man Kim, and Soo Hyung Kim. 2015. "A Micro-Chip Initiator with Controlled Combustion Reactivity Realized by Integrating Al/CuO Nanothermite Composites on a Microhotplate Platform." *Journal of Micromechaniscs and Microengineering* 26 (November): 015002.

Anton Paar GmbH. 2021. "Autosorb iQ Gas Sorption System Operating Manual." Quantachrome Instrument.

Apperson, S., R. V. Shende, S. Subramanian, D. Tappmeyer, S. Gangopadhyay, Z. Chen, K. Gangopadhyay, P. Redner, S. Nicholich, and D. Kapoor. 2007. "Generation of Fast Propagating Combustion and Shock Waves with Copper Oxide/aluminum Nanothermite Composites." *Applied Physics Letters* 91 (24): 243109.

Asay, Blaine W., Steven F. Son, James R. Busse, and David M. Oschwald. 2004. "Ignition Characteristics of Metastable Intermolecular Composites." *Propellants, Explosives, Pyrotechnics* 29 (4): 216–19.

ASTM Standard D257, 2007. Standard test methods for DC resistance or conductance of insulating materials

Bach, Arnaud, Pierre Gibot, Loïc Vidal, Roger Gadiou, and Denis Spitzer. 2015. "Modulation of the Reactivity of a WO_3/Al Energetic Material with Graphitized Carbon Black as Additive." *Journal of Energetic Materials* 33 (4): 260–76.

Bardestani, Raoof, Gregory S. Patience, and Serge Kaliaguine. 2019. "Experimental Methods in Chemical Engineering: Specific Surface Area and Pore Size Distribution measurements—BET, BJH, and DFT." *The Canadian Journal of Chemical Engineering* 97 (11): 2781–91.

Besra, Laxmidhar, and Meilin Liu. 2007. "A Review on Fundamentals and Applications of Electrophoretic Deposition (EPD)." *Progress in Materials Science* 52 (1): 1–61.

Bhattacharjee, Sourav. 2016. "DLS and Zeta Potential - What They Are and What They Are Not?" *Journal of Controlled Release: Official Journal of the*

Controlled Release Society 235 (August): 337–51.

Bockmon, B. S., M. L. Pantoya, S. F. Son, B. W. Asay, and J. T. Mang. 2005. "Combustion Velocities and Propagation Mechanisms of Metastable Interstitial Composites." *Journal of Applied Physics* 98 (6): 064903.

Brown, Michael E., Steven J. Taylor, and Michael J. Tribelhorn. 1998. "Fuel—Oxidant Particle Contact in Binary Pyrotechnic Reactions." *Propellants, Explosives, Pyrotechnics*.

Calais, Théo, Aurélien Bancaud, Alain Estève, and Carole Rossi. 2018. "Correlation between DNA Self-Assembly Kinetics, Microstructure, and Thermal Properties of Tunable Highly Energetic Al–CuO Nanocomposites for Micropyrotechnic Applications." *ACS Applied Nano Materials* 1 (9): 4716–25.

Calais, Théo, David Bourrier, Aurélien Bancaud, Yves Chabal, Alain Estève, and Carole Rossi. 2017. "DNA Grafting and Arrangement on Oxide Surfaces for Self-Assembly of Al and CuO Nanoparticles." *Langmuir: The ACS Journal of Surfaces and Colloids* 33 (43): 12193–203.

Choodamani, C., G. P. Nagabhushana, B. Rudraswamy, and G. T. Chandrappa. 2014. "Thermal Effect on Magnetic Properties of Mg-Zn Ferrite Nanoparticles." *Materials Letters* 116 (February): 227–30.

Chowdhury, Snehaunshu, Kyle Sullivan, Nicholas Piekiel, Lei Zhou, and Michael R. Zachariah. 2010. "Diffusive vs Explosive Reaction at the Nanoscale." *The Journal of Physical Chemistry. C, Nanomaterials and Interfaces* 114 (20): 9191–95.

Churaman, W., L. Currano, and C. Becker. 2010. "Initiation and Reaction Tuning of Nanoporous Energetic Silicon." *The Journal of Physics and Chemistry of Solids* 71 (2): 69–74.

Clapsaddle, Brady J., Lihua Zhao, Alex E. Gash, Joe H. Satcher, Kenneth J. Shea, Michelle L. Pantoya, and Randall L. Simpson. 2003. "Synthesis and Characterization of Mixed Metal Oxide Nanocomposite Energetic Materials." *MRS Proceedings*.

Clément, D., J. Diener, E. Gross, N. Künzner, V. Yu Timoshenko, and D. Kovalev. 2005. "Highly Explosive Nanosilicon-Based Composite Materials." *Physica Status Solidi* 202 (8): 1357–64.

Cliff, Mattew, Fred Tepper, and Vladimir Lisetsky. 2001. “Ageing Characteristics of Alexr Nanosize Aluminium.” *37th Joint Propulsion Conference and Exhibit*. Joint Propulsion Conferences. American Institute of Aeronautics and Astronautics.

Collins, Eric S., Brandon R. Skelton, Michelle L. Pantoya, Fahmida Irin, Micah J. Green, and Michael A. Daniels. 2015. “Ignition Sensitivity and Electrical Conductivity of an Aluminum Fluoropolymer Reactive Material with Carbon Nanofillers.” *Combustion and Flame* 162 (4): 1417–21.

Comet, Marc, Vincent Pichot, Benny Siegert, Fabien Schnell, Fabrice Ciszek, and Denis Spitzer. 2010. “Phosphorus-Based Nanothermites: A New Generation of Energetic Materials.” *The Journal of Physics and Chemistry of Solids* 71 (2): 64–68.

Comet, Marc, Geoffrey Vidick, Fabien Schnell, Yves Suma, Bernard Baps, and Denis Spitzer. 2015. “Sulfates-Based Nanothermites: An Expanding Horizon for Metastable Interstitial Composites.” *Angewandte Chemie* 54 (15): 4458–62.

Cooper, Paul W., and Stanley R. Kurowski. 1996. *Introduction to the Technology of Explosives*. VCH Publishers.

Dombroski, David M. B., Anqi Wang, John Z. Wen, and Marco Alfano. 2022. “Joining and Welding with a Nanothermite and Exothermic Bonding Using Reactive Multi-Nanolayers – A Review.” *Journal of Manufacturing Processes* 75 (March): 280–300.

Deganello, Francesca, and Avesh Kumar Tyagi. 2018. “Solution Combustion Synthesis, Energy and Environment: Best Parameters for Better Materials.” *Progress in Crystal Growth and Characterization of Materials* 64 (2): 23–61.

Dreizin, Edward L. 2009. “Metal-Based Reactive Nanomaterials.” *Progress in Energy and Combustion Science*.

Dunlap, Michael, and J. E. Adaskaveg. 1997. “Introduction to the Scanning Electron Microscope. Theory, Practice, & Procedure.” Facility for Advance Instrumentation. UC Davis.

Elbasuney, M., M. Zakk, M. Radwan, and S. Mostafa. 2017. “Stabilized Super-Thermite Colloids: A New Generation of Advanced Highly Energetic

Materials.” *Applied Surface Science* 419 (October): 328–36.

Engel, Thomas, and Philip Reid. 2005. *Physical Chemistry*. Edited by Katie Conley and Lisa Leung. Benjamin Cummings

Fahd, Ahmed, Alex Baranovsky, Charles Dubois, Jamal Chaouki, and John Z. Wen. 2021. “Superior Performance of Quaternary NC/GO/Al/$KClO_4$ Nanothermite for High Speed Impulse Small-Scale Propulsion Applications.” *Combustion and Flame* 232 (111527): 111527.

Fahd, Ahmed, Charles Dubois, Jamal Chaouki, J. Z. Wen, and Ehab Youssef. 2021. “Synthesis and Characterization of Tertiary Nanothermite CNMs/Al/$KClO_4$ with Enhanced Combustion Characteristics.” *Propellants, Explosives, Pyrotechnics* 46 (6): 995–1005.

Fahd, Ahmed, Mahmoud Y. Zorainy, Charles Dubois, Daria C. Boffito, Jamal Chaouki, and John Z. Wen. 2021. “Combustion Characteristics of EMOFs/oxygenated Salts Novel Thermite for Green Energetic Applications.” *Thermochimica Acta* 704 (179019): 179019.

Fehlner, F. P., and N. F. Mott. 1970. “Low-Temperature Oxidation.” *Oxidation of Metals* 2 (1): 59–99.

Fisher, S., and M. Grubelich. 1998. “Theoretical Energy Release of Thermites, Intermetallics, and Combustible Metals.” 10.2172/658208. Sandia National Lab.

Gibot, Pierre, Arnaud Bach, Loic Vidal, Fabien Schnell, Roger Gadiou, and Denis Spitzer. 2017. “Safer and Performing Energetic Materials Based on Polyaniline-Doped Nanocomposites.” *Journal of Energetic Materials* 35 (2): 136–47.

Gibot, Pierre, Quentin Miesch, Arnaud Bach, Fabien Schnell, Roger Gadiou, and Denis Spitzer. 2019. “Mechanical Desensitization of an Al/WO_3 Nanothermite by Means of Carbonaceous Coatings Derived from Carbohydrates.” *Il Nuovo Cimento: C: Geophysics and Space Physics* 5 (3): 37.

Gibot, Pierre, Franck Oudot, Bastien Lallemand, Fabien Schnell, and Denis Spitzer. 2021. “Nanosized Niobium (V) and Tantalum (V) Oxide Ceramics as Competitive Oxidizers within Aluminium-Based Nanothermites.” *Energetic Materials Frontiers* 2 (3): 167–73.

Glavier, Ludovic, Andrea Nicollet, Fabien Jouot, Bernard Martin, Jeremy Barberon, Laurent Renaud, and Carole Rossi. 2017. “Nanothermite/RDX-Based Miniature Device for Impact Ignition of High Explosives.” *Propellants, Explosives, Pyrotechnics*.

Glavier, Ludovic, Guillaume Taton, Jean-Marie Ducéré, Vincent Baijot, Stéphane Pinon, Theo Calais, Alain Estève, Mehdi Djafari Rouhani, and Carole Rossi. 2015. “Nanoenergetics as Pressure Generator for Nontoxic Impact Primers: Comparison of Al/Bi_2O_3, Al/CuO, Al/MoO_3 Nanothermites and Al/PTFE.” *Combustion and Flame* 162 (5): 1813–20.

Gorobez, Jürgen, Björn Maack, and Niklas Nilius. 2021. “Growth of Self-passivating Oxide Layers on Aluminum—pressure and Temperature Dependence.” *Physica Status Solidi. B, Basic Research* 258 (5): 2000559.

Granier, John J., and Michelle L. Pantoya. 2004. “Laser Ignition of Nanocomposite Thermites.” *Combustion and Flame* 138 (4): 373–83.

Greason, William D. 2003. “Electrostatic Discharge Characteristics for the Human Body and Circuit Packs.” *Journal of Electrostatics* 59 (3-4): 285–300.

Gromov, A. A., Yu I. Strokova, and A. A. Ditts. 2010. “Passivation Films on Particles of Electroexplosion Aluminum Nanopowders: A Review.” *Russian Journal of Physical Chemistry B* 4 (1): 156–69.

Gu, Siyong, Mingli Qin, Houan Zhang, Jidong Ma, Haoyang Wu, and Xuanhui Qu. 2017. “Facile Solution Combustion Synthesis of MoO_2 Nanoparticles as Efficient Photocatalysts.” *CrystEngComm / RSC* 19 (43): 6516–26.

Harvey, Jean-Philippe, Nooshin Saadatkhah, Guillaume Dumont-Vandewinkel, Sarah L. G. Ackermann, and Gregory S. Patience. 2018. “Experimental Methods in Chemical Engineering: Differential Scanning Calorimetry-DSC.” *The Canadian Journal of Chemical Engineering* 96 (12): 2518–25.

Haynes, W.M. (ed.). *CRC Handbook of Chemistry and Physics. 95th Edition*. CRC Press LLC, Boca Raton: FL 2014-2015, p. 3-4

Hees, Jakob, Armin Kriele, and Oliver A. Williams. 2011. “Electrostatic Self-Assembly of Diamond Nanoparticles.” *Chemical Physics Letters* 509 (1): 12–15.

Henz, Brian J., Takumi Hawa, and Michael R. Zachariah. 2010. “On the Role of Built-in Electric Fields on the Ignition of Oxide Coated Nanoaluminum:

Ion Mobility versus Fickian Diffusion." *Journal of Applied Physics* 107 (2): 024901.

Higa, Kelvin T. 2007 "Energetic Nanocomposite Lead-Free Electric Primers." *Journal of Propulsion and Power* 23 (4): 722–27.

Hobosyan, Mkhitar A., and Karen S. Martirosyan. 2020. "Novel Nanoenergetic Materials: Emerging Trends and Applications." *IEEE Nanotechnology Magazine* 14 (1): 30–36.

Holder, Cameron F., and Raymond E. Schaak. 2019. "Tutorial on Powder X-Ray Diffraction for Characterizing Nanoscale Materials." *ACS Nano* 13 (7): 7359–65.

Ivanov, Yuri F., Mirswan N. Osmonoliev, Valentin S. Sedoi, Vladimir A. Arkhipov, Sergey S. Bondarchuk, Alexander B. Vorozhtsov, Alexander G. Korotkikh, and Valery T. Kuznetsov. 2003. "Productions of Ultra-Fine Powders and Their Use in High Energetic Compositions." *Propellants, Explosives, Pyrotechnics* 28 (6): 319–33.

Jacob, Rohit J., Dylan J. Kline, and Michael R. Zachariah. 2018. "High Speed 2-Dimensional Temperature Measurements of Nanothermite Composites: Probing Thermal vs. Gas Generation Effects." *Journal of Applied Physics* 123 (11): 115902.

Kabra, Shruti, Swaroop Gharde, Prakash M. Gore, Sunil Jain, Vrushali Khire, and Balasubramanian Kandasubramainjan. n.d. "Recent Trend in Nanothermite: Fabrication, Characteristics and Applications." Accessed February 3, 2022.

Kelly, David, Pascal Beland, Patrick Brousseau, and Catalin Florin Petre. 2017a. "Electrostatic Discharge Sensitivity and Resistivity Measurements of Al Nanothermites and Their Fuel and Oxidant Precursors." *Central European Journal of Energetic Materials* 14 (1): 105–19.

Kelly, David G., Pascal Beland, Patrick Brousseau, and Catalin-Florin Petre. 2017b. "Formation of Additive-Containing Nanothermites and Modifications to Their Friction Sensitivity." *Journal of Energetic Materials* 35 (3): 331–45.

Khasainov, Boris, Marc Comet, Bernard Veyssiere, and Denis Spitzer. 2017. "Comparison of Performance of Fast-Reacting Nanothermites and Primary Explosives." *Propellants, Explosives, Pyrotechnics* 42 (7): 754–72.

Kruk, Michal, and Mietek Jaroniec. 2001. “Gas Adsorption Characterization of Ordered Organic−Inorganic Nanocomposite Materials.” *Chemistry of Materials: A Publication of the American Chemical Society* 13 (10): 3169–83.

Kusuma, M., and G. T. Chandrappa. 2019. “Effect of Calcination Temperature on Characteristic Properties of CaMoO4 Nanoparticles.” *Journal of Science: Advanced Materials and Devices* 4 (1): 150–57.

Kwok, Queenie S. M., Robert C. Fouchard, Anne-Marie Turcotte, Phillip D. Lightfoot, Richard Bowes, and David E. G. Jones. 2002. “Characterization of Aluminum Nanopowder Compositions.” *Propellants, Explosives, Pyrotechnics* 27 (4): 229–40.

Lajaunie, L., F. Boucher, R. Dessapt, and P. Moreau. 2013. “Strong Anisotropic Influence of Local-Field Effects on the Dielectric Response Of α-MoO_3.” *Physical Review B*.

Lavina, Barbara, Przemyslaw Dera, and Robert T. Downs. 2014. “Modern X-Ray Diffraction Methods in Mineralogy and Geosciences.” *Reviews in Mineralogy and Geochemistry* 78 (1): 1–31.

Levitas, Valery I., Blaine W. Asay, Steven F. Son, and Michelle Pantoya. 2006. “Melt Dispersion Mechanism for Fast Reaction of Nanothermites.” *Applied Physics Letters*.

Levitas, Valery I. Asay, Blaine W, Pantoya, Michelle. 2007. “Mechanochemical Mechanism for Fast Reaction of Metastable Intermolecular Composites Based on Dispersion of Liquid Metal.” *Journal of Applied Physics* 101 (8): 083524.

Levitas, Valery I., Michelle L. Pantoya, and Steven Dean. 2014. “Melt Dispersion Mechanism for Fast Reaction of Aluminum Nano- and Micron-Scale Particles: Flame Propagation and SEM Studies.” *Combustion and Flame*.

Levitas, Valery I., Michelle L. Pantoya, and Kyle W. Watson. 2008. “Melt-Dispersion Mechanism for Fast Reaction of Aluminum Particles: Extension for Micron Scale Particles and Fluorination.” *Applied Physics Letters* 92 (20): 201917.

Li, Rui, Jun Wang, Jin Peng Shen, Cheng Hua, and Guang Cheng Yang. 2013. "Preparation and Characterization of Insensitive HMX/graphene Oxide Composites." *Propellants, Explosives, Pyrotechnics* 38 (6): 798–804.

Lunardi, Claure N., Anderson J. Gomes, Fellipy S. Rocha, Jacopo De Tommaso, and Gregory S. Patience. 2021. "Experimental Methods in Chemical Engineering: Zeta Potential." *The Canadian Journal of Chemical Engineering* 99 (3): 627–39.

Lowry, Gregory V., Reghan J. Hill, Stacey Harper, Alan F. Rawle, Christine Ogilvie Hendren, Fred Klaessig, Ulf Nobbmann, Philip Sayre, and John Rumble. 2016. "Guidance to Improve the Scientific Value of Zeta-Potential Measurements in nanoEHS." *Environmental Science: Nano* 3 (5): 953–65.

Malchi, J. Y., R. A. Yetter, T. J. Foley, and S. F. Son. 2008. "The Effect of Added Al_2O_3on the Propagation Behavior of an Al/CuO Nanoscale Thermite." *Combustion Science and Technology* 180 (7): 1278–94.

Malvern Panalytical. 2020. "Zetasizer Advance Series: Zeta Potential Measurements Data Interpretation."

Mantina, Manjeera, Adam C. Chamberlin, Rosendo Valero, Christopher J. Cramer, and Donald G. Truhlar. 2009. "Consistent van Der Waals Radii for the Whole Main Group." *The Journal of Physical Chemistry A*.

Mao, Yaofeng, Lin Zhong, Xu Zhou, Dawei Zheng, Xingquan Zhang, Tao Duan, Fude Nie, Bing Gao, and Dunju Wang. 2019. "3D Printing of Micro-architected Al/CuO-based Nanothermite for Enhanced Combustion Performance." *Advanced Engineering Materials* 21 (12): 1900825.

Martirosyan, Karen S. 2011. "Nanoenergetic Gas-Generators: Principles and Applications." *Journal of Materials Chemistry*.

Martirosyan, Karen S., Leizheng Wang, Arol Vicent, and Dan Luss. 2009. "Nanoenergetic Gas-Generators: Design and Performance." *Propellants, Explosives, Pyrotechnics* 34 (6): 532–38.

Martirosyan, K. S., L. Wang, A. Vicent, and D. Luss. 2009. "Synthesis and Performance of Bismuth Trioxide Nanoparticles for High Energy Gas Generator Use." *Nanotechnology*.

Mathewson, A. G., and H. P. Myers. 1971. “Absolute Values of the Optical Constants of Some Pure Metals.” *Physica Scripta*.

Mehendale, Bhushan, Rajesh Shende, Senthil Subramanian, Shubhra Gangopadhyay, Paul Redner, Deepak Kapoor, and Steven Nicolich. 2006. “Nanoenergetic Composite of Mesoporous Iron Oxide and Aluminum Nanoparticles.” *Journal of Energetic Materials*.

Memon, Nasir K., Andrew W. McBain, and Steven F. Son. 2016. “Graphene Oxide/Ammonium Perchlorate Composite Material for Use in Solid Propellants.” *Journal of Propulsion and Power* 32 (3): 682–86.

Mench, M. M., K. K. Kuo, C. L. Yeh, and Y. C. Lu. 1998. “Comparison of Thermal Behavior of Regular and Ultra-Fine Aluminum Powders (Alex) Made from Plasma Explosion Process.” *Combustion Science and Technology* 135 (1-6): 269–92.

Miao, H., Xie, Y., Ni, Z., Zeng, X., Bao, H., Wu, X., Liu, L., Li, X.,and Wang, L.. 2021. “Electrophoretic Deposition and Characterization of Highly Exothermic Al/CuO Nanothermites.” *International Journal of Electrochemical Science*, 150974.

Monogarov, K. A., D. B. Meerov, Yu V. Frolov, and A. N. Pivkina. 2019. “Combustion Features of Nanothermites in Pyrotechnic Heaters.” *Russian Journal of Physical Chemistry B* 13 (4): 610–14.

Naderi, Majid. 2015. “Chapter Fourteen - Surface Area Brunauer–Emmett–Teller (BET).” In *Progress in Filtration and Separation*, edited by Steve Tarleton, 585–608. Oxford: Academic Press.

NATO Standardization Agency. 2009. “Standardization Agreement STANAG 4488.” NATO Standardization Agency.

Nie, Hongqi, Li Ping Tan, Sreekumar Pisharath, and Huey Hoon Hng. 2021. “Nanothermite Composites with a Novel Cast Curable Fluoropolymer.” *Chemical Engineering Journal* 414 (128786): 128786.

Oliveira, F., M. Oliveira, L. Gracia, R. Tranquilin, C. Paskocimas, F. Motta, E. Longo, J. Andres, and M. Bomio. 2018. “Experimental and Theoretical Study to Explain the Morphology of $CaMoO_4$ Crystals.” *The Journal of Physics and Chemistry of Solids* 114 (March): 141–52.

Osborne, Dustin T., and Michelle L. Pantoya. 2007. “Effect of Al Particle Size on the Thermal Degradation of Al/Teflon Mixtures.” *Combustion Science and Technology* 179 (8): 1467–80.

Pal, Akhilesh Kumar, and Vimal Katiyar. 2017. “Theoretical and Analyzed Data Related to Thermal Degradation Kinetics of Poly (L-Lactic Acid)/chitosan-Grafted-Oligo L-Lactic Acid (PLA/CH-G-OLLA) Bionanocomposite Films.” *Data in Brief* 10 (February): 304–11.

Pantoya, M., and J. Granier. 2005. “Combustion Behavior of Highly Energetic Thermites: Nano versus Micron Composites.” *Propellants, Explosives, Pyrotechnics*.

Pantoya, Michelle, and Keerti Kappagantula. 2016. “Fast-Reacting Nanocomposite Energetic Materials.” In *Energetic Nanomaterials*, 21–45. Elsevier.

Pantoya, Michelle L., Valery I. Levitas, John J. Granier, and Jack B. Henderson. 2009. “Effect of Bulk Density on Reaction Propagation in Nanothermites and Micron Thermites.” *Journal of Propulsion and Power* 25 (2): 465–70.

Petrantoni, M., C. Rossi, V. Conédéra, D. Bourrier, P. Alphonse, and C. Tenailleau. 2010. “Synthesis Process of Nanowired Al/CuO Thermite.” *Journal of Physics and Chemistry of Solids*.

Petre, Catalin Florin, David G. Kelly, Daniel Chamberland, and Tommy Ringuette. 2019. “Thermochemical Properties and Laser-Ignition Performance of Al/$CuMoO_4$, Al/CuO/MoO_3, Al/CuO and Al/MoO_3 Nanothermites.” *Int. J. Energ. Mater. Chem. Propuls.* 17 (4): 303–19.

Plantier, Keith B., Michelle L. Pantoya, and Alexander E. Gash. 2005. “Combustion Wave Speeds of Nanocomposite Al/Fe_2O_3: The Effects of Fe_2O_3 Particle Synthesis Technique.” *Combustion and Flame*.

Poper, Kade H., Eric S. Collins, Michelle L. Pantoya, and Michael A. Daniels. 2014. “Controlling the Electrostatic Discharge Ignition Sensitivity of Composite Energetic Materials Using Carbon Nanotube Additives.” *Journal of Electrostatics* 72 (5): 428–32.

Pramanik, N., A. Tarafdar, and P. Pramanik. 2007. “Capping Agent-Assisted Synthesis of Nanosized Hydroxyapatite: Comparative Studies of Their Physicochemical Properties.” *Journal of Materials Processing Technology* 184 (1-3): 131–38.

Prentice, Daniel, Michelle L. Pantoya, and Alexander E. Gash. 2006. “Combustion Wave Speeds of Sol−Gel-Synthesized Tungsten Trioxide and Nano-Aluminum: The Effect of Impurities on Flame Propagation.” *Energy & Fuels: An American Chemical Society Journal* 20 (6): 2370–76.

Puchades, Ivan, Lynn F. Fuller, Sergey E. Lyshevski, Mkhitar Hobosyan, Liu Ting, and Karen S. Martirosyan. 2017. “MEMS and 3D-Printing Microthrusters Technology Integrated with Hydroxide-Based Nanoenergetic Propellants.” In *2017 IEEE 37th International Conference on Electronics and Nanotechnology (ELNANO)*, 67–70.

Puszynski, Jan A. 2004. “Reactivity of Nanosize Aluminum with Metal Oxides and Water Vapor.” *MRS Online Proceedings Library* 800 (1): 221–30.

Puszynski, Jan A. 2009. “Processing and Characterization of Aluminum-Based Nanothermites.” *Journal of Thermal Analysis and Calorimetry* 96 (3): 677–85.

Qin, Lijun, Ting Gong, Haixia Hao, Keyong Wang, and Hao Feng. 2013. “Core–shell-Structured Nanothermites Synthesized by Atomic Layer Deposition.” *Journal of Nanoparticle Research: An Interdisciplinary Forum for Nanoscale Science and Technology* 15 (12): 1–15.

Qin, Lijun, Ning Yan, Jianguo Li, Haixia Hao, Fengqi Zhao, and Hao Feng. 2017. “Enhanced Energy Performance from Core–shell Structured Al@Fe2O3 Nanothermite Fabricated by Atomic Layer Deposition.” *RSC Advances* 7 (12): 7188–97.

Radel, Stanley R., and Marjorie H. Navidi. 1994. *Chemistry: 2nd Edition*. West Publishing Company.

Ramachandran, Krithikadevi, Siva Chidambaram, Balraj Baskaran, Arulmozhi Muthukumarasamy, and John Berchmans Lawrence. 2017. “Investigations on Structural, Optical and Magnetic Properties of Solution-Combustion-Synthesized Nanocrystalline Iron Molybdate.” *Bulletin of Materials Science* 40 (1): 87–92.

Rehwoldt, Miles C., Yong Yang, Haiyang Wang, Scott Holdren, and Michael R. Zachariah. 2018. “Ignition of Nanoscale Titanium/Potassium Perchlorate Pyrotechnic Powder: Reaction Mechanism Study.” *Journal of Physical Chemistry C* 122 (20): 10792–800.

Rumble, John R., ed. 2021. *CRC Handbook of Chemistry and Physics 102nd Edition*. Boca Raton, FL: CRC Press/Taylor & Francis.

Ryu, Jeong Ho, Jong-Won Yoon, Chang Sung Lim, Won-Chun Oh, and Kwang Bo Shim. 2005. "Microwave-Assisted Synthesis of $CaMoO_4$ Nano-Powders by a Citrate Complex Method and Its Photoluminescence Property." *Journal of Alloys and Compounds* 390 (1-2): 245–49.

Saadatkhah, Nooshin, Adrián Carillo Garcia, Sarah Ackermann, Philippe Leclerc, Mohammad Latifi, Said Samih, Gregory S. Patience, and Jamal Chaouki. 2020. "Experimental Methods in Chemical Engineering: Thermogravimetric analysis—TGA." *The Canadian Journal of Chemical Engineering* 98 (1): 34–43.

Saceleanu, Florin, Mahmoud Idir, Nabiha Chaumeix, and John Z. Wen. 2018. "Combustion Characteristics of Physically Mixed 40 Nm Aluminum/Copper Oxide Nanothermites Using Laser Ignition." *Frontiers in Chemistry* 6 (October): 465.

Sanders, V. Eric, Blaine W. Asay, Timothy J. Foley, Bryce C. Tappan, Adam N. Pacheco, and Steven F. Son. 2007. "Reaction Propagation of Four Nanoscale Energetic Composites (Al/MoO_3, Al/WO_3, Al/CuO, and $B1_2O_3$)." *Journal of Propulsion and Power* 23 (4): 707–14.

Schefflan, R., S. Kovenklioglu, D. Kalyon, M. Mezger, and M. Leng. 2006. "Formation of Aluminum Nanoparticles upon Condensation from Vapor Phase for Energetic Applications." *Journal of Energetic Materials* 24 (2): 141–56.

Schoenitz, Mirko, Swati Umbrajkar, and Edward Dreizin. 2006. "Kinetic Analysis of Thermite Reactions in Al-MoO3 Nanocomposites." *42nd AIAA/ASME/SAE/ASEE Joint Propulsion Conference & Exhibit*.

Seevakan, K., A. Manikandan, P. Devendran, A. Shameem, and T. Alagesan. 2018. "Microwave Combustion Synthesis, Magneto-Optical and Electrochemical Properties of $NiMoO_4$ Nanoparticles for Supercapacitor Application." *Ceramics International* 44 (12): 13879–87.

Sen, Angana, and Panchanan Pramanik. 2001. "Low-Temperature Synthesis of Nano-Sized Metal Molybdate Powders." *Materials Letters* 50 (5-6): 287–94.

Senthilkumar, Baskar, Kalimuthu Vijaya Sankar, Ramakrishnan Kalai Selvan,

Meyrick Danielle, and Minakshi Manickam. 2013. “Nano α-$NiMoO_4$ as a New Electrode for Electrochemical Supercapacitors.” *RSC Advances* 3 (2): 352–57.

Séverac, Fabrice, Pierre Alphonse, Alain Estève, Aurélien Bancaud, and Carole Rossi. 2012. “High-Energy Al/CuO Nanocomposites Obtained by DNA-Directed Assembly.” *Advanced Functional Materials* 22 (2): 323–29.

Shang, Zhijie, Shaoming Huang, Xiangju Xu, and Jiangyin Chen. 2009. “Mo/MgO from Avalanche-like Reduction of $MgMoO_4$ for High Efficient Growth of Multi-Walled Carbon Nanotubes by Chemical Vapor Deposition.” *Materials Chemistry and Physics* 114 (1): 173–78.

Shende, Rajesh, Senthil Subramanian, Shameem Hasan, Steven Apperson, Rajagopalan Thiruvengadathan, Keshab Gangopadhyay, Shubhra Gangopadhyay, et al. 2008. “Nanoenergetic Composites of CuO Nanorods, Nanowires, and Al-Nanoparticles.” *Propellants, Explosives, Pyrotechnics* 33 (2): 122–30.

Sherikar, Baburao N., Balaram Sahoo, and Arun M. Umarji. 2020. “Effect of Fuel and Fuel to Oxidizer Ratio in Solution Combustion Synthesis of Nanoceramic Powders: MgO, CaO and ZnO.” *Solid State Sciences* 109 (November): 106426.

Shen, Lianhua, Guoping Li, Yunjun Luo, Kun Gao, and Zhen Ge. 2014. “Preparation and Characterization of Al/B/Fe2O3 Nanothermites.” *Science China. Chemistry* 57 (6): 797–802.

Shi, Kaiwen, Xiaode Guo, Ling Chen, Shanshan Huang, Linlin Zhao, Jie Ji, and Xiang Zhou. 2021. “Alcohol-Thermal Synthesis of Approximately Core-Shell Structured Al@CuO Nanothermite with Improved Heat-Release and Combustion Characteristics.” *Combustion and Flame* 228 (June): 331–39.

Shimizu, Seishi, and Nobuyuki Matubayasi. 2022. “Surface Area Estimation: Replacing the Brunauer-Emmett-Teller Model with the Statistical Thermodynamic Fluctuation Theory.” Langmuir: The ACS Journal of Surfaces and Colloids, June.

Siegert, Benny, Marc Comet, Olivier Muller, Geneviève Pourroy, and Denis Spitzer. 2010. “Reduced-Sensitivity Nanothermites Containing Manganese Oxide Filled Carbon Nanofibers.” *The Journal of Physical Chemistry C.*

Solanki, Jignasa N., and Zagabathuni Venkata Panchakshari Murthy. 2011. "Controlled Size Silver Nanoparticles Synthesis with Water-in-Oil Microemulsion Method: A Topical Review." *Industrial & Engineering Chemistry Research* 50 (22): 12311–23

Song, J., T. Guo, M. Yao, J. Chen, W. Ding, F. Bei, X. Zhang, Q. Yin, J. Huang, and C. Li. 2021. "Thermal and Combustion Behavior of Al-MnO_2 Nanothermite with Poly(vinylidene Fluoride -Co- Hexafluoropropylene) Energetic Binder." *Defence Technology* 17 (4): 1289–95.

Song, J., T. Guo, M. Yao, J. Chen, W. Ding, X. Zhang, F. Bei, and J. Huang. 2020. "Hindering Effect of Graphene Oxide on Reaction Performance of Al/MnO2 Nanothermite System." *Colloid and Interface Science Communications* 37 (July): 100271.

Stacy, S. C., R. A. Massad, and M. L. Pantoya. 2013. "Pre-Ignition Laser Ablation of Nanocomposite Energetic Materials." *Journal of Applied Physics* 113 (21): 213107.

Starchuk, Angela J. H. 2019. "The Effect of Settling on Nanothermite Sensitivity." Edited by Fiona Kelly. Master of Engineering in Advanced Ammunition Engineering, Royal Military College of Canada.

Starink, M. J. 2004. "Analysis of Aluminium Based Alloys by Calorimetry: Quantitative Analysis of Reactions and Reaction Kinetics." *International Materials Reviews* 49 (3-4): 191–226.

Steelman, Ryan, Billy Clark, Michelle L. Pantoya, Ronald J. Heaps, and Michael A. Daniels. 2015. "Desensitizing Nano Powders to Electrostatic Discharge Ignition." *Journal of Electrostatics* 76 (August): 102–7.

Sullivan, K. T., N. W. Piekiel, S. Chowdhury, C. Wu, M. R. Zachariah, and C. E. Johnson. 2010. "Ignition and Combustion Characteristics of Nanoscale Al/AgIO3: A Potential Energetic Biocidal System." *Combustion Science and Technology* 183 (3): 285–302.

Sun, Chang Q., Y. Wang, B. K. Tay, S. Li, H. Huang, and Y. B. Zhang. 2002. "Correlation between the Melting Point of a Nanosolid and the Cohesive Energy of a Surface Atom." *The Journal of Physical Chemistry. B* 106 (41): 10701–5.

Sun, Juan, Michelle L. Pantoya, and Sindee L. Simon. 2006. "Dependence of Size

and Size Distribution on Reactivity of Aluminum Nanoparticles in Reactions with Oxygen and MoO3." *Thermochimica Acta*.

Sun, J., and S. L. Simon. 2007. "The Melting Behavior of Aluminum Nanoparticles." *Thermochimica Acta* 463 (1): 32–40.

Sun, Y., J. Ma, J. Fang, Z. Song, C. Gao, and Z. Liu. 2010. "Ethylene Glycol-Assisted Electrochemical Synthesis of CaMoO4 Crystallites with Different Morphology and Their Luminescent Properties." *Solid State Sciences* 12 (7): 1283–86.

Sundaram, D. S., V. Yang, and V. E. Zarko. 2015. "Combustion of Nano Aluminum Particles (Review)." *Combustion, Explosion, and Shock Waves* 51 (2): 173–96.

Tai, Yu, Jianbing Xu, Fei Wang, Ji Dai, Wei Zhang, Yinghua Ye, and Ruiqi Shen. 2018. "Experimental and Modeling Investigation on the Self-Propagating Combustion Behavior of Al-MoO_3 Reactive Multilayer Films." *Journal of Applied Physics* 123 (23): 235302.

Talawar, M. B., A. P. Agrawal, M. Anniyappan, D. S. Wani, M. K. Bansode, and G. M. Gore. 2006. "Primary Explosives: Electrostatic Discharge Initiation, Additive Effect and Its Relation to Thermal and Explosive Characteristics." *Journal of Hazardous Materials* 137 (2): 1074–78.

Thiruvengadathan, Rajagopalan, Stephen W. Chung, Sagnik Basuray, Balamurugan Balasubramanian, Clay S. Staley, Keshab Gangopadhyay, and Shubhra Gangopadhyay. 2014. "A Versatile Self-Assembly Approach toward High Performance Nanoenergetic Composite Using Functionalized Graphene." *Langmuir: The ACS Journal of Surfaces and Colloids* 30 (22): 6556–64.

Thommes, Matthias, Katsumi Kaneko, Alexander V. Neimark, James P. Olivier, Francisco Rodriquez-Reinoso, Jean Rouquerol, and Kenneth S. W. Sing. 2015. "Physisorption of Gases, with Special Reference to the Evaluation of Surface Area and Pore Size Distribution (IUPAC Technical Report)." *Pure and Applied Chemistry* 87 (9-10): 1052–69.

Thongtem, Titipun, Sukjit Kungwankunakorn, Budsabong Kuntalue, Anukorn Phuruangrat, and Somchai Thongtem. 2010. "Luminescence and Absorbance of Highly Crystalline $CaMoO_4$, $SrMoO_4$, $CaWO_4$ and $SrWO_4$

Nanoparticles Synthesized by Co-Precipitation Method at Room Temperature." *Journal of Alloys and Compounds* 506 (1): 475–81.

Tro, Nivaldo J. 2010. *Principles of Chemistry A Molecular Approach*. Edited by Nicole Folchetti, Andrew Filfillan, Hart Jennifer, and Kristen Wallerius. Pearson Education, Inc.

Tytko, K.-H., W.-D. Fleischmann, D. Gras, E. Warkentin, K.-H. Tytko, W.-D. Fleischmann, D. Gras, E. Warkentin, H. Katscher and F. Schröder.1985. *Gmelin Handbook of Inorganic Chemistry: Molybdate Hydrates with Subgroup 2 Metals*. Springer-Verlag Berlin Heidelberg GmbH

United Nations. 2019. *Manual of Tests and Criteria: 7th Revised Edition*. United Nations.

U.S. Coast Guard. 1999. *Chemical Hazard Response Information System (CHRIS) - Hazardous Chemical Data. Commandant Instruction 16465.12C*. Washin gton, D.C.: U.S. Government Printing Office.

Varma, Arvind, Alexander S. Mukasyan, Alexander S. Rogachev, and Khachatur V. Manukyan. 2016. "Solution Combustion Synthesis of Nanoscale Materials." *Chemical Reviews* 116 (23): 14493–586.

Vukasovich, M. S., and J. P. G. Farr. 1986. "Molybdate in Corrosion Inhibition – A Review." *Polyhedron* 5 (1/2): 551–59.

Vyawahare, Pradeep, Hla Tun, Mark W. Vaughn, and Chau-Chyun Chen. 2022. "From Langmuir Isotherm to Brunauer–Emmett–Teller Isotherm." *AIChE Journal. American Institute of Chemical Engineers* 68 (3).

Walter, Kevin C., David R. Pesiri, and Dennis E. Wilson. 2007. "Manufacturing and Performance of Nanometric Al/MoO3 Energetic Materials." *Journal of Propulsion and Power*.

Wang, Haiyang, Guoqiang Jian, Garth C. Egan, and Michael R. Zachariah. 2014. "Assembly and Reactive Properties of Al/CuO Based Nanothermite Microparticles." *Combustion and Flame* 161 (8): 2203–8.

Wang, L. L., Z. A. Munir, and Y. M. Maximov. 1993. "Thermite Reactions: Their Utilization in the Synthesis and Processing of Materials." *Journal of Materials Science*.

Wang, L., D. Luss, and K. S. Martirosyan. 2011. “The Behavior of Nanothermite Reaction Based on Bi_2O_3/Al.” *Journal of Applied Physics*.

Wang, Ning, Yubing Hu, Xiang Ke, Lei Xiao, Xiang Zhou, Shisi Peng, Gazi Hao, and Wei Jiang. 2020. “Enhanced-Absorption Template Method for Preparation of Double-Shell NiO Hollow Nanospheres with Controllable Particle Size for Nanothermite Application.” *Chemical Engineering Journal* 379 (122330): 122330.

Wang, Qihui, Shengbo Yang, Hebin Bao, Qianyu Wang, Xueming Li, and Wenjing Yang. 2019. “Self–assembled Core–shell Structured Si@CuO Energetic Materials for Enhanced Exothermic Performance.” *Vacuum* 169 (108881): 108881.

Wang, Yueting, Ji Dai, Jianbing Xu, Yun Shen, Cheng-Ai Wang, Yinghua Ye, and Ruiqi Shen. 2021. “Experimental and Numerical Investigations of the Effect of Charge Density and Scale on the Heat Transfer Behavior of Al/CuO Nano-Thermite.” *Vacuum* 184 (February): 109878.

Wang, Yue-Ting, Xiao-Ting Zhang, Jian-Bing Xu, Shen Yun, Cheng-Ai Wang, Fu-Wei Li, Ze-Hua Zhang, Jian Chen, Ying-Hua Ye, and Rui-Qi Shen. 2021. “Fabrication and Characterization of Al–CuO Nanocomposites Prepared by Sol-Gel Method.” *Defence Technology* 17 (4): 1307–12.

Weir, Chelsea, Michelle L. Pantoya, and Michael A. Daniels. 2013. “The Role of Aluminum Particle Size in Electrostatic Ignition Sensitivity of Composite Energetic Materials.” *Combustion and Flame.*

Weir, Chelsea, Michelle L. Pantoya, Gautham Ramachandran, Tim Dallas, Daniel Prentice, and Michael Daniels. 2013. “Electrostatic Discharge Sensitivity and Electrical Conductivity of Composite Energetic Materials.” *Journal of Electrostatics* 71 (1): 77–83.

Weiser, Volker, Evelin Roth, Angelika Raab, Maria del Mar Juez-Lorenzo, Stefan Kelzenberg, and Norbert Eisenreich. 2010. “Thermite Type Reactions of Different Metals with Iron-Oxide and the Influence of Pressure.” *Propellants, Explosives, Pyrotechnics* 35 (3): 240–47.

Weismiller, M. R., J. Y. Malchi, R. A. Yetter, and T. J. Foley. 2009. “Dependence of Flame Propagation on Pressure and Pressurizing Gas for an Al/CuO Nanoscale Thermite.” *Proceedings of the Combustion Institute* 32 (2): 1895–1903.

Winston, Paul W., and Donald H. Bates. 1960. “Saturated Solutions for the Control of Humidity in Biological Research.” *Ecology*.

Xiang, Yubin, Jimei Song, Gang Hu, and Ya Liu. 2015. “Synthesis of $CaMoO_4$ Hierarchical Structures via a Simple Slow-Release Co-Precipitation Method.” *Applied Surface Science* 349 (September): 374–79.

Xu, Jianbing, Yuxuan Zhou, Yun Shen, Cheng-Ai Wang, Yueting Wang, Yinghua Ye, and Ruiqi Shen. 2022. “Characteristics of Micro Energetic Semiconductor Bridge Initiator by Depositing Al/MoO_3 Reactive Multilayered Films on Micro Bridge with Different Bridge Size.” *Sensors and Actuators. A, Physical* 336 (April): 113406.

Yan, Ning, Lijun Qin, Haixia Hao, Longfei Hui, Fengqi Zhao, and Hao Feng. 2017. “Iron Oxide/aluminum/graphene Energetic Nanocomposites Synthesized by Atomic Layer Deposition: Enhanced Energy Release and Reduced Electrostatic Ignition Hazard.” *Applied Surface Science* 408 (June): 51–59.

Yarrington, Cole D., Steven F. Son, Timothy J. Foley, Stephen J. Obrey, and Adam N. Pacheco. 2011. “Nano Aluminum Energetics: The Effect of Synthesis Method on Morphology and Combustion Performance.” *Propellants, Explosives, Pyrotechnics* 36 (6): 551–57.

Yen, Ng Hsiao, and Lee Yiew Wang. 2012. “Reactive Metals in Explosives.” *Propellants, Explosives, Pyrotechnics* 37 (2): 143–55.

Zhang, Kaili, Carole Rossi, G. A. Ardila Rodriguez, Christophe Tenailleau, and Pierre Alphonse. 2007a. “Development of a Nano-Al/CuO Based Energetic Material on Silicon Substrate.” *Applied Physics Letters*.

Zhang, Lifeng, Wenjie He, Kechao Shen, Yi Liu, and Shouwu Guo. 2018. “Controllable Synthesis of Hierarchical MgMoO4 Nanosheet-Arrays and Nano-Flowers Assembled with Mesoporous Ultrathin Nanosheets.” *The Journal of Physics and Chemistry of Solids* 115 (April): 215–20.

Zhang, Wei, Jiajia Yin, Fanqi Min, Lili Jia, Daoming Zhang, Quansheng Zhang, and Jingying Xie. 2017. “Preparation and Photoluminescence Properties of $MMoO_4$ (M = Cu, Ni, Zn) Nano-Particles Synthesized via Electrolysis.” *Journal of Molecular Structure* 1127 (January): 777–83.

Zhang, Zhenyu, Wenyue Li, Tsz-Wai Ng, Wenpei Kang, Chun-Sing Lee, and

Wenjun Zhang. 2015. “Iron (II) Molybdate ($FeMoO_{4)}$ Nanorods as a High-Performance Anode for Lithium Ion Batteries: Structural and Chemical Evolution upon Cycling.” *Journal of Materials Chemistry. A, Materials for Energy and Sustainability* 3 (41): 20527–34.

Zhu, Yuhua, Xueming Li, Daixiong Zhang, Hebin Bao, Yuanjie Shu, Xiaogang Guo, and Yanjun Yin. 2016. “Tuning the Surface Charges of MoO3 by Adsorption of Polyethylenimine to Realize the Electrophoretic Deposition of High-Exothermic Al/MoO3 Nanoenergetic Films.” *Materials & Design* 109 (November): 652–58.

Zou, H., S. Chen, Z. Zhao, and W. Lin. 2013. “Hydrogen Production by Hydrolysis of Aluminum.” *Journal of Alloys and Compounds* 578 (November): 380–84.

7. Appendix A – XRD Patterns

$MgMoO_4$

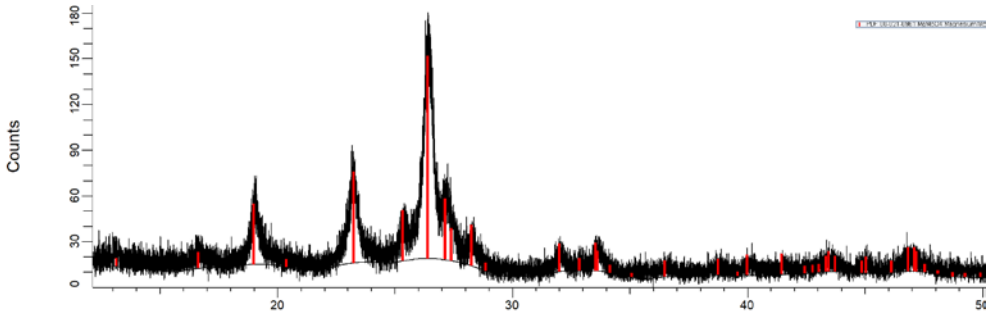

Figure 7.54 XRD pattern of $MgMoO_4$ synthesized using SCS.

$CaMoO_4$

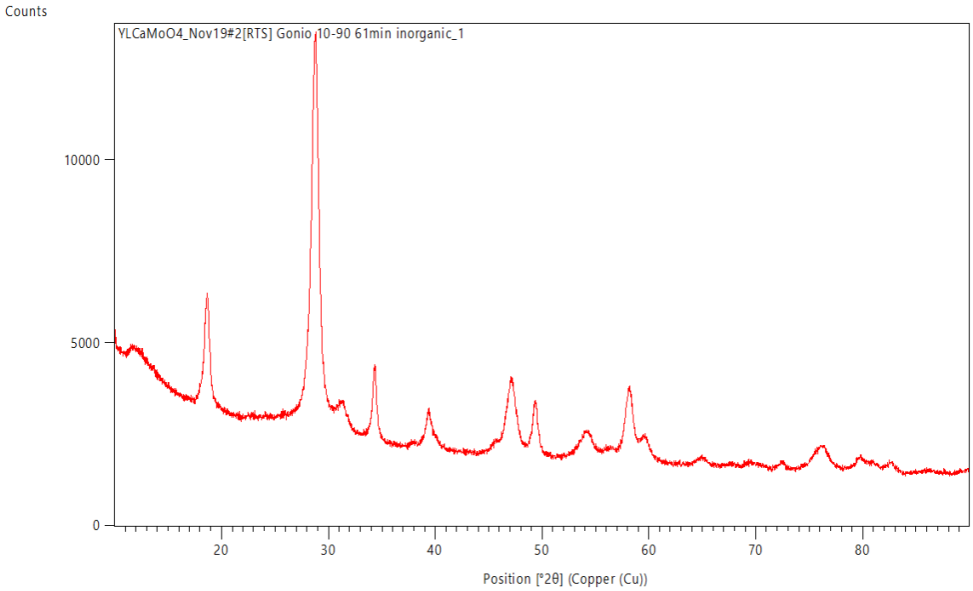

Figure 7.55 XRD pattern of $CaMoO_4$ synthesized using CPS Protocol 1.

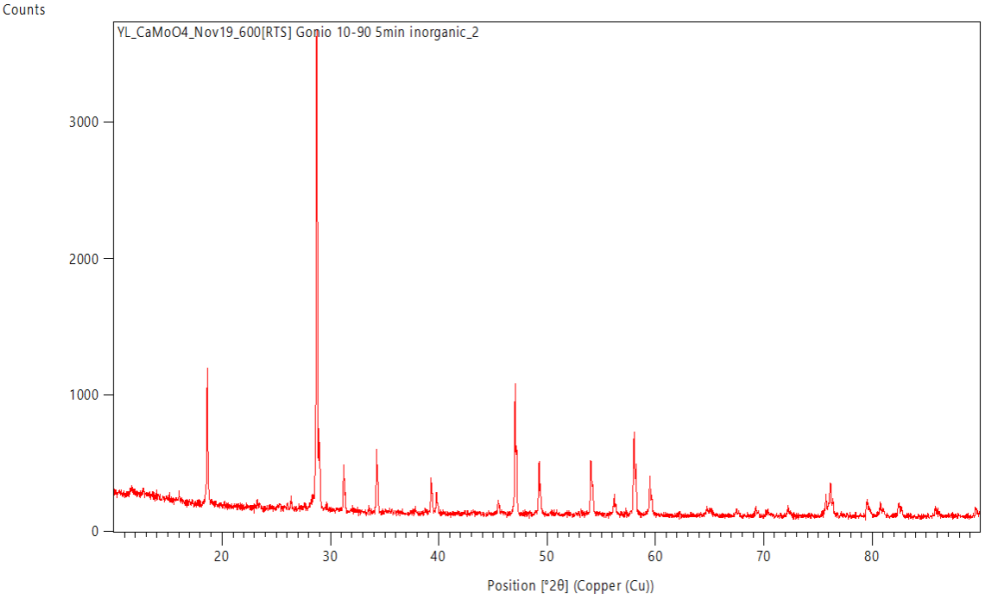

Figure 7.56 XRD pattern of $CaMoO_4$ synthesized using CPS Protocol 1, after calcination at 600ºC.

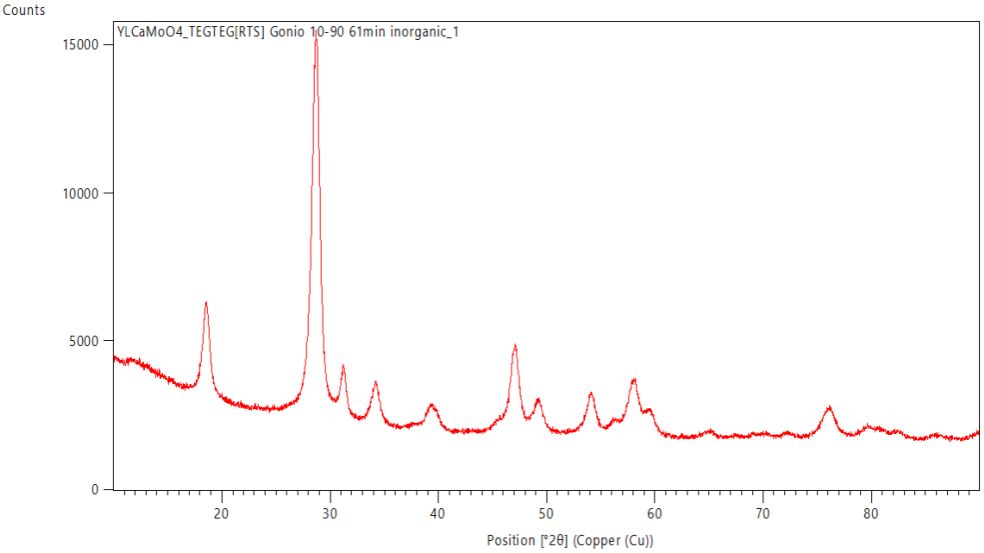

Figure 7.57 XRD pattern of $CaMoO_4$ synthesized using CPS Protocol 2.

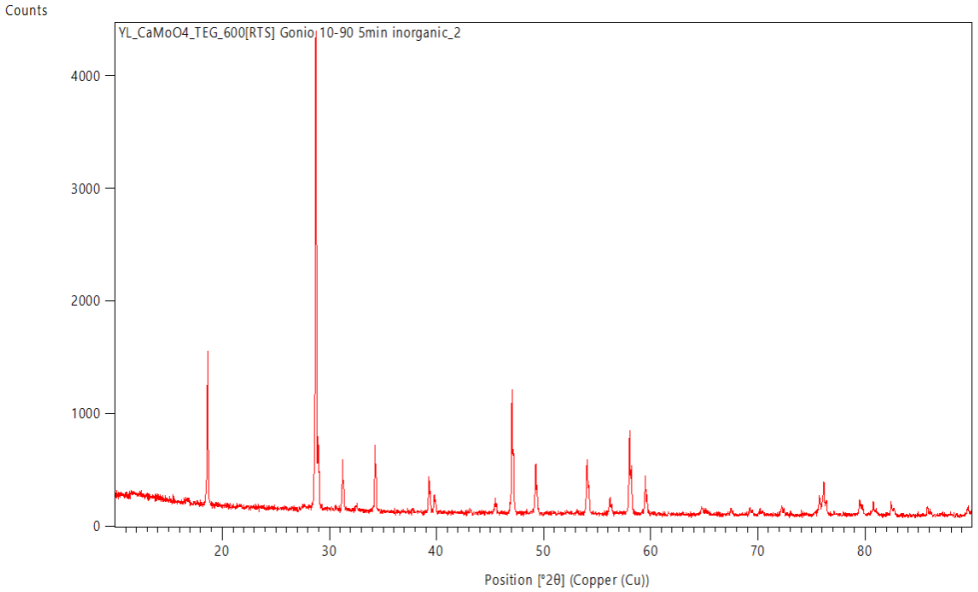

Figure 7.58 XRD pattern of $CaMoO_4$ synthesized using CPS Protocol 2, after calcination at 600ºC.

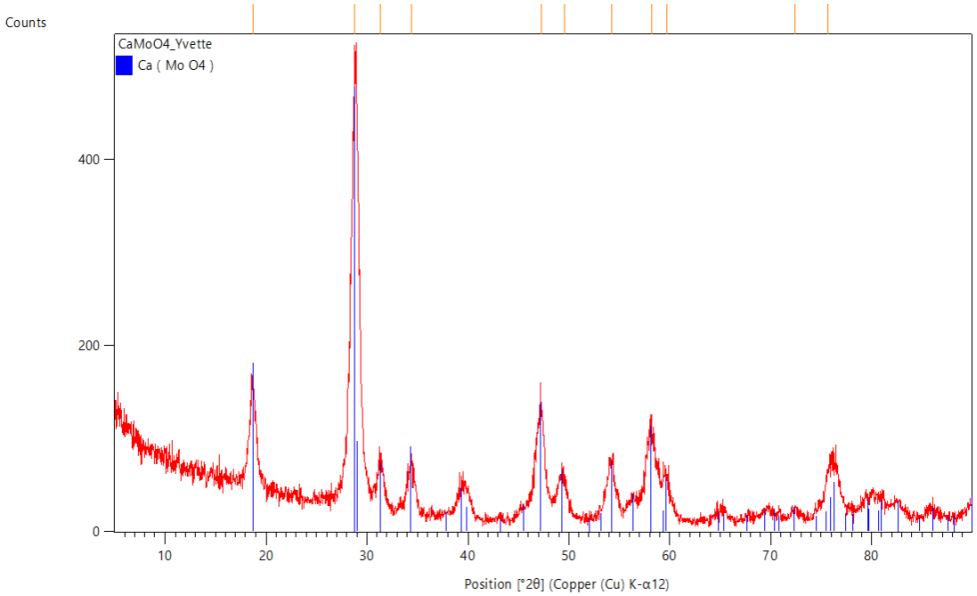

Figure 7.59 XRD pattern of $CaMoO_4$ synthesized using CPS Protocol 3.

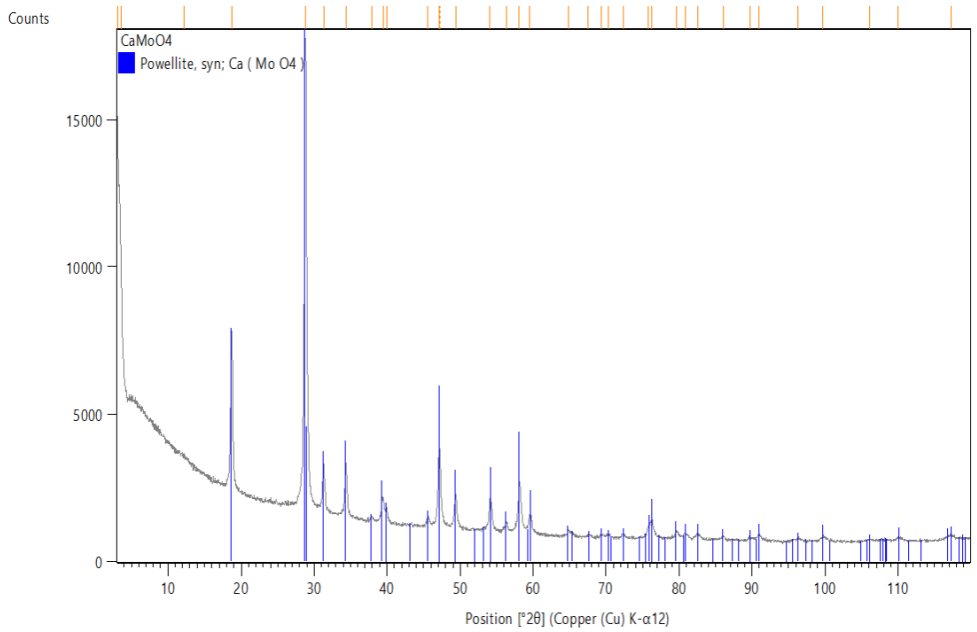

Figure 7.60 XRD pattern of $CaMoO_4$ synthesized using SCS.

$SrMoO_4$

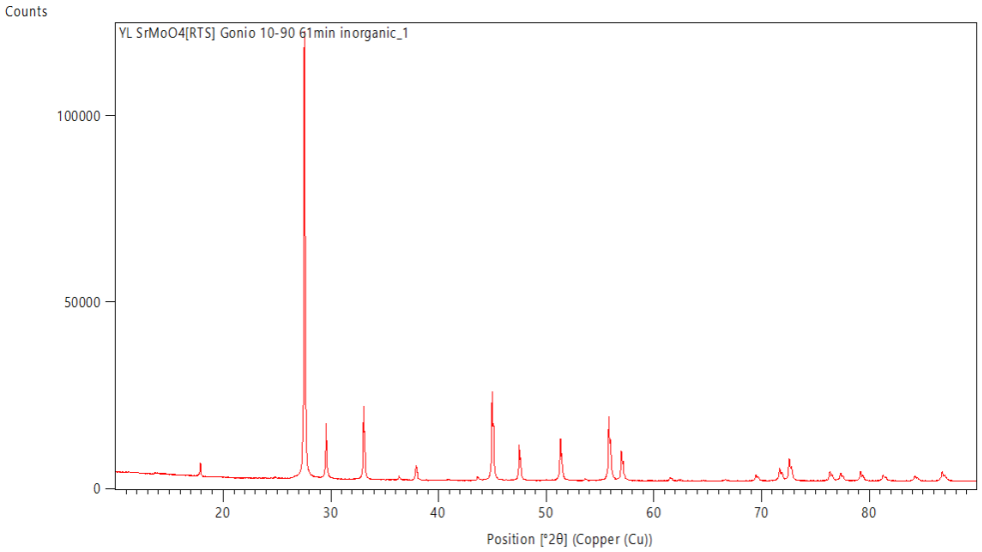

Figure 7.61 XRD pattern of $SrMoO_4$ synthesized using CPS Protocol 1

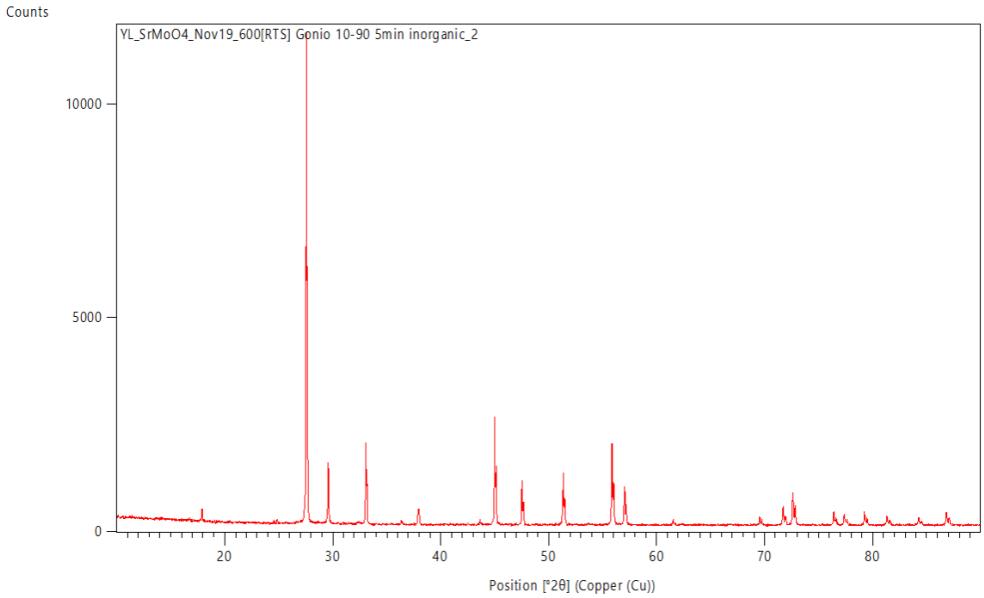

Figure 7.62 XRD pattern of $SrMoO_4$ synthesized using CPS Protocol 1, after calcination at 600ºC.

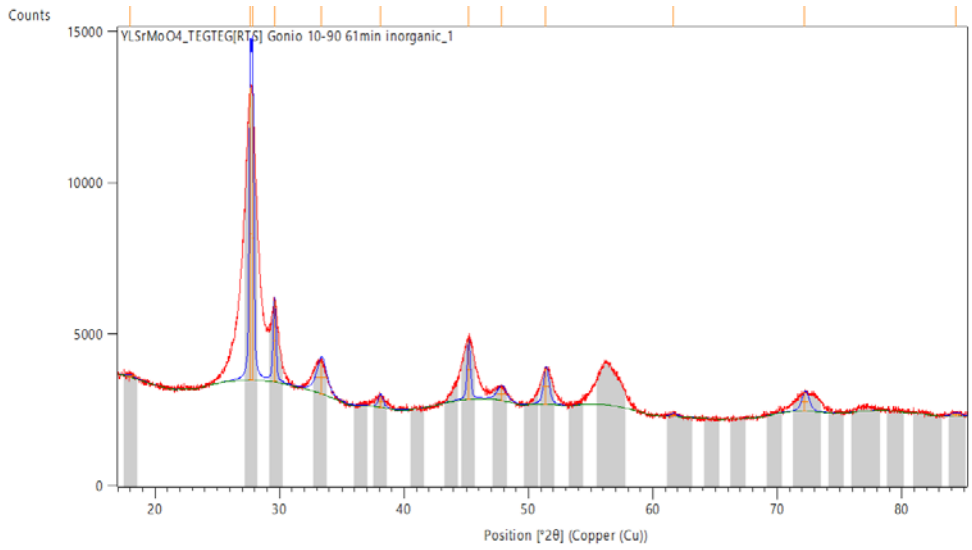

Figure 7.63 XRD pattern of $SrMoO_4$ synthesized using CPS Protocol 2

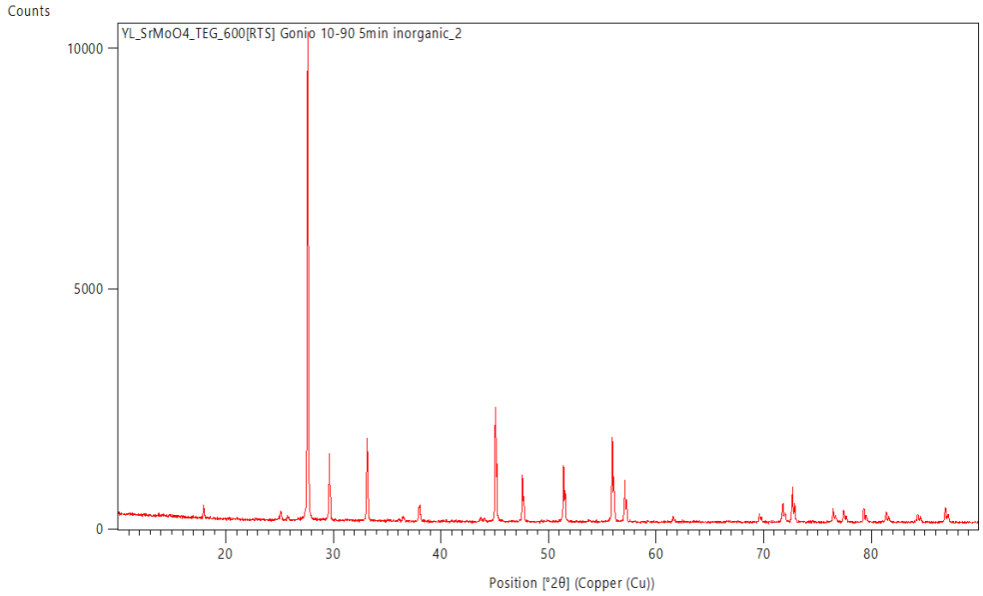

Figure 7.64 XRD pattern of $SrMoO_4$ synthesized using CPS Protocol 2, after calcination at 600ºC.

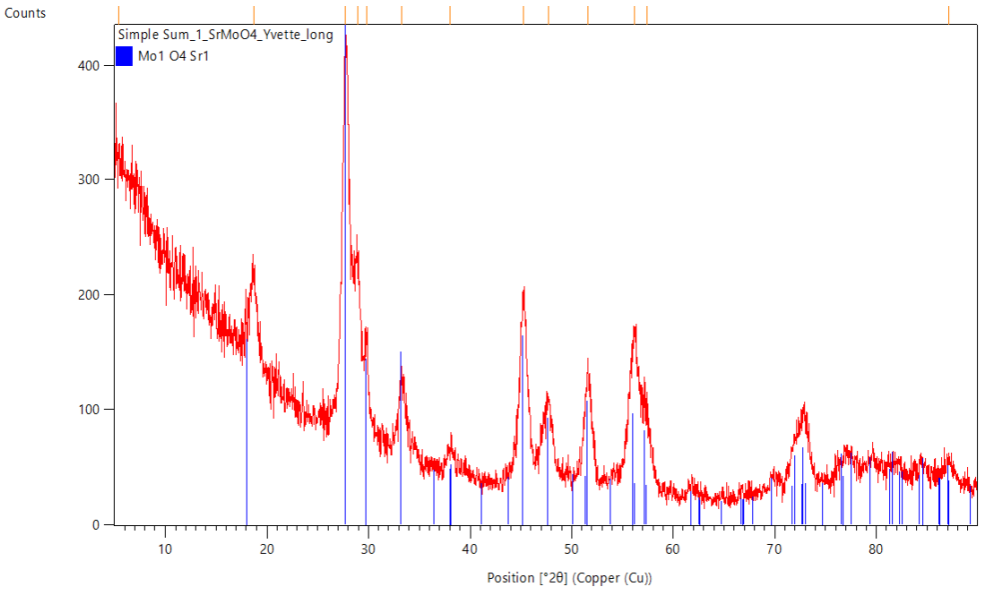

Figure 7.65 XRD pattern of $SrMoO_4$ synthesized using CPS Protocol 3

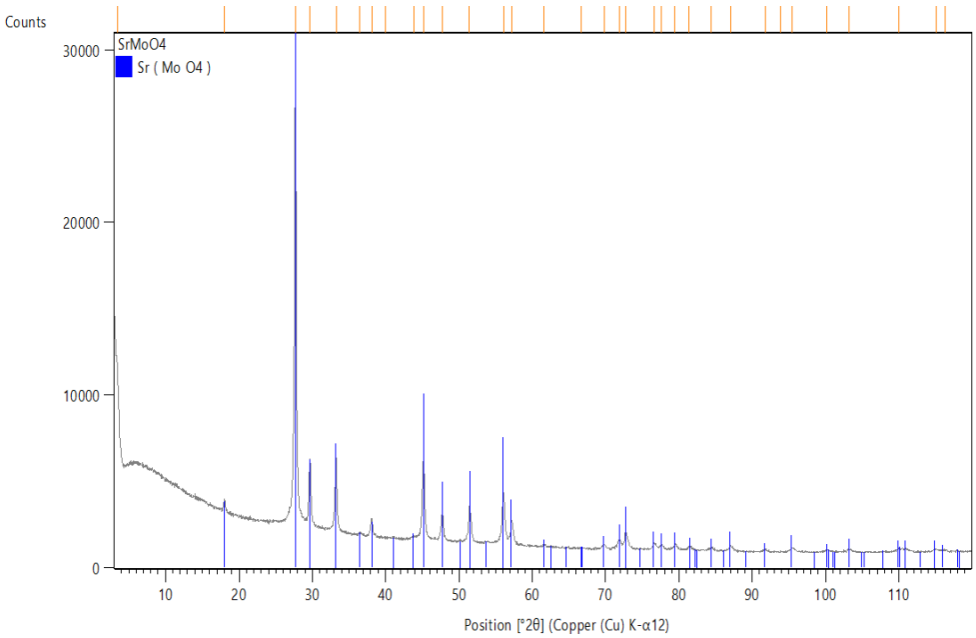

Figure 7.66 XRD pattern of $SrMoO_4$ synthesized using SCS.

$BaMoO_4$

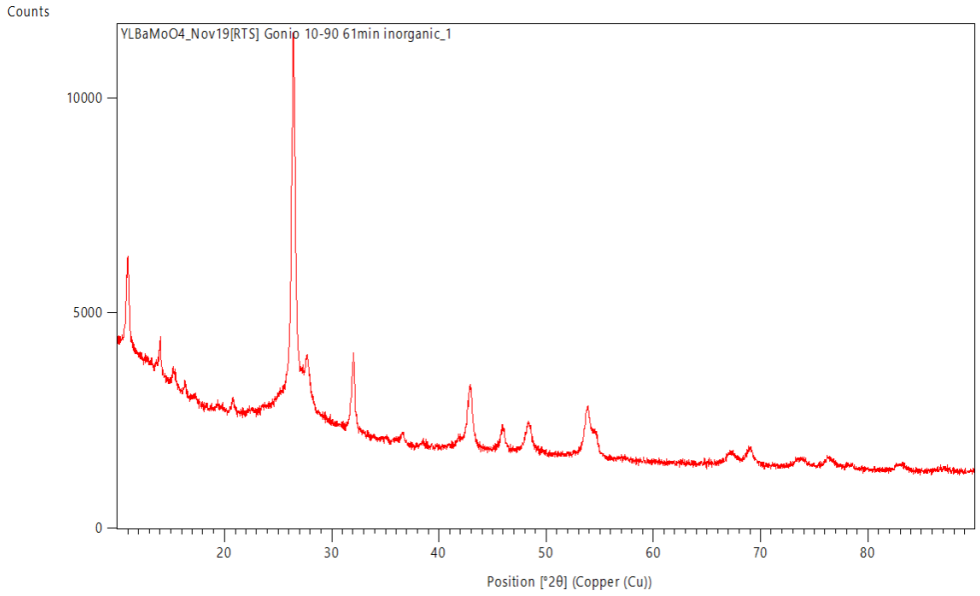

Figure 7.67 XRD pattern of $BaMoO_4$ synthesized using CPS Protocol 1

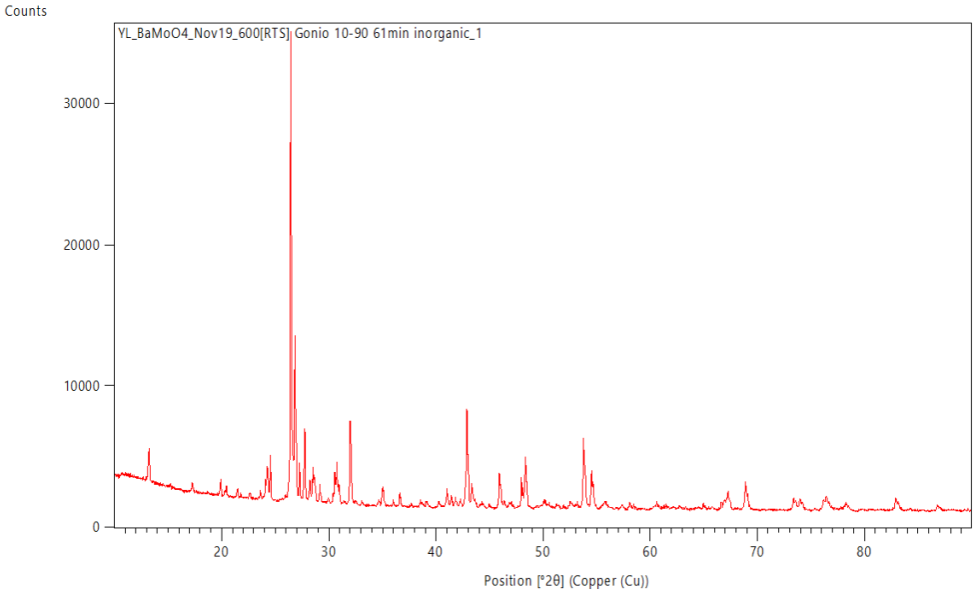

Figure 7.68 XRD pattern of $BaMoO_4$ synthesized using CPS Protocol 1, after calcination at 600ºC.

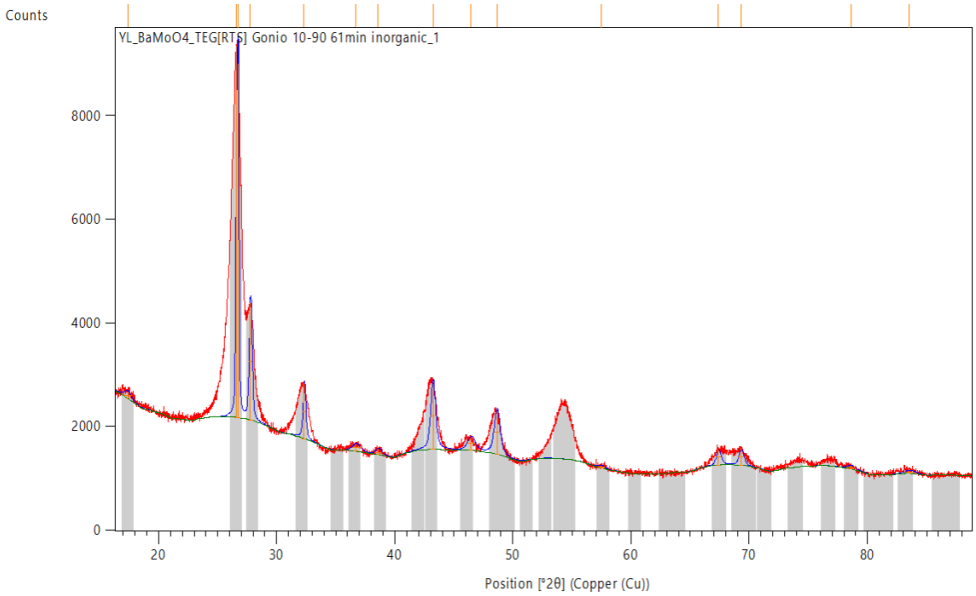

Figure 7.69 XRD pattern of $BaMoO_4$ synthesized using CPS Protocol 2

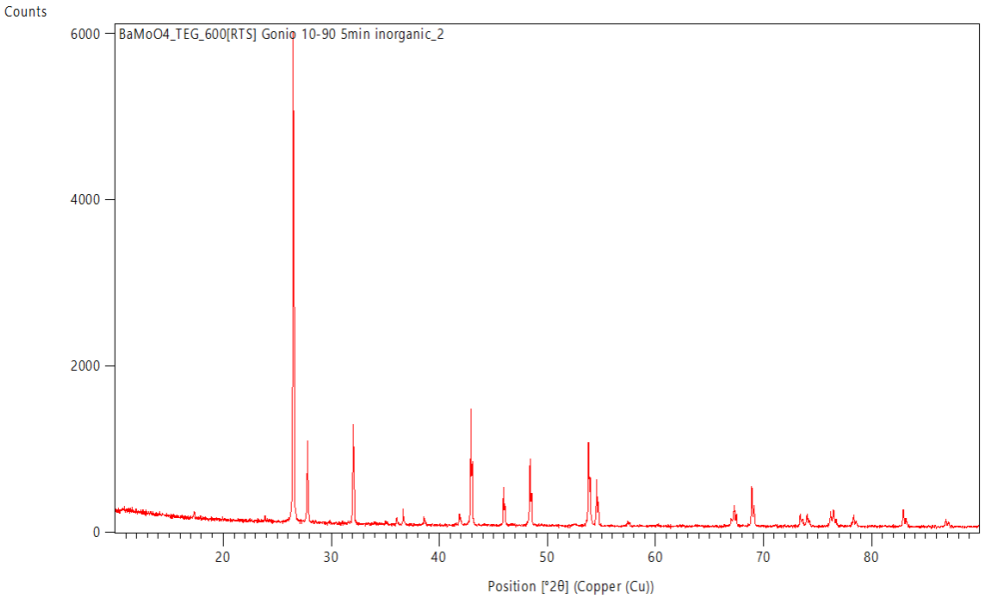

Figure 7.70 XRD pattern of $BaMoO_4$ synthesized using CPS Protocol 2, after calcination at 600ºC.

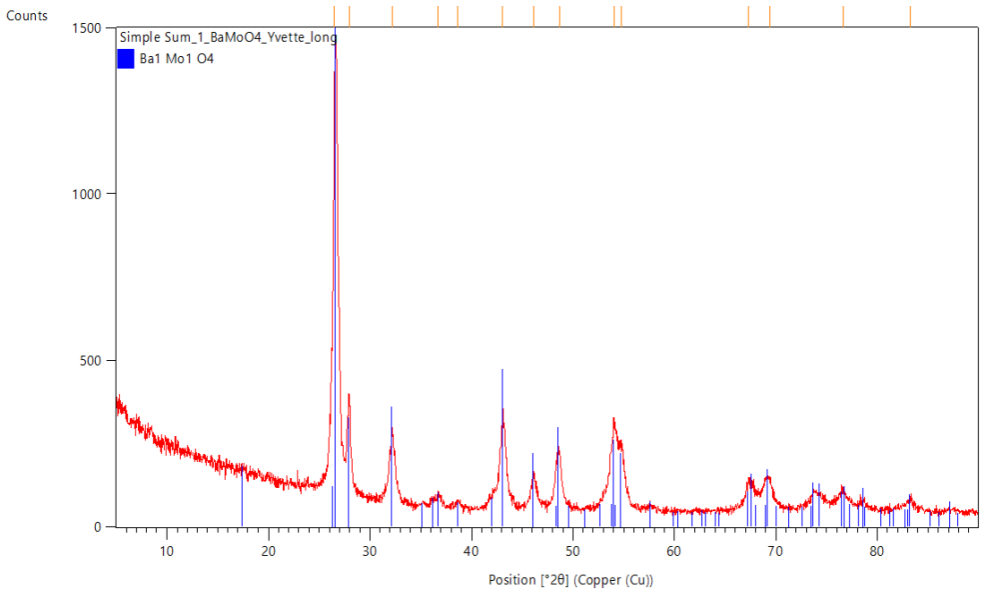

Figure 7.71 XRD pattern of $BaMoO_4$ synthesized using CPS Protocol 3

$NiMoO_4$

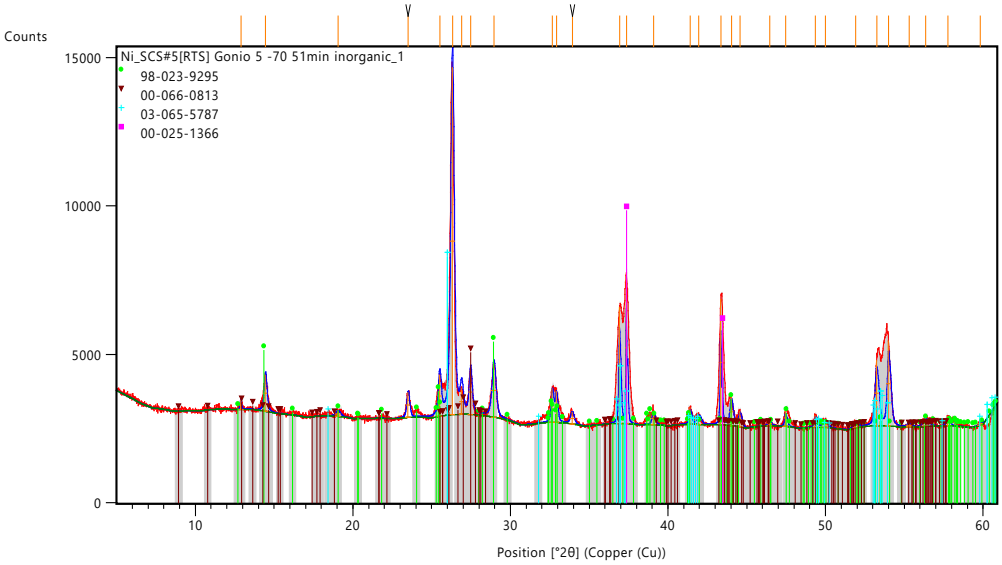

Figure 7.72 XRD pattern of $NiMoO_4$ alpha phase, (98-023-9295) synthesized using the microwave at 800W. Impurities include carbon nitride, C_3N_4, (00-066-0813), molybdenum oxide, MoO_2, (03-065-5787), and molybdenum nitride, Mo_2N, (00-025-1366).

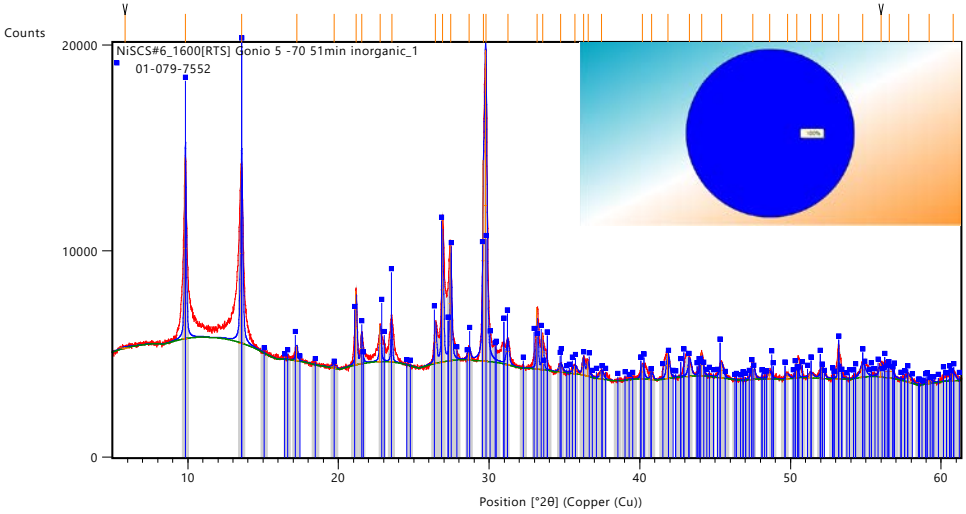

Figure 7.73 XRD pattern of $NiMoO_4 \cdot 0.7H_2O$ synthesized using the microwave at 1600 W.

$ZnMoO_4$

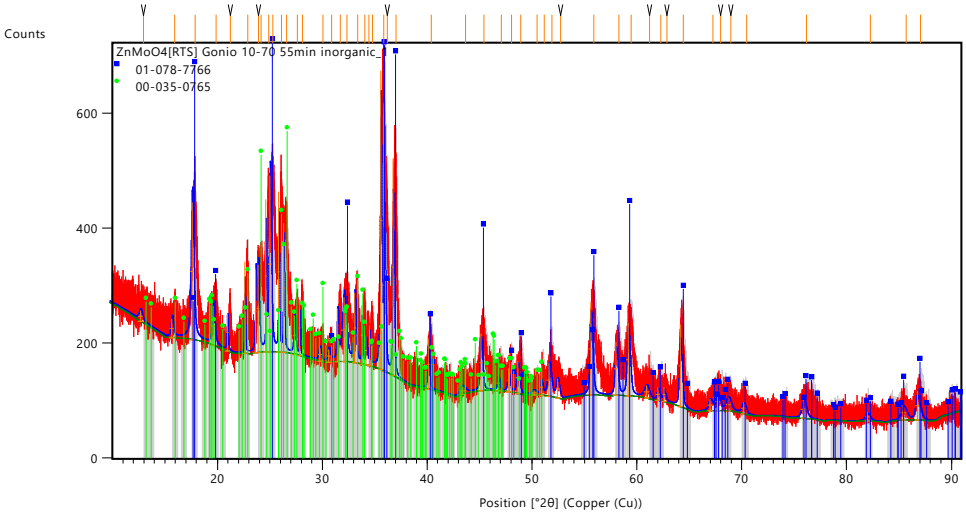

Figure 7.74 XRD pattern of $ZnMoO_4$ (00-035-0765) synthesized in the microwave at 800W. $Zn_2Mo_3O_8$ (01-078-7766) is a byproduct.

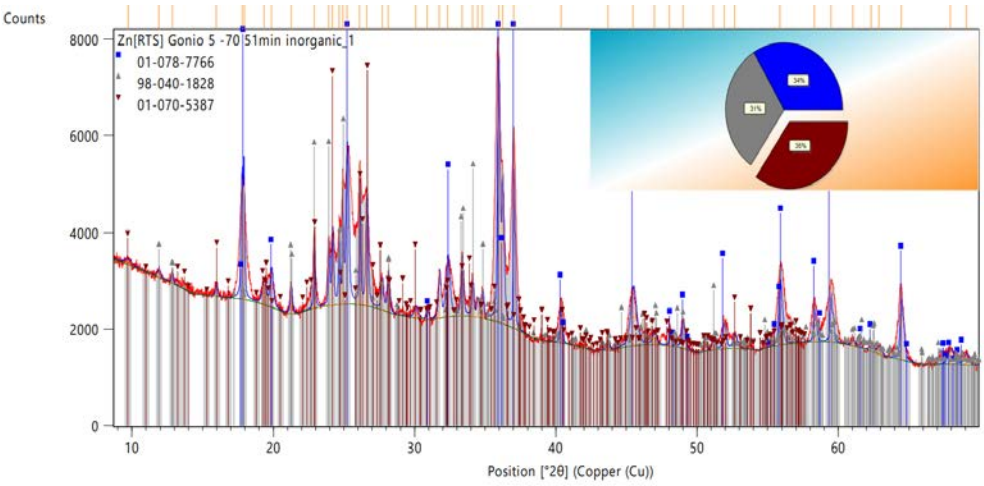

Figure 7.75 XRD pattern of $ZnMoO_4$ (01-070-5387) synthesized in muffle furnace. The product also contained $Zn_3Mo_2O_9$ (98-048-1828) and $Zn_2Mo_3O_8$ (01-078-7766).

$Fe_2(MoO_4)_3$

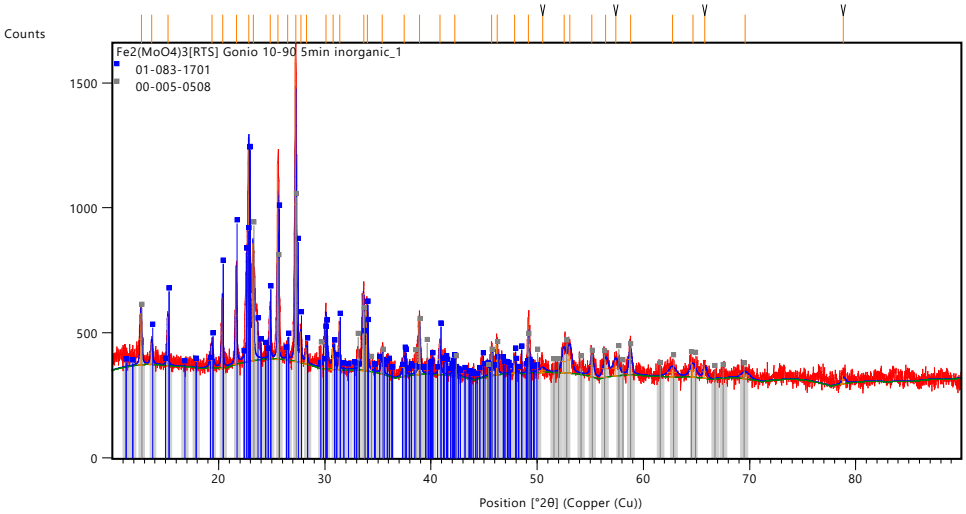

Figure 7.76 XRD pattern of $Fe_2(MoO4)_3$ (01-083-1701) synthesized using the muffle furnace. The product also contained MoO_3(01-083-1701).

$CuMoO_4$

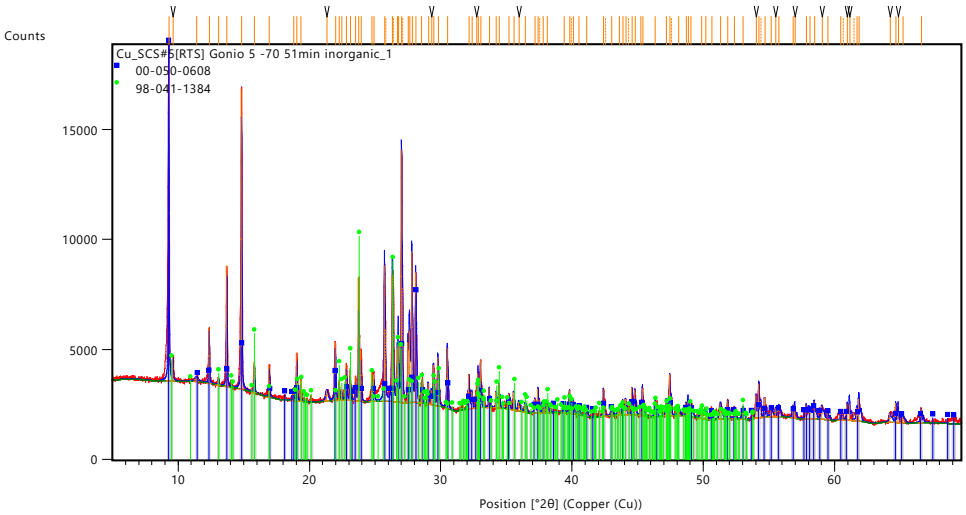

Figure 7.77 XRD pattern of $CuMoO_4$ (98-041-1384) synthesized in the microwave. $(NH_4)_2Mo_4O_{13}$ (00-050-0608) was a byproduct.

8. Appendix B – TGA Curves

$MgMoO_4$

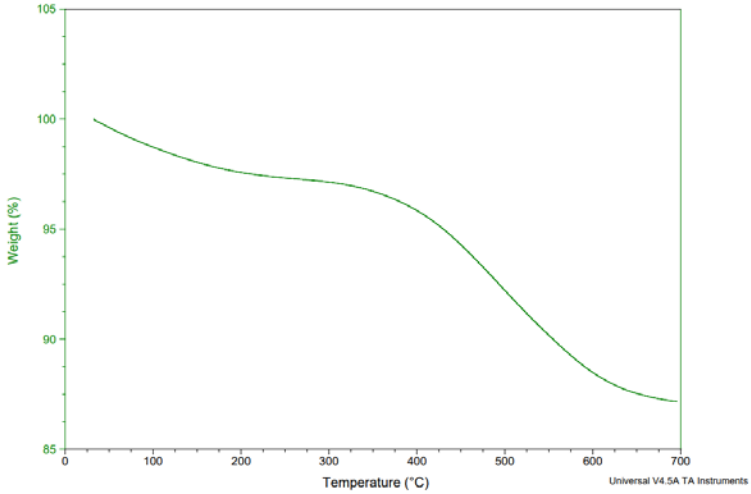

Figure 8.78 TGA curve of $MgMoO_4$ synthesized using SCS.

$CaMoO_4$

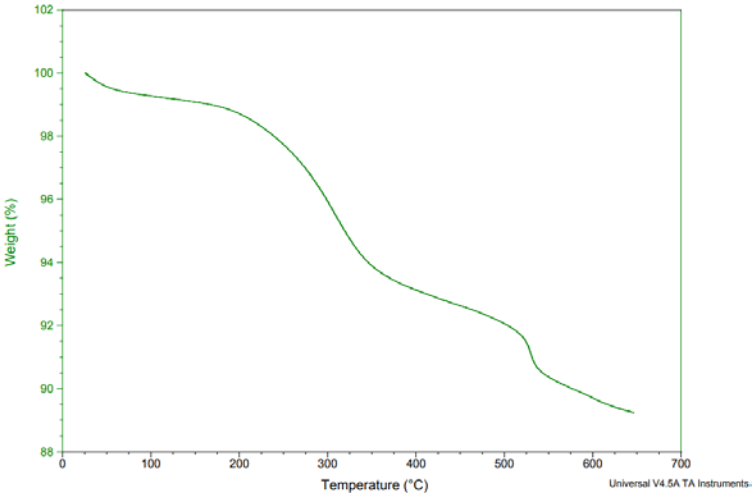

Figure 8.79 TGA curve of pre-calcined $CaMoO_4$ synthesized using CPS Protocol 1.

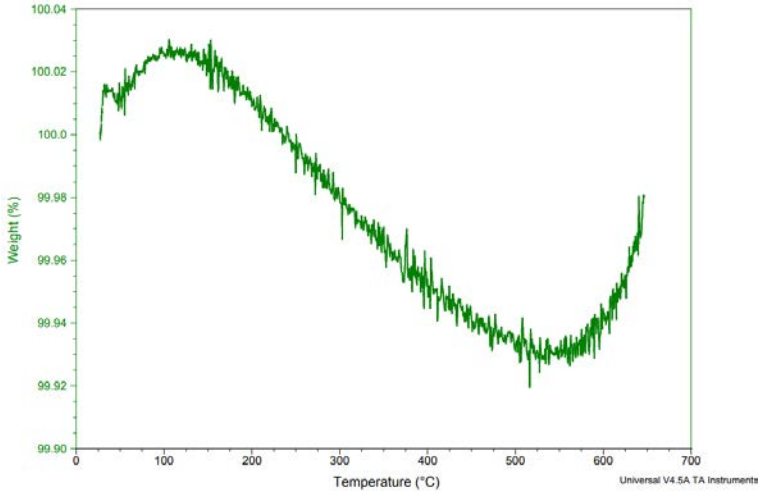

Figure 8.80 TGA curve of post-calcined $CaMoO_4$ synthesized using CPS Protocol 1.

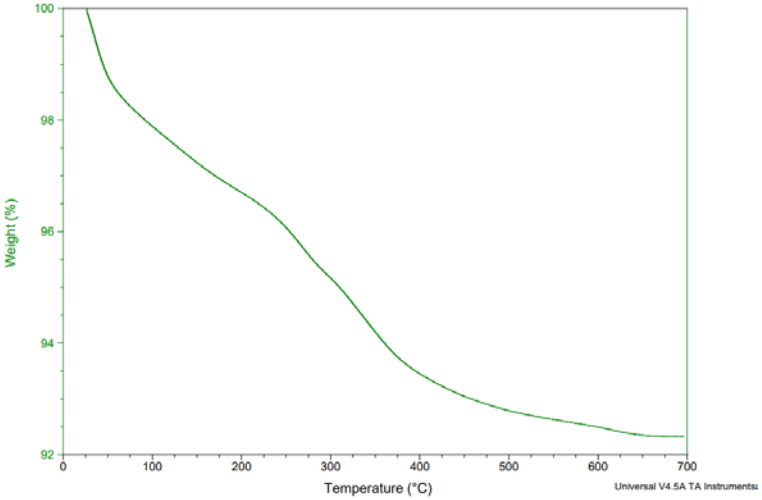

Figure 8.81 TGA curve of $CaMoO_4$ synthesized using CPS Protocol 3.

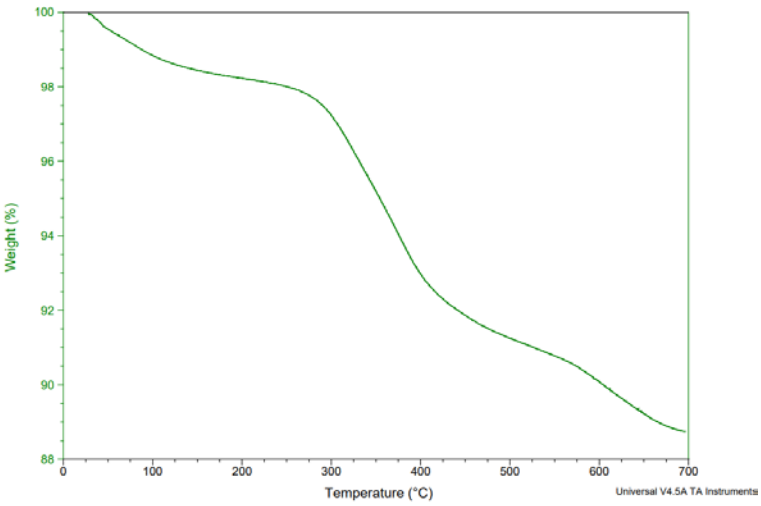

Figure 8.82 TGA curve of $CaMoO_4$ synthesized using SCS.

$SrMoO_4$

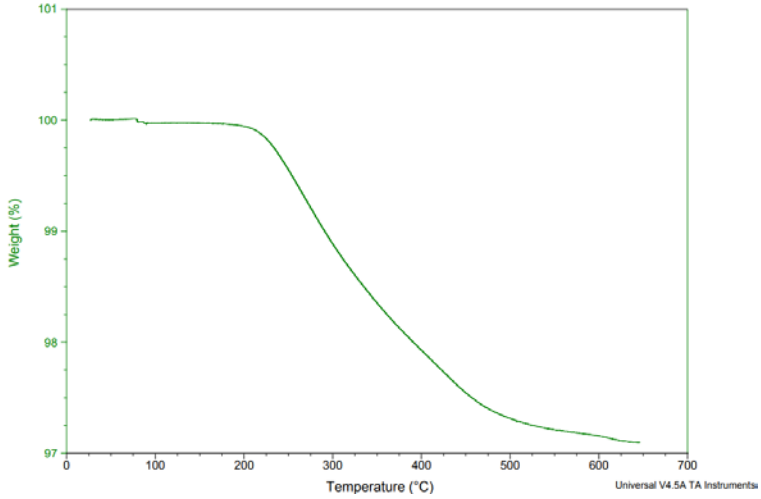

Figure 8.83 TGA curve of pre-calcined $SrMoO_4$ synthesized using CPS Protocol 1.

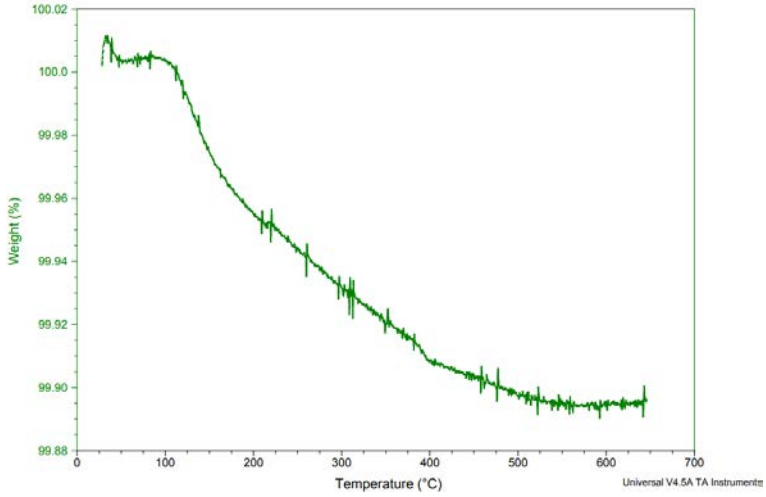

Figure 8.84 TGA curve of post-calcined $SrMoO_4$ synthesized using CPS Protocol 1.

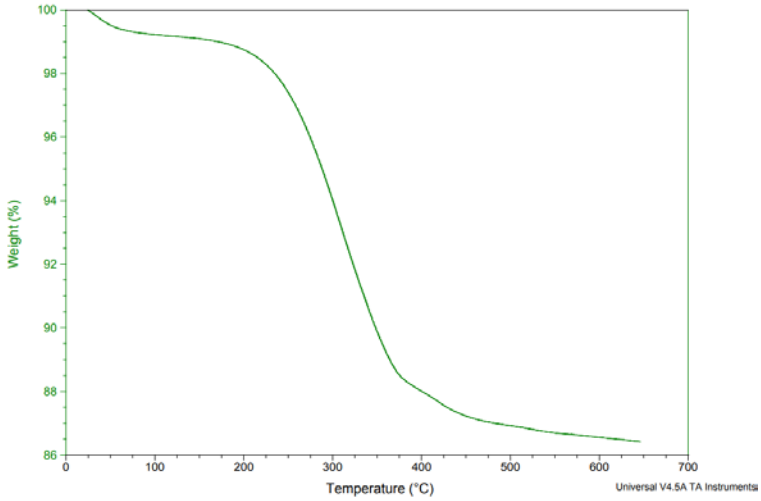

Figure 8.85 TGA curve of pre-calcined $SrMoO_4$ synthesized using CPS Protocol 2.

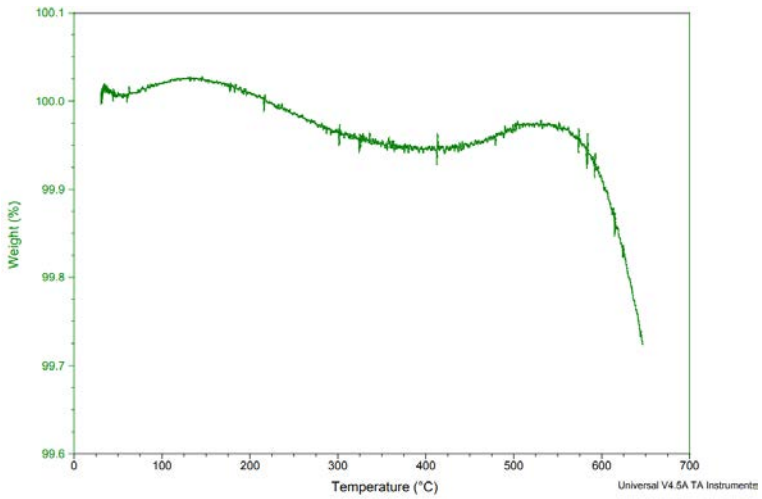

Figure 8.86 TGA curve of post-calcined $SrMoO_4$ synthesized using CPS Protocol 2.

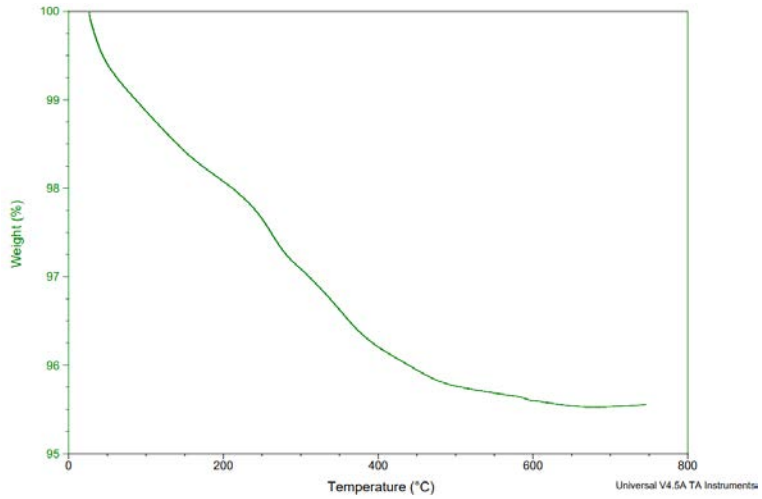

Figure 8.87 TGA curve of $SrMoO_4$ synthesized using CPS Protocol 3.

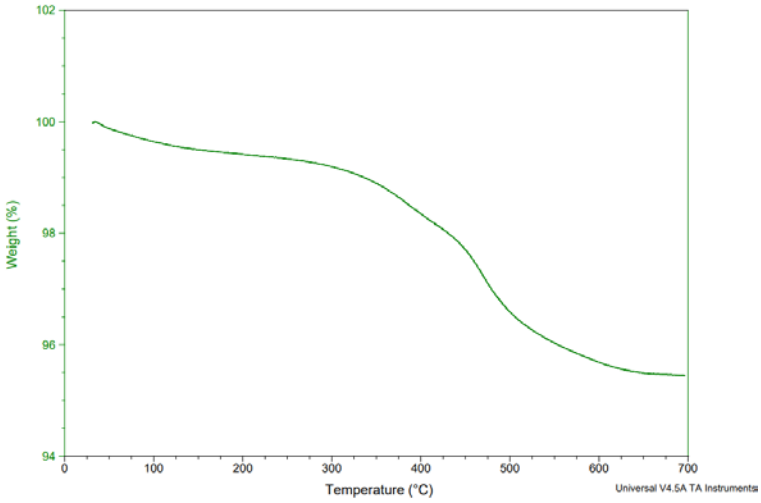

Figure 8.88 TGA curve of $SrMoO_4$ synthesized using SCS.

$BaMoO_4$

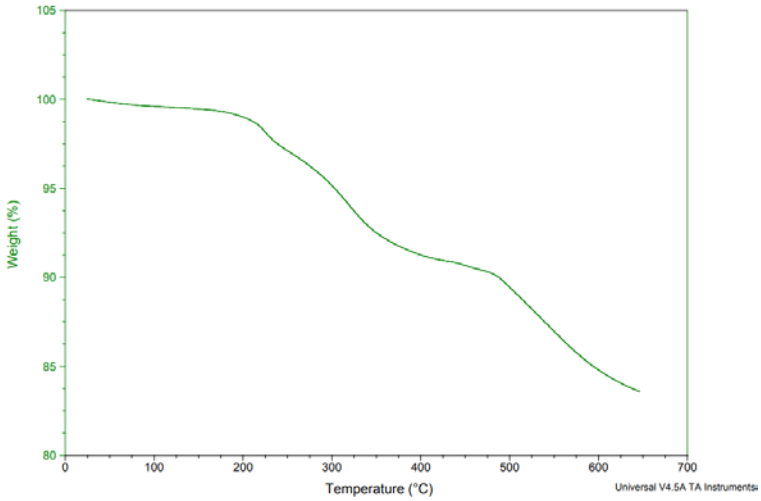

Figure 8.89 TGA curve of pre-calcined $BaMoO_4$ synthesized using CPS Protocol 1.

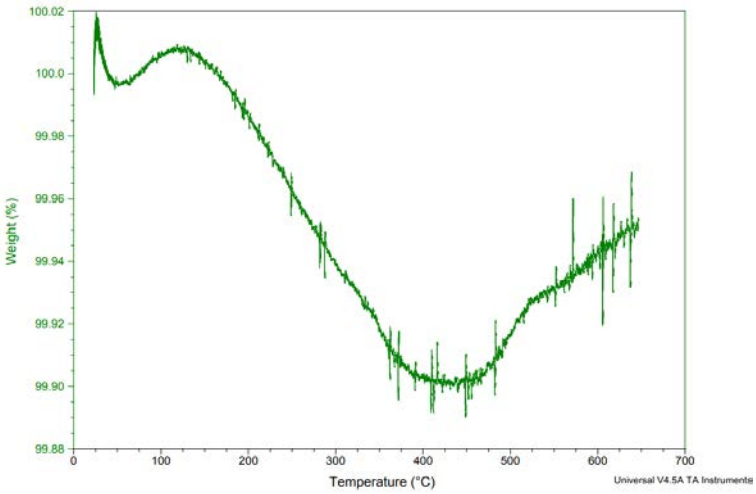

Figure 8.90 TGA curve of post-calcined $BaMoO_4$ synthesized using CPS Protocol 1.

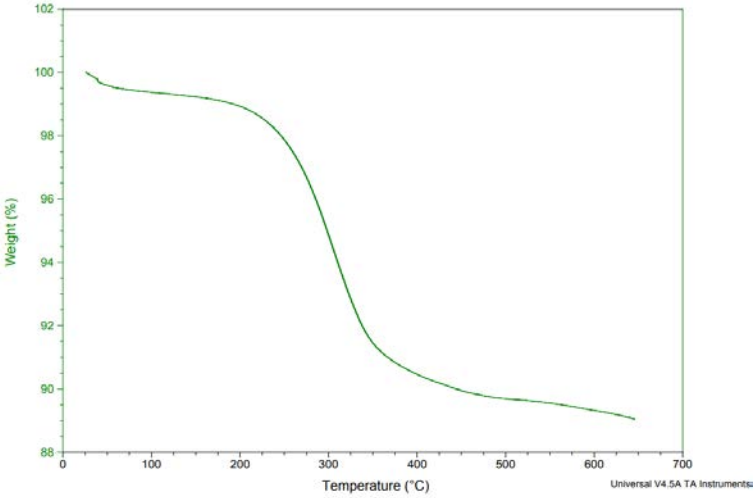

Figure 8.91 TGA curve of pre-calcined $BaMoO_4$ synthesized using CPS Protocol 2.

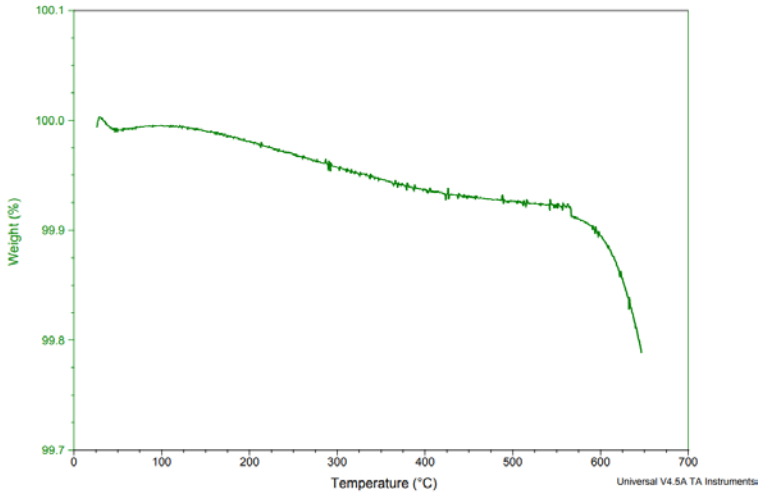

Figure 8.92 TGA curve of post-calcined $BaMoO_4$ synthesized using CPS Protocol 2.

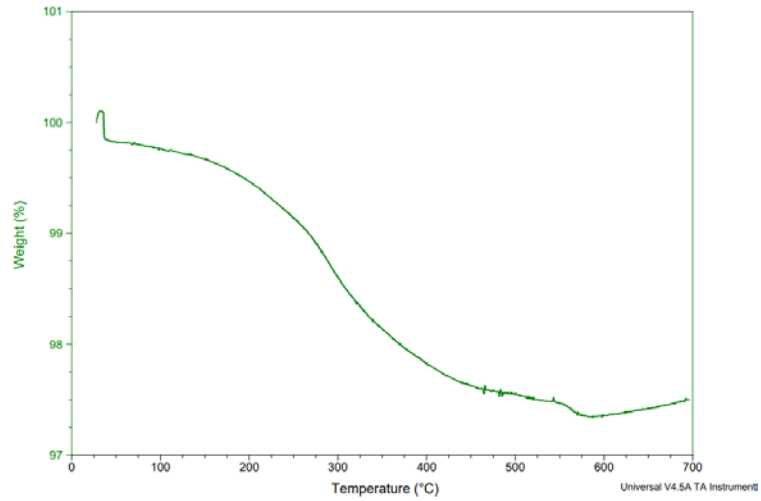

Figure 8.93 TGA curve of $BaMoO_4$ synthesized using CPS Protocol 3.

9. Appendix C – SEM Images

Sedimentation

O-Al/MoO_3

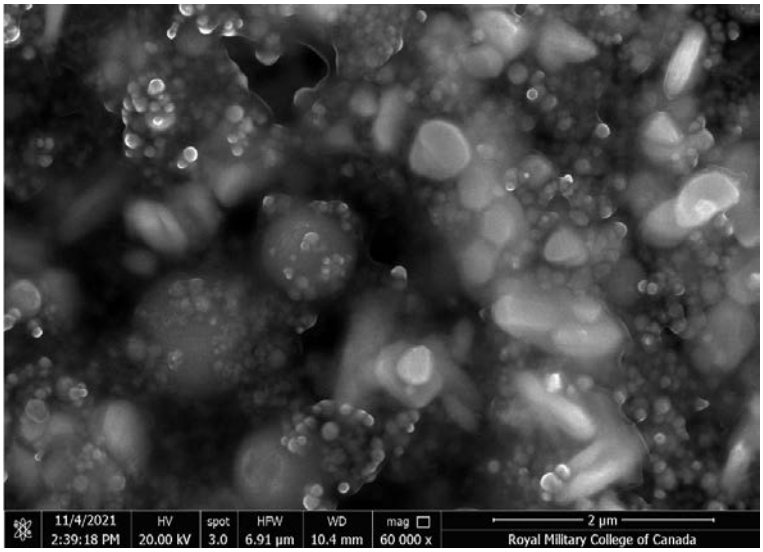

Figure 9.94 0-minute wait time O-Al/MoO_3 Layer 1.

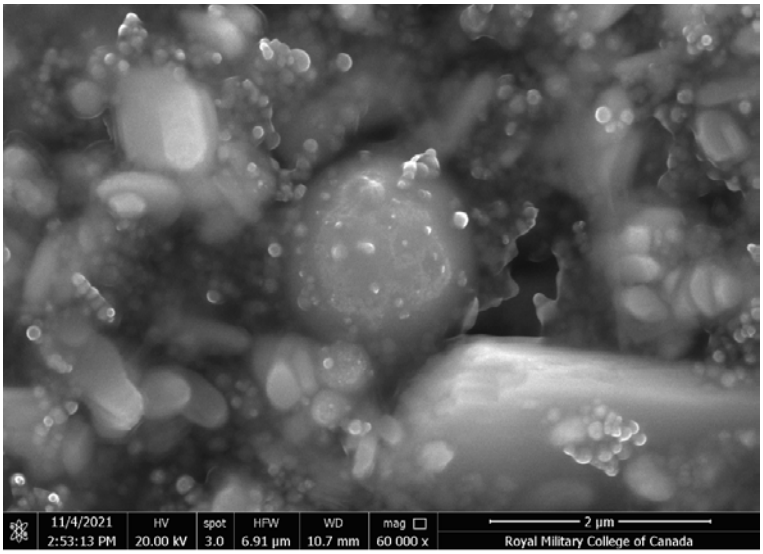

Figure 9.95 0-minute wait time O-Al/MoO_3 Layer 2.

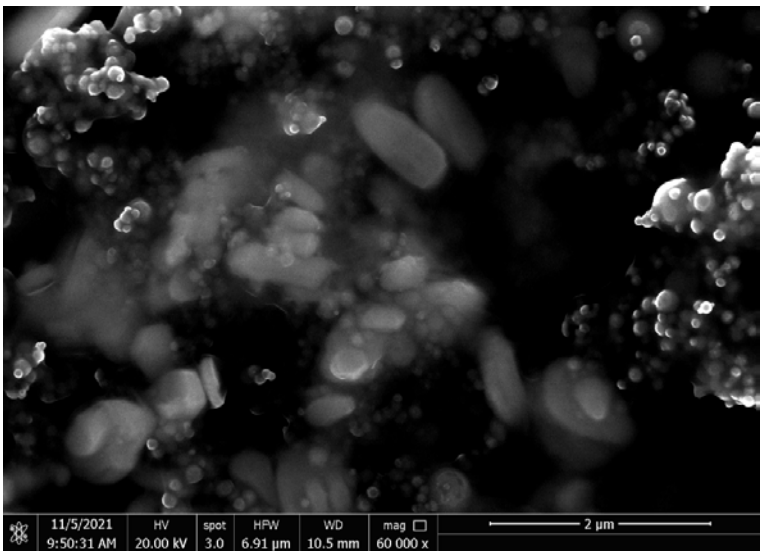

Figure 9.96 0-minute wait time O-Al/MoO_3 Layer 3.

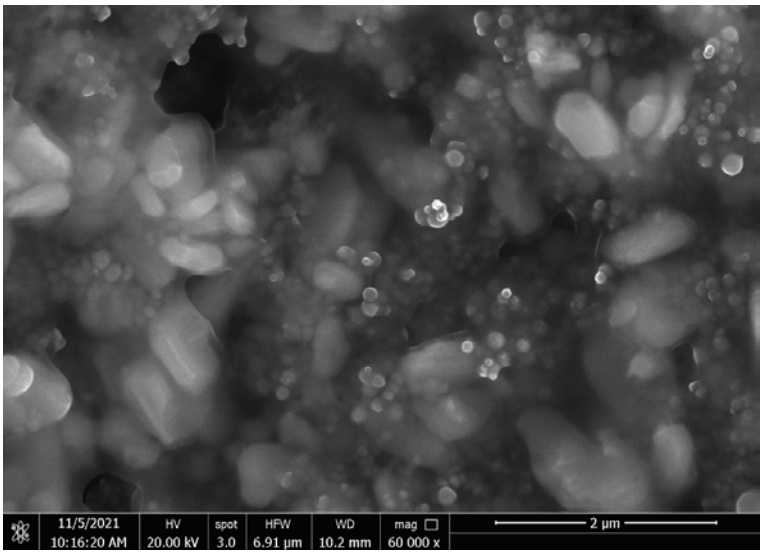

Figure 9.97 0-minute wait time O-Al/MoO_3 Layer 4.

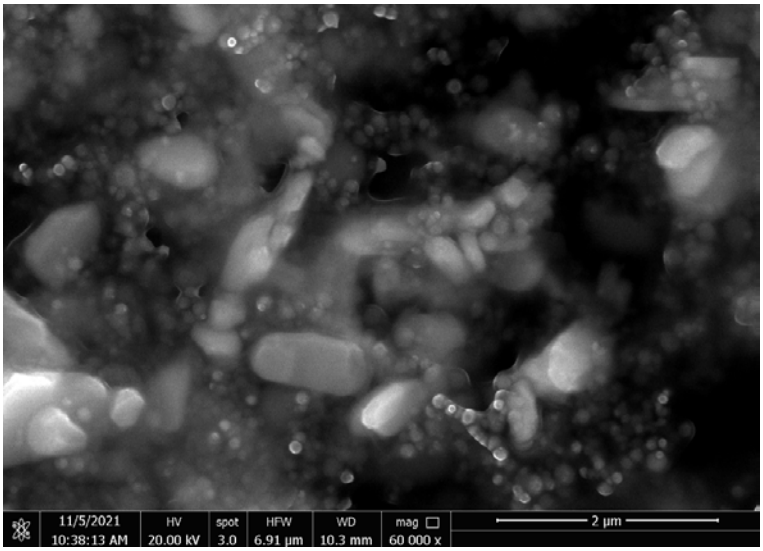

Figure 9.98 0-minute wait time O-Al/MoO_3 Layer 5.

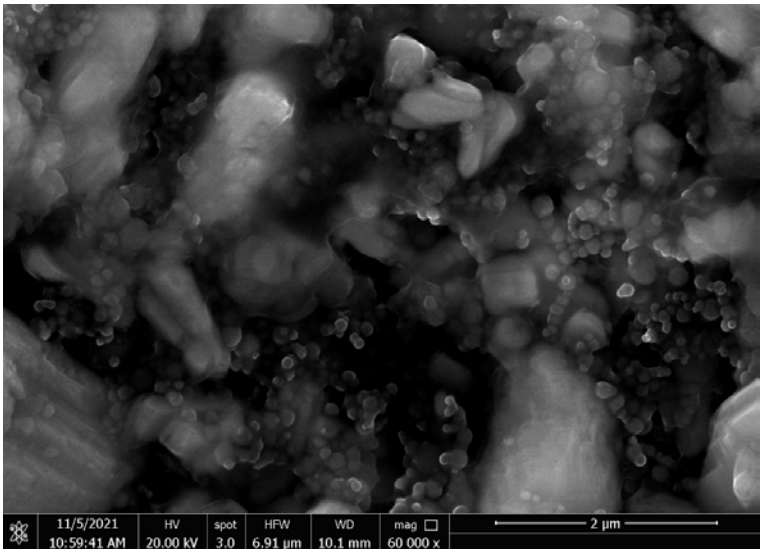

Figure 9.99 0-minute wait time O-Al/MoO_3 Layer 6.

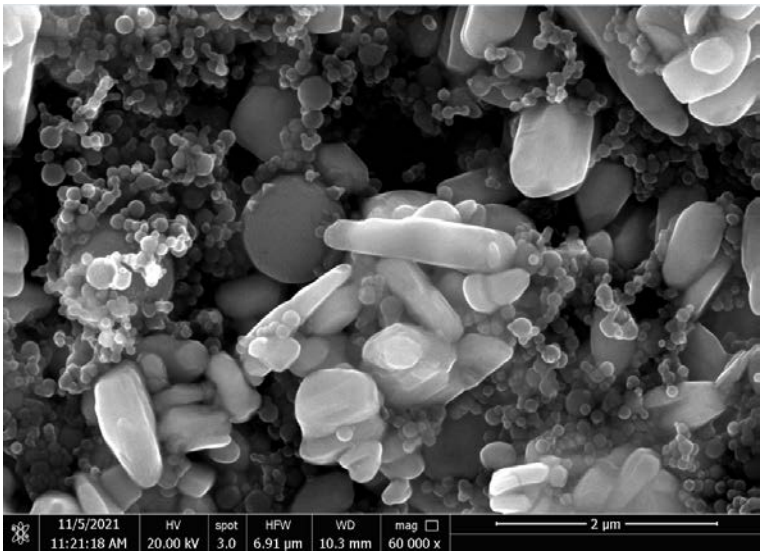

Figure 9.100 0-minute wait time O-Al/MoO_3 Layer 7.

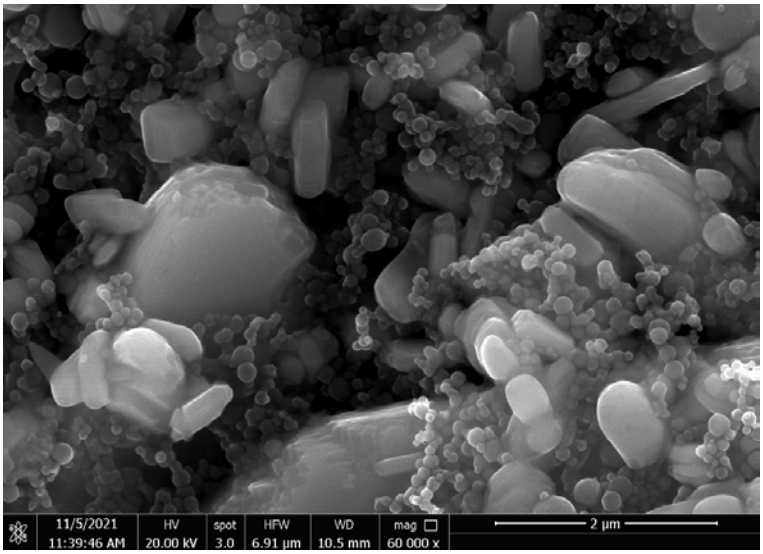

Figure 9.101 0-minute wait time O-Al/MoO_3 Layer 8.

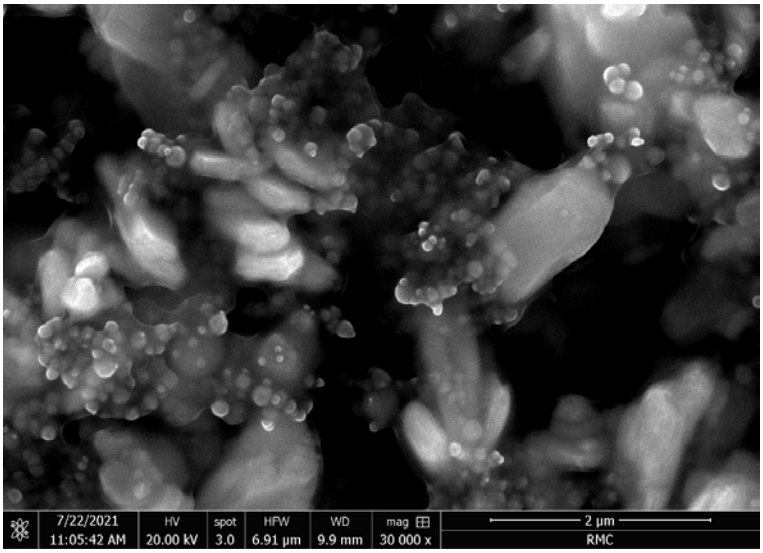

Figure 9.102 15-minute wait time O-Al/MoO_3 Layer 6.

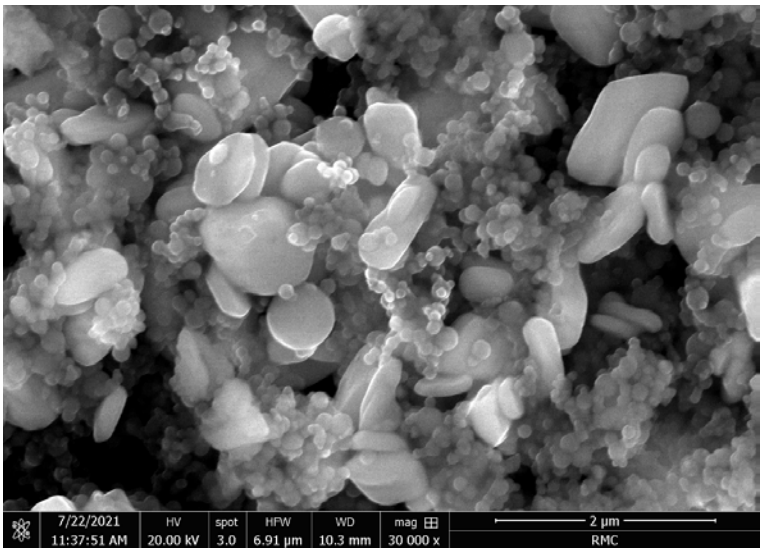

Figure 9.103 15-minute wait time O-Al/MoO_3 Layer 7.

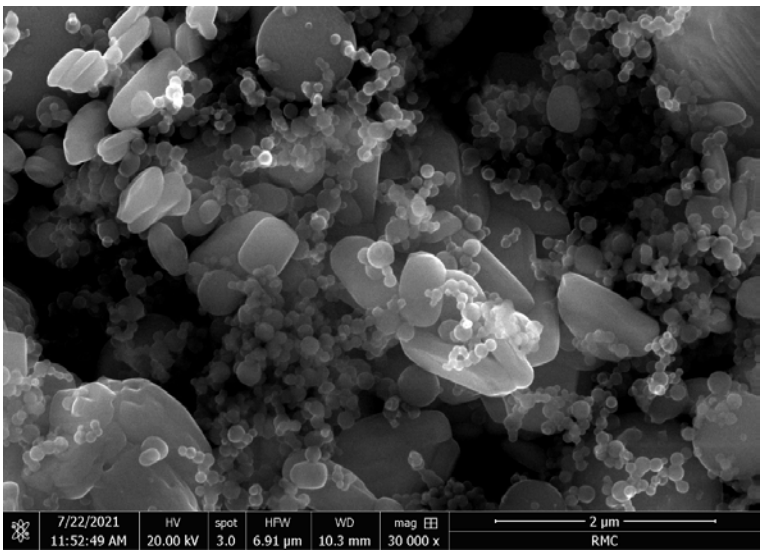

Figure 9.104 15-minute wait time O-Al/MoO_3 Layer 8.

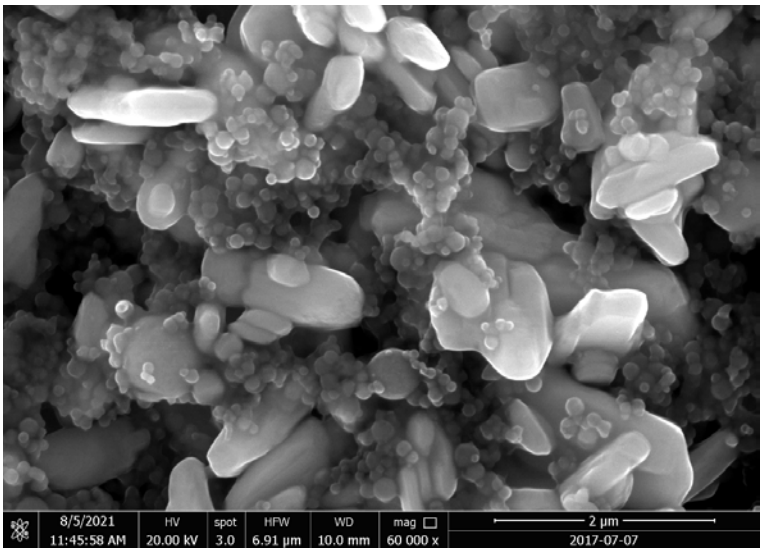

Figure 9.105 60-minute wait time O-Al/MoO_3 Layer 7.

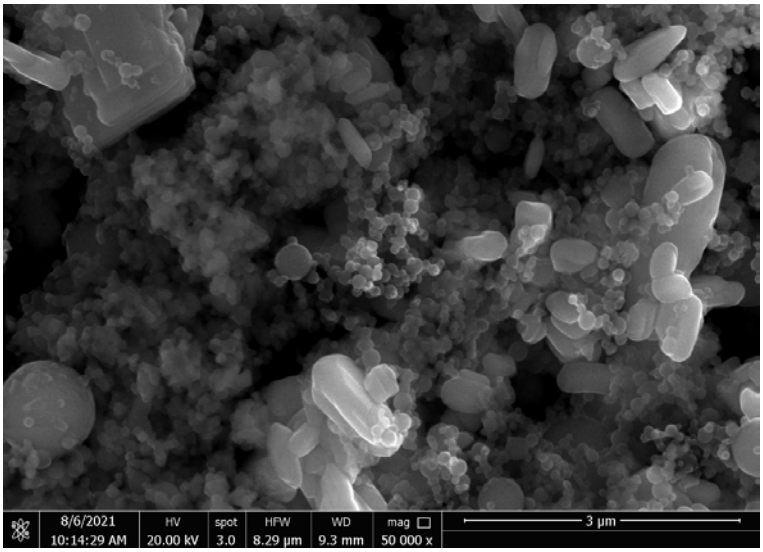

Figure 9.106 60-minute wait time O-Al/MoO_3 Layer 8.

L-Al/MoO_3

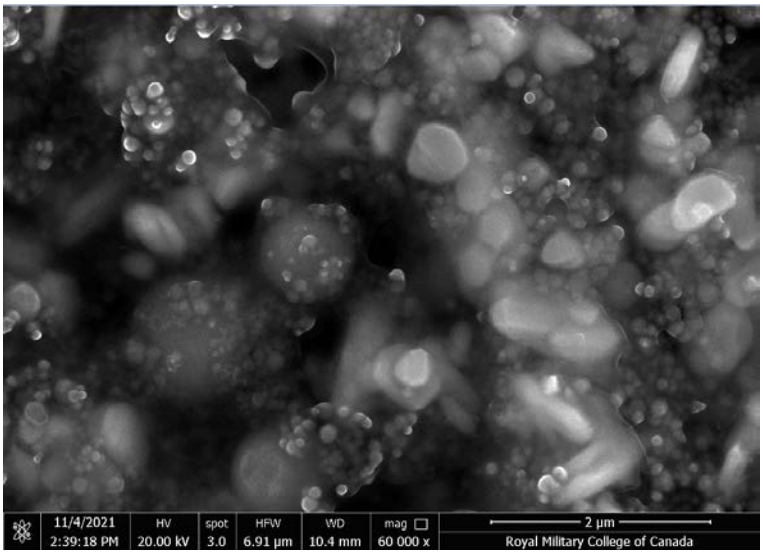

Figure 9.107 0-minute wait time L-Al/MoO_3 Layer 1.

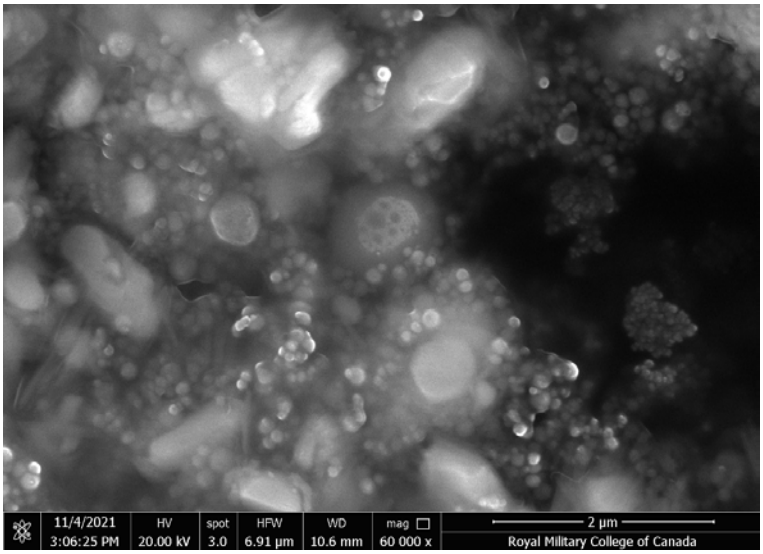

Figure 9.108 0-minute wait time L-Al/MoO_3 Layer 2.

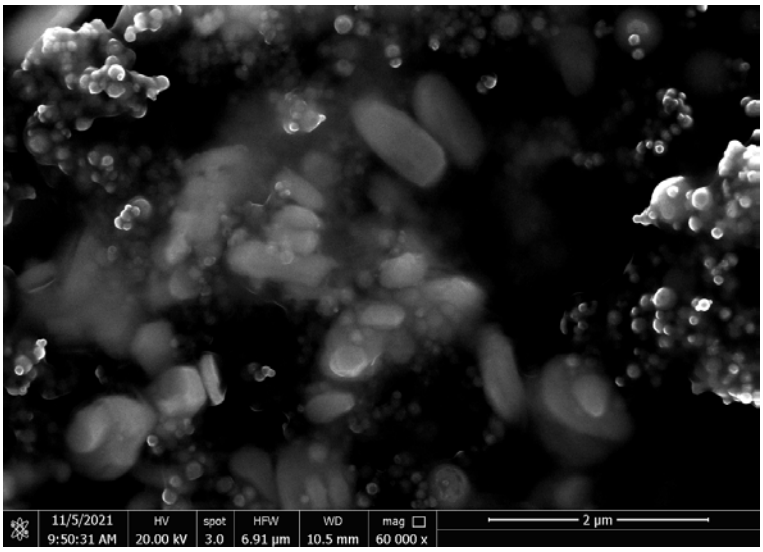

Figure 9.109 0-minute wait time L-Al/MoO_3 Layer 3.

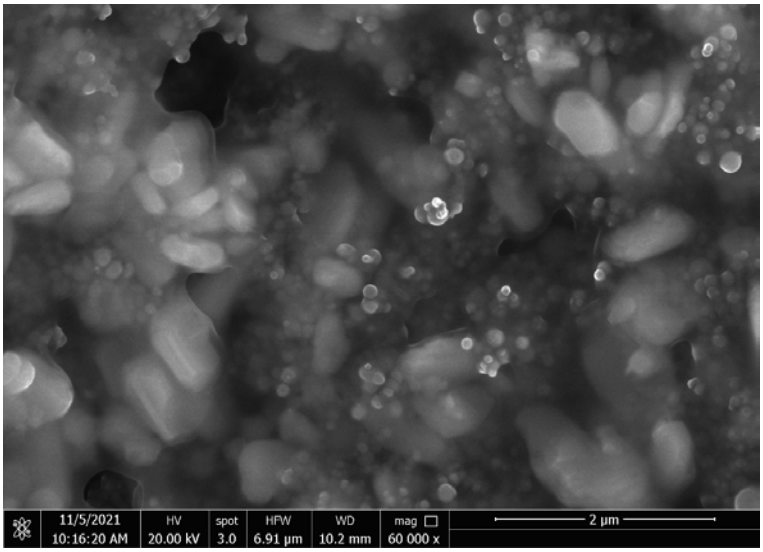

Figure 9.110 0-minute wait time L-Al/MoO_3 Layer 4.

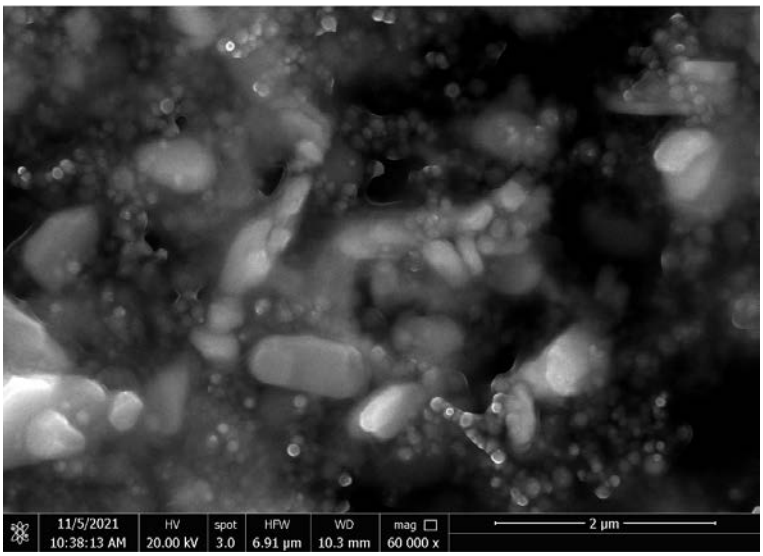

Figure 9.111 0-minute wait time L-Al/MoO_3 Layer 5.

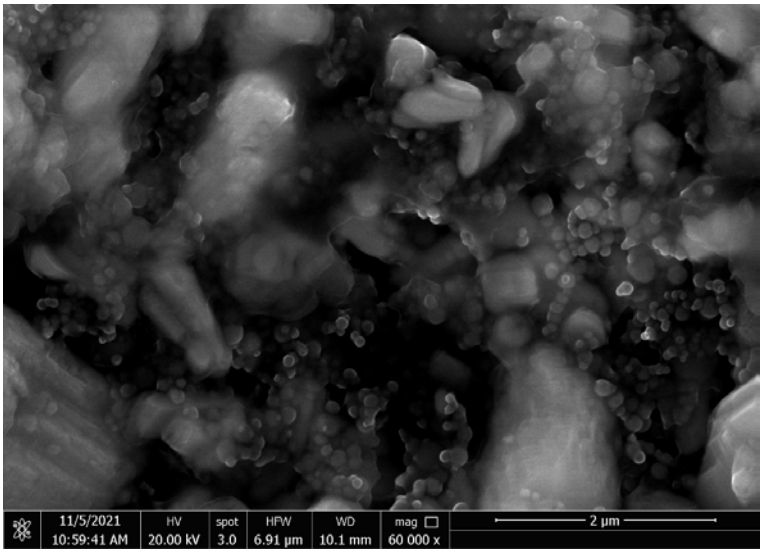

Figure 9.112 0-minute wait time L-Al/MoO_3 Layer 6.

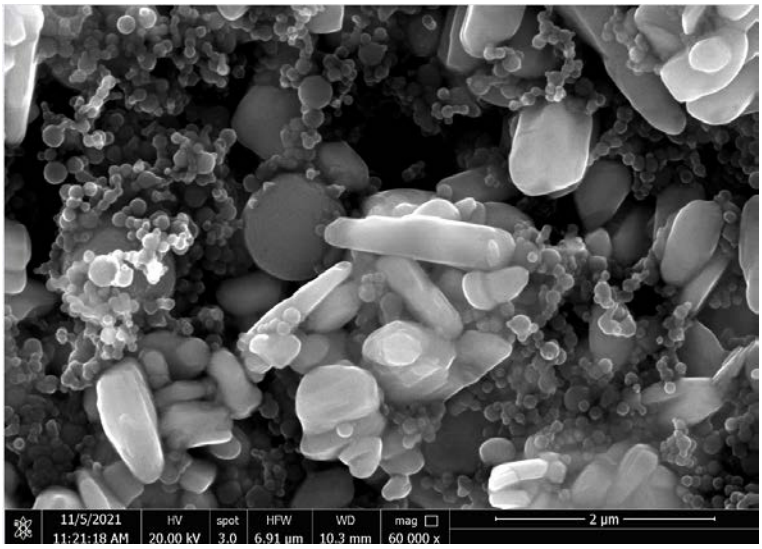

Figure 9.113 0-minute wait time L-Al/MoO_3 Layer 7/

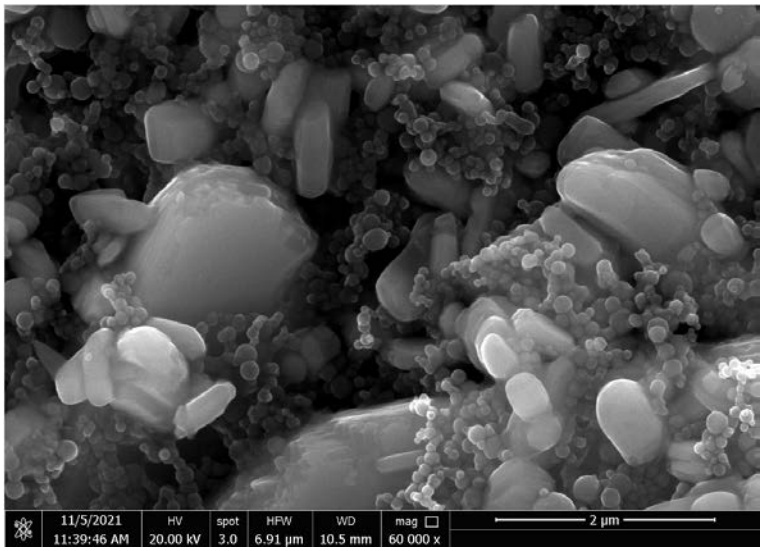

Figure 9.114 0-minute wait time L-Al/MoO_3 Layer 8.

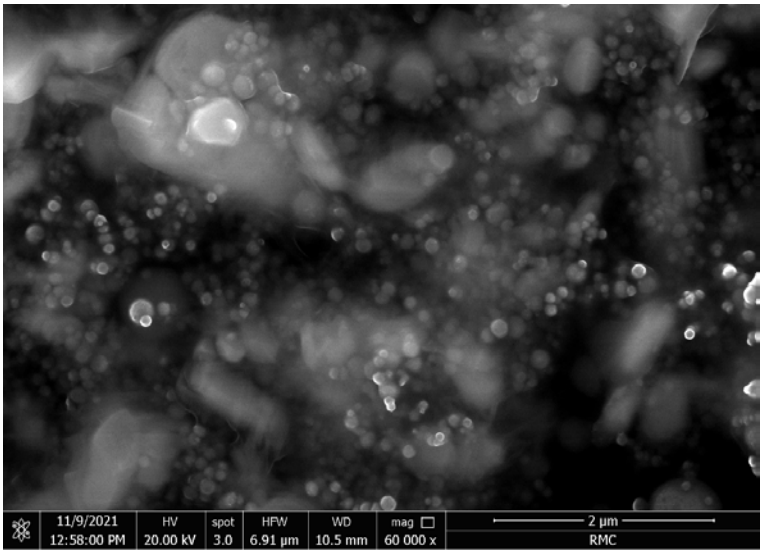

Figure 9.115 15-minute wait time L-Al/MoO_3 Layer 6.

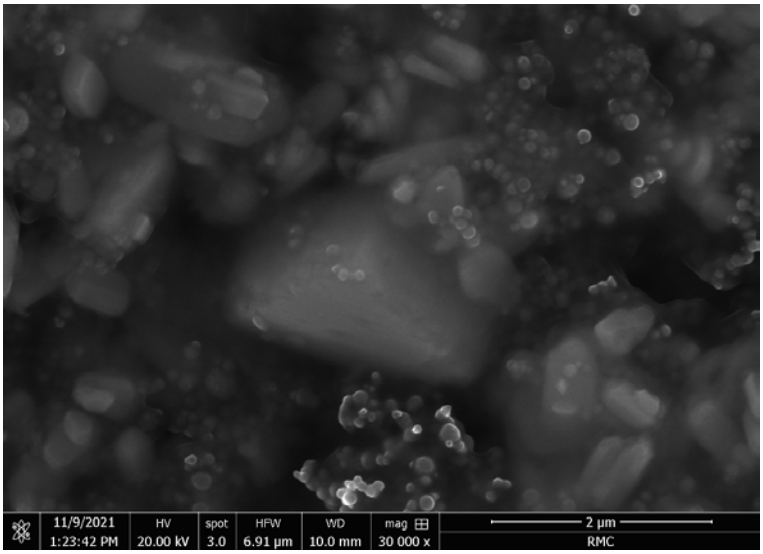

Figure 9.116 15-minute wait time L-Al/MoO_3 Layer 7.

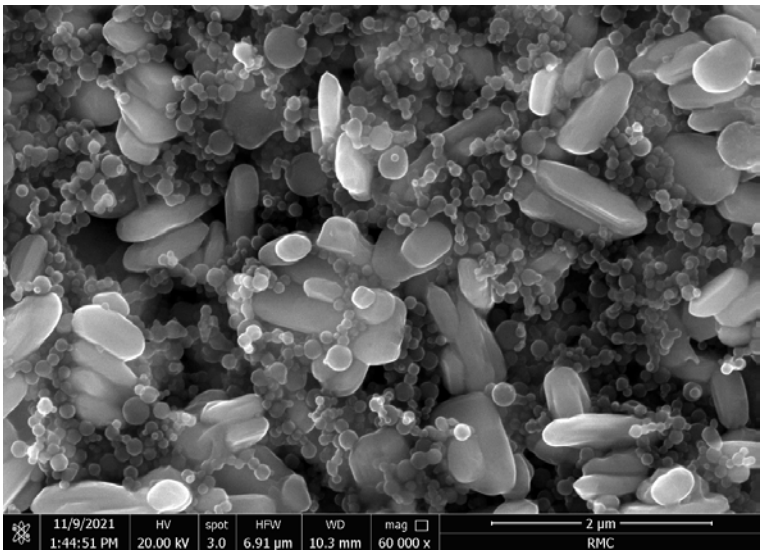

Figure 9.117 15-minute wait time L-Al/MoO_3 Layer 8.

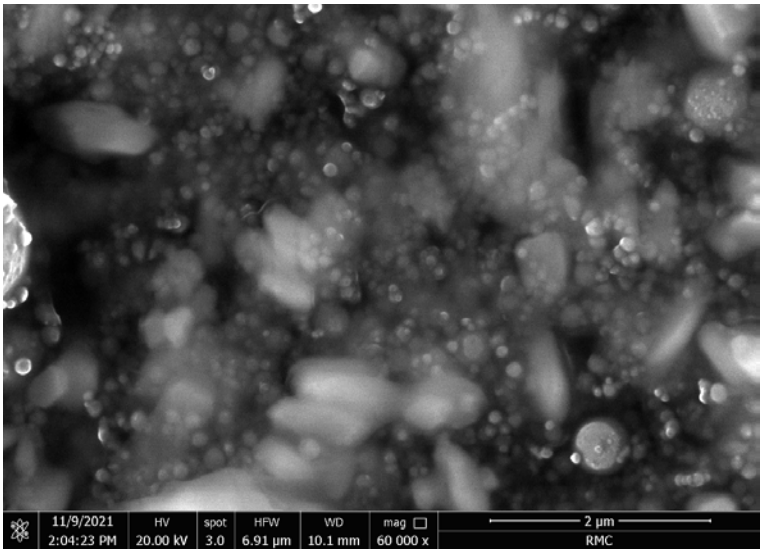

Figure 9.118 60-minute wait time L-Al/MoO_3 Layer 6.

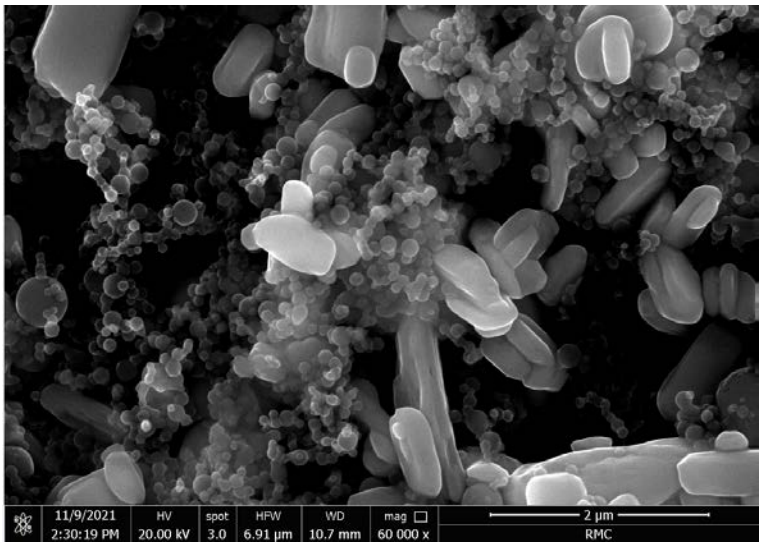

Figure 9.119 60-minute wait time L-Al/MoO_3 Layer 7.

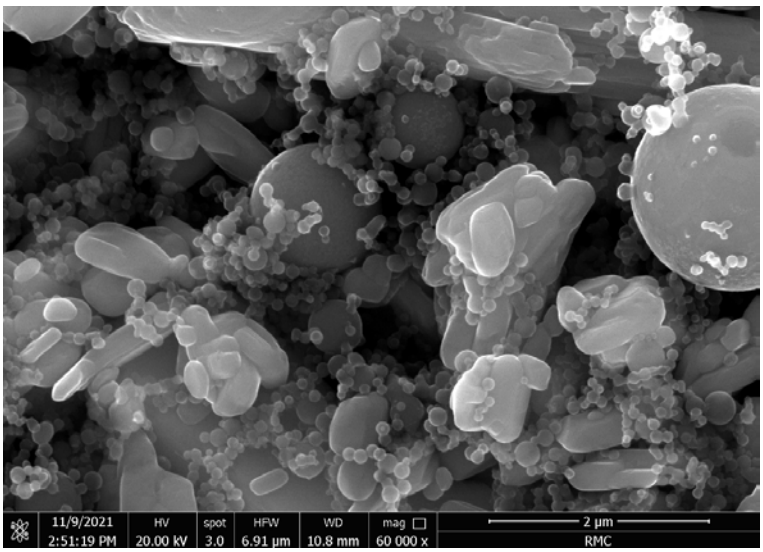

Figure 9.120 60-minute wait time L-Al/MoO_3 Layer 8.

V-Al/MoO_3

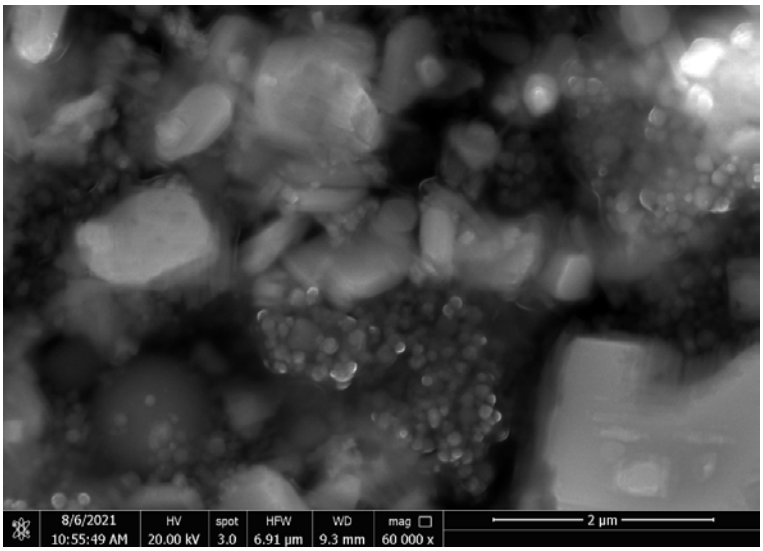

Figure 9.121 0-minute wait time V-Al/MoO_3 Layer 1.

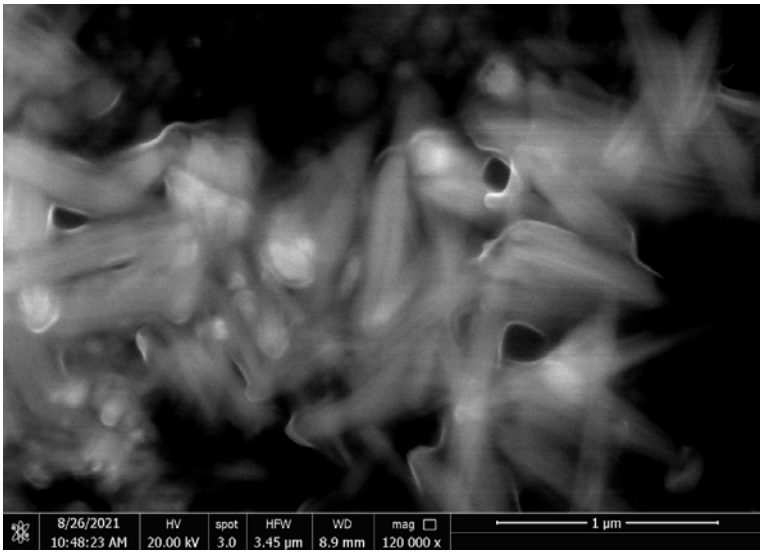

Figure 9.122 0-minute wait time V-Al/MoO_3 Layer 5.

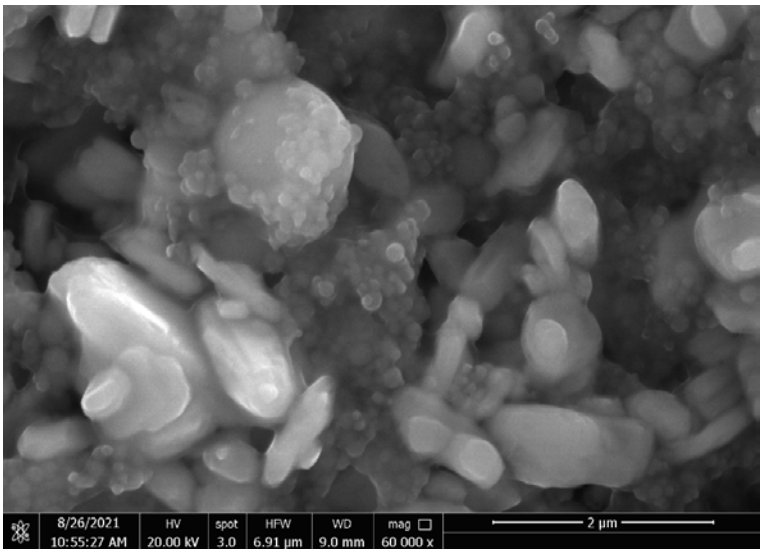

Figure 9.123 0-minute wait time V-Al/MoO_3 Layer 6.

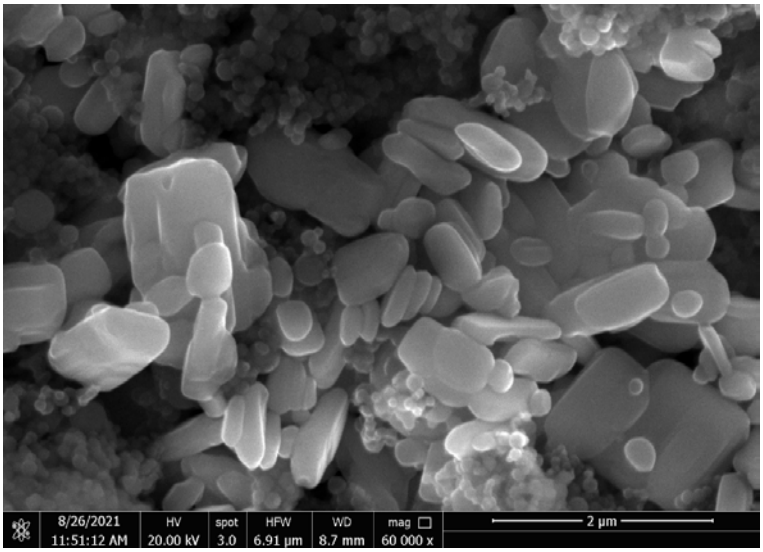

Figure 9.124 0-minute wait time V-Al/MoO_3 Layer 7.

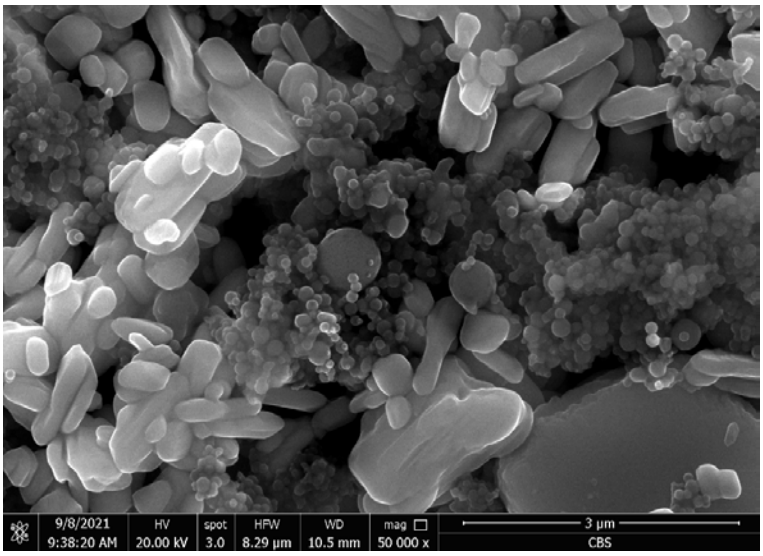

Figure 9.125 0-minute V-Al/MoO_3 Layer 8.

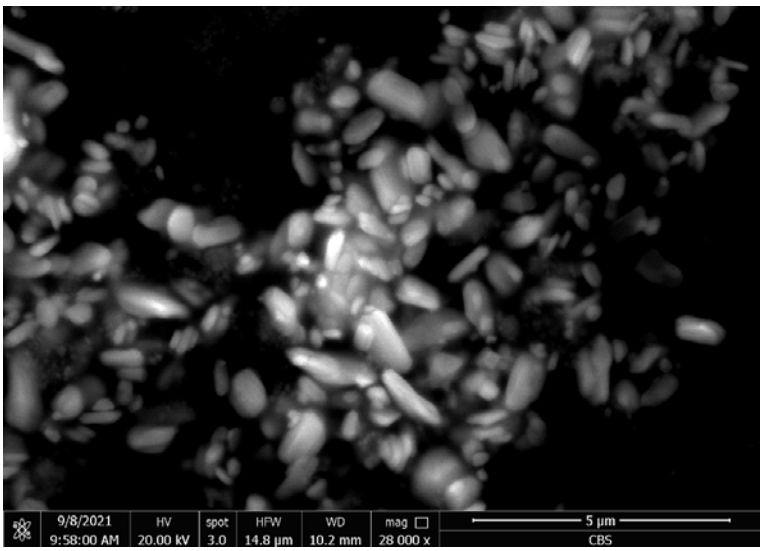

Figure 9.126 15-minute wait time V-Al/MoO_3 Layer 2.

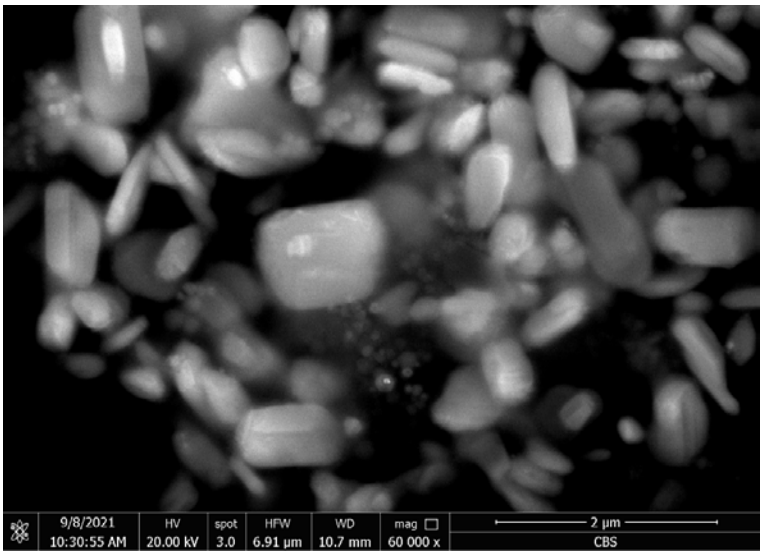

Figure 9.127 15-minute wait time V-Al/MoO_3 Layer 3.

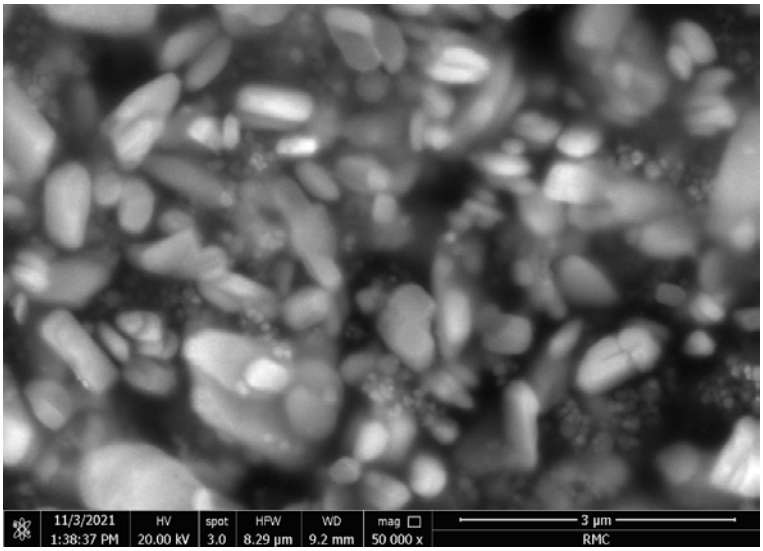

Figure 9.128 15-minute wait time V-Al/MoO_3 Layer 4.

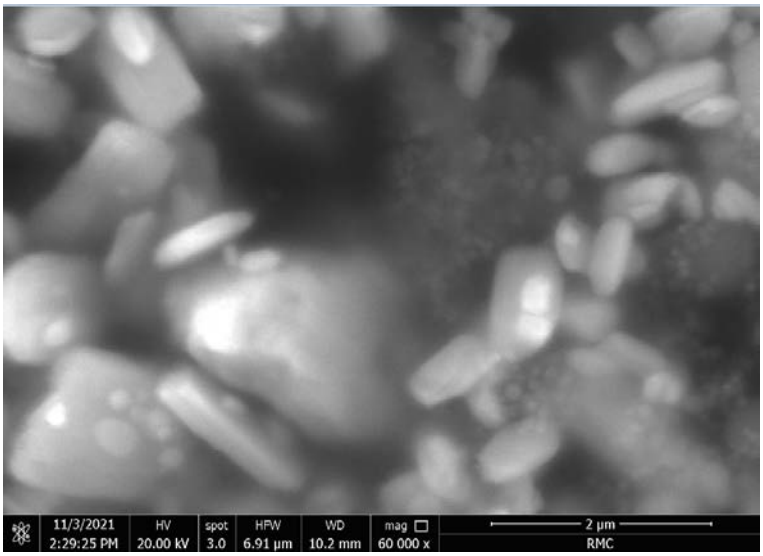

Figure 9.129 15-minute wait time V-Al/MoO_3 Layer 5.

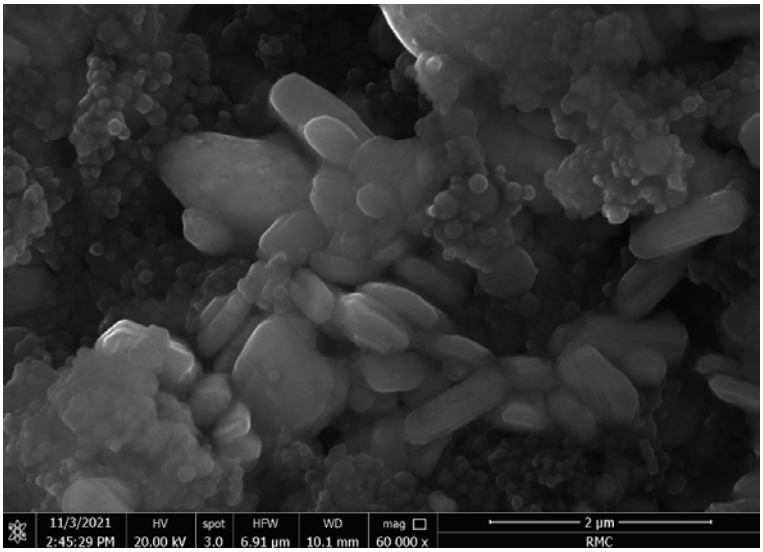

Figure 9.130 15-minute wait time V-Al/MoO_3 Layer 7.

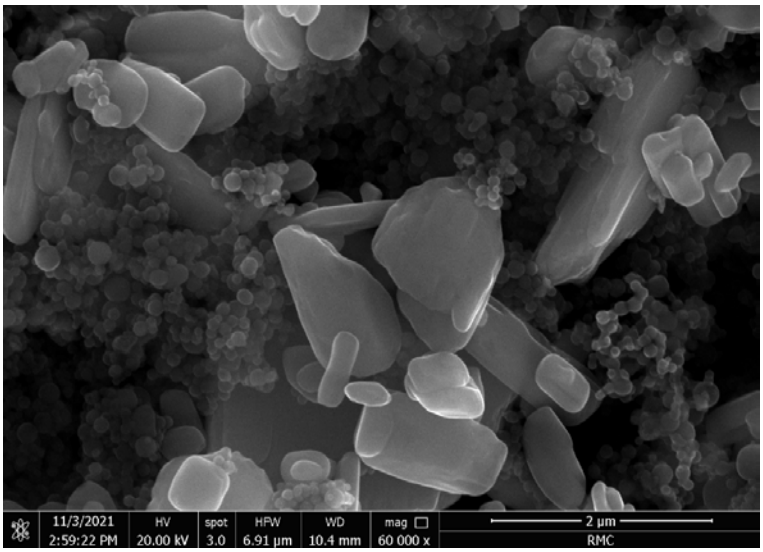

Figure 9.131 15-minute wait time V-Al/MoO_3 Layer 8.

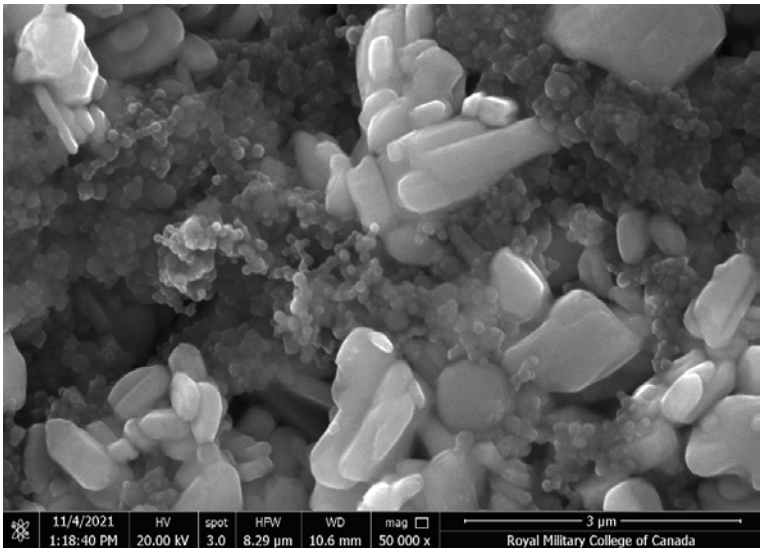

Figure 9.132 60-minute wait time V-Al/MoO_3 Layer 7.

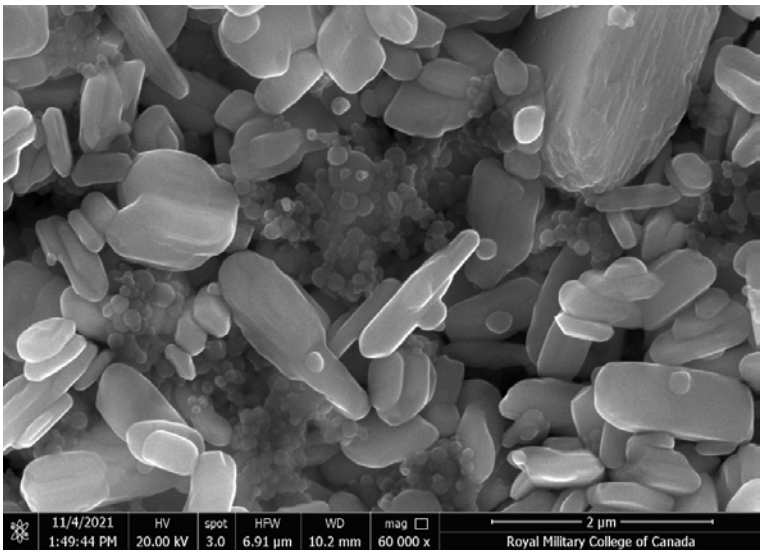

Figure 9.133 60-minute wait time V-Al/MoO_3 Layer 8.

Metal Molybdate

$MgMoO_4$

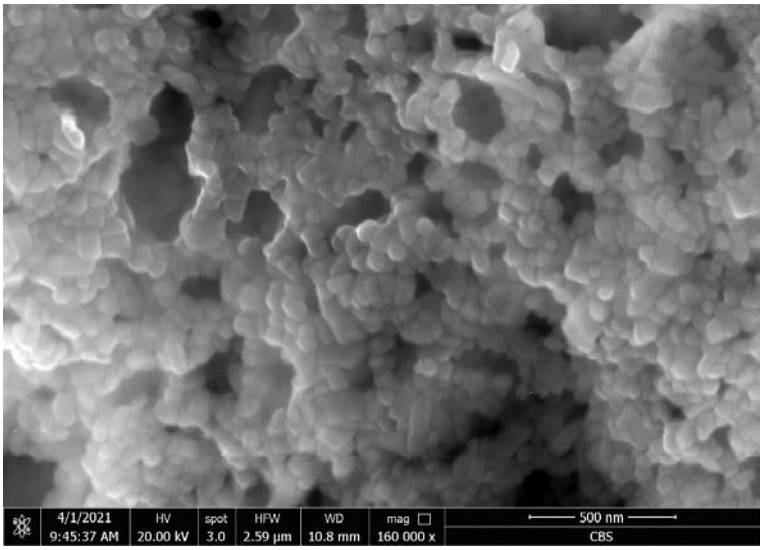

Figure 9.134 Pre-calcined $MgMoO_4$ synthesized using SCS.

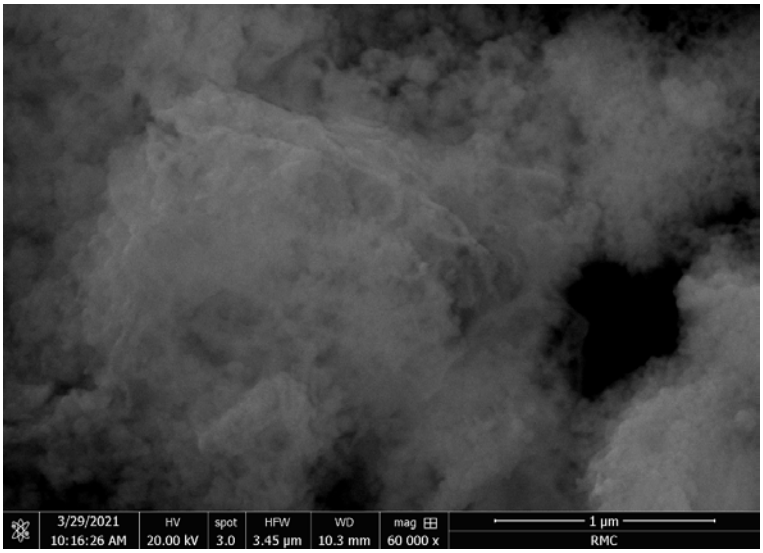

Figure 9.135 Post-calcinated $MgMoO_4$ synthesized using SCS.

$CaMoO_4$

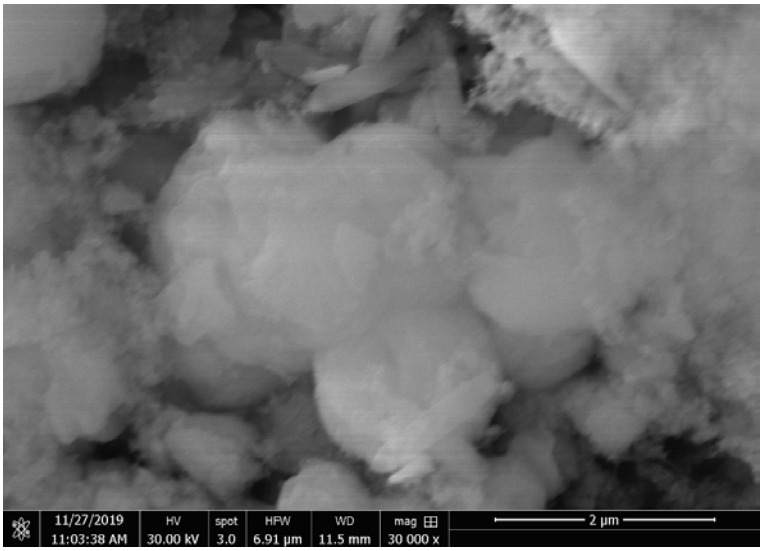

Figure 9.136 Pre-calcined $CaMoO_4$ synthesized using CPS Protocol 1.

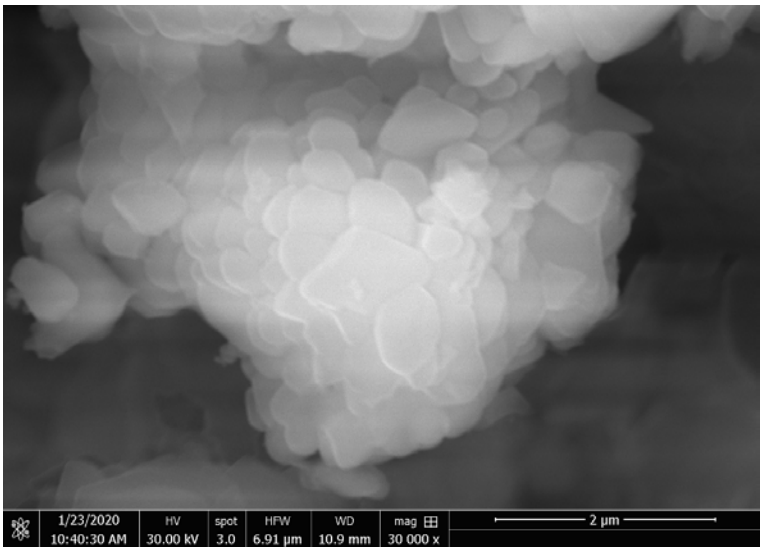

Figure 9.137 Post-calcined $CaMoO_4$ synthesized using CPS Protocol 1.

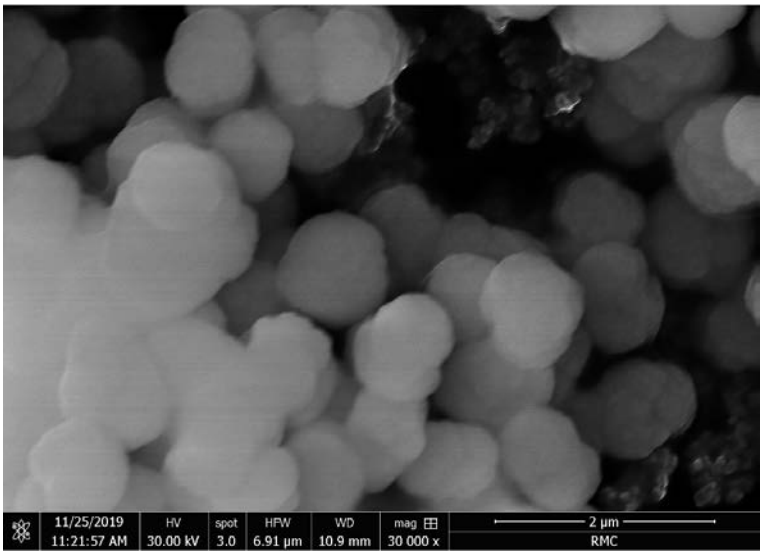

Figure 9.138 Pre-calcined $CaMoO_4$ synthesized using CPS Protocol 2.

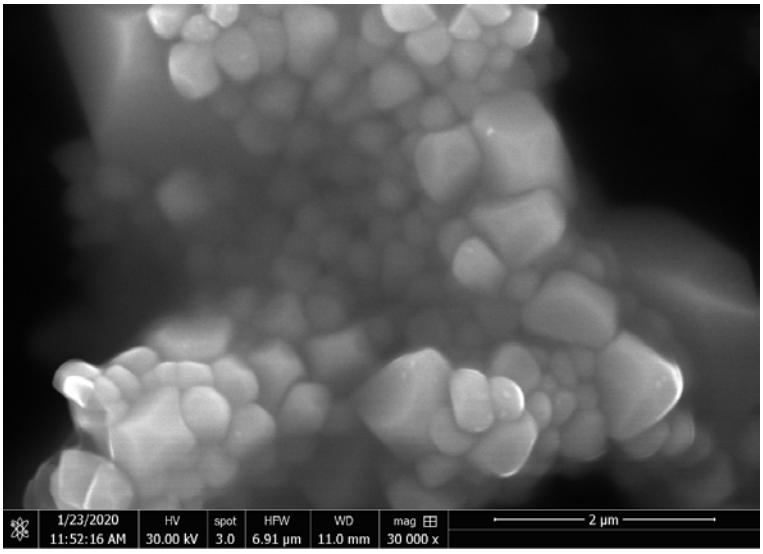

Figure 9.139 Post-calcined $CaMoO_4$ synthesized using CPS Protocol 2.

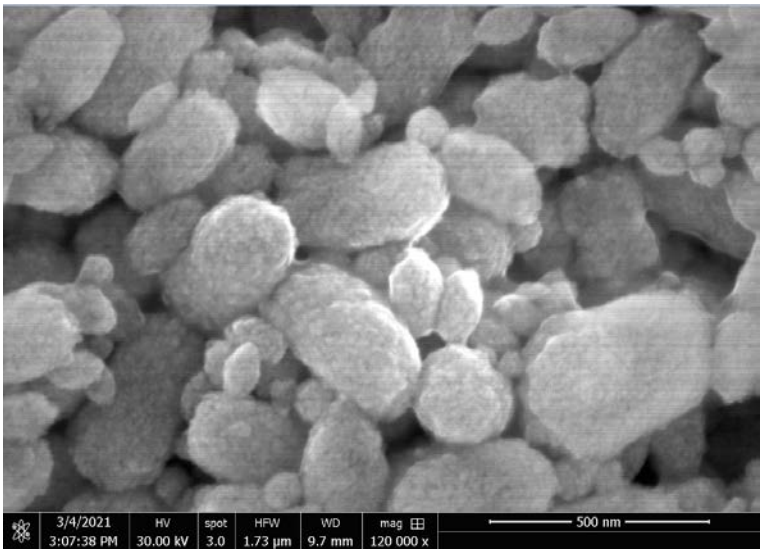

Figure 9.140 $CaMoO_4$ synthesized using CPS Protocol 3.

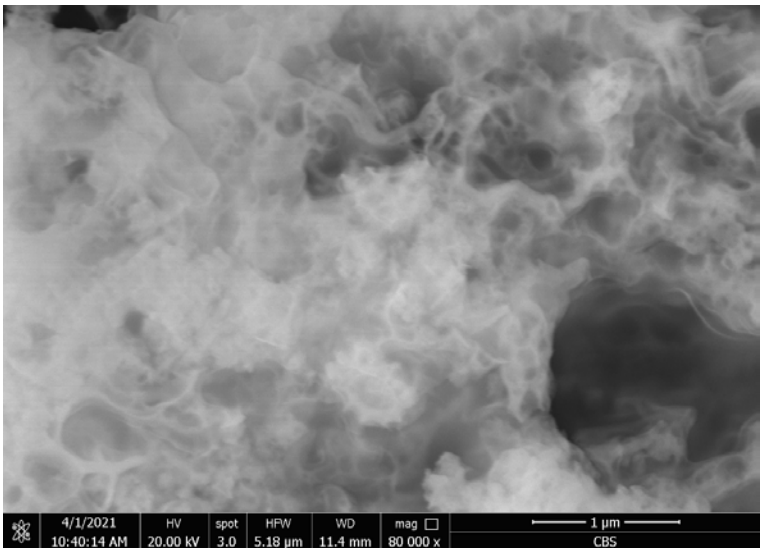

Figure 9.141 Pre-calcined $CaMoO_4$ synthesized using SCS.

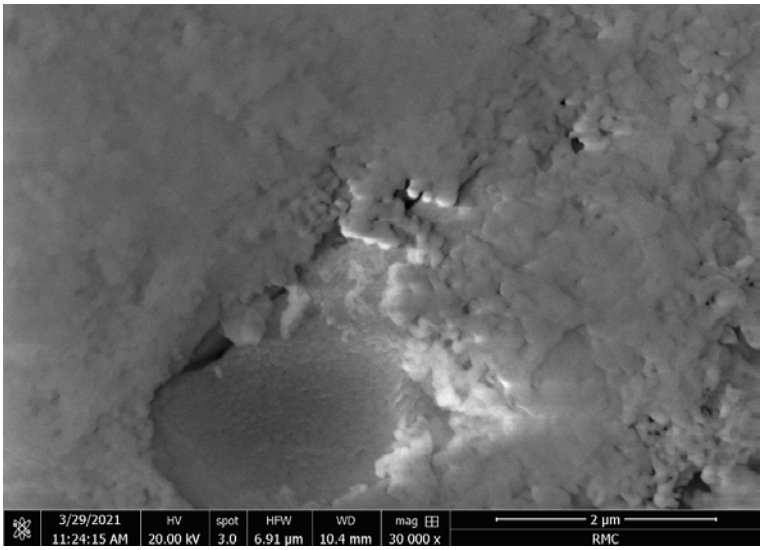

Figure 9.142 Post-calcined $CaMoO_4$ synthesized using SCS.

$SrMoO_4$

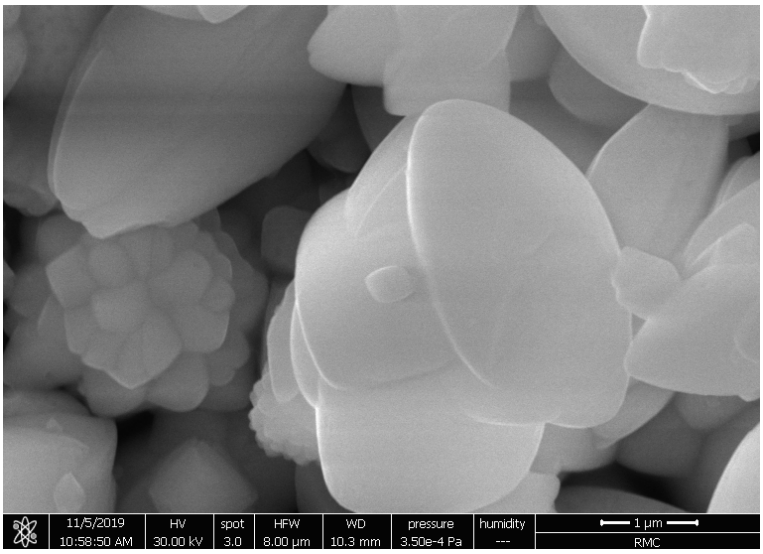

Figure 9.143 Pre-calcined $SrMoO_4$ synthesized using CPS Protocol 1.

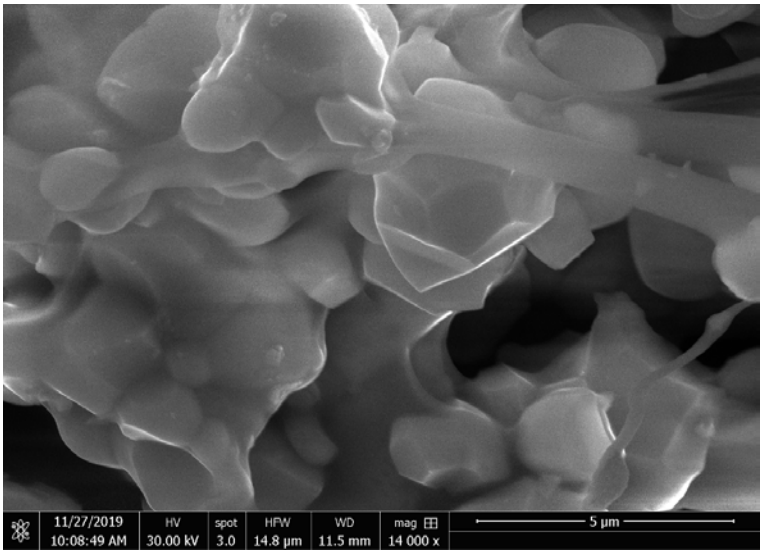

Figure 9.144 Post-calcined $SrMoO_4$ synthesized using CPS Protocol 1.

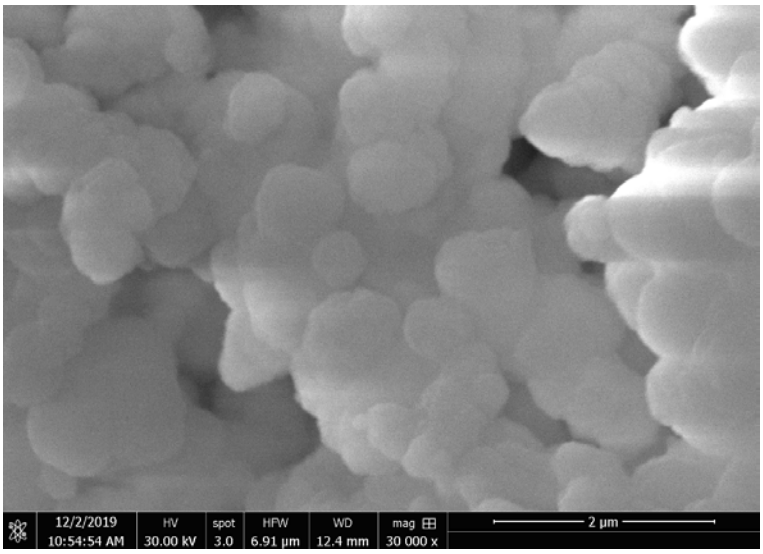

Figure 9.145 Pre-calcined $SrMoO_4$ synthesized using CPS Protocol 2.

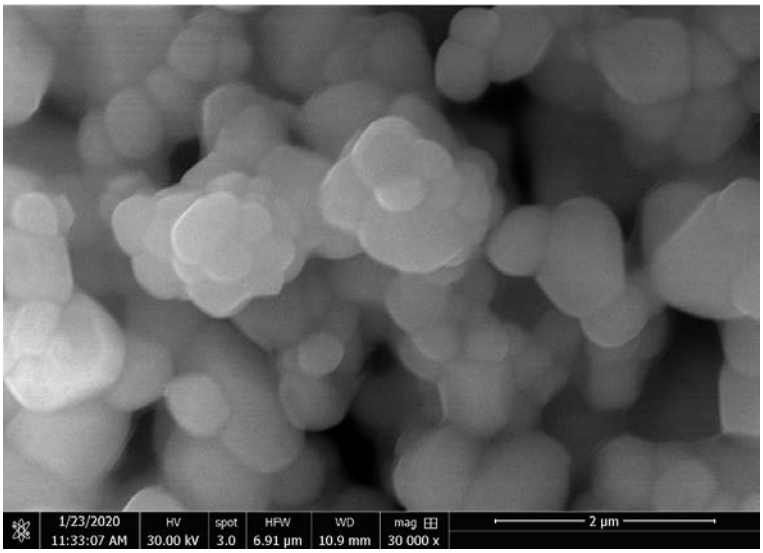

Figure 9.146 Post-calcined $SrMoO_4$ synthesized using Protocol 2.

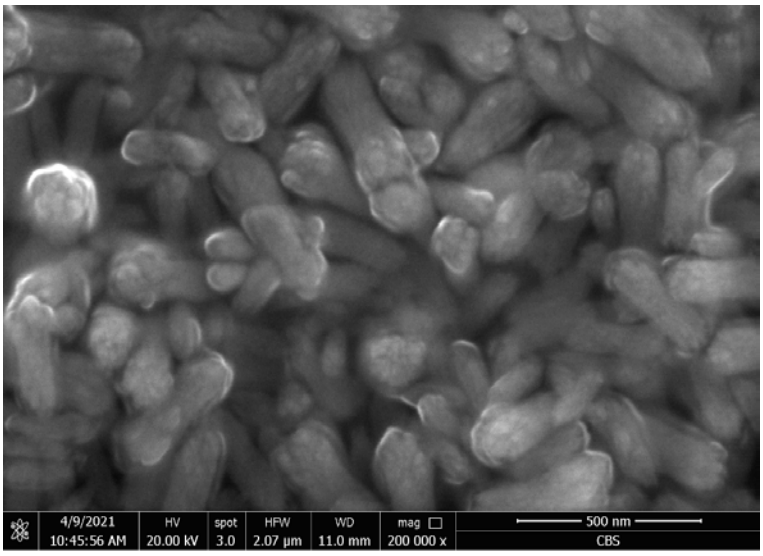

Figure 9.147 $SrMoO_4$ synthesized using CPS Protocol 3.

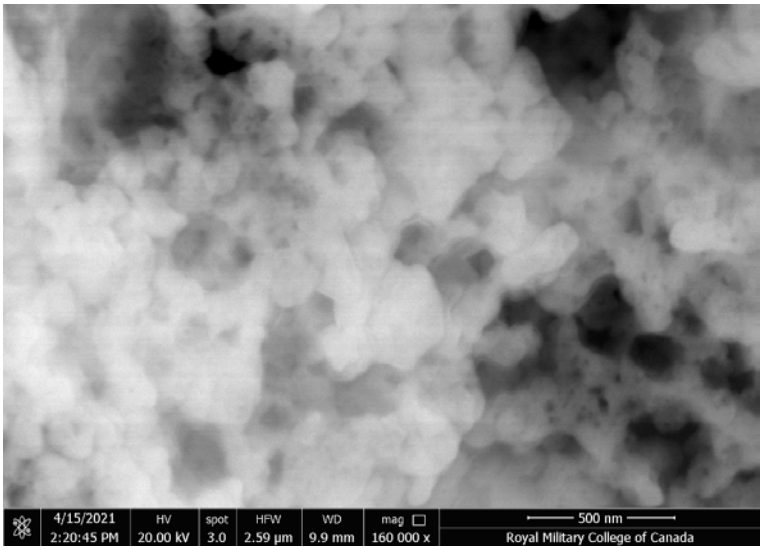

Figure 9.148 Pre-calcined $SrMoO_4$ synthesized using SCS.

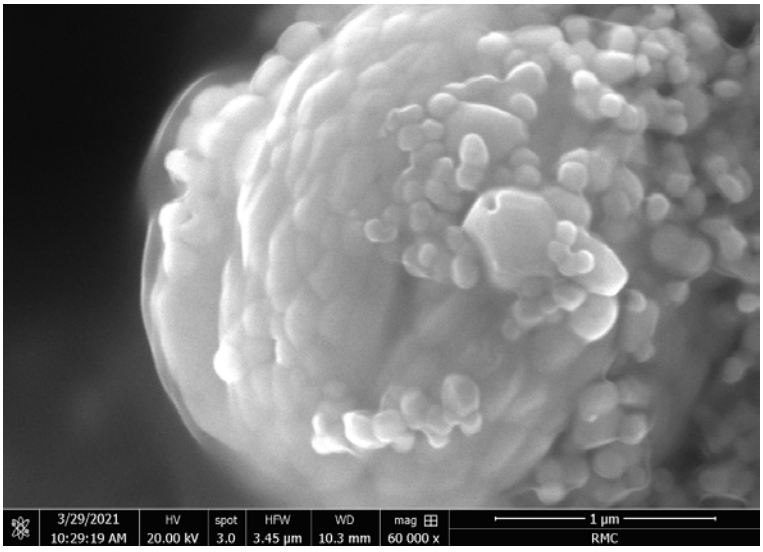

Figure 9.149 Post-calcined $SrMoO_4$ synthesized using SCS.

$BaMoO_4$

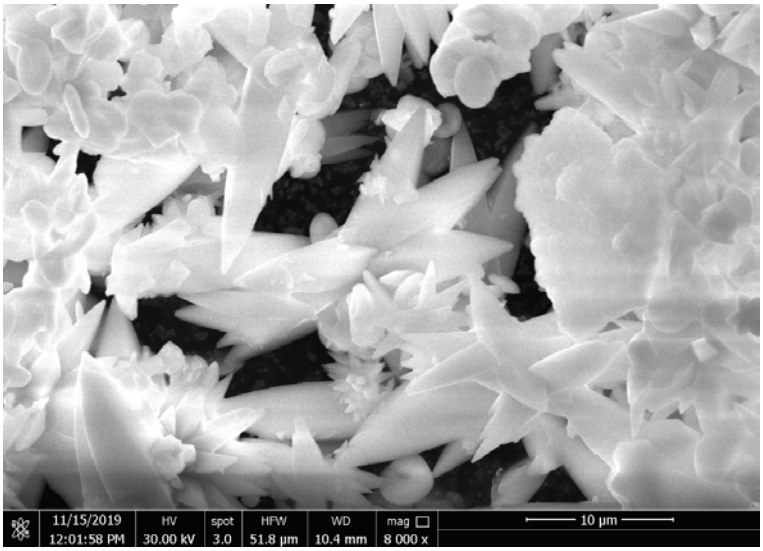

Figure 9.150 Pre-calcined $BaMoO_4$ synthesized using CPS Protocol 1.

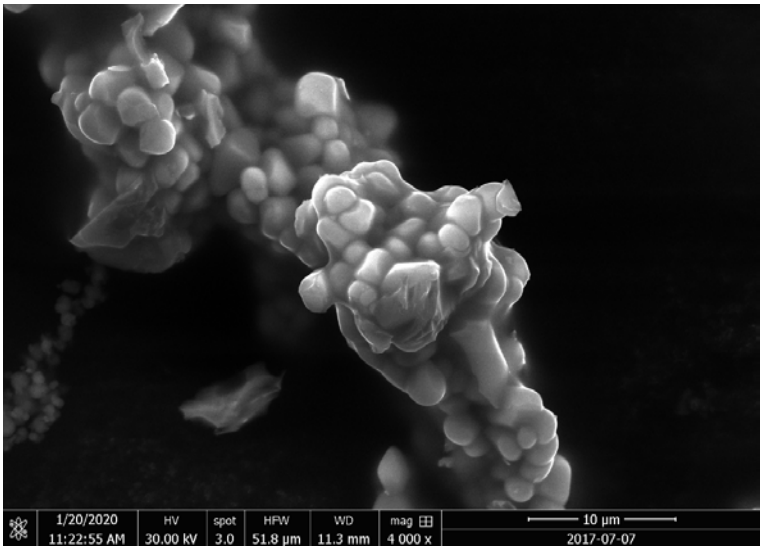

Figure 9.151 Post-calcined $BaMoO_4$ synthesized using CPS Protocol 1.

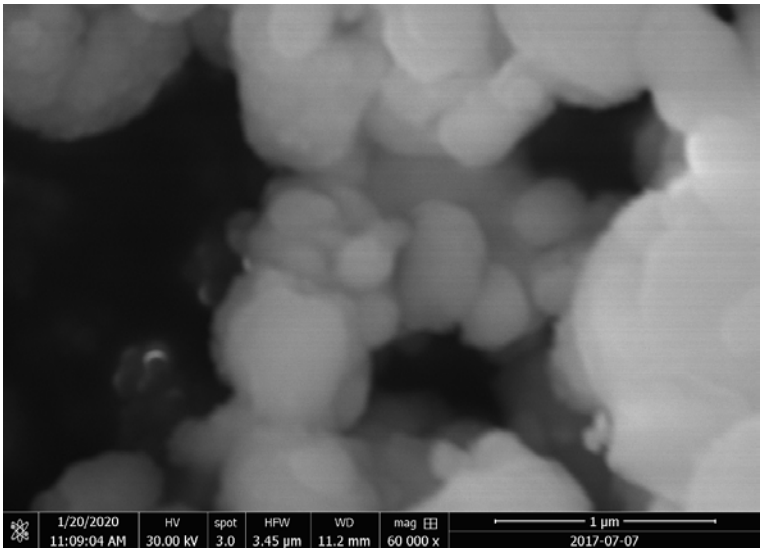

Figure 9.152 Pre-calcined $BaMoO_4$ synthesized using CPS Protocol 2.

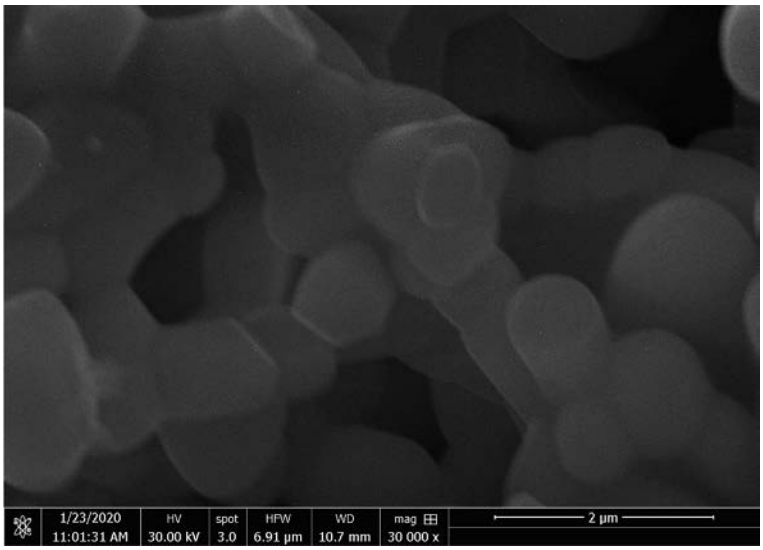

Figure 9.153 Post-calcined $BaMoO_4$ synthesized using CPS Protocol 2.

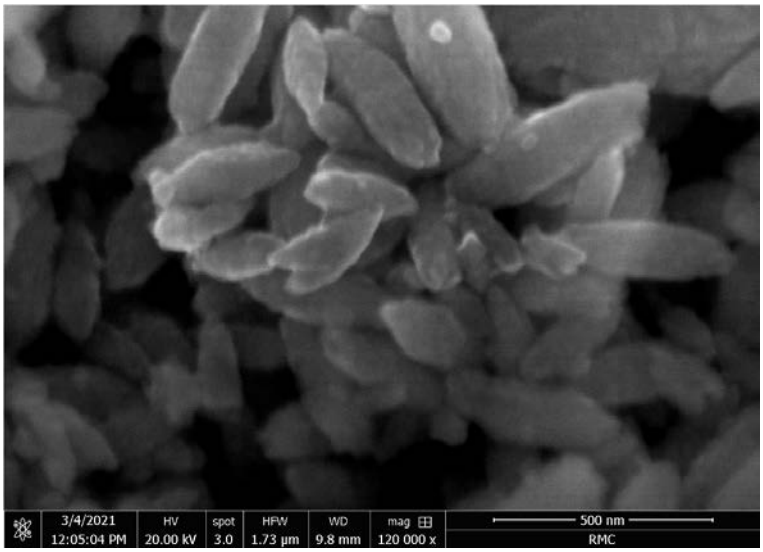

Figure 9.154 $BaMoO_4$ synthesized using CPS Protocol 3.

$NiMoO_4$

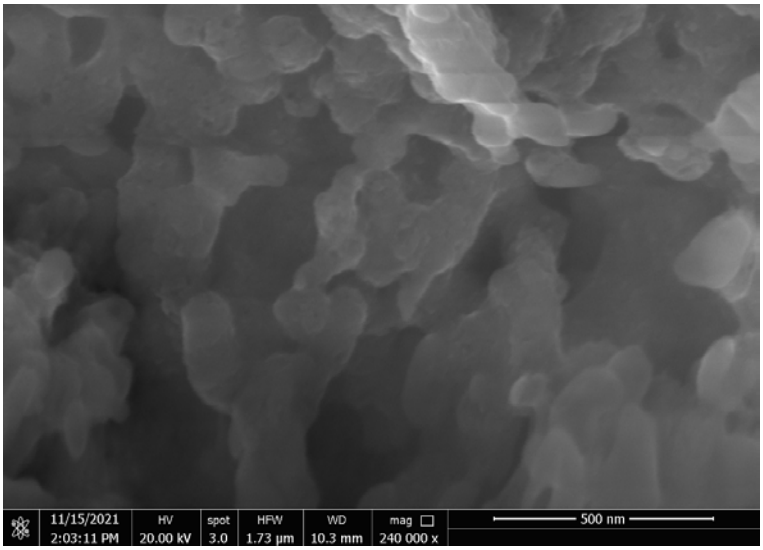

Figure 9.155 $NiMoO_4$ synthesized using SCS in the microwave at 800W.

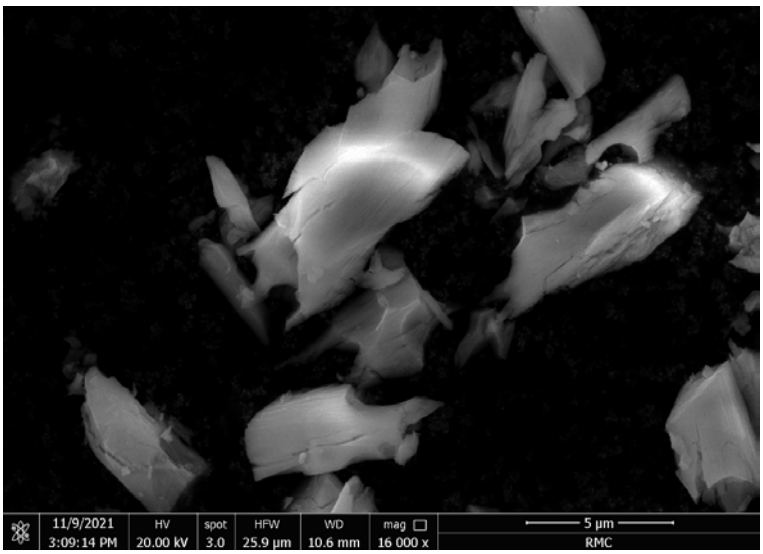

Figure 9.156 $NiMoO_4$ synthesized using SCS in the microwave at 1600W.

$ZnMoO_4$

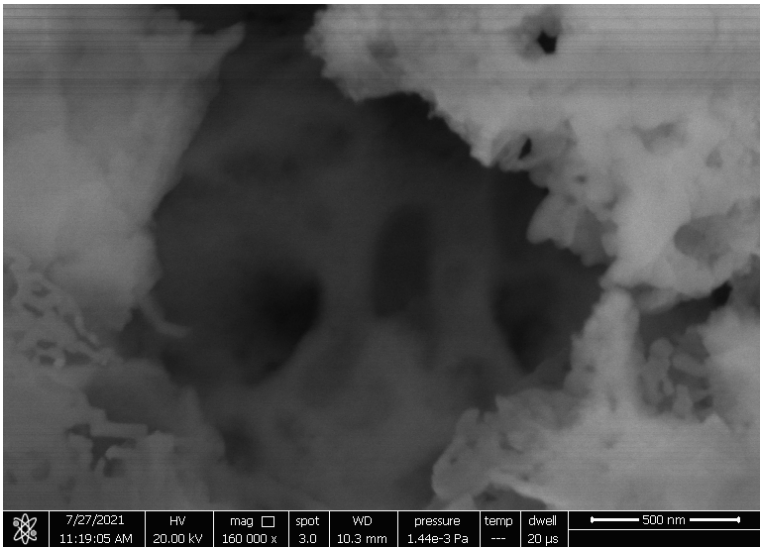

Figure 9.157 $ZnMoO_4$ synthesized using the muffle furnace at 550^oC.

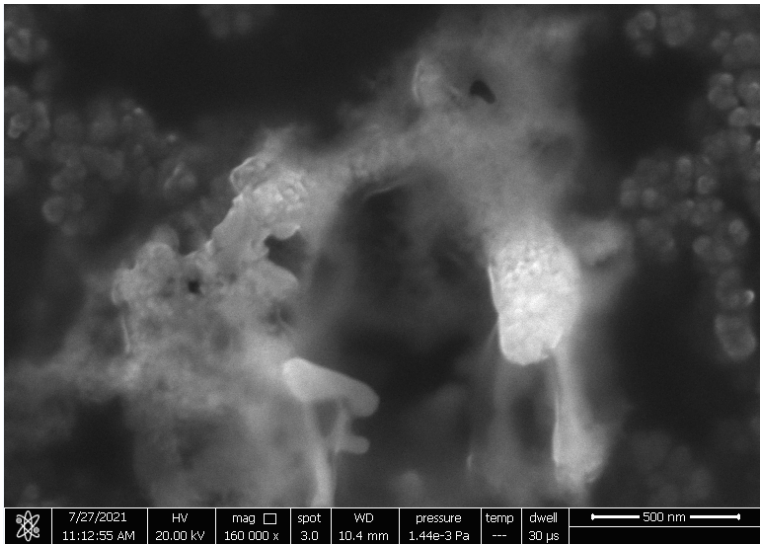

Figure 9.158 $ZnMoO_4$ synthesized using SCS in the microwave at 800ºC.

$Fe_2(MoO_4)_3$

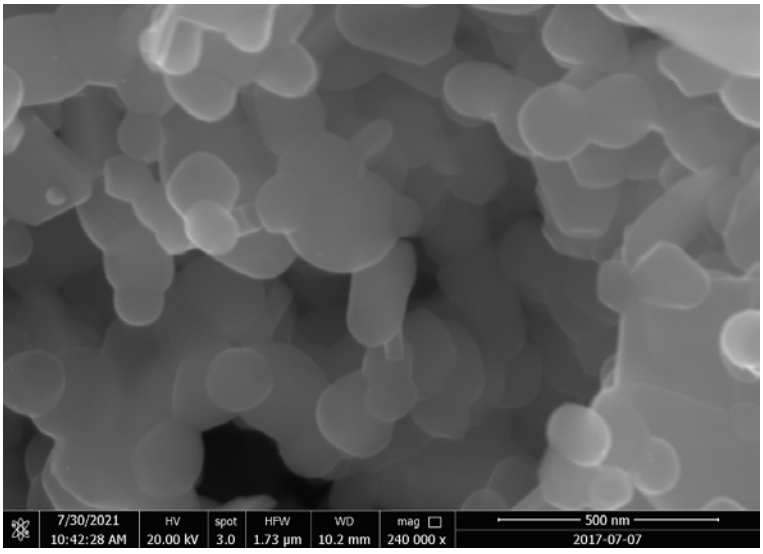

Figure 9.159 $Fe_2(MoO_4)_3$ synthesized using SCS in the muffle furnace.

Nano Aluminum

Alex

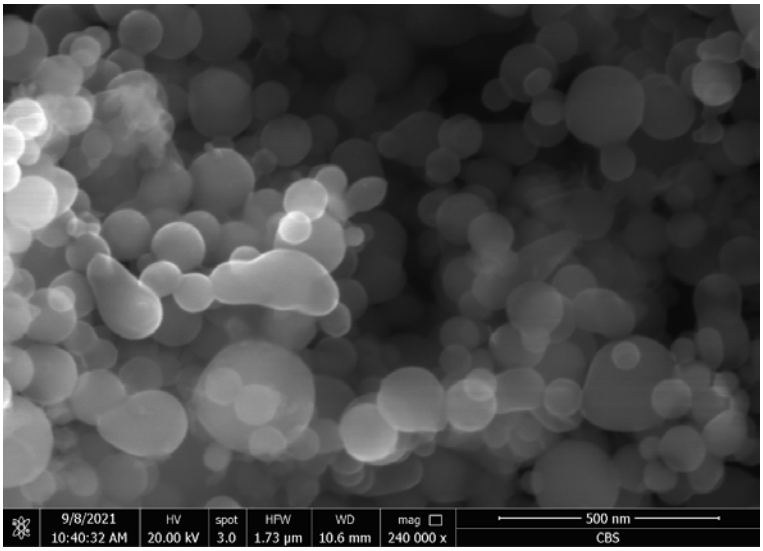

Figure 9.160 Alex.

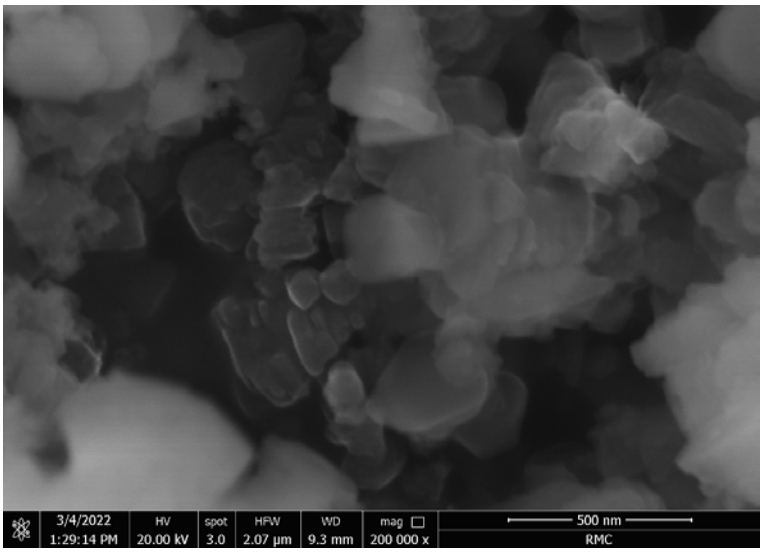

Figure 9.161 Oxidized Alex.

Al/Molybdate Nanothermites

Al/$MgMoO_4$

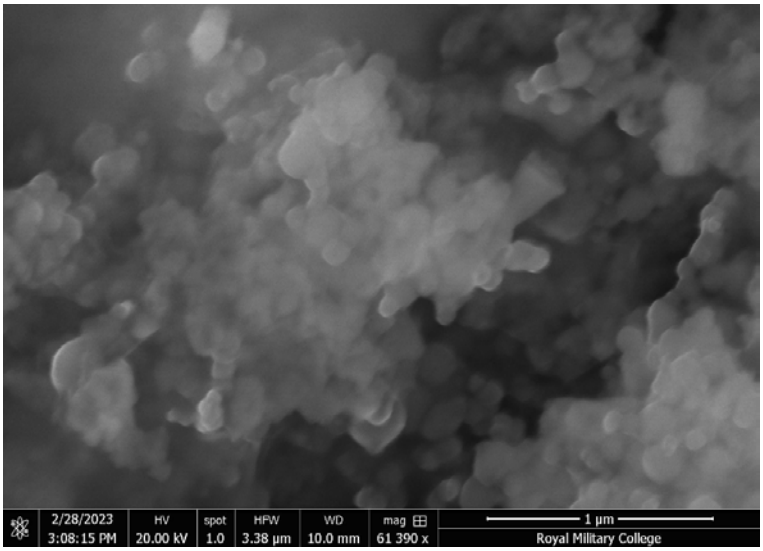

Figure 9.162 Al/$MgMoO_4$ (SCS).

Al/$CaMoO_4$

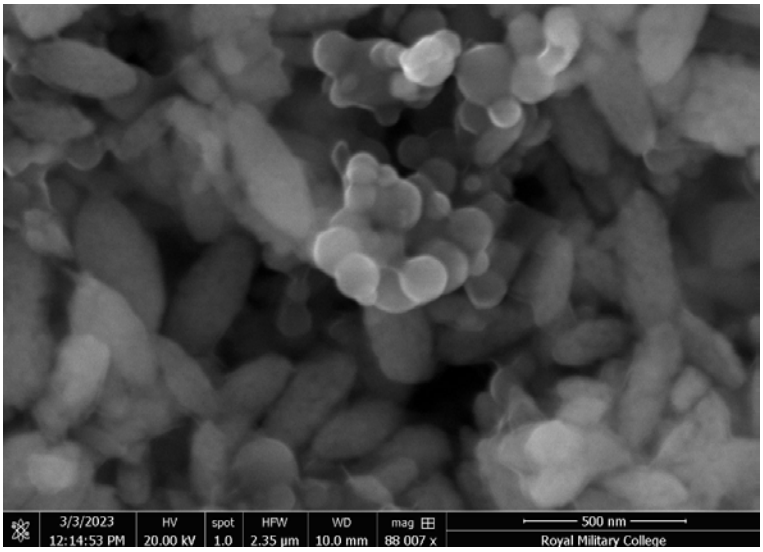

Figure 9.163 Al/$CaMoO_4$ (CPS).

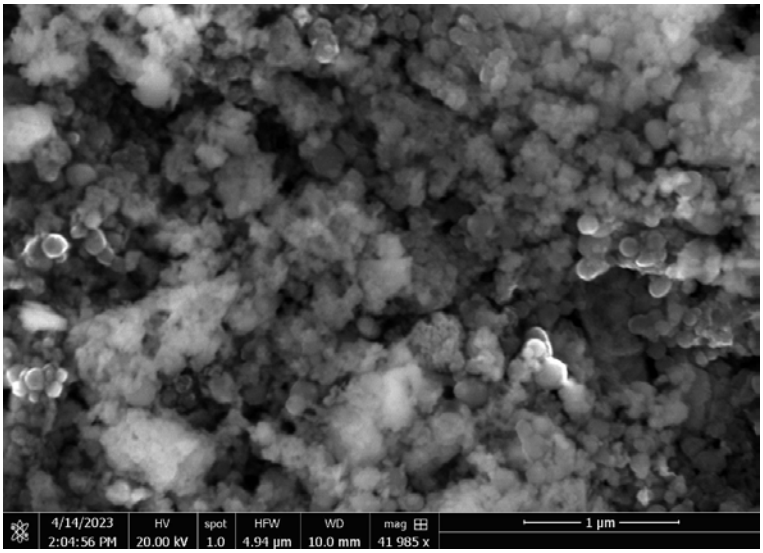

Figure 9.164 Al/$CaMoO_4$ (SCS).

Al/$SrMoO_4$

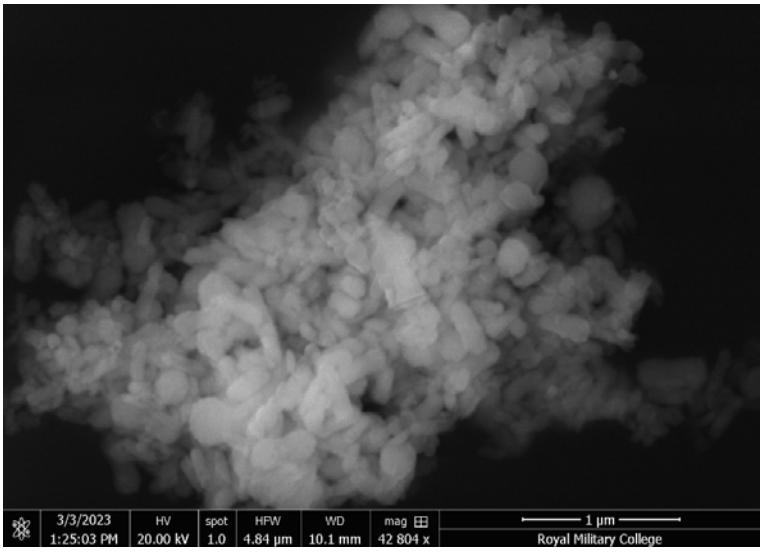

Figure 9.165 Al/$SrMoO_4$ (CPS).

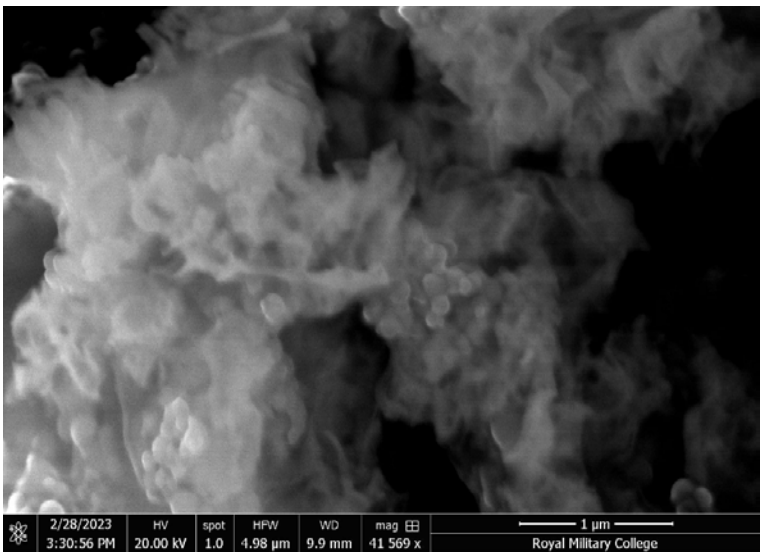

Figure 9.166 Al/$SrMoO_4$ (SCS).

Al/$BaMoO_4$

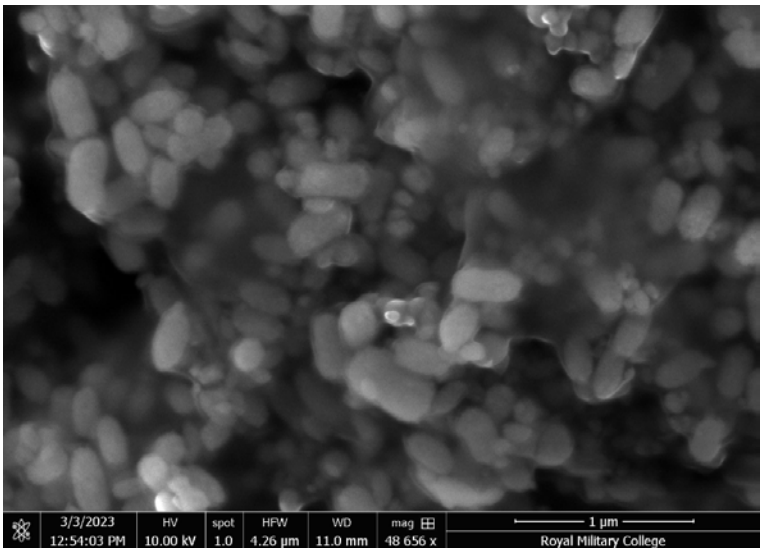

Figure 9.167 Al/$BaMoO_4$ (CPS).

10. Appendix D – Zeta Potential Spectrum

MoO_3

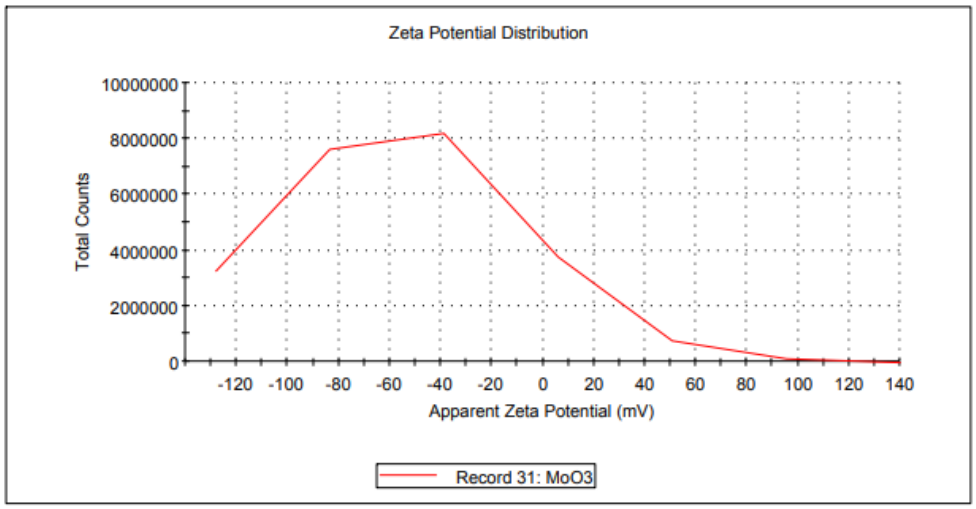

Figure 10.168 Zeta potential distribution of MoO_3 in IPA at 0.5% loading

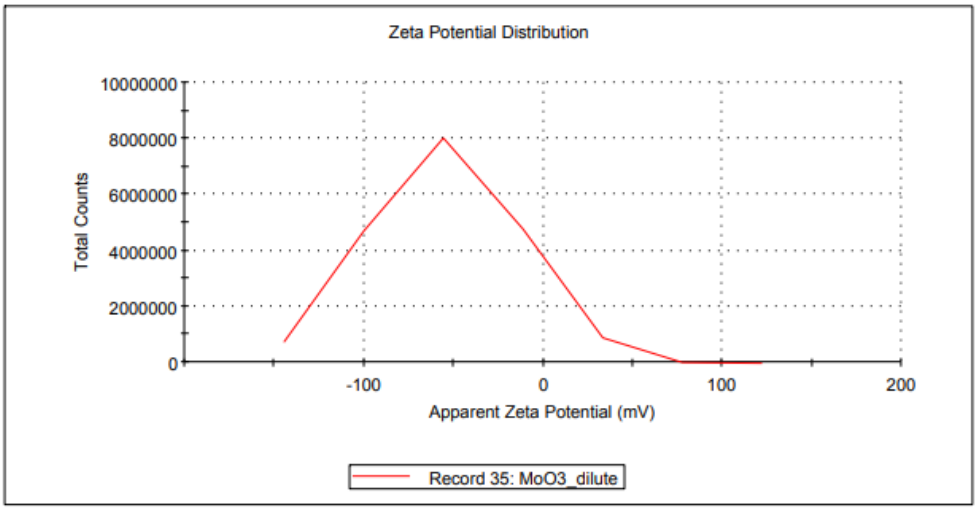

Figure 10.169 Zeta potential distribution of MoO_3 in IPA at 0.1% loading

O-Al

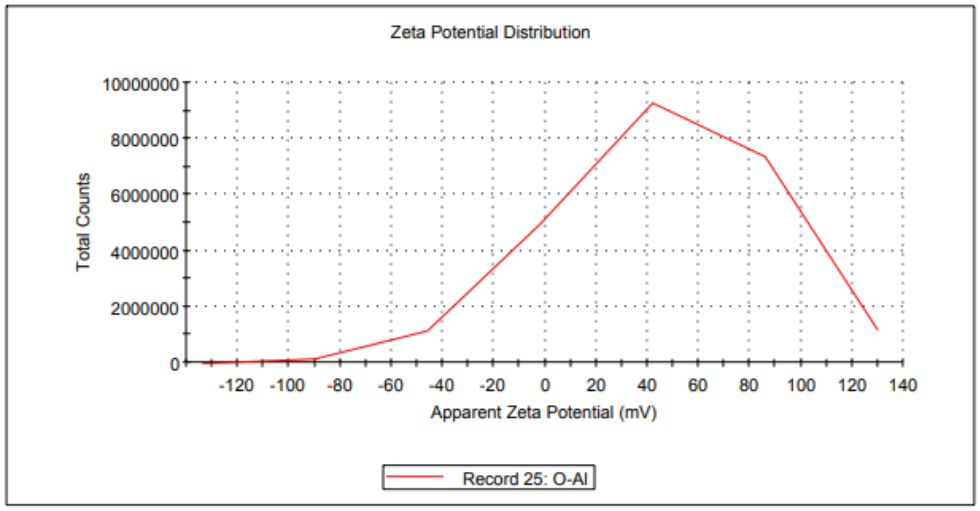

Figure 10.170 Zeta potential distribution of O-Al in IPA at 0.5% loading

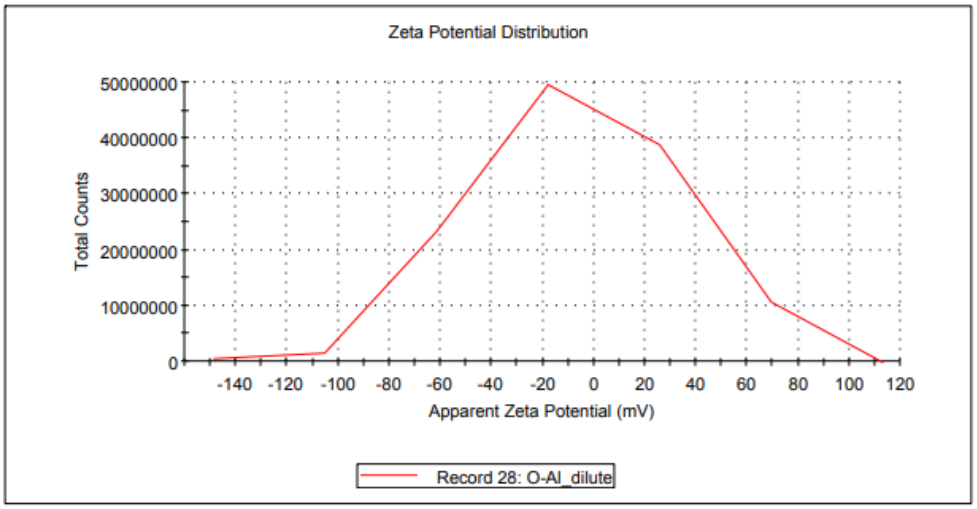

Figure 10.171 Zeta potential distribution of O-Al in IPA at 0.1% loading

L-Al

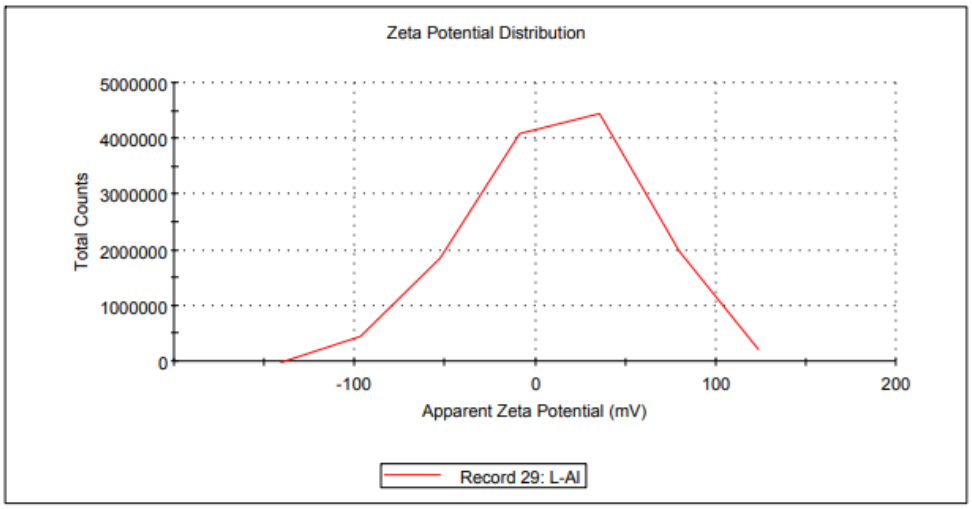

Figure 10.172 Zeta potential distribution of L-Al in IPA at 0.5% loading

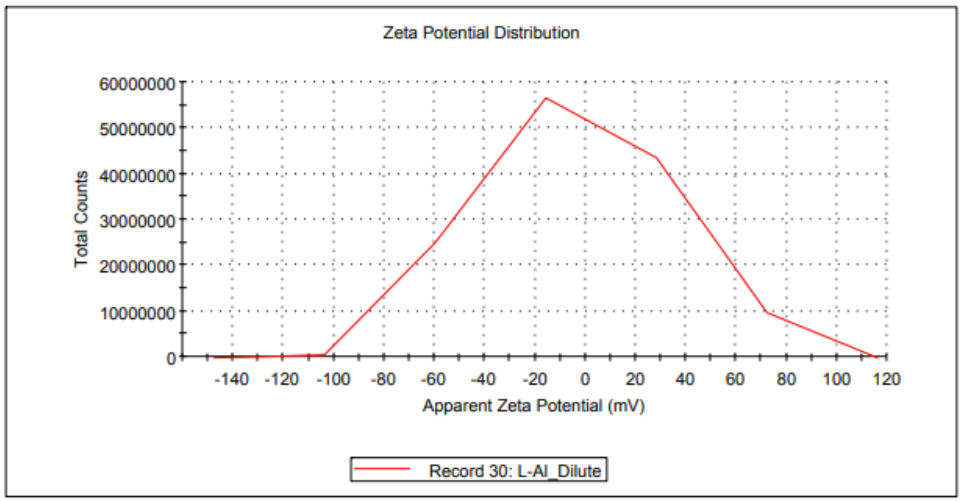

Figure 10.173 Zeta potential distribution of L-Al in IPA at 0.1% loading.

V-Al

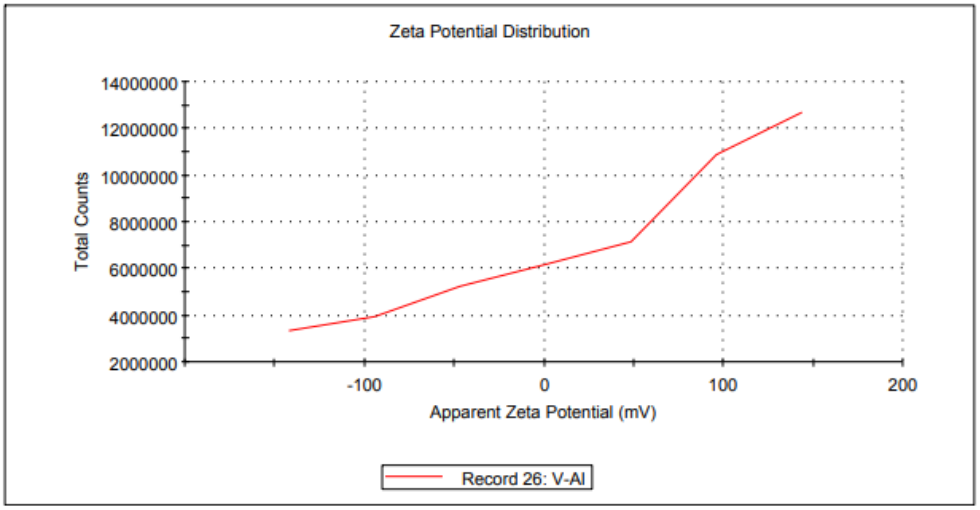

Figure 10.174 Zeta potential distribution of V-Al in IPA at 0.5% loading.

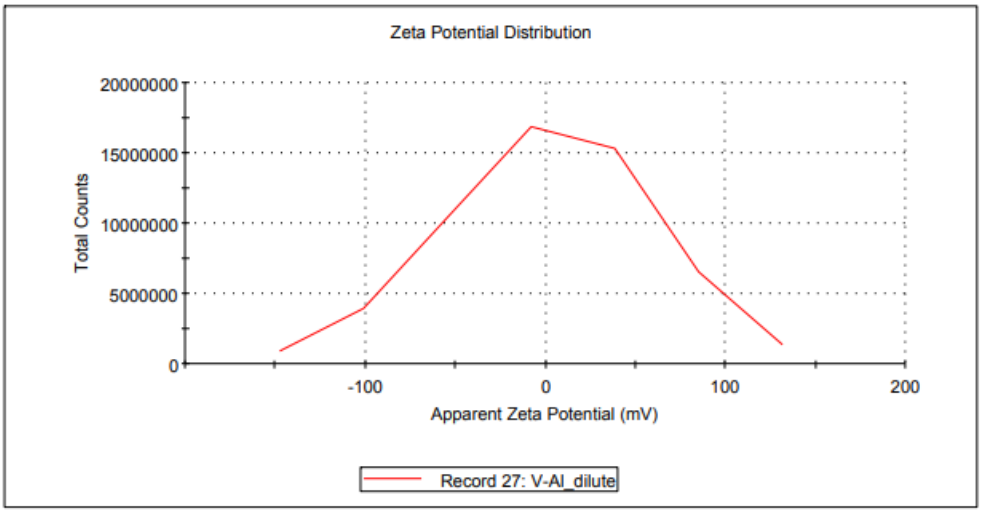

Figure 10.175 Zeta potential distribution of V-Al in IPA at 0.1% loading.

11. Appendix E – Autosorb Isotherms

$MgMoO_4$

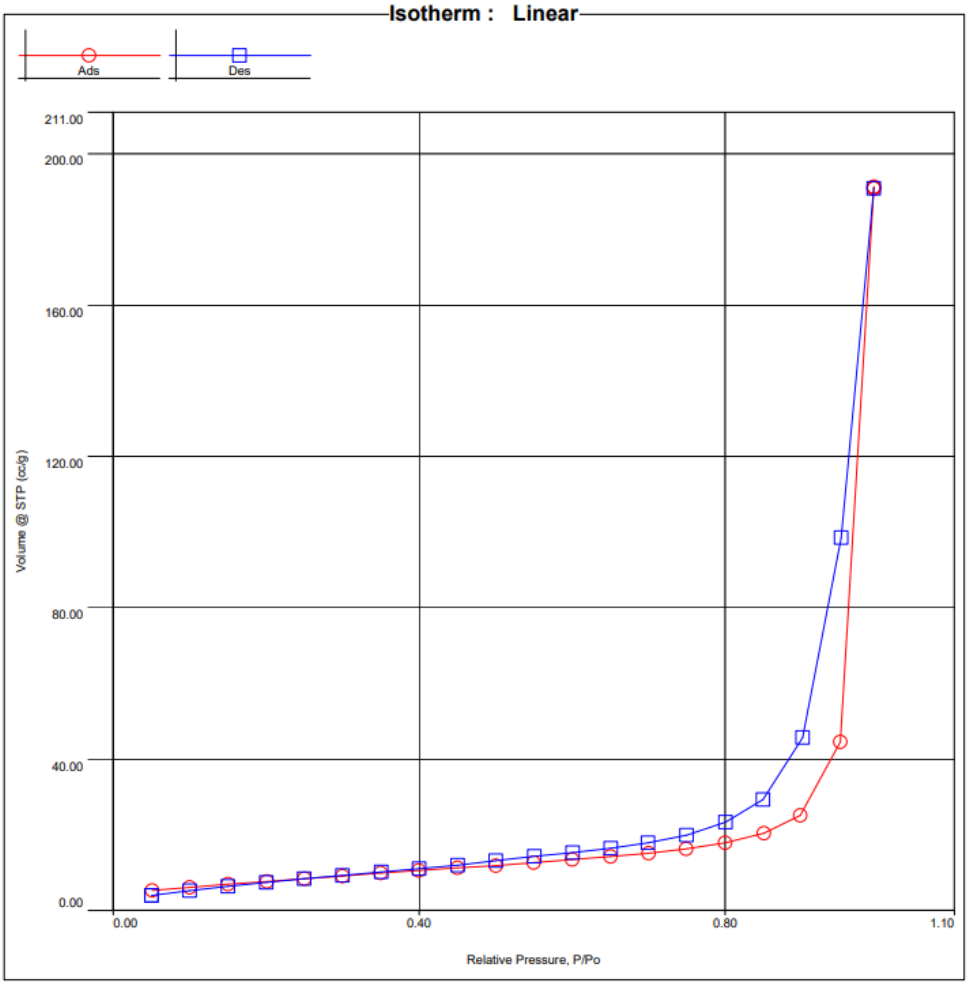

Figure 11.176 Isotherm of $MgMoO_4$ synthesized using SCS.

$CaMoO_4$

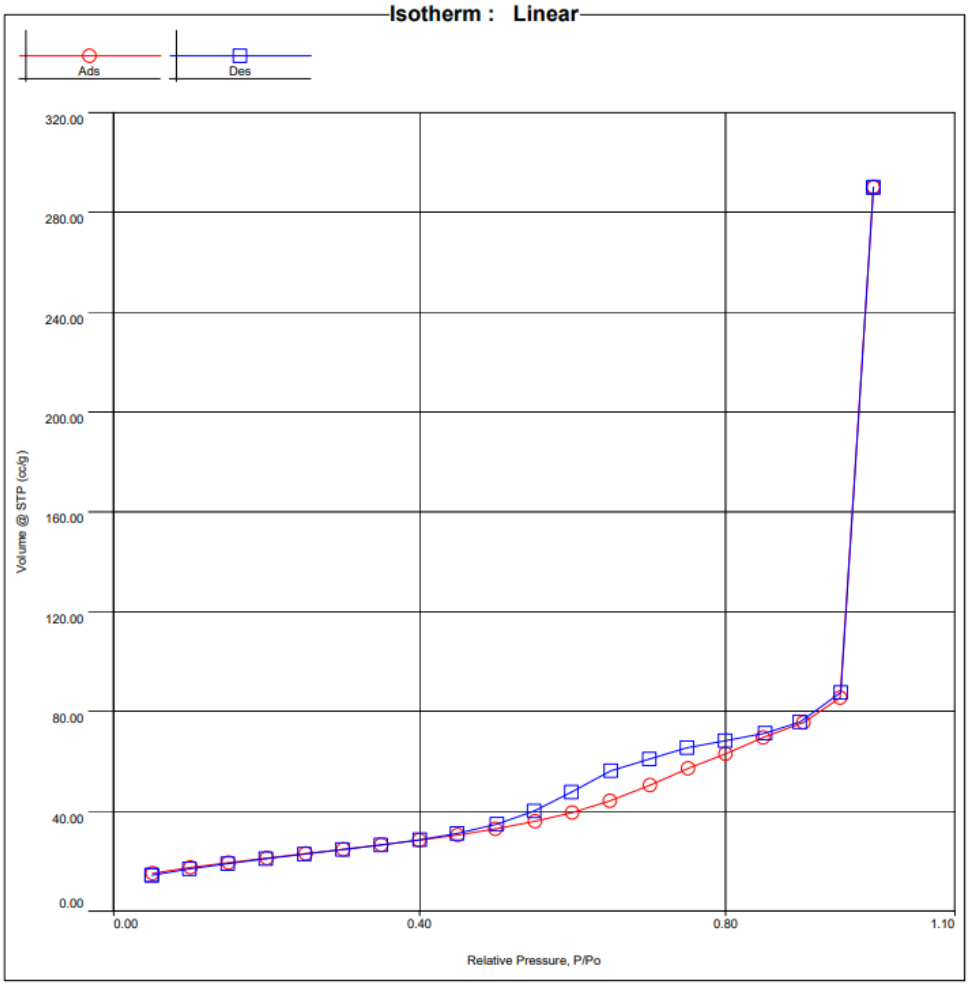

Figure 11.177 Isotherm of $CaMoO_4$ synthesized using CPS Protocol 3.

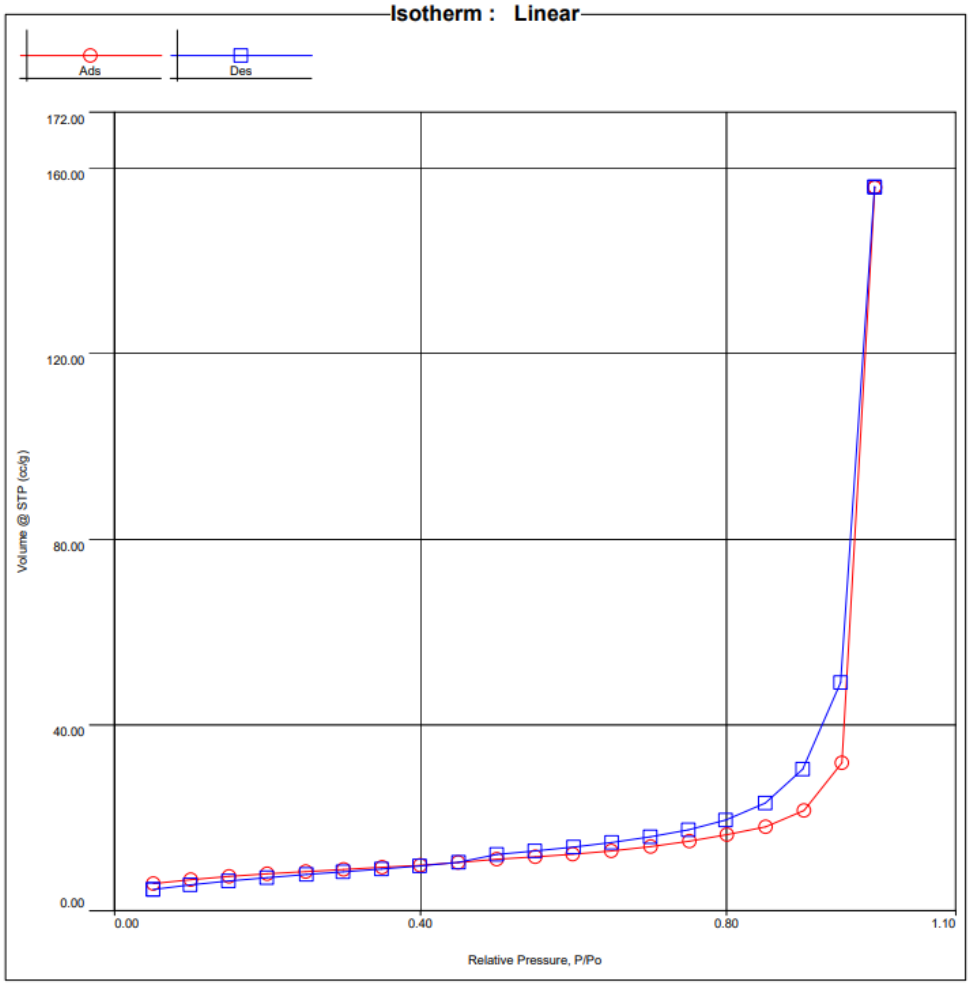

Figure 11.178 Isotherm of $CaMoO_4$ synthesized using SCS.

$SrMoO_4$

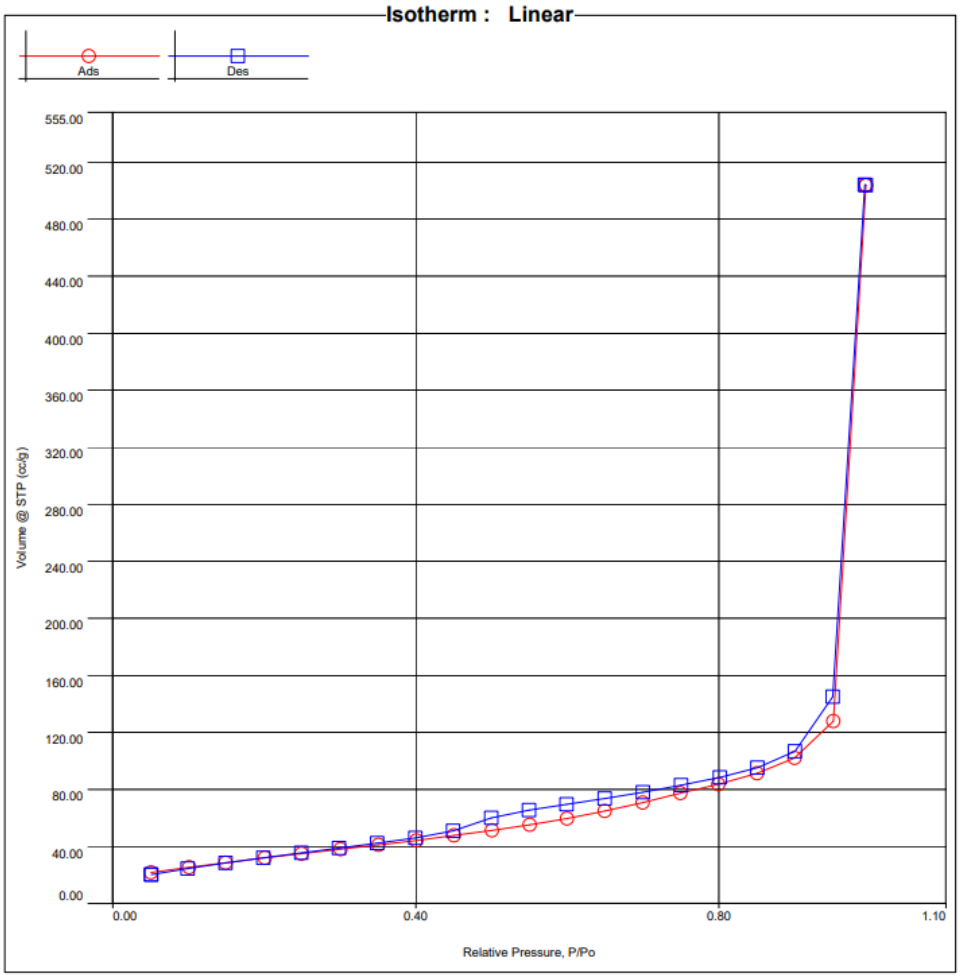

Figure 11.179 Isotherm of $SrMoO_4$ synthesized using CPS Protocol 3.

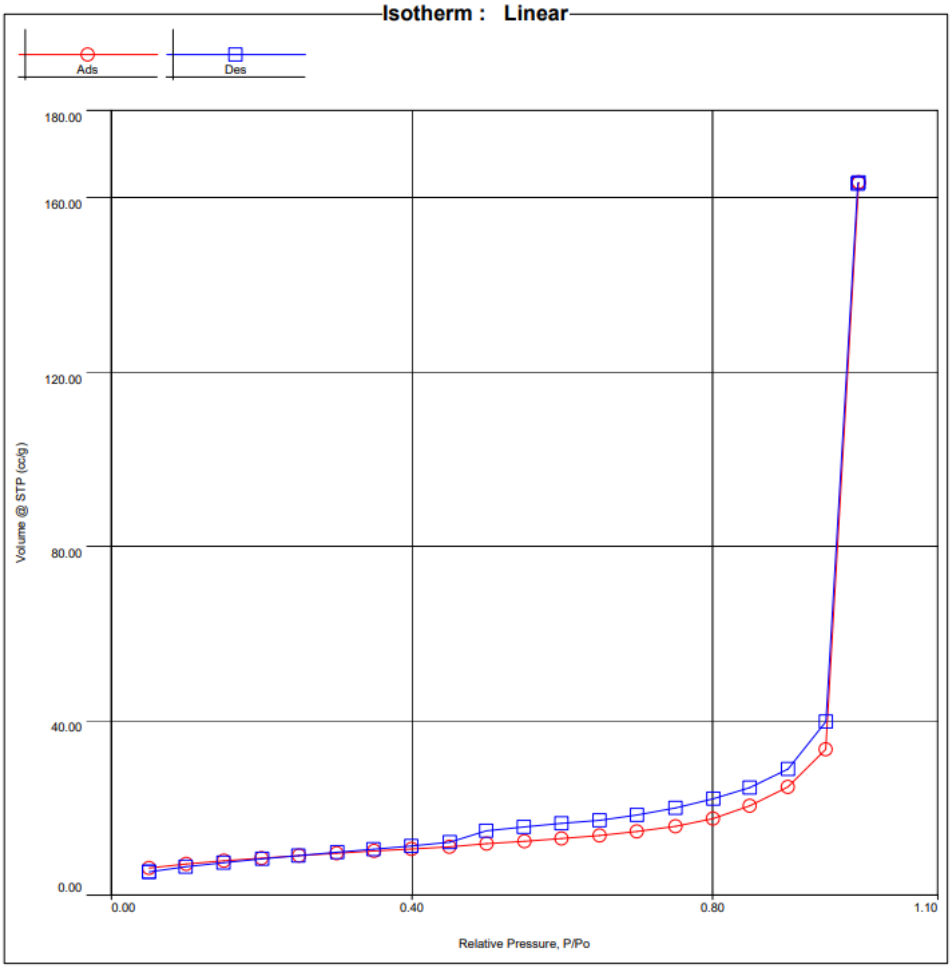

Figure 11.180 Isotherm of $SrMoO_4$ synthesized using SCS.

$BaMoO_4$

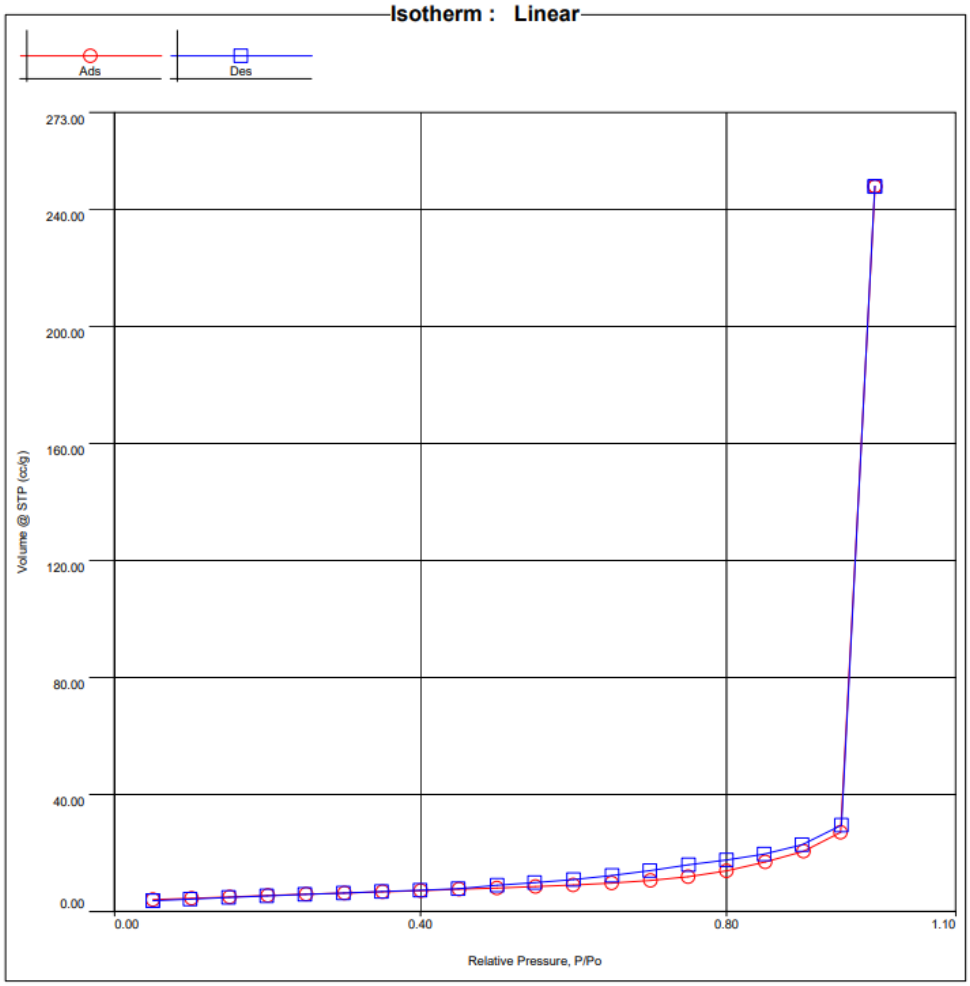

Figure 11.181 Isotherm of $BaMoO_4$ synthesized using CPS Protocol 3.